THÈSE

Pour obtenir le grade de

DOCTEUR DE L'UNIVERSITÉ GRENOBLE ALPES

École doctorale : EEATS - Electronique, Electrotechnique, Automatique, Traitement du Signal Spécialité : Génie électrique
Unité de recherche : Laboratoire de Génie Electrique

Interopérabilité multi-fournisseur des réseaux à courant continu multi- terminaux basés sur des convertisseurs modulaires multiniveaux

Évaluation de la stabilité et amélioration des procédures d'essais de conformité.

Multi-Vendor Interoperability of Modular Multilevel Converter-Based Multi-Terminal HVDC Grids

Stability Assessment and Improvement of Compliance Testing Procedures

Présentée par :

Mohamed ELSODANY

Direction de thèse :

Seddik BACHA PROFESSEUR DES UNIVERSITES, Université de Guyane	Directeur de thèse
Jing DAI MCF, Université Paris-Saclay GS Sciences de l'ingénierie et des systèmes	Co-encadrant de thèse
Kosei SHINODA Ingénieur docteur, SuperGrid Institute	Co-encadrant de thèse

Rapporteurs :

Kambiz TEHRANI
MAITRE DE CONFERENCES, INP Clermont-Auvergne
Mohamad Alaa Eddin ALALI
MAITRE DE CONFERENCES, École Nationale Supérieure de l'Électronique et de ses Applications, Cergy

Thèse soutenue publiquement le **28 mai 2026**, devant le jury composé de :

Raphaël CAIRE, PROFESSEUR DES UNIVERSITES, Universite Claude Bernard	Président de jury
Seddik BACHA, PROFESSEUR DES UNIVERSITES, Université de Guyane	Directeur de thèse
Kambiz TEHRANI, MAITRE DE CONFERENCES, INP Clermont-Auvergne	Rapporteur
Mohamad Alaa Eddin ALALI, MAITRE DE CONFERENCES, École Nationale Supérieure de l'Électronique et de ses Applications, Cergy	Rapporteur

Invités :

Taoufik QORIA
INGENIEUR DOCTEUR, GE Vernova
Vincent DEBUSSCHERE
MAITRE DE CONFERENCES, Grenoble INP – UGA
Sebastian SILVANT
INGENIEUR, SuperGrid Institute

Abstract

The transition from point-to-point (PtP) high-voltage direct current (HVDC) systems to multi-terminal HVDC (MTDC) grids for the bulk transmission of offshore wind energy offers significant opportunities while simultaneously introducing new challenges related to control and protection. Future large-scale MTDC grids will likely integrate converter stations from multiple manufacturers. Consequently, these converters must operate securely without access to proprietary internal models due to intellectual property constraints.

The Modular Multilevel Converter (MMC) represents the state-of-the-art technology for MTDC applications, and its control system is critical to ensuring stable and reliable grid operation. Several control functionalities are essential, notably primary DC voltage control and grid-forming (GFM) control, which support the regulation of the DC voltage and AC grid frequency, respectively. However, the absence of standardized MMC control strategies, combined with the wide variety of their existing implementations, may lead to interoperability challenges that compromise MTDC grid performance and stability. Furthermore, interactions between MMC control and the interconnected DC network may give rise to adverse dynamic phenomena. Developing a clear understanding of these interactions is, therefore, essential for de-risking future multi-vendor HVDC grids.

This thesis addresses control interoperability in future multi-vendor MTDC systems, primarily through a small-signal stability analysis framework. Particular emphasis is placed on the dynamic considerations for primary DC voltage control, which constitutes the main local mechanism for maintaining the DC voltage within acceptable limits. Different implementation options are analyzed alongside their associated small-signal stability constraints, including their interaction with grid-forming control strategies. Subsequently, a new implementation of DC voltage droop combined with GFM control is proposed and analyzed, offering improved stability margins and enhanced dynamic performance compared to traditional approaches.

Furthermore, the interaction between MMC control dynamics and passive DC grid elements, including DC reactors (DCR), is investigated to identify stability limitations and underlying physical mechanisms. The impact of the MMC operating point and control mode, combined with the DCR size, is analyzed, and stability constraints are studied. A lead compensator is then proposed to mitigate identified stability issues, with its effectiveness validated through small-signal analysis and time-domain simulations on a four-terminal MTDC grid benchmark. The impact of the DC reactor on DC voltage support is also examined. This result challenges the common assumption that the DC grid can be represented as a simple aggregation of the capacitances of converter stations and cables.

Finally, a methodology for deriving representative DC grid equivalent models suitable for standalone converter compliance testing is proposed and validated. This approach enables the accurate and efficient verification of converter control performance without requiring detailed knowledge of the complete MTDC grid, thereby reducing interoperability risks prior to grid integration. The proposed equivalent models are validated against the full grid model in both the frequency and time domains. Additionally, the frequency-dependent reduced-order equivalent model is implemented in a time-domain setup, allowing the capture of higher-frequency grid dynamics and interactions that are often overlooked by traditional models.

Keywords: Multi-terminal HVDC, Modular Multilevel Converter, Control interoperability, Small-signal stability, DC voltage droop, Grid-forming control, DC grid equivalents, Standalone compliance testing.

Résumé

La transition des systèmes à courant continu haute tension (HVDC) point-à-point (PtP) vers des réseaux HVDC multiterminaux (MTDC) pour le transport massif de l'énergie éolienne offshore offre des opportunités considérables tout en introduisant de nouveaux défis en matière de contrôle commande et de protection. Les futurs réseaux MTDC à grande échelle intégreront probablement des stations de conversion provenant de plusieurs fabricants. Par conséquent, ces convertisseurs doivent fonctionner sans avoir accès à des modèles internes propriétaires. Le convertisseur modulaire multiniveau (MMC) représente la technologie de référence pour les applications MTDC. Plusieurs fonctionnalités de contrôle commande sont indispensables, notamment la commande primaire de la tension continue et la commande de type grid-forming (GFM), qui assurent respectivement la régulation des réseaux DC et AC. Toutefois, l'absence de stratégies de commande MMC standardisées, combinée à la grande diversité de leurs implémentations existantes, peut engendrer des problèmes d'interopérabilité susceptibles de compromettre les performances et la stabilité des réseaux MTDC. La compréhension claire des interactions est donc essentielle pour réduire les risques associés aux futurs réseaux HVDC multi-fournisseurs.

Cette thèse traite de l'interopérabilité des commandes dans les futurs systèmes MTDC multi-fournisseurs, principalement au moyen d'un cadre d'analyse de stabilité aux petits signaux. Une attention particulière est portée aux aspects dynamiques de la commande primaire de la tension continue, qui constitue le principal mécanisme local permettant de maintenir la tension DC dans des limites acceptables. Différentes options d'implémentation sont analysées ainsi que leurs contraintes de stabilité aux petits signaux associées, y compris leurs interactions avec les stratégies de commande grid-forming. Par la suite, une nouvelle implémentation de la commande de tension DC par statisme (droop control) combinée à la commande GFM est proposée et analysée, offrant des marges de stabilité améliorées et de meilleures performances dynamiques par rapport aux approches traditionnelles.

Par ailleurs, l'interaction entre la dynamique de la commande des MMC et les éléments passifs du réseau DC est étudiée afin d'identifier les limites de stabilité. L'impact du point de fonctionnement du MMC et de son mode de commande, combiné à la valeur du réacteur DC, est analysé, et les contraintes de stabilité sont examinées. Un compensateur avance de phase (lead compensator) est ensuite proposé afin d'atténuer les problèmes de stabilité identifiés, son efficacité étant validée par simulations temporelles sur un réseau MTDC de référence à quatre terminaux. L'impact de la réacteur DC sur le soutien de la tension DC entre stations est également étudié, remettant en question l'hypothèse courante selon laquelle le réseau DC peut être représenté comme une simple agrégation des capacités des stations de conversion et des câbles.

Enfin, une méthodologie permettant de dériver des modèles équivalents représentatifs du réseau DC, adaptés aux essais de conformité des convertisseurs, est proposée et validée. Cette approche permet une vérification précise et efficace des performances de la commande des convertisseurs sans nécessiter une connaissance détaillée de l'ensemble du réseau MTDC, réduisant ainsi les risques d'interopérabilité avant l'intégration au réseau. Les modèles équivalents proposés sont validés par comparaison avec le modèle complet du réseau dans les domaines fréquentiel et temporel. De plus, l'équivalent réduit du réseau DC dépendant de la fréquence est implémenté dans un environnement temporel, permettant de capturer les dynamiques haute fréquence du réseau DC et des interactions souvent négligées par les modèles traditionnels.

Mots-clés : HVDC multiterminal, convertisseur modulaire multiniveau, interopérabilité de la commande, stabilité aux petits signaux, commande grid-forming, équivalents de réseau DC, essais de conformité autonomes.

Acknowledgements

Throughout these past years, I have conducted research on multi-terminal DC grids, which has led me to earn this PhD degree. These three years have not been isolated in time; rather, they have been shaped by the contributions and support of the wonderful people around me. Although this journey was challenging and marked by many ups and downs, it was made bearable and filled with many joyful moments.

First of all, I would like to express my gratitude to Professor Ahmed Zewail, Nobel Laureate in Chemistry in 1999, a true example of dedication and excellence in science and academia. However, I believe that his greatest achievement, one that has helped me and many others, was the creation of Zewail City of Science and Technology, a research-based university with multidisciplinary programmes and high-quality education that has played a fundamental role in shaping who I am today. It is astonishing how a single deed, project, or idea can have such a profound impact on so many students. To me, this is an inspiration to think beyond the present, both in terms of time and impact.

At Zewail City, and very much in the same spirit, a shining example of making an impact and helping others was Dr Mostafa Abdallah. He was a mentor with whom, unfortunately, I did not have the opportunity to spend as much time as I would have liked. I learned a great deal from him, not only through our interactions but also simply by observing how he dedicated himself to helping others with such sincerity and generosity.

During my thesis, I was privileged to have the support of my supervisors, Seddik Bacha, Kosei Shinoda, and Jing Dai.

Seddik provided me with constant support, encouragement, and, above all, the trust that I could produce quality work. I am deeply grateful for this confidence and for the many enjoyable interdisciplinary discussions we shared.

To Kosei, your passion for understanding how systems work and your exceptional technical expertise have greatly contributed to making this work something I am truly proud of. Having you nearby in the open-space was always a source of reassurance. It is rare to find a supervisor with the patience to mentor, guide, and tolerate the inevitable silly mistakes of a PhD student. I know that this effort was never wasted, and it is something I will carry with me throughout my career.

To Jing, beyond your technical advice, I sincerely appreciate your support, thoughtful suggestions, and the constructive feedback you consistently provided throughout this work. Your guidance has been invaluable, and I am truly grateful for your encouragement and kindness.

I would like to extend my sincere thanks to the members of the jury, Professor Raphaël Caire, Dr Mohamed Alali, Dr Kambiz Tehrani, Dr Taoufik Qoria, Dr Vincent Debusschere, and Dr Sébastien Silvant, for their valuable feedback on my work and for the enriching discussions during my thesis defence.

I am deeply thankful for the time I spent at SuperGrid Institute and for having the opportunity to begin my career in such a welcoming environment, surrounded by motivated, dynamic, and supportive people. At SuperGrid Institute, I had the opportunity to present my research to partners in the European InterOPERA project and to exchange ideas with HVDC converter manufacturers and transmission system operators—an experience that I consider myself very fortunate to have had.

Beyond the technical exposure, I was privileged to work on a daily basis with wonderful colleagues: Ying, Filipe, Gianni, Heitor, Hind, Eugène, Paul, Pascal, Daniel, Myriam, Abdelkrim, Juan Carlos, Ahmed, and Rosalie. Thank you all for the many enjoyable moments we shared.

This journey would not have been as enriching without the support of my friends in France. Although we are now in different places, I will always cherish the moments we shared together. To

Sameh, my roommate and friend, from whom I still have so much to learn. To Ahmed Hany, for sharing the challenges of the PhD journey and for always bringing the perfect smile. To Omar, for our countless conversations about football and tennis. To Ahmed Abdou, the planner of all our trips and the constant problem solver for every issue I brought to him. To Fadi, the very first friend I made in France on the day I arrived. Thank you all for these unforgettable memories. To Omar and Yara, I wish you even more happiness and smiles along the road.

To my friends from university in Egypt, whom I am proud to still consider among my closest friends, thank you for your unwavering support throughout this journey. To Ibrahim, I am grateful that our friendship has only grown stronger over the years, thank you for our long conversations. To Hossam, the person I probably relate to the most in life. To Seif, Hamad, Sayed, and Hazem, thank you for all the football matches and the memories that I will never forget.

Finally, I would not have been able to reach this milestone without the unconditional love and support of my family, for which I am truly blessed.

To my father and mother, one of my greatest motivations has always been to make you proud. Your constant words of encouragement and your prayers have always been with me.

To my brother Ahmed, I am proud to see you succeed and build such a wonderful family.

To my sister Maram, my best friend, whenever I face the slightest doubt or problem, you are always the first person I turn to. Your support and belief in me have meant more than words can express.

Table of Contents

Abstract i

Résumé ii

Acknowledgements iii

Table of Contents v

1 General Introduction: Interoperability and Stability Challenges in MTDC Grids 1

1.1 A paradigm shift towards MTDC grids 1

1.2 Interoperability challenges in multi-vendor MTDC grids 2

1.3 InterOPERA project 3

1.4 Problem statement and research objectives 5

1.5 Stability phenomena in AC vs DC grids 5

1.5.1 AC-side converter-driven interactions 6

1.5.2 DC-side converter-driven interactions 6

1.6 Modeling methodologies for DC grid components 7

1.7 Stability analysis tools 7

1.7.1 Time-domain simulations 8

1.7.2 Eigenvalue analysis 8

1.7.3 Impedance-based stability analysis 10

1.8 Mitigating small-signal instability in multi-vendor HVDC grids 13

1.8.1 Testing of control combinations and grid configurations 13

1.8.2 Dedicated active damping solutions 13

1.8.3 Stability by design: impedance specifications 13

1.8.4 Defining requirements of standalone converter stations 14

1.9 Thesis outline 14

1.10 Thesis contributions 15

1.11 List of publications 17

2 Modular Multilevel Converters: Modeling and Control 20

2.1 Introduction 20

2.2 MMC topology and modeling 21

2.3 Dynamic analysis of the MMC Arm Average Model 23

2.4 Linear time-invariant modeling of the MMC 26

2.5 Average Value Model of the MMC 30

2.6 MMC control strategies 31

2.6.1 Modulation strategies 33

2.6.2 Synchronization with the AC grid . . . 34
2.6.3 Inner control loops . . . 36
2.6.4 Outer control loops . . . 38
2.6.5 GFM control . . . 41
2.7 Validation of the MMC LTI models . . . 42
2.8 Chapter summary . . . 46

3 Primary DC voltage control in MV-MTDC grids 48
3.1 Introduction . . . 48
3.2 Operation of MTDC grids . . . 48
3.2.1 Dispatch-level control . . . 49
3.2.2 Operational-level control . . . 50
3.2.3 Station-level control . . . 50
3.2.4 Unit-level control . . . 50
3.3 Primary DC voltage control in MTDC grids . . . 50
3.4 Static considerations of primary DC voltage control . . . 51
3.4.1 DC voltage operating ranges . . . 51
3.4.2 DC power flow management . . . 52
3.4.3 DC voltage static control options . . . 53
3.5 Dynamic considerations of primary DC voltage control . . . 56
3.5.1 DC voltage droop implementation options . . . 57
3.5.2 Three-terminal DC grid under study . . . 58
3.5.3 Small-signal stability analysis . . . 59
3.5.4 Time-domain validation . . . 62
3.5.5 Design space of DC voltage droop in MV-MTDC grids . . . 64
3.6 Compatibility with GFM implementations options . . . 64
3.6.1 Literature review of GFM control structures . . . 65
3.6.2 Combining DC voltage droop with GFM control . . . 67
3.6.3 Study of a standalone MMC operating with DC voltage droop and GFM control 69
3.6.4 Three-terminal DC grid with the two combinations of droop schemes and GFM controls . . . 72
3.7 Considerations on the design space for DC voltage droop with GFM control . . . 78
3.8 Conclusion . . . 78

4 Impact of passive elements on the dynamic performance and stability of MTDC grids 81
4.1 Introduction . . . 81
4.2 Literature review . . . 82
4.3 Low-frequency MMC DC-side impedance . . . 83
4.3.1 Constant power mode operation . . . 85
4.3.2 DC-voltage droop control . . . 87
4.4 Full MMC impedance . . . 88
4.4.1 Impact of the operating point . . . 89
4.4.2 Impact of the DCR size . . . 90

4.4.3 Impact of outer control . . . 91
4.4.4 Stability map . . . 91
4.5 Mitigation solution for the impact of DCR . . . 92
4.6 Case study 1: small-signal stability analysis of a four-terminal DC grid with DCRs . . . 94
4.6.1 Impact of the DCR size . . . 95
4.6.2 Time-domain validation of the 4T DC grid . . . 99
4.7 Case study 2: DCR impact on DC voltage support in MTDC grid . . . 101
4.8 Conclusion . . . 105

5 Development of DC grid equivalent models for standalone converter compliance and stability assessment 107
5.1 Introduction . . . 107
5.2 Literature review . . . 108
5.3 System modeling and DC grid impedance derivation . . . 110
5.4 DC-grid impedance dependencies . . . 112
5.4.1 Impact of the DC reactor size . . . 112
5.4.2 Impact of the operating point . . . 114
5.4.3 Impact of the control mode of remote stations . . . 114
5.4.4 Impact of the grid strength of the remote stations . . . 116
5.4.5 Impact of the GFM control strategy of the remote stations . . . 117
5.5 Development of the equivalent grid model . . . 117
5.5.1 Low-frequency RLC-based equivalent model . . . 118
5.5.2 Frequency-dependent equivalent model . . . 121
5.6 Time-domain validation of the equivalent models . . . 123
5.7 Case study: small-signal stability analysis using the equivalent models . . . 125
5.8 Guidelines for the application of the proposed equivalent models in a multi-vendor compliance testing process . . . 127
5.9 Conclusions . . . 129

6 Conclusions and Perspectives 132
6.1 Main conclusions . . . 132
6.2 General recommendations and perspectives for future work . . . 135

A System parameters 139

B Definitions 141
B.1 Base values and per-unit system . . . 141
B.2 Park transformation . . . 141
B.3 Clarke transformation . . . 142

C Validation of the MMC-LTI models 143

D LTI model of the MMC 149
D.1 Capacitor voltages dynamics - Δ capacitor voltages . . . 150
D.2 Inserted voltages dynamics - Δ inserted voltages . . . 152
D.3 Capacitor voltage dynamics - Σ capacitor voltages . . . 153

D.4 Inserted voltages dynamics - Σ inserted voltages 154
D.5 Δ currents dynamics 155
D.6 Σ currents dynamics 156

E DC Cable state-space model **157**

List of Figures **160**

List of Tables **166**

Bibliography **I**

1

General Introduction: Interoperability and Stability Challenges in MTDC Grids

1.1 A paradigm shift towards MTDC grids

The main objective of power systems is to guarantee a secure and reliable supply of energy with minimal cost and environmental impact. Environmental ambitions set by the European Union's Green Deal, which aims for climate neutrality by 2050 [1], have accelerated the energy transition and the integration of renewable energy sources. This transition has led to a fundamental transformation in power systems, marked by a significant shift from traditional AC transmission to high-voltage direct current (HVDC) technology. This shift is primarily motivated by the need to integrate large amounts of renewable energy, particularly offshore wind, into the grid, as well as to enable long-distance transmission and the interconnection of asynchronous AC areas.

Compared to AC transmission, HVDC technology offers several advantages, including higher usable transmission capacity since there is no reactive power flow, the ability to control power flow more precisely, and the capability to use long cables without the need for intermediate reactive power compensation [2]. These advantages have led to the increasing deployment of HVDC systems, particularly in point-to-point (PtP) configurations.

The past two decades have witnessed a significant increase in the number of commissioned HVDC projects. The first demonstration of a Voltage Sourced Converter (VSC)-based HVDC link was in Sweden with the Gotland link in the late 1990s [3]. VSCs offer enhanced controllability of active and reactive power, faster response times, and the ability to provide grid support services compared to line-commutated converters (LCCs). While LCCs are also suitable for bulk power transmission over long distances, they lack the same level of control flexibility since they are thyristor-based [4]. In addition, VSCs have proven to be more effective when connected to weak grids, which is often the case for offshore wind farms [5]. Furthermore, VSCs have benefited from recent developments in power electronics, particularly Insulated-Gate Bipolar Transistors (IGBTs), which have become the primary

switching devices in VSCs. IGBTs have enabled VSCs to achieve higher efficiency, reliability, and cost-effectiveness, further driving the adoption of HVDC systems based on VSC technology. For these reasons, most newly planned links are based on VSC technology rather than LCC systems.

Recent HVDC developments indicate a clear increase in transmission capacities and operating voltages. While the largest existing installations reach capacities of up to 8 GW for VSC systems [6] and 12 GW for LCC systems [7], the majority of projects expected to be commissioned in the near future fall within the 1–2 GW range [8]. DC voltage levels are also rising, with projects operating typically between 320 kV and 525 kV, alongside developments targeting even higher voltage levels to enable efficient long-distance bulk power transfer. Several ongoing projects exploit HVDC's suitability for very long submarine and underground connections, including long interconnections extending thousands of kilometers, although most planned links remain shorter than 750 km [9].

Over the past decades, HVDC technology trends have evolved from PtP links to multi-terminal DC (MTDC) grids. The increasing integration of offshore wind power, interconnection of asynchronous AC areas, and the need for controllable long-distance transmission are among the main motivations for the deployment of VSC-based MTDC systems. Compared to PtP links, MTDC grids offer enhanced operational flexibility, availability, and better utilization of transmission assets. [10]. While most of the currently installed HVDC systems are still based on PtP configurations, some multi-terminal projects can be found in China [8], proving their technical feasibility.

The widespread adoption of MTDC grids is heavily reliant on the Modular Multilevel Converter (MMC), which has become the state-of-the-art VSC technology in recent years. As highlighted in [10], MMCs offer features such as high efficiency, modularity and scalability enabling operation at higher voltage levels, improved harmonic performance, and fault tolerance. Consequently, MMCs have established themselves as the fundamental building block for future MTDC systems.

Another defining feature of emerging MTDC grids is their multi-vendor nature. Due to the high cost of a large MTDC grid, it is expected to include converters and protection devices supplied by different manufacturers. In Europe, several possible multi-vendor MTDC projects are expected, such as the North Sea Wind Power Hub [11], the Aquila project [12]. The multi-vendor nature of future MTDCs creates a fundamental challenge: ensuring interoperability while preserving performance.

1.2 Interoperability challenges in multi-vendor MTDC grids

The interoperability of multi-vendor MTDC grids is a critical concern that encompasses various technical challenges, ranging from control and protection to communication architectures and protocols. Currently, converter control and protection systems are proprietary to their manufacturers and are often treated as black boxes. As a result, there is no standardization in control or protection strategies. This lack of standardization can create significant challenges in ensuring that components from different manufacturers operate together safely.

Regarding protection, compared to AC protection, an additional challenge arises in DC systems due to the absence of natural current zero crossings [13], which are typically exploited in AC systems to facilitate fault interruption. This has necessitated the development of DC circuit breakers (DCCBs) with fast switching capabilities to interrupt fault currents within a few milliseconds. Considering a multi-vendor MTDC grid, the main challenges regarding HVDC protection include specifying the functional requirements for DCCBs, converter DC fault ride-through (DC-FRT) capabilities and DC protection intelligent electronic devices (IEDs) [13]. Such requirements should cover different protection

philosophies, whether non-selective, partially selective or fully selective philosophies [14]. In addition, standardized interfaces and communication protocols for HVDC protection is also required to ensure interoperability. Considering different protection devices coming from different manufacturers, the ratings of these components must be coordinated to ensure that the protection system can operate effectively under all fault conditions. [13].

From a control perspective, interactions between converters and the grid, as well as among converters themselves, can lead to stability issues. These interactions are influenced by the control strategies implemented by the converters, grid impedance, and operating conditions. In a multi-vendor MTDC grid, the converter manufacturers design their control systems independently, often using their own simplified assumptions about the grid and other converters. This method is insufficient to mitigate potential stability issues that may arise from the interactions between the designed control system and the actual grid, which may differ significantly from the assumptions made during the design phase. This leads to increased iterations during the integration phase, which can be costly and time-consuming.

Different initiatives have been launched to address the interoperability challenges of multi-vendor MTDC grids. For instance, the CIGRE Working Group B4.85 has published a technical brochure [15] providing guidelines for the design and operation of multi-vendor MTDC grids, including recommendations on control and protection strategies, communication protocols, and testing procedures. Standardization efforts are also underway within ENTSO-E [16], IEC [17], and CENELEC [18] to define technical standards for future MTDC grids.

In addition, EU-funded projects such as BestPaths [19] and PROMOTioN [20] have addressed interoperability issues in multi-vendor MTDC grids. Finally, the ongoing R&D project InterOPERA, to which this PhD thesis contributes, focuses on tackling interoperability challenges in multi-vendor MTDC grids together with major European HVDC stakeholders.

1.3 InterOPERA project

InterOPERA project, funded by the European Union's Horizon Europe research and innovation program [21], addresses the key interoperability challenges associated with the development and deployment of multi-vendor multi-terminal HVDC grids in Europe. These grids are expected to play a central role in integrating large volumes of offshore renewable energy, notably offshore wind, into the European power systems, and in supporting the European Green Deal objective of achieving climate neutrality by 2050.

InterOPERA unites a diverse consortium of transmission system operators (TSOs), wind developers and manufacturers, converter manufacturers, and research institutions to define technical frameworks, common standards and collaboration mechanisms that enable HVDC systems and components from different manufacturers to operate seamlessly together, as shown in Fig. 1.1.

InterOPERA's objective is to make future HVDC systems interoperable by design, improving grid-forming capabilities of both offshore and onshore converters and establishing the foundations for modular HVDC grids with common functional specifications and standard interfaces [21]. Alongside technical standardization, the project also addresses commercial, legal, regulatory and procurement frameworks that will facilitate competitive tendering and deployment of full-scale multi-vendor multi-terminal HVDC systems in Europe.

Activities within the project are organized into two main phases: Phase I develops the necessary frameworks and functional specifications; Phase II focuses on consolidating these results in a real-time

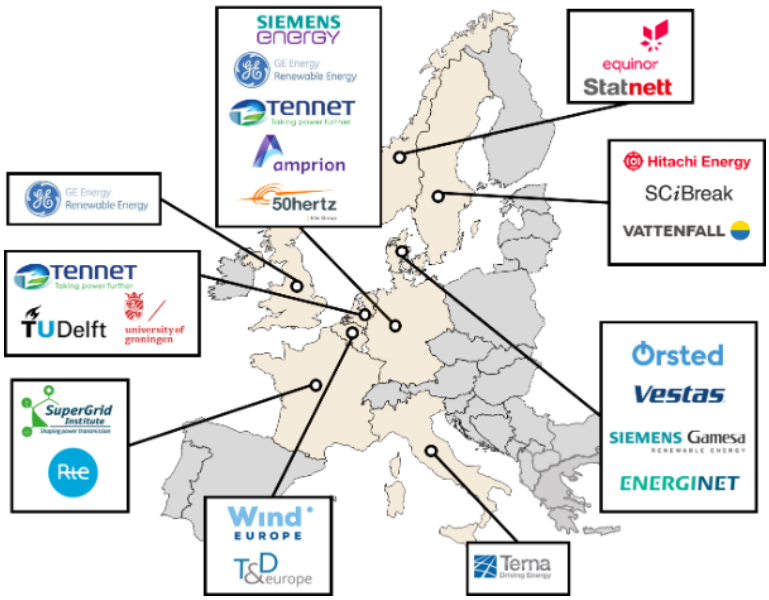

Figure 1.1: InterOPERA project consortium [21].

physical demonstrator and defining procurement strategies to prepare for future real-world projects.

InterOPERA is well positioned to drive the necessary technical and market innovations to enable interoperable multi-vendor multi-terminal HVDC grids in Europe. The project's vision for the future of multi-vendor MTDC grids is illustrated in Fig. 1.2, where offshore grid expansion is supported by a sufficient level of coordination and de-risking technical specifications.

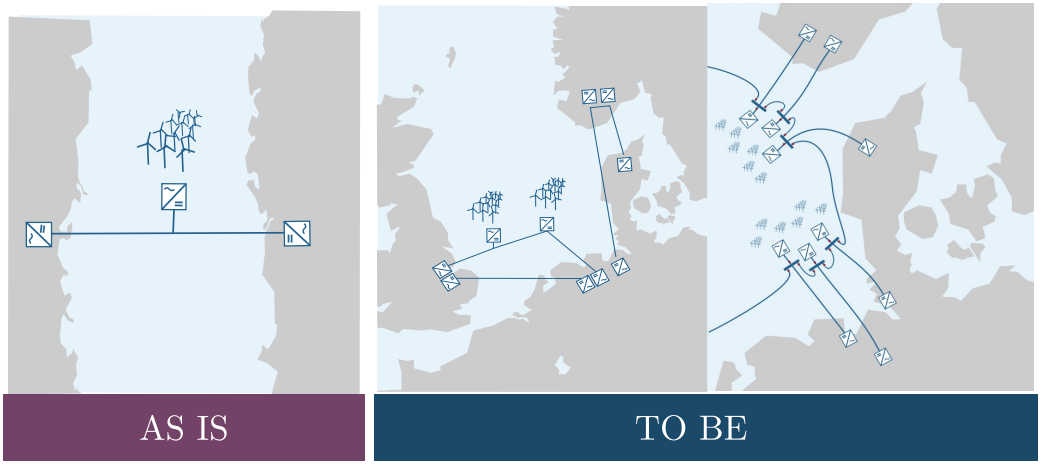

Figure 1.2: Future vision of multi-vendor MTDC grids [21].

To achieve these aims, InterOPERA has identified several specific objectives [21]:

- Making HVDC grids modular and interoperable by design through the development of common specifications and models.
- Standardizing simulation models and interaction study processes for interoperability assessment.
- Performing a real-time physical demonstration of a multi-vendor control and protection system with grid-forming capabilities.

- Paving the way for real-life multi-vendor, multi-terminal HVDC applications suitable for future grid extensions.
- Supporting grid operation by enhancing grid-forming control features for integration with onshore AC systems.
- Fostering multi-stakeholder cooperation to build confidence in the interoperability frameworks and maximize industry uptake.

This PhD thesis contributes to the activities of Work Package 2 of the InterOPERA project, which focuses on the requirements and assessment of interoperability for multi-vendor multi-terminal HVDC systems. This thesis places a special focus on stability problems arising from such interactions and proposes a structured framework for their analysis and mitigation.

1.4 Problem statement and research objectives

From the above discussion, it is clear that the stability of multi-vendor MTDC grids is a critical concern that must be addressed to ensure the reliable operation of future HVDC systems. The possible extension of these grids to include more terminals may lead to further interactions that are not dependent on a specific grid configuration, and that may be difficult to predict without a proper understanding of the underlying mechanisms.

This thesis aims to provide a comprehensive understanding of these interactions and develop effective strategies to mitigate potential stability issues. In addition, to facilitate interoperability, this thesis also develops methodologies that allow for the assessment of converter station stability in standalone setups. The specific research objectives of this thesis are as follows:

- To investigate the dynamic impacts of different primary DC voltage control strategies on the stability of a multi-vendor MTDC grid, identifying potential sources of instability and their mechanisms.
- To perform small-signal stability analysis of MTDC grids under various control strategies, operating conditions, and grid configurations, identifying critical factors that contribute to instability.
- To propose and evaluate mitigation strategies, including active damping techniques, to enhance the stability of multi-vendor MTDC grids.
- To develop methodologies for deriving DC grid equivalents that can be used for standalone compliance testing of converter stations, facilitating interoperability and stability assessment without requiring detailed access to the complete grid configuration.

Before presenting the main contributions of this thesis, a general introduction to the stability phenomena in AC and DC grids is provided in the next section, along with a literature review of modeling methodologies and stability analysis tools that are relevant for the analysis of MTDC grids. In addition, the main mitigation strategies that are proposed in the literature are briefly discussed.

1.5 Stability phenomena in AC vs DC grids

Qualitatively, a system is considered stable if it can return to its equilibrium when subjected to small perturbations around it [22]. In AC power systems, stability phenomena are well known and

extensively studied. One primary classification of stability phenomena in AC systems is based on the size of the disturbance: large-signal stability refers to the system's ability to maintain synchronism after a severe disturbance, such as a fault or a sudden loss of generation [23]. Small-signal stability, conversely, concerns the system's response to small perturbations around an operating point, which can lead to growing oscillations if not properly damped. Another classification is based on the physical phenomena involved, categorizing issues into rotor angle stability, frequency stability, and voltage stability [23]. These classifications have been instrumental in guiding the analysis and design of AC power systems, providing a framework for understanding the various modes of instability and their underlying mechanisms.

1.5.1 AC-side converter-driven interactions

With the increasing penetration of power electronic converters in power systems, new stability phenomena have emerged because converters behave significantly differently from traditional synchronous machines. The fast control dynamics and capabilities of these converters can lead to interactions previously unseen in AC systems, as documented in [24, 25]. Such interactions have already occurred in real-world events [26], prompting a revision of phenomena-based classifications to include converter-driven stability [27].

Converter-driven instability in AC grids occurs mainly due to the interaction between converter controllers and grid resonances. These interactions are contingent on the control strategy employed by the converters, the grid impedance, and the operating conditions. They may occur at different frequencies, ranging from sub-synchronous to high-frequency oscillations. In general, low-frequency oscillations are typically associated with converter outer control loops, while high-frequency oscillations are often linked to control time delays [28]. A comprehensive literature review of converter-driven interactions in AC systems can be found in [29, 30].

1.5.2 DC-side converter-driven interactions

Past classifications and observed phenomena have mainly focused on the interaction between converters and the AC grid. However, similar interactions can also arise on the DC side between the converter and the DC grid, potentially leading to new instability modes. To date, a comprehensive understanding of these phenomena remains limited, even though such interactions have already been observed in practice [31, 32].

Similar to AC systems, converter-grid interactions in DC systems can occur at various frequencies. In [33], low-frequency oscillations were observed due to the tuning of the outer DC voltage control. Inner MMC control loops can also induce resonances at higher frequencies. For instance, [34] showed that the tuning of the circulating current control loop can lead to undamped oscillations at 150 Hz.

Control delays can also impact resonances on the DC side. In [35], both passive elements, such as the DC Reactor (DCR), and the internal MMC control tuning were shown to induce high-frequency oscillations, which are primarily due to the interaction between control delays and grid resonances.

Although it is tempting to classify these phenomena strictly by frequency ranges, this thesis will demonstrate that outer control tuning, such as DC voltage droop control, might also induce higher frequency resonances (see Chapter 3). Furthermore, a specific source of instability cannot always be trusted to impact only a certain frequency range. For example, while large DC reactors have been shown to stabilize higher frequency oscillations around 2 kHz [35], they can also induce low-frequency

poorly-damped oscillations, as demonstrated in Chapter 4.

To achieve a proper understanding of stability phenomena in MTDC grids, valuable experience from AC system practice can be used, provided the specific characteristics of DC systems are carefully accounted for. In general, a thorough analysis requires appropriate, context-aware modeling strategies along with corresponding stability assessment tools. Finally, mitigation strategies must be designed by considering the unique features of DC systems and the interoperability challenges associated with multi-vendor MTDC grids. These aspects are detailed in the following sections.

1.6 Modeling methodologies for DC grid components

Before performing any stability analysis, it is essential to develop an appropriate model for the specific phenomenon under study. The modeling choices for this thesis are discussed in detail in Chapter 2, while a brief overview of common modeling approaches is provided below. Depending on the level of detail and available information, various methods can be adopted, including white-box, black-box, and gray-box models [36].

White-box models are based on detailed knowledge of the system's internal structure and parameters. They are typically derived from basic dynamic equations and can capture the dynamics of individual components with high fidelity. However, they require comprehensive information about the system, which may not always be available, especially in multi-vendor scenarios where proprietary information is often withheld.

Black-box models do not reveal the internal structure or dynamics of the system. Instead, they are developed using input–output data, often obtained through system identification techniques such as frequency scans. The motivation behind these models is to keep valuable vendor intellectual property confidential while still providing accurate converter behavior. However, root cause analysis and the design of mitigation strategies can be more challenging compared with white-box models.

Gray-box models combine elements of both approaches [37]. Their advantage lies in the potential for root-cause identification while protecting proprietary information. Recently, they have increasingly been associated with robust control approaches, as introduced in [38].

In this thesis, we opt for white-box modeling approaches for the analysis of specific phenomena, as they allow for a deeper understanding of the underlying mechanisms and the design of targeted mitigation strategies. However, most of the results obtained, which are applicable to many other studies, can also be derived using black-box models if the interest is solely in stability assessment rather than root-cause analysis.

When modeling the different subsystems of an MTDC, particular attention must be given to the MMC, whose dynamics exhibit a multi-frequency nature due to arm capacitor voltages and circulating currents. The modeling strategies for the MMC are outlined in Chapter 2. Additionally, modeling DC cables and accounting for their frequency-dependent behavior is critical for accurate stability analysis.

1.7 Stability analysis tools

To assess the stability of MTDC grids, various tools can be employed, each with its own advantages and limitations. This section provides an overview of the most commonly used methods, including time-domain simulations, eigenvalue analysis, and impedance-based stability analysis.

1.7.1 Time-domain simulations

An initial intuitive approach to stability assessment is to perform time-domain simulations of the system's response to disturbances. This method captures nonlinear dynamics and provides insights into transient (large-signal) behavior. It can also be used for small-signal stability assessment, determining whether the system exhibits well-damped oscillations. However, this approach has some limitations:

- It can be computationally intensive. Without a proper understanding of stability margins and instability risks, a large number of simulations may be required to explore different operating conditions and control parameter values. Hence, an expensive trial-and-error process may be necessary to identify instability phenomena.
- For slow-growing oscillations, it may be difficult to determine whether the system is stable, as the response may not diverge significantly within the simulation time frame.
- Root-cause analysis can be challenging, as it is often unclear which specific interactions or modes are responsible for the observed instability.

An alternative approach to time-domain simulations is the use of nonlinear analysis tools, such as Lyapunov-based methods. This approach has the advantage of providing a theoretical guarantee of stability. However, energy functions are difficult to identify in many practical systems, where a positive definite function of the state variables is required. In addition, Lyapunov-based nonlinear analysis provides only sufficient conditions for stability, which may be conservative. These challenges motivate a shift toward linear analysis tools, such as eigenvalue analysis within the state-space framework and impedance-based analysis in the frequency domain [39, 40].

1.7.2 Eigenvalue analysis

Eigenvalue analysis is a powerful tool for small-signal stability assessment. To perform eigenvalue analysis, state-space modeling is typically required. By linearizing the nonlinear system around an operating point, the eigenvalues of the system matrix can be computed to determine stability. This method is also traditionally used for analyzing the small-signal stability of AC power systems.

Formally, the original non-linear system is written as a system of non-linear differential equations:

$$\dot{\boldsymbol{x}} = f(\boldsymbol{x}, \boldsymbol{u}) \tag{1.1}$$

where $\boldsymbol{x}$ is the state vector, $\boldsymbol{u}$ is the input vector, and f is a non-linear function describing the system dynamics. The system is assumed to be time-invariant. In the context of a converter system, $\boldsymbol{x}$ includes variables such as inductor currents, capacitor voltages, and internal integral states associated with control, while $\boldsymbol{u}$ includes variables such as reference signals and external physical disturbances.

The relation between the output variables and the state/input variables is given by:

$$\boldsymbol{y} = g(\boldsymbol{x}, \boldsymbol{u}) \tag{1.2}$$

where $\boldsymbol{y}$ is the output vector and g is a non-linear function describing the output dynamics.

The system is then linearized around an equilibrium point $(\boldsymbol{x}_0, \boldsymbol{u}_0)$, where $f(\boldsymbol{x}_0, \boldsymbol{u}_0) = 0$, leading to the following linearized system:

$$\Delta\dot{\boldsymbol{x}} = A\Delta\boldsymbol{x} + B\Delta\boldsymbol{u} \tag{1.3}$$

where $\Delta \boldsymbol{x} = \boldsymbol{x} - \boldsymbol{x}_0$ and $\Delta \boldsymbol{u} = \boldsymbol{u} - \boldsymbol{u}_0$ are the deviations from the equilibrium point, and A and B are the Jacobian matrices of f with respect to $\boldsymbol{x}$ and $\boldsymbol{u}$ evaluated at the equilibrium point:

$$A = \left.\frac{\partial f}{\partial \boldsymbol{x}}\right|_{(\boldsymbol{x}_0, \boldsymbol{u}_0)}, \quad B = \left.\frac{\partial f}{\partial \boldsymbol{u}}\right|_{(\boldsymbol{x}_0, \boldsymbol{u}_0)} \tag{1.4}$$

Similarly, the output equation can be linearized as:

$$\Delta \boldsymbol{y} = C\Delta \boldsymbol{x} + D\Delta \boldsymbol{u} \tag{1.5}$$

where C and D are the Jacobian matrices of g with respect to $\boldsymbol{x}$ and $\boldsymbol{u}$ evaluated at the equilibrium point:

$$C = \left.\frac{\partial g}{\partial \boldsymbol{x}}\right|_{(\boldsymbol{x}_0, \boldsymbol{u}_0)}, \quad D = \left.\frac{\partial g}{\partial \boldsymbol{u}}\right|_{(\boldsymbol{x}_0, \boldsymbol{u}_0)} \tag{1.6}$$

The stability of the linearized system can then be assessed by analyzing the eigenvalues λ of the matrix A, by solving the characteristic equation

$$\det(A - \lambda I) = 0 \tag{1.7}$$

where I is the identity matrix of appropriate dimension.

According to Lyapunov's first method [41], stability conditions can be determined from the eigenvalues of the system matrix as follows:

- If all eigenvalues have strictly negative real parts, the system is locally asymptotically stable around the equilibrium point.
- If at least one eigenvalue has a positive real part, the system is unstable.
- If no eigenvalue has a positive real part and at least one eigenvalue has a zero real part, the method is inconclusive, and further analysis is required to determine stability [42, 43].

A major advantage of eigenvalue analysis is its ability to provide insights into the root causes of instability through participation factors [43]. These factors quantify the contribution of each state variable to a given mode, thereby facilitating the design of appropriate mitigation strategies.

To compute the participation factors, the right and left eigenvectors of the system matrix A are determined. The right eigenvector ϕ_j associated with the jth eigenvalue λ_j satisfies

$$A\phi_j = \lambda_j \phi_j, \tag{1.8}$$

while the corresponding left eigenvector ψ_j satisfies

$$\psi_j^T A = \lambda_j \psi_j^T. \tag{1.9}$$

Assuming proper normalization of the left and right eigenvectors (e.g. $\psi_j^T \phi_j = 1$), the participation factor of the i-th state variable in the j-th mode is defined as

$$p_{ij} = \phi_{ij}\psi_{ij}. \tag{1.10}$$

where ϕ_{ij} and ψ_{ij} are the i-th components of the right and left eigenvectors, respectively.

The above two properties, eigenvalues and participation factors, will be used in this thesis to analyze the stability of DC grid interactions. However, other properties of the same method, such as mode shapes and mode controllability/observability, can also be used to gain further insight into the system dynamics.

In the literature, eigenvalue analysis has been widely applied to the study of VSC-based MTDC grids [44–46], as well as MMC-based DC grids [47, 48].

1.7.3 Impedance-based stability analysis

Impedance-based stability analysis relies on assessing the small-signal interactions between subsystems by analyzing their terminal impedance characteristics. It started with the work of Middlebrook [49], where the method was used to analyze the impact of the input filter on the stability of DC-DC converters, without the need to remodel the converter including the filter. The method was later extended to AC systems and has been widely applied in the analysis of converter-grid interactions [50–52].

By electrically partitioning the system into two main subsystems, a source and a load, as shown in Fig. 1.3, the stability of the interconnected system can be assessed by analyzing the impedance ratio at the point of interconnection.

The source dynamics are represented by its output impedance Z_s, while the load is represented by its input admittance Y_l. From the circuit diagram in Fig. 1.3, in the small-signal sense, the current $I_{dc}(s)$ can be expressed as a function of the source voltage $V_s(s)$, the load current $I_l(s)$, and the respective impedances:

$$I_{dc}(s) = \frac{Y_l(s)}{1 + Y_l(s)Z_s(s)} V_s(s) - \frac{1}{1 + Y_l(s)Z_s(s)} I_l(s) \tag{1.11}$$

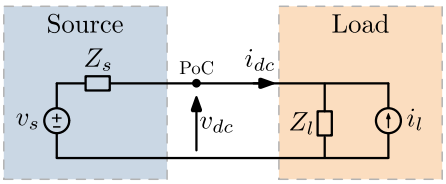

Figure 1.3: Source-load partitioning for impedance-based stability analysis.

From (1.11), a block diagram representation can be derived, as shown in Fig. 1.4, representing a feedback system where the return ratio is given by the product of the source impedance and the load admittance, $\mathcal{L}(s) = Z_s(s)Y_l(s)$. The closed-loop stability of the entire system can then be assessed by analyzing the return ratio $\mathcal{L}(s)$ in the frequency domain, to which the Nyquist stability criterion can be applied [42].

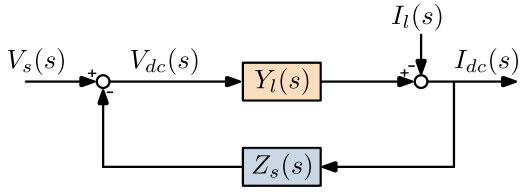

Figure 1.4: Block diagram of the source-load relationship for impedance-based stability analysis.

The Nyquist stability criterion states that the closed-loop system is stable if and only if the Nyquist plot of the return ratio $\mathcal{L}(s)$ makes P counterclockwise encirclements of the critical point (-1,0) in the complex plane, where P is equal to the number of right-half-plane (RHP) poles of $\mathcal{L}(s)$. This can be mathematically expressed as

$$Z = P - N \tag{1.12}$$

where N is the number of counterclockwise encirclements of the critical point, and Z is the number of RHP zeros of $\mathcal{L}(s)$, which correspond to the unstable poles of the closed-loop system. Therefore, for closed-loop stability, we require $Z = 0$, which implies that N must equal P.

A special condition arises when there are no RHP poles in $\mathcal{L}(s)$, which implies that $P = 0$. In this case, the Nyquist criterion simplifies to requiring that there are no encirclements of the critical point (-1,0).

The main advantage of applying the impedance-based stability criterion is its compatibility with black-box models, that is, the impedance can be measured or scanned directly at the terminals of the subsystems. However, a major challenge lies in ensuring the absence of RHP poles in the return ratio, or in identifying them without full analytical impedance models, which are generally required for a rigorous application of the Nyquist criterion.

One common argument is that, in practice, the source subsystem should be stable before being connected to the load, and the load should also be stable when connected to an ideal source [50]. Under this assumption, neither the output impedance of the source nor the input admittance of the load contains right-half-plane (RHP) poles $P = 0$, and stability can be assessed directly by checking whether an encirclement occurs. An example of such application can be found in AC grids, where a Grid-Forming (GFM) converter is typically represented by its Thévenin equivalent, which does not contain RHP poles, while a Grid-Following (GFL) converter is represented by its Norton equivalent, which does not contain RHP poles in its input admittance either, since it is designed to be stable when connected to an ideal source.

However, considering an MTDC grid, this assumption may not hold in the presence of constant power loads (CPLs), which, as will be discussed in Chapter 4, can naturally introduce RHP poles in the converter impedance without necessarily causing instability. In such cases, the Nyquist criterion must be applied in its general form, and the presence of RHP poles must be explicitly taken into account.

Moreover, the assumptions regarding source and load stability may not directly apply to HVDC grids, where both the source and the load can be converter-based, and the choice of representing them using Thévenin or Norton equivalents may be arbitrary. In these situations, RHP poles in the return ratio are more likely to appear, making their identification essential for an accurate stability assessment.

Another argument, presented in [53] and more directly related to MTDC grids, is to infer the presence of RHP poles in the return ratio based on the control mode. For example, a converter station operating under constant DC voltage control naturally introduces an RHP pole in the admittance of the MMC. Consequently, such a converter should be represented by its Thévenin equivalent to avoid RHP poles in the return ratio. However, these assumptions based solely on control modes may not capture all possible dynamics of an MMC, especially when multiple control loops are active. Therefore, this approach is not sufficiently general to cover all cases.

A possible alternative is to identify RHP poles based on Bode plots of the corresponding impedance responses. This method is presented in [54], where the existence of an RHP pole is inferred from the

slopes of the magnitude and phase responses as a function of frequency. Specifically, an RHP pole is identified if the magnitude plot exhibits a slope of +20 dB/decade and the phase plot shows a phase change of +90 degrees at the same frequency. However, this approach can be challenged when RHP poles and zeros are closely located, making their identification difficult from the Bode plot, particularly when the frequency resolution is insufficient during frequency scans.

Overall, the problem of identifying RHP poles, given the default assumption of nonminimum-phase behavior in converter-based systems, remains an open research question in the application of impedance-based stability analysis to MTDC grids, especially when black-box models are used.

In the literature, the application of impedance-based stability analysis to HVDC grids has been explored. In [55], the impact of power flow direction on the stability of a VSC-HVDC system was analyzed. In [56], a DC impedance-model-based resonance analysis of a VSC-HVDC system was presented. The stability of an MMC-based HVDC system under different control variations using the impedance framework was investigated in [33]. In [57], the DC-side impedance of an MMC is derived and a small-signal stability analysis is performed at each terminal of an MTDC grid, by analyzing the impedance ratio of each converter and the grid.

However, the above literature focused on what is called Single-Input Single-Output (SISO) stability analysis, where the entire system is partitioned into two subsystems. For larger systems, a more general Multi-Input Multi-Output (MIMO) impedance-based stability analysis can be applied, where multiple partitioning points are considered, and the return ratio matrix is analyzed using the Generalized Nyquist Criterion. In the context of MTDC grids, MIMO impedance-based stability analysis can be particularly useful for analyzing interactions between multiple converters and the grid, as it can capture the dynamic interactions at each point of connection. In addition, possible root causes of instability can be allocated to the specific converter station using this method, which is not possible with SISO analysis. Previous studies applying MIMO impedance-based stability analysis to MTDC grids include [58–61].

Although eigenvalue analysis and impedance-based stability analysis are distinct tools, they should lead to the same stability conclusions when applied correctly, as both are derived from the same underlying system dynamics [62]. In fact, a state-space model can be transformed into an impedance representation by appropriately defining the input and output variables. This transformation will be demonstrated later in this thesis, where state-space modeling is used throughout, while impedance analysis is applied in selected cases to provide additional insight.

After reviewing the various modeling frameworks and stability analysis methods, it is natural to question the validity of results obtained from linearized models and small-signal stability analysis, given the inherently nonlinear nature of the system.

One possible answer is that linear analysis provides the theoretical foundation for the utilization of linear controllers in nonlinear systems. Most control strategies in power systems, including those used for converters, are based on linear control theory (e.g., PI controllers). In addition, small-signal stability analysis offers valuable insight into the root causes of instability, at least in the vicinity of a given equilibrium point. If such analysis is conducted over a sufficiently wide range of operating conditions, greater confidence in the system's stability can be achieved.

1.8 Mitigating small-signal instability in multi-vendor HVDC grids

Ensuring stability in multi-vendor MTDC grids requires a systematic and scalable approach. Several philosophies can be adopted to mitigate instability, each with its own advantages and limitations.

1.8.1 Testing of control combinations and grid configurations

One approach consists of testing and retuning numerous combinations of control parameters iteratively. This approach can be effective for small systems with a limited number of converters and control options. It has been adopted in [63] to identify possible interactions between different control principles in an MTDC grid. Admittedly, this approach has also been used in some of the studies presented in this thesis, in parallel with analytical tools such as eigenvalue analysis, which provides a more systematic way to identify instability phenomena and their root causes. However, iterative control testing of large systems has the following significant limitations:

- It is time-consuming and computationally intensive, especially as the number of converters and control options increases.
- It may not guarantee a global solution, as it relies on local adjustments without a comprehensive understanding of the underlying dynamics.
- It is not suitable for multi-vendor scenarios, where proprietary control strategies and parameters may not be accessible for testing and retuning until late stages of the project.

1.8.2 Dedicated active damping solutions

Outer-control active damping techniques involve modifying the input reference (DC voltage or active power) of converter stations to introduce additional damping into the system. Such an approach is adopted in [58, 64], where supplementary control loops are added to the existing control structure to mitigate emerging instability phenomena. However, the limitations of this approach when applied to black-box systems include:

- It lacks the root-cause analysis capability, as it focuses on mitigating symptoms rather than addressing the underlying mechanisms of instability.
- It may not be universally applicable across different converter types or grid configurations, as the effectiveness of active damping can depend on specific system characteristics and operating conditions.
- There are uncertainties regarding the global impact of the added damping solution on other converter dynamics, which might lead to new interactions and instability phenomena.

1.8.3 Stability by design: impedance specifications

A more proactive approach is to design the converter control systems with a passive behavior across the whole frequency range, ensuring that they do not introduce destabilizing interactions when connected to the grid. If such requirement is imposed on all converters, the stability of the entire system can be guaranteed by design, without the need for extensive testing and retuning [65, 66]. However, passivity-based specifications suffer from the following limitations:

- They can be overly restrictive, as they may limit the dynamic performance of the converters and may not be necessary for stability in all cases. For instance, certain non-passive behaviors may be acceptable if they are sufficiently damped or if they do not interact with other components in a destabilizing manner, as will be shown in Chapter 4.

- Imposing passivity as a design requirement may limit the performance of the converters, as it may impact other important dynamic requirements, such as overall response speed.

A less conservative approach is to impose frequency-dependent impedance specifications across different frequency ranges, which represent a potential compromise, balancing stability and performance. Impedance specifications to mitigate CPL behavior in the low-frequency range and high-frequency instability due to time-delay effects are discussed in [53].

However, defining appropriate specifications shall be combined with a continued analysis of new stability phenomena, as the design of the specifications should be based on a root-cause understanding of the underlying mechanisms of instability. At the time of writing this thesis, the state of the art in this area is still in its early stages, and further research is needed to establish comprehensive and practical impedance specifications for multi-vendor MTDC grids.

1.8.4 Defining requirements of standalone converter stations

Rather than dictating a specific control solution, this approach focuses on specifying the standalone behavior of the converter at the DC-PoC. It is particularly suitable for multi-vendor systems, where the control solution is proprietary to each vendor. Testing the converter control in a standalone manner represents the first step before conducting system-level studies, in which all HVDC grid subsystems are interconnected. If well-defined requirements are satisfied at the standalone level, the risk of instability after connecting the converter to the grid can be significantly reduced, even without detailed knowledge of the complete grid information.

However, defining such requirements is not straightforward, as it requires a clear justification of why standalone behavior will be reflected in system-level stability, which is not always guaranteed. The concept of specifying standalone requirements has been adopted in InterOPERA [14].

The main contribution of this thesis falls within the category of defining requirements for the standalone behavior of converter stations. By developing accurate test setups, extracting the relevant grid dynamics, and providing them in the standalone test setup, the stability of the converter station can be assessed without requiring detailed knowledge of other converters and the complete grid configuration. This approach will be detailed in Chapter 5.

1.9 Thesis outline

This thesis consists of four core chapters, excluding the introduction and conclusion. The structure of the thesis is illustrated in Fig. 1.5. The contents of each chapter are detailed as follows:

- **Chapter 2** presents the modeling details of the MMC Arm Average Model (AAM), highlighting the multi-frequency behavior and internal dynamics associated with circulating currents and capacitor voltage ripples. The focus is on obtaining a Linear Time-Invariant (LTI) model of the MMC that captures the internal dynamics relevant for stability analysis. Moreover, the chapter details the MMC control structures considered in this thesis, starting with different modulation

strategies, moving to inner loop control structures, and finally to the outer control loops. The respective modeling approach used for specific control structures is also explained. All developed LTI models are then validated against non-linear EMT models in the time domain, demonstrating their accuracy for the stability analysis conducted in the subsequent chapters.

- **Chapter 3** focuses on primary DC voltage control in MTDC grids, initially addressing static aspects and subsequently exploring dynamic performance and small-signal stability. Two implementation options for DC voltage droop control are presented, highlighting their inherent differences and analyzing interoperability limitations when used within the same grid. Furthermore, a critical aspect of interoperability is investigated: the interaction between DC voltage droop control and Grid-Forming (GFM) control. A novel implementation of the combined DC voltage droop and GFM control is proposed, to overcome the limitations of traditional approaches. This new implementation leverages specific DC voltage droop options to offer small-signal stability performance comparable to the traditional method. Finally, guidelines for droop gain limits for the respective implementations are discussed to assist in the design of multi-vendor MTDC grids.

- **Chapter 4** examines the critical elements impacting MTDC grid stability. Starting from simplified analytical models, the intuition behind the root causes of specific instability phenomena is established. The chapter then performs an extensive small-signal stability analysis, highlighting the impact of DC fault-limiting reactors (DCRs), operating points, and internal MMC control strategies on the stability of the MTDC grid. Additionally, the chapter proposes an active damping solution to mitigate the instability caused by large DCR values, applying it to a four-terminal DC grid. Finally, a critical but often overlooked aspect is investigated: the sharing of electrostatic inertia and DC voltage support among converter stations considering the existence of DCRs. This analysis invalidates certain oversimplified assumptions about DC grid behavior and is validated through case studies in a four-terminal meshed DC grid.

- **Chapter 5** builds on the results and insights obtained in the previous chapters to address a critical gap in the state of the art: the lack of standardized approaches for representing DC grid dynamics at the DC Point of Connection (DC-PoC) for standalone compliance testing of converter stations. A step-by-step methodology for deriving the DC grid impedance is presented, considering its dependencies on passive grid elements, operating points, and control strategies of other converters in the grid. Two equivalent models are proposed: a simplified RLC equivalent capturing dominant low-frequency dynamics and a more accurate frequency-dependent equivalent model representing grid behavior across a wider frequency range. Both models are validated and implemented in time domain, allowing for small-signal stability analysis and control design without requiring detailed access to the complete MTDC grid configuration.

- **Chapter 6** summarizes the key conclusions of the thesis and proposes directions for future research.

1.10 Thesis contributions

The key contributions of this thesis are summarized as follows:

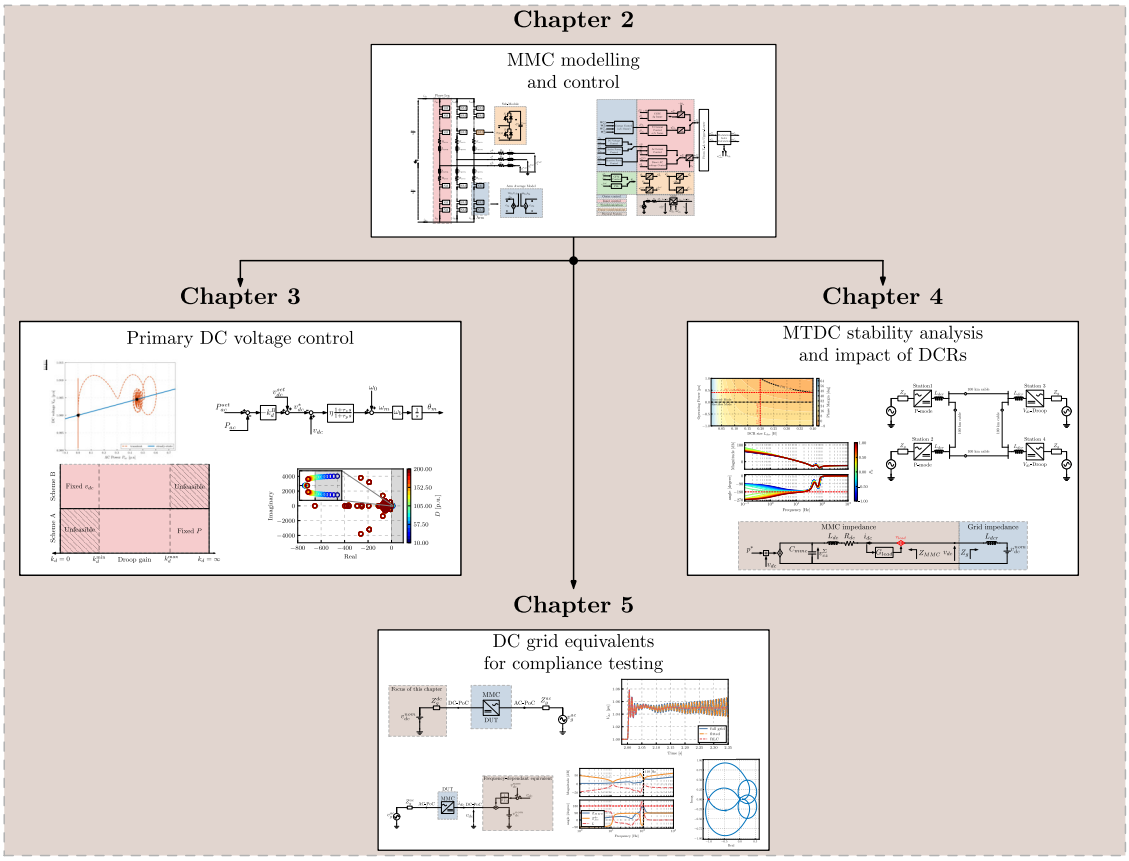

Figure 1.5: Thesis structure.

1. **Assessment of primary DC voltage control implementations in MTDC grids.** Different implementation strategies for primary DC voltage control have been investigated using the developed small-signal models, allowing a detailed evaluation of their dynamic behavior and interoperability in multi-vendor MTDC systems. The study identifies fundamental limitations and interaction mechanisms associated with these control approaches.

2. **Proposal of a novel combined DC voltage droop and grid-forming control implementation.** Based on the comparative analysis of existing control schemes, a new implementation combining DC voltage droop control with grid-forming operation is proposed. The proposed approach introduces favorable small-signal stability characteristics, addressing limitations observed in conventional implementations.

3. **Comprehensive analysis of small-signal stability in MTDC grids across control and passive components.** A detailed investigation of factors influencing MTDC grid stability is conducted, spanning converter control dynamics and passive network elements. Particular emphasis is placed on DC fault-limiting reactors (DCRs), demonstrating their dual role in stability behavior and dynamic coupling among converter stations, thereby providing new insight into interaction mechanisms and DC voltage support.

4. **Design of an inner control mitigation strategy for instability induced by large DC reactors.** To address instability risks associated with large DCRs, a lead-compensator-based control solution is proposed and integrated within the MMC control structure. The controller enhances damping of the critical oscillatory mode while preserving system performance.

5. **Development of DC grid equivalent models for standalone compliance and interoperability assessment.** To support standalone testing of converter stations prior to connection in multi-vendor MTDC grids and performing system-level studies, equivalent DC grid models are derived and validated. The proposed models capture variations in grid conditions, including remote station control modes, DC reactor sizing, and operating-point dependencies, enabling stability-oriented compliance assessment without full system information. This is schematically illustrated in Fig. 1.6.

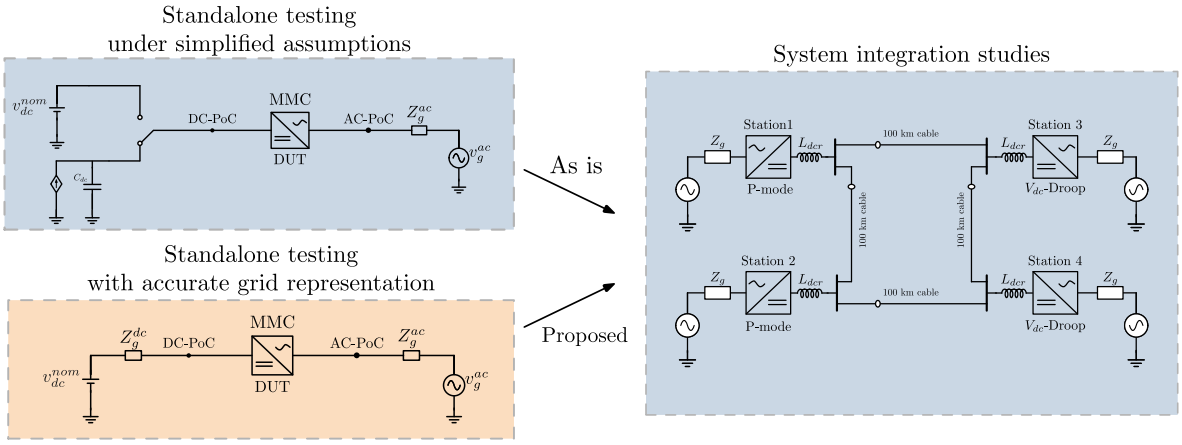

Figure 1.6: Schematic representation of the contribution related to DC grid equivalent models for standalone compliance and interoperability assessment.

1.11 List of publications

The following is a list of publications resulting from the research conducted for this thesis.

Journal articles

- **M. Elsodany**, K. Shinoda, J. Dai, and S. Bacha, "Development of frequency-dependent DC equivalent models for multi-terminal DC grids" International Journal of Electrical Power & Energy Systems, vol. 173, p. 111427, Dec. 2025, doi: 10.1016/j.ijepes.2025.111427.

- **M. Elsodany**, K. Shinoda, J. Dai, and S. Bacha, "On the damping and coupling impacts of DC fault-limiting reactors in multi-terminal DC grids" International Journal of Electrical Power & Energy Systems, vol. 174, p. 111543, Jan. 2026, doi: 10.1016/j.ijepes.2025.111543.

Conference articles

- **M. Elsodany**, K. Shinoda, J. Dai, A. Bertinato, and S. Bacha, "Assessment of two DC voltage droop options for small-signal stability in MMC-based multi-terminal DC grids" in 13th International Conference on Power Electronics, Machines and Drives (PEMD 2024), Institution of Engineering and Technology, 2024, pp. 497–504. doi: 10.1049/icp.2024.2199.

- **M. Elsodany**, K. Shinoda, J. Dai, and S. Bacha, "Analysis of Interoperability between DC-Voltage-Droop-Controlled MMCs with Grid-Forming Functionality in a MTDC Grid" in 2025 IEEE Kiel PowerTech, IEEE, Jun. 2025, pp. 1–6. doi: 10.1109/powertech59965.2025.11180302.

- K. Shinoda, **M. Elsodany**, J.-C. Gonzalez, J. Dai, A. Benchaib, and S. Bacha, "Comparison between DC Voltage Droop Schemes and Grid-Following & Grid-Forming Control in AC Systems in View of Interoperability of MTDC grids" in 2023 25th European Conference on Power Electronics and Applications (EPE23 ECCE Europe), IEEE, Sep. 2023.

2

Modular Multilevel Converters: Modeling and Control

2.1 Introduction

The Modular Multilevel Converter (MMC) is widely regarded as the state-of-the-art converter topology for HVDC applications. Since its introduction by Prof. Marquardt in 2002 [67], the MMC has gained significant attention in both academia and industry. It offers several advantages compared with existing LCC technology and other VSC topologies, such as two-level and three-level converters. The first commissioned MMC-HVDC project was the Trans Bay Cable project, commissioned by Siemens in 2010. [68]. Although cascaded converter topologies existed prior to the MMC, they required individual isolated feeding by transformers and lacked modularity.

The modular structure of the MMC allows for scalability to high voltage and power ratings, making it suitable for various applications. By generating a staircase voltage waveform with low harmonic distortion, the MMC reduces the need for bulky AC filters., leading to superior technical and economic characteristics compared to prior topologies. Today, most HVDC converter vendors offer MMC-based solutions [69], and several large-scale MMC-HVDC projects have been successfully commissioned worldwide [9].

Despite these advantages, the MMC exhibits complex multi-frequency dynamics that pose challenges for accurate modeling and stability-oriented system design. The MMC exhibits internal dynamics associated with circulating currents and capacitor voltage ripples, which can interact with the connected AC and DC grids. Understanding these interactions is crucial for accurate modeling and stability analysis of MMC-based HVDC systems. This chapter aims to provide a comprehensive overview of the MMC topology, its dynamic modeling approaches, and control strategies. It serves as a foundation for the subsequent chapters, which aim to investigate the stability and control interoperability considerations of MMC-based HVDC grids.

2.2 MMC topology and modeling

A schematic of a three-phase MMC is shown in Fig. 2.1. Each phase leg consists of an upper (u) and a lower (l) arm, which in turn consist of N submodules stacked in series with an inductor L_{arm} to limit the current in case of DC faults [70]. On the AC side, a wye-delta transformer connects the MMC to the AC Point of Connection (AC-PoC), providing galvanic isolation. The secondary (converter) side of the transformer is connected in delta configuration to block any DC components in the current from flowing into the AC grid [70].

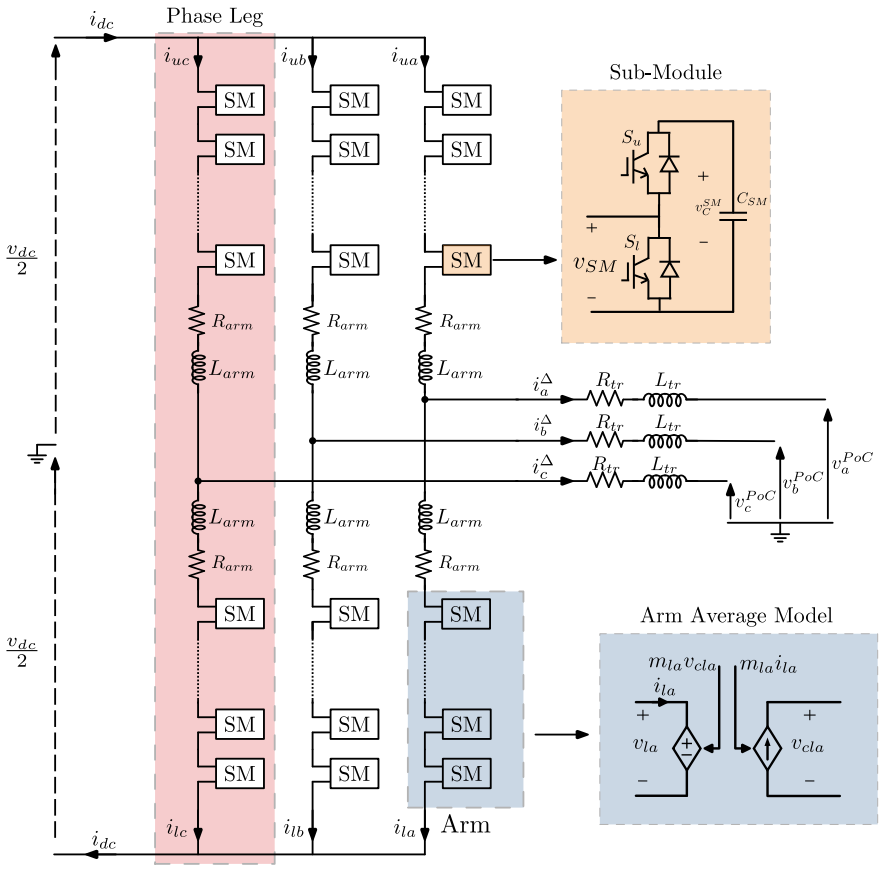

Figure 2.1: Schematic of the Modular Multilevel Converter with its Arm Average Model (MMC-AAM).

The most common submodule topologies are the half-bridge and full-bridge configurations. The half-bridge submodule (Fig. 2.2a) uses two switches and a capacitor, whereas the full-bridge submodule (Fig. 2.2b) uses four switches and a capacitor. Other topologies include clamped-double submodules, cross-connected configurations, and soft-switching configurations [71]. A key advantage of the full-bridge submodule over the half-bridge one is its ability to block fault currents, thereby providing protection against uncontrolled AC fault currents and preventing uncontrolled rectification that can occur with half-bridge submodules. However, full-bridge submodules require more switches, leading to higher cost and complexity [71]. The remainder of this chapter focuses on the half-bridge submodule topology.

The half bridge submodule is shown in Fig. 2.2a. It consists of two switches, S_u and S_l, each switch comprising an IGBT and an antiparallel diode, and a capacitor C_{SM}. The submodule inserted voltage v_{SM} is dependent on the states of switches s_u and s_l. In this regard, three states are possible for the submodule operation.

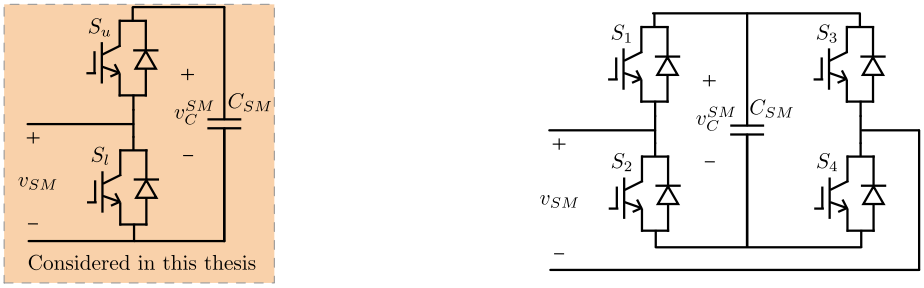

(a) Half-bridge submodule

(b) Full-bridge submodule

Figure 2.2: Common MMC submodule topologies.

- *Inserted*: S_u is on and S_l is off, $v_{SM} = v_c^{SM}$.
- *Bypassed*: S_u is off and S_l is on, $v_{SM} = 0$.
- *Blocked*: both S_u and S_l are off, $v_{SM} = 0$.

The direction of the arm current determines whether the submodule capacitor is charged or discharged, provided that the submodule is inserted. Typically, a capacitor voltage balancing algorithm (CBA) is implemented to decide which submodules are inserted or bypassed at each instant in order to avoid overcharging or undercharging of the submodules capacitors, meaning to keep the capacitor voltage of each submodule close to the others [72]. From Fig. 2.2a, for the ith submodule, the submodule inserted voltage is given by

$$v_{u,l}^{SM,i} = m_{u,l}^{i} v_{cu,l}^{SM,i} \tag{2.1}$$

where $v_{cu,l}^{SM,i}$ is the submodule capacitor voltage, and $m_{u,l}^{i}$ is the corresponding insertion index.

When a sufficiently large number of submodules is utilized, the sequential insertion and bypass of submodules enables the arm output voltage, and consequently the AC terminal voltage, to have a staircase waveform that closely approximates a sinusoidal waveform with low harmonic distortion. This characteristic reduces the need for additional filters to mitigate switching harmonics, representing one of the key advantages of the MMC topology.

When selecting a suitable MMC model for analysis, the choice ultimately depends on the specific objectives of the study. Various MMC models have been proposed in the literature, differing in both complexity and accuracy. These models can generally be classified into four categories: detailed switching models, submodule-level averaged models, arm-level averaged models, and equivalent MMC capacitor models [71, 73–75].

Detailed switched MMC models retain all switching dynamics of the submodules, providing the highest accuracy. However, they are computationally intensive and impractical for system-level studies, due to the need for very small simulation time steps. Submodule-level averaged models simplify the representation by representing individual submodules by an equivalent voltage source. Arm-level averaged models further simplify the MMC representation by averaging the submodule voltages and insertion indices over each arm, under the assumption that submodule capacitor voltage balancing is ensured by a proper balancing algorithm. Finally, equivalent MMC capacitor models represent the entire MMC as a single equivalent capacitor, significantly simplifying the analysis but potentially sacrificing accuracy in capturing internal dynamics.

The scope of this thesis focuses on the dynamic performance and system-level studies of MTDC grids. Considering that MMCs typically consist of around 300–400 submodules per arm, using detailed switching models would significantly increase computational complexity, especially when system-level analysis is required. Therefore, in this thesis, only the Arm Average Model (AAM) and the equivalent MMC capacitor model, also called the Average-Value Model (AVM), are considered for the analysis.

The accuracy of the AAM has been validated through both time-domain simulations [75] and experimental results [76,77]. Although the equivalent MMC capacitor model is computationally simpler and has been used in many previous studies [78–80], it lacks sufficient accuracy in the medium- to high-frequency range, as highlighted in [81].

In this chapter, both the MMC-AAM and MMC-AVM are utilized depending on the adopted control strategy. They are then linearized to be suitable for small-signal stability analysis.

2.3 Dynamic analysis of the MMC Arm Average Model

The MMC-AAM is based on the representation of each arm by a voltage source, and aggregating the submodule capacitors into a single equivalent arm capacitor C_{arm}, as shown in Fig. 2.1. The charging and discharging dynamics of the submodule capacitors are represented by the equivalent arm capacitor voltage dynamics. The first step in deriving the AAM dynamics is to sum (2.1) over all N submodules per arm, the arm inserted voltage is then given by

$$v_{u,l} = \sum_{i=1}^{N} m_{u,l}^{i} v_{cu,l}^{SM,i} \tag{2.2}$$

As discussed in the previous section, when a CBA is assumed to be working properly, the capacitor voltages of all submodules can be assumed to be equal with sufficient accuracy. Therefore, the equivalent arm capacitor voltage can be defined as

$$v_{cu,l} = \sum_{i=1}^{N} v_{cu,l}^{SM,i} = N v_{cu,l}^{SM} \tag{2.3}$$

As a consequence, the inserted arm voltage in (2.2) can be simplified to

$$v_{u,l} = \frac{v_{cu,l}}{N} \sum_{i=1}^{N} m_{u,l}^{i} = m_{u,l} v_{cu,l} \tag{2.4}$$

where $m_{u,l}$ is the arm modulation index. It is the output of the MMC control system, which will be discussed in Section 2.6. $m_{u,l}$ has a range $[0, 1]$ for half-bridge submodules, and $[-1, 1]$ for full-bridge submodules. The equivalent arm capacitor voltage $v_{cu,l}$ can be derived by analyzing the individual submodule capacitor dynamics

$$C_{SM} \frac{dv_{cu,l}^{SM,i}}{dt} = m_{u,l}^{i} i_{u,l} \tag{2.5}$$

Similarly, summing (2.5) over the N submodules in each arm yields the arm capacitor voltage dynamics

$$C_{SM} \sum_{i=1}^{N} \frac{dv_{cu,l}^{SM,i}}{dt} = \sum_{i=1}^{N} m_{u,l}^{i} i_{u,l} = i_{u,l} \sum_{i=1}^{N} m_{u,l}^{i} \tag{2.6}$$

leading to

$$C_{arm}\frac{dv_{cu,l}}{dt} = m_{u,l}i_{u,l} \tag{2.7}$$

where $C_{arm} = \frac{C_{SM}}{N}$. Applying Kirchhoff's voltage law to the per-phase quantities shown in Fig. 2.1, the following equations are obtained for phase $k \in \{a, b, c\}$

$$\frac{v_{dc}}{2} - v_{uk} - L_{arm}\frac{di_{uk}}{dt} - R_{arm}i_{uk} - L_{tr}\frac{d}{dt}(i_{uk} - i_{lk}) - R_{tr}(i_{uk} - i_{lk}) = v_k^{PoC} \tag{2.8a}$$

$$-\frac{v_{dc}}{2} + v_{lk} + L_{arm}\frac{di_{lk}}{dt} + R_{arm}i_{lk} - L_{tr}\frac{d}{dt}(i_{uk} - i_{lk}) - R_{tr}(i_{uk} - i_{lk}) = v_k^{PoC} \tag{2.8b}$$

with R_{arm} aggregating the ohmic losses of the arm inductor L_{arm} and the SM conduction losses, and the converter transformer modeled by a series inductance L_{tr} and resistance R_{tr}.

Since the MMC arm capacitor voltages and currents contain multiple harmonics in steady-state [82], it is common to utilize the $\Sigma - \Delta$ transformation [34]. This notation helps in isolating the MMC variables associated with different harmonic components. The Δ variables are primarily linked with the fundamental frequency component, while the Σ variables correspond to the DC component and the negative sequence double-frequency components [34]. Accordingly, the following variables are defined for each MMC phase leg.

$$i^{\Sigma} \triangleq \frac{i_u + i_l}{2} \qquad i^{\Delta} \triangleq i_u - i_l \tag{2.9a}$$

$$v^{\Sigma} \triangleq \frac{v_u + v_l}{2} \qquad v^{\Delta} \triangleq \frac{v_l - v_u}{2} \tag{2.9b}$$

$$v_c^{\Delta} \triangleq \frac{v_{cu} - v_{cl}}{2} \qquad v_c^{\Sigma} \triangleq \frac{v_{cu} + v_{cl}}{2} \tag{2.9c}$$

$$m^{\Delta} \triangleq m_u - m_l \qquad m^{\Sigma} \triangleq m_u + m_l \tag{2.9d}$$

Observing Fig. 2.1 and the definitions in (2.9), it can be seen that i^{Δ} represents the MMC current flowing to the AC grid, while i^{Σ} represents the circulating current within the converter. The variables v^{Δ} and v^{Σ} will later be shown to correspond to the voltages driving the AC-side current and the circulating current, respectively, highlighting the practicality of the $\Sigma-\Delta$ transformation. Moreover, v_c^{Δ} represents half of the difference between the capacitor voltages of the upper and lower arms, while v_c^{Σ} is closely related to the total energy stored in one leg.

Respectively summing and subtracting (2.8a) and (2.8b), and applying the definitions in (2.9), the dynamic equations of the Δ and Σ currents are obtained, for phase k, as follows:

$$\underbrace{\left(\frac{L_{arm}}{2} + L_{tr}\right)}_{L_{ac}}\frac{di_k^{\Delta}}{dt} = v_k^{\Delta} - v_k^{PoC} - \underbrace{\left(\frac{R_{arm}}{2} + R_{tr}\right)}_{R_{ac}}i_k^{\Delta} \tag{2.10a}$$

$$L_{arm}\frac{di_k^{\Sigma}}{dt} = \frac{v_{dc}}{2} - v_k^{\Sigma} - R_{arm}i_k^{\Sigma} \tag{2.10b}$$

The inserted voltages v_k^{Δ} and v_k^{Σ} are obtained by utilizing the definitions in (2.9) and (2.4) leading

to

$$v_k^{\Delta} = \frac{-1}{2}(m_k^{\Delta} v_{ck}^{\Sigma} + m_k^{\Sigma} v_{ck}^{\Delta}) \tag{2.11a}$$

$$v_k^{\Sigma} = \frac{1}{2}(m_k^{\Sigma} v_{ck}^{\Sigma} + m_k^{\Delta} v_{ck}^{\Delta}) \tag{2.11b}$$

A similar derivation can be conducted for the arm capacitor voltages. Starting from (2.7) and apply the $\Sigma - \Delta$ transformation to obtain

$$2C_{arm}\frac{dv_{ck}^{\Delta}}{dt} = m_k^{\Delta} i_k^{\Sigma} + \frac{m_k^{\Sigma} i_k^{\Delta}}{2} \tag{2.12a}$$

$$2C_{arm}\frac{dv_{ck}^{\Sigma}}{dt} = m_k^{\Sigma} i_k^{\Sigma} + \frac{m_k^{\Delta} i_k^{\Delta}}{2} \tag{2.12b}$$

Hence, the MMC can be represented by the set of differential equations in (2.10) and (2.12), together with the algebraic relations in (2.11), as schematically illustrated in Fig. 2.3. From the figure, the arm capacitor voltages and currents are the states of the MMC-AAM, while the modulation indices m_k^{Σ} and m_k^{Δ} are the control inputs. The AC-side voltage v_k^{PoC} and the DC voltage v_{dc} are treated as external inputs to the MMC model.

These equations highlight the inherent frequency coupling among the MMC variables, revealing their multi-frequency steady-state behavior. Unlike conventional two-level VSCs, whose variables are only time-periodic at the fundamental frequency, the MMC presents components at different frequencies in steady state. This characteristic complicates the derivation of a steady-state time-invariant (SSTI) model required for small-signal analysis based on Linear Time-Invariant (LTI) methods.[1]

Two main insights arise from this observation. First, since the equations are expressed in the *abc* frame, the MMC variables remain time-periodic in steady state, which makes direct LTI-based small-signal analysis difficult. This is a similar challenge to two-level VSC modeling. Second, although transforming the system into the rotating *dq* frame may appear straightforward, the presence of multiple frequency components and nonlinear couplings requires additional derivations to properly capture these interactions. Accurately modeling these multi-frequency effects is therefore essential for any small-signal stability-oriented MMC representation.

This harmonic content of the different MMC variables can be further demonstrated by conducting a time-domain simulation, where a simple setup is considered. The MMC is connected to ideal DC and AC voltage sources on the respective connections and operating in rated inverter power. For simplicity, only basic control scheme is utilized. Controllers dedicated to the suppression of the circulating currents are not considered. The objective is to empirically observe the harmonic content of the main MMC states.

Fig. 2.4 shows the MMC arm capacitor voltages and currents in steady state along with their corresponding Fast Fourier Transform (FFT) analysis conducted only on phase *a*. It can be observed that the Δ currents contain only the fundamental-frequency component, which is expected since they represent the currents flowing to the AC side. The Δ capacitor voltages contain a small-magnitude

[1]For instance, from (2.12b), if m_k^{Σ} and i_k^{Σ} contain DC and double-frequency components, while m_k^{Δ} and i_k^{Δ} contain fundamental-frequency components, the resulting capacitor voltages v_{ck}^{Σ} and v_{ck}^{Δ} will include higher-order harmonics generated by the products of these signals.

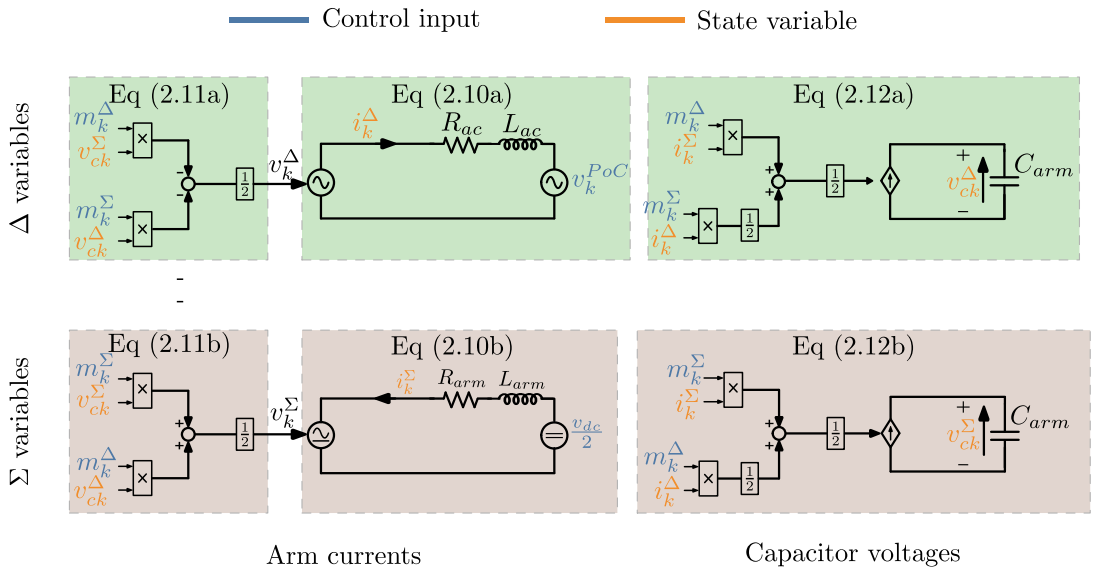

Figure 2.3: MMC equivalent circuit utilizing the $\Sigma - \Delta$ variables.

fundamental-frequency component and a 3rd-harmonic component. The Σ currents contain a DC component (equal to $i_{dc}/3$) and a significant negative-sequence second-harmonic component, which is a known characteristic of the MMC circulating currents [83]. Similarly, the Σ capacitor voltages contain a dominant DC component ($\approx v_{dc}$) and a negative-sequence second-harmonic component. These results align with the analysis presented in [34, 81, 82].

2.4 Linear time-invariant modeling of the MMC

It is evident from the previous analysis that the MMC capacitor voltages and arm currents contain multiple harmonic components under steady-state conditions. When these states are multiplied by the control inputs, which are themselves time-varying, harmonic coupling arises, see Equations (2.10) - (2.12). This complicates the derivation of a steady-state solution where the equilibrium point is time-invariant, which is a prerequisite for conducting small-signal analysis. To address this challenge, various modeling techniques have been proposed in the literature. This section provides an overview of these approaches and justifies the use of the multi-*dq* frame representation for the MMC.

A common method for modeling the MMC in small-signal stability studies is the state-space representation with assumptions to simplify the modeling [78, 79, 84–86]. These models aggregate the arm capacitors into a single equivalent MMC capacitor, neglecting the circulating current dynamics, inspired by similar modeling used for two-level VSCs [87]. This leads to an LTI model by applying a Park transformation to the AC signals leading to a *dq* frame rotating at the fundamental frequency. While this simplification reduces the model order, it may introduce inaccuracies under certain conditions, such as weak grid connections [88]. Moreover, the second-harmonic circulating current dynamics have been shown to cause instabilities [89, 90]. Nevertheless, these models have proven accurate for specific control schemes.

The internal MMC dynamics have been incorporated into state-space small-signal modeling in [91–93] using multiple *dq* frame transformations, one at the fundamental frequency and another at double the fundamental frequency. This approach was further extended to include third-harmonic dynamics in [34]. Its advantage lies in directly leading to an LTI representation, making it compatible

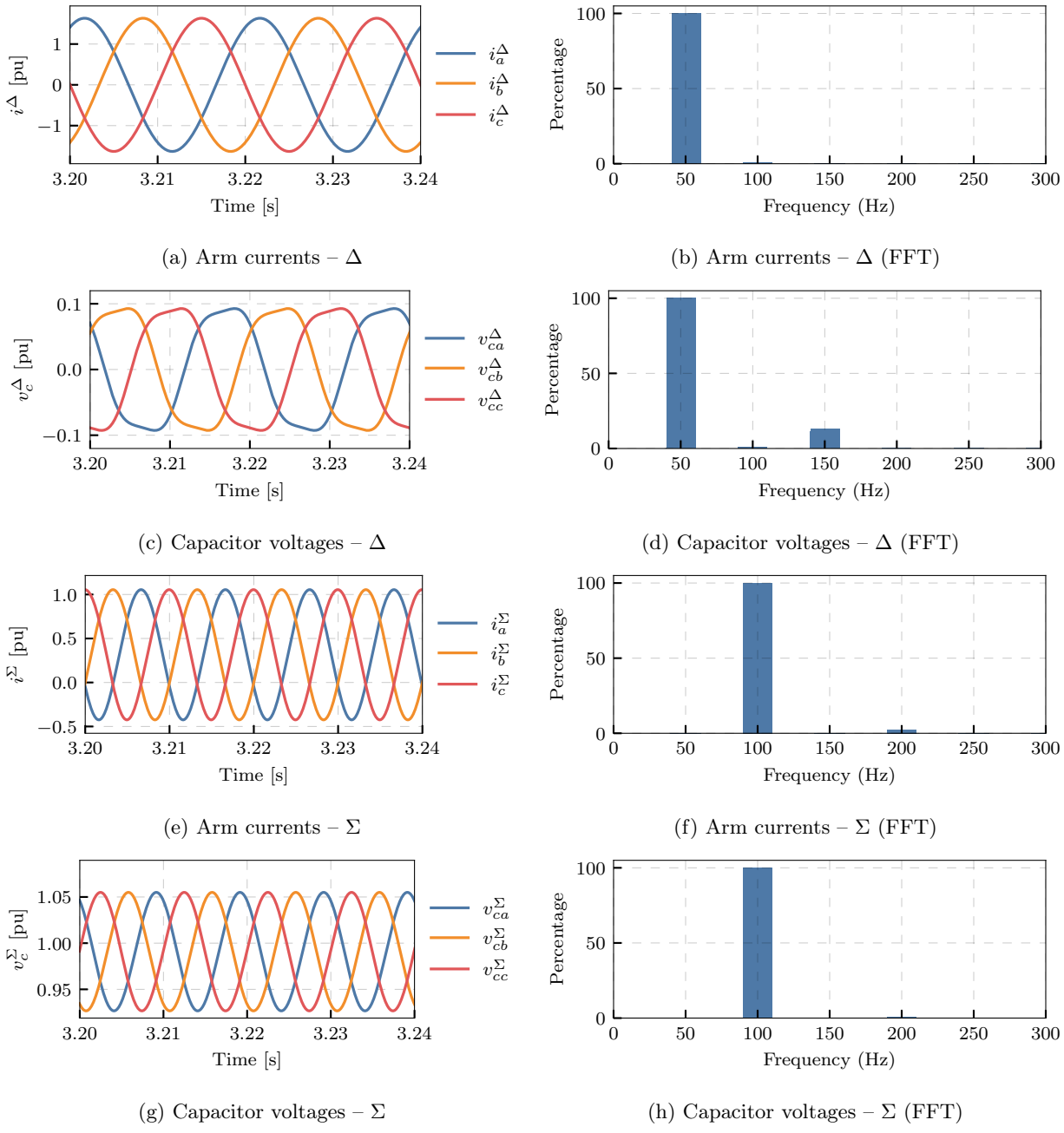

(a) Arm currents – Δ

(b) Arm currents – Δ (FFT)

(c) Capacitor voltages – Δ

(d) Capacitor voltages – Δ (FFT)

(e) Arm currents – Σ

(f) Arm currents – Σ (FFT)

(g) Capacitor voltages – Σ

(h) Capacitor voltages – Σ (FFT)

Figure 2.4: MMC arm capacitor voltages and currents in steady state with their corresponding FFT decomposition.

with other LTI system components. Consequently, eigenvalue and participation factor analyses can be readily conducted to gain insights into interaction modes. The model proposed in [34] has been further utilized in the literature for small-signal stability studies, proving its applicability for offshore system stability analysis [94] and for control design considering protection limitations in [95].

In [81], a comparison between the equivalent MMC capacitor model (AVM) and the MMC-AAM is presented, demonstrating through eigenvalue analysis and time-domain simulations that the AVM models can only accurately capture MMC dynamics when the internal circulating currents are explicitly controlled. In [96], a stability analysis of the MMC was conducted, revealing the existence of poorly damped internal harmonic resonant modes associated with circulating currents and capacitor voltage ripples. These modes cannot be captured by the simplified AVM. Hence, one should identify the possible modeling simplifications that can be made without compromising the accuracy required for the specific study.

It should be noted, however, that even the multi-dq frame transformation modeling contains certain simplifications. The model still neglects some harmonic components in the MMC (notably the 6ω harmonics) and is valid only under balanced conditions (i.e., it does not account for negative-sequence harmonics) [34]. To address these limitations, a possible solution is to retain Linear Time-Periodic (LTP) models and perform a small-signal stability analysis using Floquet multipliers. The essence of this method is to discretize the system over one period of the time-varying coefficients, and use it to numerically compute the state transition matrix, whose eigenvalues (Floquet multipliers) determine the system stability. This approach has been employed in [97,98]. However, this method is computationally intensive and provides limited insight into the system dynamics.

Another modeling approach involves the use of Harmonic State-Space (HSS) models [29,99–101]. In this framework, the Linear Time-Periodic (LTP) system is transformed into a complex-valued, higher-dimensional Linear Time-Invariant (LTI) representation by expressing the system's periodic coefficients and signals through Fourier series expansions and applying harmonic balance [102]. This allows the application of conventional eigenvalue-based stability tools, similar to multi-dq models but without restricting the analysis to a small number of harmonic components. HSS models are particularly effective capturing harmonic couplings over different frequency ranges. However, this increased accuracy comes at the expense of a substantial rise in model order, as each additional harmonic introduces further state variables. Despite this, the method has shown strong suitability for analyzing harmonic interactions in MMC-based systems.

Dynamic phasor (DP) modeling represents another widely used technique for capturing the internal dynamics of the MMC. The core of the DP framework is the hypothesis that the signal can be modeled as nearly-periodic during transients, allowing it to be represented by time-varying Fourier coefficients (Dynamic Phasors). The derivation first makes the nonlinear system time-invariant using the DP representation, and then linearizes it around a constant steady-state operating point to yield an LTI system. This allows for a lower-order model that focuses on the dominant dynamic trends of selected harmonics [102]. This makes DP modeling especially attractive for system-level studies where computational efficiency is critical. However, the real-valued nature of the DP formulation makes it more suitable for eigenvalue-based stability analysis than for impedance-based stability analysis. This method offers higher accuracy than simplified state-space AVM or AAM models while maintaining a more manageable computational burden than full HSS or full LTP representations.

Overall, both HSS and DP approaches bridge the gap between simplified LTI models and fully time-domain LTP formulations. The two methods originate from similar initial hypotheses, yielding

state-space models with the same dynamic behavior.

In this thesis, the approach presented in [34] is adapted to derive a linear time-invariant (LTI) state-space model based on a multi-*dq* frame state-space representation. This modeling choice is motivated by its ability to accurately capture the dominant internal dynamics of the MMC within the frequency range relevant to the conducted studies, while avoiding the high dimensionality associated with HSS or LTP formulations. The resulting LTI model offers a suitable balance between fidelity and computational efficiency, making it well-suited for eigenvalue-based small-signal stability analysis, and also frequency-domain impedance analysis at the converter AC and DC terminals. Moreover, the method has been validated in several studies addressing offshore system stability [94] and control design under protection constraints [95], demonstrating its practical applicability.

As explained in Section 2.3, the Δ capacitor voltages v_{ck}^{Δ} and arm currents i_{k}^{Δ} primarily contain fundamental-frequency components; therefore, they are transformed to a *dq* frame rotating at ω. Conversely, the Σ capacitor voltages v_{ck}^{Σ} and arm currents i_{k}^{Σ} mainly contain DC and second-harmonic components, and are thus transformed to a *dq* frame rotating at -2ω. The Park matrix used for the *dq* transformation is given in Appendix B. Accordingly, the *abc* components of the MMC variables can be expressed in terms of their *dqz* components as follows

$$\boldsymbol{i}_{abc}^{\Delta} = \boldsymbol{P}_{\boldsymbol{\theta}}^{-1}\boldsymbol{i}_{dqz}^{\Delta} \qquad \boldsymbol{i}_{abc}^{\Sigma} = \boldsymbol{P}_{-\boldsymbol{2\theta}}^{-1}\boldsymbol{i}_{dqz}^{\Sigma} \tag{2.13a}$$

$$\boldsymbol{v}_{abc}^{\Delta} = \boldsymbol{P}_{\boldsymbol{\theta}}^{-1}\boldsymbol{v}_{dqz}^{\Delta} \qquad \boldsymbol{v}_{abc}^{\Sigma} = \boldsymbol{P}_{-\boldsymbol{2\theta}}^{-1}\boldsymbol{v}_{dqz}^{\Sigma} \tag{2.13b}$$

$$\boldsymbol{m}_{abc}^{\Delta} = \boldsymbol{P}_{\boldsymbol{\theta}}^{-1}\boldsymbol{m}_{dqz}^{\Delta} \qquad \boldsymbol{m}_{abc}^{\Sigma} = \boldsymbol{P}_{-\boldsymbol{2\theta}}^{-1}\boldsymbol{m}_{dqz}^{\Sigma} \tag{2.13c}$$

$$\boldsymbol{v}_{cabc}^{\Delta} = \boldsymbol{P}_{\boldsymbol{\theta}}^{-1}\boldsymbol{v}_{cdqz}^{\Delta} \qquad \boldsymbol{v}_{cabc}^{\Sigma} = \boldsymbol{P}_{-\boldsymbol{2\theta}}^{-1}\boldsymbol{v}_{cdqz}^{\Sigma} \tag{2.13d}$$

Substituting (2.13) into (2.10), (2.11) and (2.12) yields the following equations in the *dq* frames

$$2C_{arm}\frac{d}{dt}(\boldsymbol{P}_{\boldsymbol{\theta}}^{-1}\boldsymbol{v}_{cdqz}^{\Delta}) = \boldsymbol{P}_{\boldsymbol{\theta}}^{-1}\boldsymbol{m}_{dqz}^{\Delta} \circ \boldsymbol{P}_{-\boldsymbol{2\theta}}^{-1}\boldsymbol{i}_{dqz}^{\Sigma} + \frac{1}{2}\boldsymbol{P}_{-\boldsymbol{2\theta}}^{-1}\boldsymbol{m}_{dqz}^{\Sigma} \circ \boldsymbol{P}_{\boldsymbol{\theta}}^{-1}\boldsymbol{i}_{dqz}^{\Delta} \tag{2.14a}$$

$$2C_{arm}\frac{d}{dt}(\boldsymbol{P}_{-\boldsymbol{2\theta}}^{-1}\boldsymbol{v}_{cdqz}^{\Sigma}) = \boldsymbol{P}_{-\boldsymbol{2\theta}}^{-1}\boldsymbol{m}_{dqz}^{\Sigma} \circ \boldsymbol{P}_{-\boldsymbol{2\theta}}^{-1}\boldsymbol{i}_{dqz}^{\Sigma} + \frac{1}{2}\boldsymbol{P}_{\boldsymbol{\theta}}^{-1}\boldsymbol{m}_{dqz}^{\Delta} \circ \boldsymbol{P}_{\boldsymbol{\theta}}^{-1}\boldsymbol{i}_{dqz}^{\Delta} \tag{2.14b}$$

$$\boldsymbol{P}_{\boldsymbol{\theta}}^{-1}\boldsymbol{v}_{dqz}^{\Delta} = \frac{-1}{2}\left(\boldsymbol{P}_{\boldsymbol{\theta}}^{-1}\boldsymbol{m}_{dqz}^{\Delta} \circ \boldsymbol{P}_{-\boldsymbol{2\theta}}^{-1}\boldsymbol{v}_{cdqz}^{\Sigma} + \boldsymbol{P}_{-\boldsymbol{2\theta}}^{-1}\boldsymbol{m}_{dqz}^{\Sigma} \circ \boldsymbol{P}_{\boldsymbol{\theta}}^{-1}\boldsymbol{v}_{cdqz}^{\Delta}\right) \tag{2.14c}$$

$$\boldsymbol{P}_{-\boldsymbol{2\theta}}^{-1}\boldsymbol{v}_{dqz}^{\Sigma} = \frac{1}{2}\left(\boldsymbol{P}_{-\boldsymbol{2\theta}}^{-1}\boldsymbol{m}_{dqz}^{\Sigma} \circ \boldsymbol{P}_{-\boldsymbol{2\theta}}^{-1}\boldsymbol{v}_{cdqz}^{\Sigma} + \boldsymbol{P}_{\boldsymbol{\theta}}^{-1}\boldsymbol{m}_{dqz}^{\Delta} \circ \boldsymbol{P}_{\boldsymbol{\theta}}^{-1}\boldsymbol{v}_{cdqz}^{\Delta}\right) \tag{2.14d}$$

$$L_{ac}\frac{d}{dt}(\boldsymbol{P}_{\boldsymbol{\theta}}^{-1}\boldsymbol{i}_{dqz}^{\Delta}) = \boldsymbol{P}_{\boldsymbol{\theta}}^{-1}\boldsymbol{v}_{dqz}^{\Delta} - \boldsymbol{P}_{\boldsymbol{\theta}}^{-1}\boldsymbol{v}_{dqz}^{PoC} - R_{ac}\boldsymbol{P}_{\boldsymbol{\theta}}^{-1}\boldsymbol{i}_{dqz}^{\Delta} \tag{2.14e}$$

$$L_{arm}\frac{d}{dt}(\boldsymbol{P}_{-\boldsymbol{2\theta}}^{-1}\boldsymbol{i}_{dqz}^{\Sigma}) = \frac{v_{dc}}{2}\mathbf{1} - \boldsymbol{P}_{-\boldsymbol{2\theta}}^{-1}\boldsymbol{v}_{dqz}^{\Sigma} - R_{arm}\boldsymbol{P}_{-\boldsymbol{2\theta}}^{-1}\boldsymbol{i}_{dqz}^{\Sigma} \tag{2.14f}$$

where $\circ$ is the element-wise multiplication operator. Since the complete derivation of the final expressions starting from (2.14) is lengthy, they are presented in Appendix D for readability. The resulting MMC state variables in the *dq* frames are represented by the vector $\boldsymbol{x}_{\text{MMC}}^{\text{AAM}} \in \mathbb{R}^{12}$, defined as

$$\boldsymbol{x}_{\text{MMC}}^{\text{AAM}} = \begin{bmatrix} i_d^{\Delta} & i_q^{\Delta} & i_d^{\Sigma} & i_q^{\Sigma} & i_z^{\Sigma} & v_{cd}^{\Delta} & v_{cq}^{\Delta} & v_{czd}^{\Delta} & v_{czq}^{\Delta} & v_{cd}^{\Sigma} & v_{cq}^{\Sigma} & v_{cz}^{\Sigma} \end{bmatrix}^T \tag{2.15}$$

The variables v_{czd}^{Δ} and v_{czq}^{Δ} are included to represent the third-harmonic component of the zero-sequence

Δ capacitor voltage, See Appendix D. The MMC control inputs in the dq frames are defined as

$$\boldsymbol{u}_{\text{MMC}}^{\text{AAM}} = \Big[\underbrace{m_d^{\Delta} \quad m_q^{\Delta} \quad m_{zd}^{\Delta} \quad m_{zq}^{\Delta} \quad m_d^{\Sigma} \quad m_q^{\Sigma} \quad m_z^{\Sigma}}_{\text{control inputs}} \quad \underbrace{v_{dc} \quad v_d^{PoC} \quad v_q^{PoC}}_{\text{physical inputs}}\Big]^T \tag{2.16}$$

This formulation is suitable for small-signal analysis, as all variables are now expressed in time-invariant dq frames. The control inputs in (2.16) will later be specified according to the chosen control strategies, which will be discussed in Section 2.6.

2.5 Average Value Model of the MMC

As detailed in Section 2.4, the MMC-AAM provides sufficient accuracy for conducting small-signal stability analysis. However, as reported in [81], implementing certain control structures related to the internal energy of the MMC, specifically energy-based control involving horizontal and vertical balancing, leads to increased complexity and longer implementation times.

To address this, a reduced-order MMC model, referred to as the MMC-AVM, is utilized in this thesis when internal energy control is considered, inspired by the approach presented in [81]. The AVM simplifies the MMC representation by aggregating the arm capacitors into a single equivalent capacitor. In fact, this model is similar to that of a 2-level VSC, with the added specificity of MMC control regarding the decoupled regulation between the AC and DC sides. The primary assumption of the MMC-AVM is that, for each phase leg, the capacitor voltages of the upper and lower arms are equal (i.e., $v_{cu} = v_{cl} = \frac{v_{dc}}{2}$) and that the energy stored across the three legs is distributed equally. In other words, the internal energy balancing control of the MMC is assumed to be effective enough to maintain capacitor voltages at the desired levels; therefore, only the dynamics of the total energy stored in the MMC are considered.

The MMC-AVM is shown in Fig. 2.5. The equivalent MMC capacitor C_{eq} represents the total capacitance of the MMC, given by $C_{eq} = 6C_{arm}$, where C_{arm} is the arm capacitance. The DC-side impedance is represented by $R_{dc} = 2/3R_{arm}$ and $L_{dc} = 2/3L_{arm}$. The AC-side impedance is identical to that of the MMC-AAM, consisting of the inductance L_{ac} and the resistance R_{ac}. Fig. 2.5 also illustrates the main state variables of the MMC-AVM, which include the AC-side currents $\boldsymbol{i}_{dq}^{\Delta}$, the DC-side current i_{dc}, and the zero-sequence Σ component of the MMC capacitor voltage v_{cz}^{Σ}. The AVM dynamics are described by [81]:

$$L_{ac}\frac{di_d^{\Delta}}{dt} = v_d^{\Delta} - v_d^{PoC} - R_{ac}i_d^{\Delta} + \omega L_{ac}i_q^{\Delta} \tag{2.17a}$$

$$L_{ac}\frac{di_q^{\Delta}}{dt} = v_q^{\Delta} - v_q^{PoC} - R_{ac}i_q^{\Delta} - \omega L_{ac}i_d^{\Delta} \tag{2.17b}$$

$$L_{dc}\frac{di_{dc}}{dt} = v_{dc} - 2v_z^{\Sigma} - R_{dc}i_{dc} \tag{2.17c}$$

$$C_{mmc}\frac{dv_{cz}^{\Sigma}}{dt} = \underbrace{\frac{2v_z^{\Sigma}i_{dc}}{v_{cz}^{\Sigma}}}_{i_{mdc}} - \underbrace{\frac{3}{2}\frac{v_d^{\Delta}i_d^{\Delta} + v_q^{\Delta}i_q^{\Delta}}{v_{cz}^{\Sigma}}}_{i_{mac}} \tag{2.17d}$$

where v_d^{Δ} and v_q^{Δ} are the d and q components of the MMC AC inserted voltages, respectively, while v_z^{Σ} is the MMC DC-side inserted voltage. These inserted voltages are the output of the control system, which will be discussed in Section 2.6.

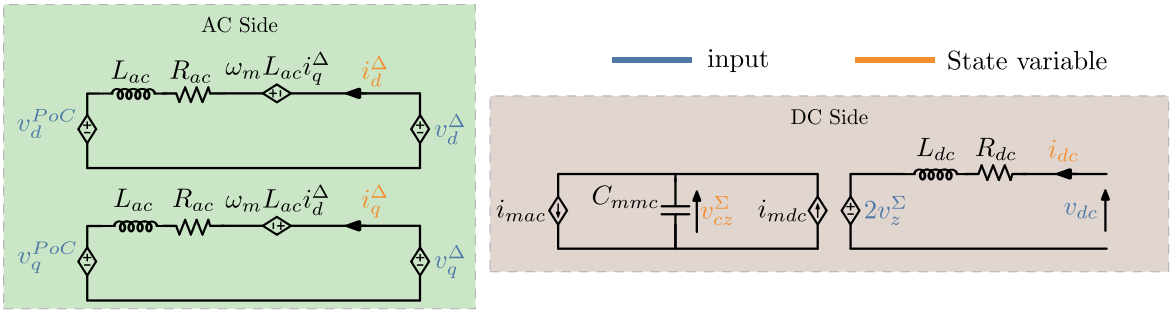

Figure 2.5: Average Value Model (AVM) MMC considered when internal energy control is implemented.

It should be noted that, since the circulating currents dynamics and the second-order arm capacitor voltage ripples are neglected in this model, the state variables described in (2.15) are described in a single dq frame rotating at the fundamental frequency ω. Hence, the state vector of the MMC-AVM is defined as

$$\boldsymbol{x}_{\text{MMC}}^{\text{AVM}} = \begin{bmatrix} i_d^\Delta & i_q^\Delta & i_{dc} & v_{cz}^\Sigma \end{bmatrix}^T \tag{2.18}$$

The control inputs of the MMC-AVM are defined as

$$\boldsymbol{u}_{\text{MMC}}^{\text{AVM}} = \Big[\underbrace{v_d^\Delta \quad v_q^\Delta \quad v_z^\Sigma}_{\text{control inputs}} \quad \underbrace{v_{dc} \quad v_d^{PoC} \quad v_q^{PoC}}_{\text{physical inputs}} \Big]^T \tag{2.19}$$

By comparing the input vector of the AAM (2.16) with that of the AVM (2.19), the reader may notice that the control inputs of the AVM are the inserted voltages themselves, whereas in the AAM they are the modulation indices. This is because, in the AVM, as will be explained in Section 2.6, the Compensated Modulation (CM) strategy is always employed. This strategy directly tracks the reference inserted voltages, rendering the modulation step redundant.

In general, the modulation step can still be included in the AVM if the Uncompensated Modulation (UCM) strategy is selected. However, this case is not considered in this thesis due to the invalidity of the AVM assumption when using UCM [81].

2.6 MMC control strategies

A schematic of the general MMC control structure and the different control strategies analyzed in this thesis is shown in Fig. 2.6. It follow a generic cascaded control structure and can be generally divided into inner control layers, outer control layers, synchronization mechanism, and modulation strategy. The inner control layers are responsible for producing the inserted voltages, from which the modulation indices can be calculated according to the chosen modulation strategy. The outer control layers generate the reference values for the inner control loops based on the desired operation mode of the MMC. Additionally, a synchronization mechanism is required to ensure proper phase alignment with the AC grid. Depending on the application, different control strategies can be implemented in each of these control blocks. In the following subsections, a description of the control strategies considered for each control layer is provided.

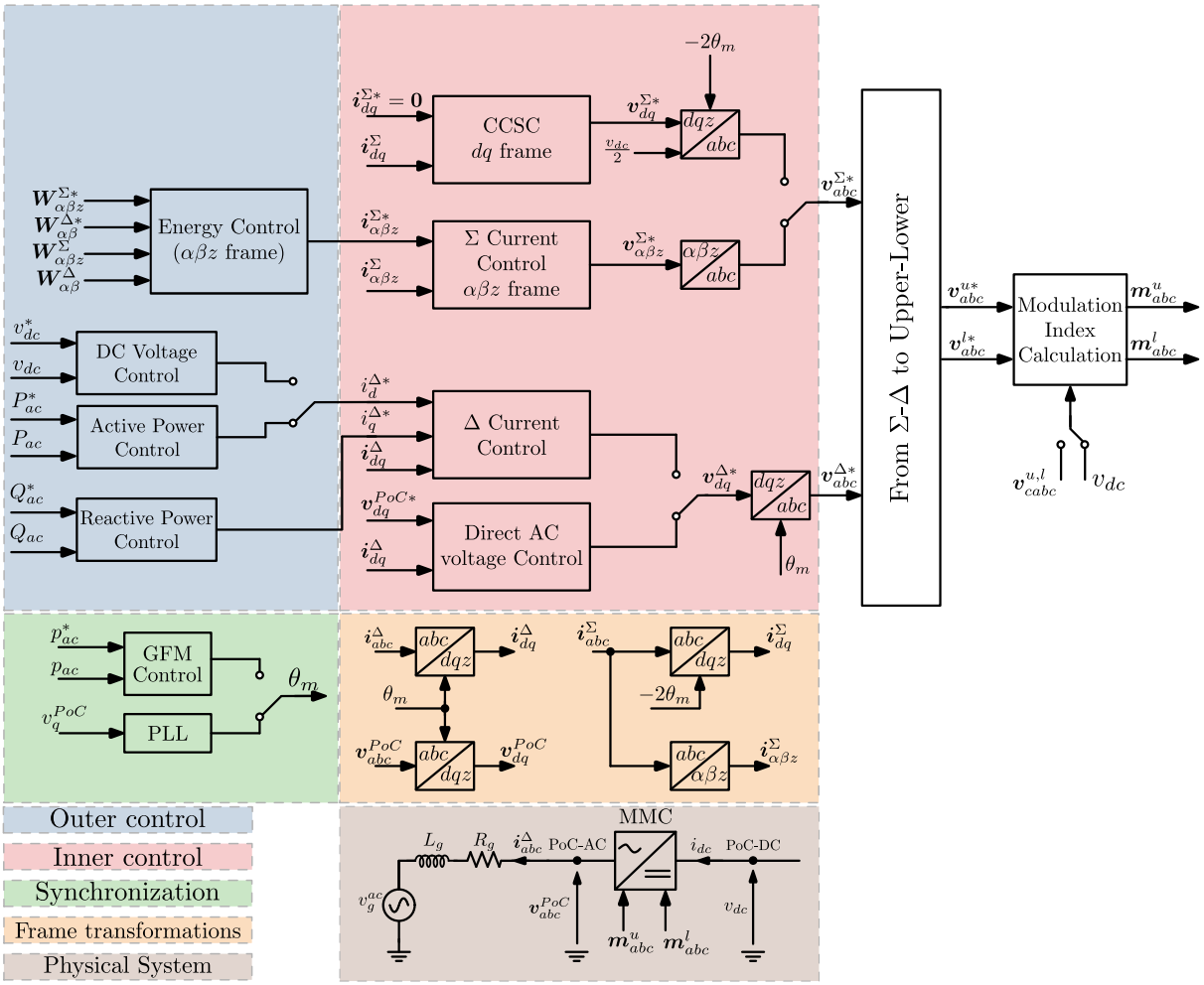

Figure 2.6: Overall MMC control structure.

2.6.1 Modulation strategies

The first control choice is the modulation strategy. The objective of the modulation step is to calculate the appropriate modulation indices $\boldsymbol{m}_{abc}^{u,l}$ from the reference signals of the inserted voltages generated by the inner control loops. The modulation indices are then translated into switching signals in the low-level control, which is out of this thesis scope since only averaged models are considered. Although different modulation strategies exist in the literature [71], the most common for the MMC are the Uncompensated Modulation (UCM) and the Compensated Modulation (CM) [92]. In the UCM, also called direct modulation [71], the modulation indices are calculated directly from the reference inserted voltages and the DC voltage measurement

$$m_u^* = \frac{v_u^*}{v_{dc}} \tag{2.20a}$$

$$m_l^* = \frac{v_l^*}{v_{dc}} \tag{2.20b}$$

If we assume that $m_{u,l} = m_{u,l}^*$ and considering (2.4), the arm inserted voltages can be expressed as

$$v_u = m_u^* v_{cu} = \frac{v_{cu}}{v_{dc}} v_u^* \tag{2.21a}$$

$$v_l = m_l^* v_{cl} = \frac{v_{cl}}{v_{dc}} v_l^* \tag{2.21b}$$

Hence, the condition for $v_{u,l} = v_{u,l}^*$ is that $v_{cu} = v_{cl} = v_{dc}$, which is not always the case due to capacitor voltage ripples (see Fig. 2.4). In other words, the UCM does not compensate for the capacitor voltage oscillations, which may lead to steady-state errors in the arm inserted voltages. Although global asymptotic stability of the UCM has been demonstrated in [103], significant circulating current appear in the MMC arms, increasing losses. As will be discussed in Section 2.6.3, circulating current suppression control is required when using UCM.

On the other hand, the CM strategy, also called closed-loop modulation [71], calculates the modulation indices from the actual arm capacitor voltage measurements as follows

$$m_u^* = \frac{v_u^*}{v_{cu}} \tag{2.22a}$$

$$m_l^* = \frac{v_l^*}{v_{cl}} \tag{2.22b}$$

A similar assumption as in UCM is made, $m_{u,l} = m_{u,l}^*$, leading to the following arm inserted voltages

$$v_u = m_u^* v_{cu} = v_u^* \tag{2.23a}$$

$$v_l = m_l^* v_{cl} = v_l^* \tag{2.23b}$$

Therefore, the CM naturally tracks the reference inserted voltages, leading to no mismatch between them, hence no undesired circulating currents. The CM strategy also allows for a clear decoupling

between the AC and DC dynamics. Employing the CM strategy inherently enables independent control of the AC and DC circuit dynamics. However, the CM strategy requires additional explicit energy balancing controllers since the balancing between the upper and lower arms and between the legs is not naturally guaranteed like in the case of UCM [71].

In this thesis, both modulation strategies are considered, depending on the adopted energy control strategy. The difference between the two modulation strategies is also highlighted in Fig. 2.7.



(a) Uncompensated Modulation

(b) Compensated Modulation

Figure 2.7: MMC modulation strategies: (a) Uncompensated Modulation (b) Compensated Modulation.

2.6.2 Synchronization with the AC grid

The AC grid is modeled as a Thévenin equivalent with a voltage source $\boldsymbol{v}_{gdq}^{ac}$ in series with an impedance R_g and L_g, as shown in Fig. 2.6. This impedance indicates the strength of the AC grid connected to the MMC. The nominal AC grid frequency is denoted ω_0. Unlike a two-level VSC, which typically employs capacitive filters at the AC-PoC to reduce output voltage harmonics, the MMC is directly connected to the grid without requiring additional filtering. Consequently, the AC current $\boldsymbol{i}^{dq}$ flows directly from the MMC into the AC grid, via the MMC transformer represented by a series impedance R_{tr} and L_{tr}. Hence, the AC voltage at the PoC-AC $\boldsymbol{v}^{PoC}$ is neither a state variable nor a system input. Instead, the dq components of the voltage at the AC-PoC are computed from the grid voltage $\boldsymbol{v}_{gdq}^{ac}$, the AC current $\boldsymbol{i}_{dq}^{\Delta}$, and the inserted voltage $\boldsymbol{v}_{dq}^{\Delta}$ as follows [81]

$$v_d^{PoC} = \left(\frac{L_{ac}}{L_{ac}+L_g}\right) v_{gd}^{ac} + \left(\frac{R_g L_{ac} - R_{ac} L_g}{L_{ac}+L_g}\right) i_d^{\Delta} + \left(\frac{L_g}{L_{ac}+L_g}\right) v_d^{\Delta} \tag{2.24a}$$

$$v_q^{PoC} = \left(\frac{L_{ac}}{L_{ac}+L_g}\right) v_{gq}^{ac} + \left(\frac{R_g L_{ac} - R_{ac} L_g}{L_{ac}+L_g}\right) i_q^{\Delta} + \left(\frac{L_g}{L_{ac}+L_g}\right) v_q^{\Delta} \tag{2.24b}$$

The algebraic calculation of $\boldsymbol{v}^{PoC}$ is adopted in this thesis instead of introducing an artificial small capacitance at the AC-PoC, as done in [104], to avoid any potential impact on the model accuracy.

A Phase-Locked Loop (PLL) is utilized to synchronize the MMC with the AC grid. Its role is to provide the phase angle θ_m, which is required to perform all the Park transformations between the abc and dq frames.

Before presenting the PLL dynamics, it is essential to distinguish between two dq reference frames. The first is the *global* (physical) reference frame defined by the actual grid voltage angle. The second is the *local* reference frame used by the MMC controllers, which is aligned with the angle estimated by the PLL at the AC-PoC. Since the control loops operate in the local frame defined by the PLL angle but must be correctly interpreted in the global frame, all locally expressed variables must be rotated using the appropriate rotation matrix. The conceptual difference between the two reference frames is

illustrated in Fig. 2.8. The transformation from the local to the global dq frame is given by

$$\begin{bmatrix} x_d \\ x_q \end{bmatrix} = \underbrace{\begin{bmatrix} \cos(\theta_m) & \sin(\theta_m) \\ -\sin(\theta_m) & \cos(\theta_m) \end{bmatrix}}_{\boldsymbol{R}(\theta_m)} \begin{bmatrix} x_d^c \\ x_q^c \end{bmatrix} \tag{2.25}$$

where θ_m is the PLL-estimated angle defining the local frame, and $\boldsymbol{R}(\theta_m)$ is the rotation matrix relating a generic vector $\boldsymbol{x}_{dq}^c$ defined in the local reference frame to the vector $\boldsymbol{x}_{dq}$ defined in the local global frame. It should be noted that $\boldsymbol{R}(\theta_m)$ must be adjusted to $\boldsymbol{R}(-2\theta_m)$ when transforming variables rotating at -2ω, such as the Σ variables of the MMC.

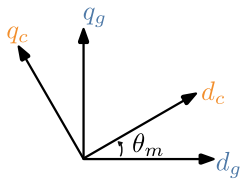

Figure 2.8: Different dq reference frames used in the MMC control.

In this thesis, a Synchronous Reference Frame PLL (SRF-PLL) is employed, which is widely used in grid-connected converters [105]. The SRF-PLL regulates the q-component of the AC-PoC voltage to zero through a PI controller, hence aligning the d component of the rotating frame to phase a of the AC-PoC voltage. The PLL reference frame rotates at the estimated grid frequency ω_m, adjusted based on the PI controller output.

The block diagram of the implemented SRF-PLL is shown in Fig. 2.9. The associated dynamic equations are

$$\frac{d\epsilon_{pll}}{dt} = k_i^{pll} v_q^{PoC} \tag{2.26a}$$

$$\frac{d\theta_m}{dt} = \omega_b \omega_m \tag{2.26b}$$

$$\omega_m = k_p^{pll} v_q^{PoC} + \epsilon_{pll} \tag{2.26c}$$

where ϵ_{pll} is the PLL integral state, ω_b is the base angular frequency, θ_m and ω_m are the estimated angle and frequency at the AC-PoC, k_p^{pll} and k_i^{pll} are the proportional and integral gains of the PLL PI controller. The PLL state vector is therefore $\boldsymbol{x}_{pll} = [\epsilon_{pll}, \theta_m]^T$.

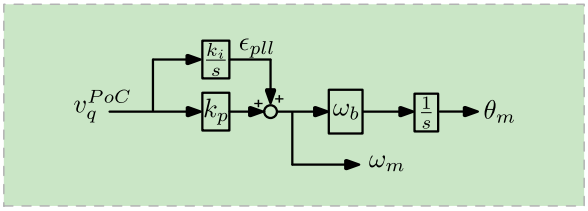

Figure 2.9: Block diagram of the SRF-PLL.

2.6.3 Inner control loops

Δ currents control

The AC current control of the MMC is similar to that of a two-level VSC, relying on the conventional vector current control approach [105], which decouples the dq components of the AC current. Two PI controllers regulate the i_d^{Δ} and i_q^{Δ} components to their respective reference values. The objective is to realize the current values required by the outer-loop control, based on the phase angle provided by the PLL. The Δ current control structure is shown in Fig. 2.10. Feedforward terms of the PoC-AC voltage, v_d^{PoC} and v_q^{PoC}, as well as the cross-coupling terms, are added to the outputs of the PI controllers to enhance the dynamic response.

The tuning of the PI controllers follows guidelines similar to those used in two-level VSCs [105], mainly considering the AC-side impedance and the desired bandwidth of the current control loop. Note that anti-windup mechanisms are typically included in practical implementations to prevent integrator windup during large transients when voltage references saturate [106]. However, for small-signal stability analysis, these mechanisms are excluded from the developed models.

The AC current control structure shown in Fig. 2.10 is implemented only when the MMC operates in GFL mode, since the main function of GFL is to control the AC current injection into the grid and follow the voltage angle provided by the PLL. In GFM mode, current control acts solely as a current-limiting function, as will be discussed in Section 2.6.5. The outputs of the Δ current controllers generate the reference values for the Δ inserted voltages, $v_d^{\Delta *}$ and $v_q^{\Delta *}$, which, after an inverse Park transformation and the modulation step, are translated into the modulation indices $\boldsymbol{m}_{abc}^{ul}$ according to the selected modulation strategy.

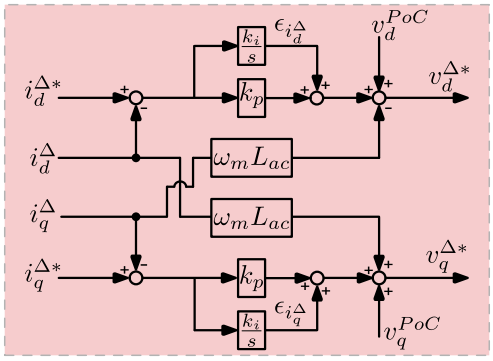

Figure 2.10: Block diagram of the Δ currents control.

As can be seen from Fig. 2.10, the dynamics of the Δ current controllers can be expressed as follows

$$\frac{d\epsilon_{i_d^{\Delta}}}{dt} = k_i^{i^{\Delta}}(i_d^{\Delta *} - i_d^{\Delta}) \tag{2.27a}$$

$$\frac{d\epsilon_{i_q^{\Delta}}}{dt} = k_i^{i^{\Delta}}(i_q^{\Delta *} - i_q^{\Delta}) \tag{2.27b}$$

$$v_d^{\Delta *} = k_p^{i^{\Delta}}(i_d^{\Delta *} - i_d^{\Delta}) + \epsilon_{i_d^{\Delta}} + v_d^g - \omega L_{ac} i_q^{\Delta} \tag{2.27c}$$

$$v_q^{\Delta *} = k_p^{i^{\Delta}}(i_q^{\Delta *} - i_q^{\Delta}) + \epsilon_{i_q^{\Delta}} + v_q^g + \omega L_{ac} i_d^{\Delta} \tag{2.27d}$$

where $\epsilon_{i_d^{\Delta}}$ and $\epsilon_{i_q^{\Delta}}$ are the corresponding integral states of the Δ current controllers. The state vector

of the AC current control is then $\boldsymbol{x}_{i_{dq}^{\Delta}} = \begin{bmatrix} \epsilon_{i_d^{\Delta}} & \epsilon_{i_q^{\Delta}} \end{bmatrix}^T$.

Σ currents control

The regulation of the Σ currents is a control functionality specific to the MMC. As explained in Section 2.3, during normal operation, the MMC exhibits non-negligible circulating currents that flow between its arms. These circulating currents can lead to increased losses. The control structure for the Σ currents depends on the selected modulation strategy. Under UCM, since the arm capacitor voltage ripples are not compensated for, circulating currents must be actively suppressed to minimize losses. On the other hand, when using CM, the circulating currents are inherently eliminated through the modulation mechanism itself. In this case, the Σ current controllers serve different control objectives, i.e., energy balancing within the MMC arms and legs.

Circulating currents appearing in the case of UCM are commonly eliminated using a Circulating Current Suppression Controller (CCSC) [83]. This approach is adopted in this thesis and is implemented in a dq reference frame rotating at -2ω, as shown in Fig. 2.11.

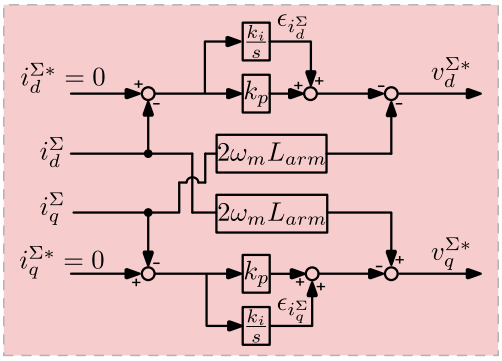

Figure 2.11: Block diagram of the Circulating Current Suppression Controller (CCSC) structure under UCM strategy.

A pair of PI controllers are utilized to regulate the i_d^{Σ} and i_q^{Σ} components to their respective reference values, which are set to zero since the objective is to eliminate the circulating currents. The output of the CCSC generates the reference values for the Σ inserted voltages, $v_d^{\Sigma*}$ and $v_q^{\Sigma*}$. The i_z^{Σ} component is left uncontrolled. The outputs of the CCSC are then transformed back to the *abc* frame by an inverse Park transformation and used to calculate the modulation indices according to the UCM strategy.

The dynamics of the Σ current controllers (CCSC) can be represented in the following form.

$$\frac{d\epsilon_{i_d^{\Sigma}}}{dt} = k_i^{i^{\Sigma}}(i_d^{\Sigma*} - i_d^{\Sigma}) \tag{2.28a}$$

$$\frac{d\epsilon_{i_q^{\Sigma}}}{dt} = k_i^{i^{\Sigma}}(i_q^{\Sigma*} - i_q^{\Sigma}) \tag{2.28b}$$

$$v_d^{\Sigma*} = k_p^{i^{\Sigma}}(i_d^{\Sigma*} - i_d^{\Sigma}) + \epsilon_{i_d^{\Sigma}} + 2\omega L_{arm} i_q^{\Sigma} \tag{2.28c}$$

$$v_q^{\Sigma*} = k_p^{i^{\Sigma}}(i_q^{\Sigma*} - i_q^{\Sigma}) + \epsilon_{i_q^{\Sigma}} - 2\omega L_{arm} i_d^{\Sigma} \tag{2.28d}$$

$$v_z^{\Sigma*} = \underbrace{\frac{v_{dc}}{2}}_{\text{Feedforward term}} \tag{2.28e}$$

where $\epsilon_{i_d^{\Sigma}}$ and $\epsilon_{i_q^{\Sigma}}$ are the corresponding integral states of the CCSC, leading to the state vector of the

CCSC as $\boldsymbol{x}_{i_{dq}^{\Sigma}} = \begin{bmatrix} \epsilon_{i_d^{\Sigma}} & \epsilon_{i_q^{\Sigma}} \end{bmatrix}^T$.

It should be noted that proper tuning of the CCSC is crucial to ensure effective suppression of circulating currents in order not to undermine the small-signal stability of the MMC, since an increased bandwidth of the CCSC loop has been shown to negatively impact the MMC stability [34].

In the case of CM, the Σ current controllers explicitly regulate the circulating currents to the references generated by the outer energy balancing control loops. The adopted control strategy for the Σ currents is performed in the $\alpha\beta$ frame [107]. The control structure of the Σ currents for the CM strategy is shown in Fig. 2.12.

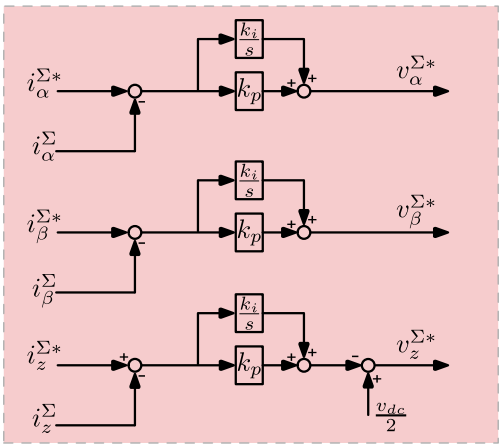

Figure 2.12: Σ currents control structure for the CM strategy. Only i_z^{Σ} control is implemented in the MMC-AVM.

To express the dynamics of the Σ current controllers under the CM strategy and for small-signal stability analysis, the MMC-AVM in Section 2.5 is utilized. Therefore, only the control of the i_z^{Σ} component is considered, see Fig. 2.12. The dynamics of the i_z^{Σ} current controller can be expressed as follows

$$\frac{d\epsilon_{i_z^{\Sigma}}}{dt} = k_i^{i^{\Sigma}}(i_z^{\Sigma*} - i_z^{\Sigma}) \tag{2.29a}$$

$$v_z^{\Sigma*} = k_p^{i^{\Sigma}}(i_z^{\Sigma*} - i_z^{\Sigma}) + \epsilon_{i_z^{\Sigma}} + \underbrace{\frac{v_{dc}}{2}}_{\text{Feedforward term}} \tag{2.29b}$$

2.6.4 Outer control loops

The outer control loops are responsible for generating the reference values for the inner control loops based on the desired operation mode of the MMC. The subsections below describe the different outer control strategies considered in this thesis.

Active and reactive power control

Active power control mode refers to the operation of the MMC maintaining its active power exchange at the PoC-AC, irrespective of the DC voltage level. Similarly, reactive power control mode involves regulating the reactive power exchange at the PoC-AC to a reference value. This control mode is typically employed when the MMC operates in GFL mode. The block diagram of the active/reactive power control structure is shown in Fig. 2.13. The active and reactive power controllers generate the

reference values for the i_d^{Δ} and i_q^{Δ} current controllers, respectively. The dynamic equations of the active/reactive power controllers can be expressed as follows

$$\frac{d\epsilon_{P_{ac}}}{dt} = k_i^{P_{ac}}(P_{ac}^* - P_{ac}) \tag{2.30a}$$

$$\frac{d\epsilon_{Q_{ac}}}{dt} = k_i^{Q_{ac}}(Q_{ac}^* - Q_{ac}) \tag{2.30b}$$

$$i_d^{\Delta *} = k_p^{P_{ac}}(P_{ac}^* - P_{ac}) + \epsilon_{P_{ac}} \tag{2.30c}$$

$$i_q^{\Delta *} = k_p^{Q_{ac}}(Q_{ac}^* - Q_{ac}) + \epsilon_{Q_{ac}} \tag{2.30d}$$

where $\epsilon_{P_{ac}}$, $\epsilon_{Q_{ac}}$ are the corresponding integral states of the active power and reactive power controllers, respectively.

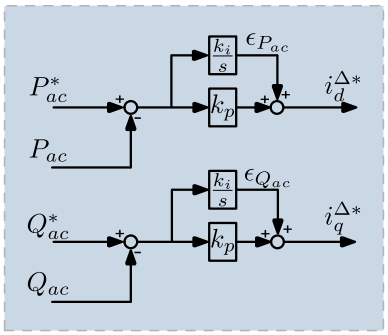

Figure 2.13: Active/Reactive power control block diagram.

DC voltage control

The objective of the DC voltage controller is to maintain the DC voltage at its reference value by adjusting the active power injected into the DC grid. Similarly, with a PI controller, the DC voltage controller generates the reference for the d-axis AC current controller, as shown in Fig. 2.14.

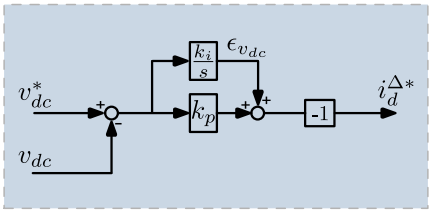

Figure 2.14: DC voltage control block diagram.

The dynamic equations of the DC voltage controller can be expressed as

$$\frac{d\epsilon_{v_{dc}}}{dt} = k_i^{v_{dc}}(v_{dc}^* - v_{dc}) \tag{2.31a}$$

$$i_d^{\Delta *} = -k_p^{v_{dc}}(v_{dc}^* - v_{dc}) - \epsilon_{v_{dc}} \tag{2.31b}$$

where $\epsilon_{v_{dc}}$ is the integral state of the DC voltage controller.

MMC energy control

To generate the references for the Σ current controllers under the CM strategy, energy control loops are required. These controllers balance the energy in the MMC arms and legs and regulate the total energy stored in the MMC capacitors [107–109]. The control structure for MMC internal energy management is shown in Fig. 2.15.

Horizontal Energy balancing control is responsible for regulating the energy among the three phases of the MMC. In the utilized simulation model, this control is implemented in the $\alpha\beta$ frame [107], leading to the references values $\boldsymbol{i}^{\Sigma*}_{\alpha\beta,dc}$. Vertical energy balancing control regulates the energy between the upper and lower arms of each phase. This controller is implemented in *abc* frame, by three PI controllers. Then, an inverse Clarke transformation is applied to the output, leading to the references $\boldsymbol{i}^{\Sigma*}_{\alpha\beta,ac}$. The summation of the respective outputs of the horizontal and vertical energy balancing loops provides the references $\boldsymbol{i}^{\Sigma*}_{\alpha\beta}$ for the Σ current controllers described in Section 2.6.3. The references $W^{\Sigma*}_{\alpha}$, $W^{\Sigma*}_{\beta}$, and $\boldsymbol{W}^{\Delta*}_{abc}$ are set to zero. The calculation of the measured energy values W^{Σ}_{α}, W^{Σ}_{β}, and $\boldsymbol{W}^{\Delta}_{abc}$ is based on the arm capacitor voltage measurements and the arm currents, as detailed in [81, 107].

Finally, the total energy controller regulates the total average capacitor energy W^{Σ}_{z} to its reference $W^{\Sigma*}_{z}$, generating the input for the i^{Σ}_{z} controller. All the energy control loops employ PI controllers. Details on the design and tuning of these controllers can be found in [81].

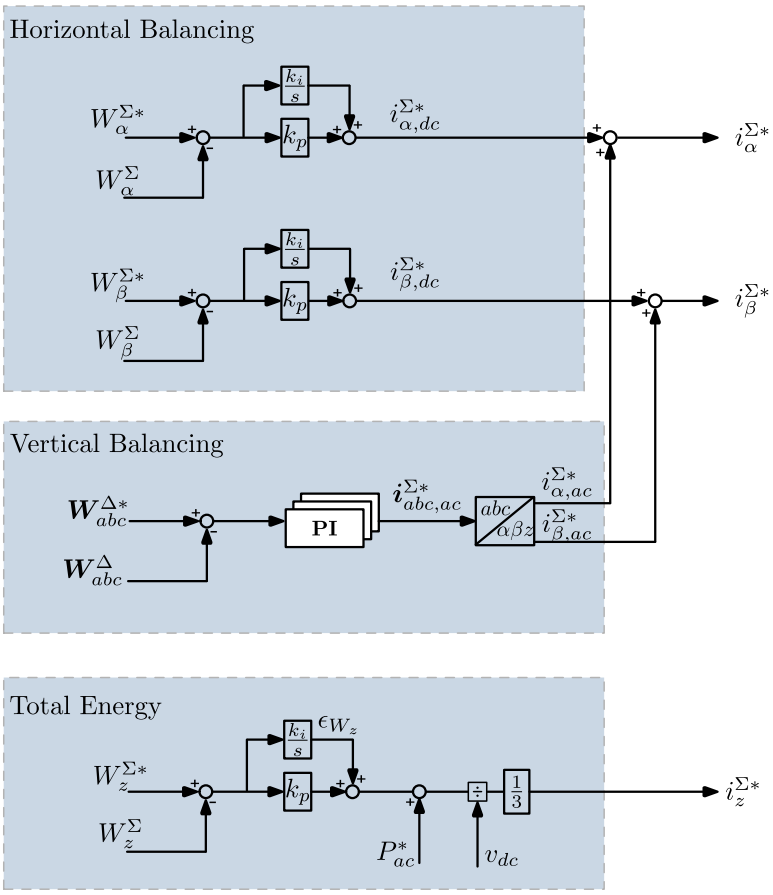

Figure 2.15: MMC energy control structure for CM strategy.

In this thesis, based on the discussion in Section 2.5, the AVM is adopted for small-signal stability analysis when using the energy control structure with the CM strategy. Only the total energy controller is retained in the outer loop to generate the reference for the i^{Σ}_{z} controller, assuming the horizontal and

vertical energy balancing loops are behaving ideally. Under this assumption, the total energy controller dynamics are given by

$$\frac{d\epsilon_{W_z}}{dt} = k_i^{W_z}(W_z^* - W_z) \tag{2.32a}$$

$$i_z^{\Sigma *} = \frac{1}{3v_{dc}}\left(k_p^{W_z}(W_z^* - W_z) + p_{ac}^* + \epsilon_{W_z}\right) \tag{2.32b}$$

where ϵ_{W_z} is the integral state of the total energy controller.

2.6.5 GFM control

According to [110], GFM capability is the ability of the device to emulate a voltage source behavior behind an impedance at the AC-PoC, within its capability limits. This is typically achieved by implementing two main control functionalities. The first one is the synchronization control where the phase angle of the AC voltage at the AC-PoC with respect to the grid angle is generated. This functionality also provides active power support in response to AC-grid frequency deviations. The second functionality is voltage control, where the AC voltage magnitude at the AC-PoC is regulated to its reference value.

Different synchronization mechanisms have been proposed in the literature for GFM converters, such as the Virtual Synchronous Machine (VSM), Virtual oscillator Control (VOC), and Matching-GFM control [111–113]. More details on these synchronization mechanisms will be provided in Chapter 3. The most commonly used synchronization loop is the VSM-GFM control, shown in Fig. 2.16, due to its simplicity in implementation and its resemblance to the conventional synchronous machine dynamics. In this control strategy, the phase angle is generated by integrating the frequency deviation, which is calculated based on the active power mismatch. The dynamic equations of the VSM-GFM synchronization control can be expressed as follows

$$\frac{d\omega_m}{dt} = \frac{1}{2H}(P_{ac}^* - P_{ac} - D(\omega_m - \omega_0)) \tag{2.33a}$$

$$\frac{d\theta_m}{dt} = \omega_m \tag{2.33b}$$

where ω_m and θ_m are the generated converter frequency and phase angle, respectively, H is the inertia constant, and D is the damping coefficient.

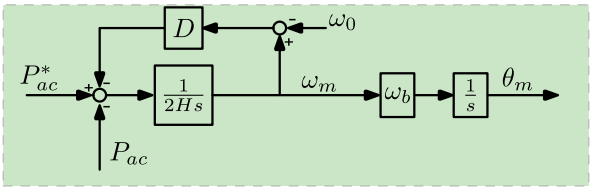

Figure 2.16: VSM-GFM synchronization control structure.

Considering the second control functionality, namely shaping the magnitude of the AC voltage at the AC-PoC, The AC voltage control is typically directly regulated in open-loop manner. To improve the damping of the voltage dynamics, a transient damping resistor (TDR) is implemented [114], as

shown in Fig. 2.17 . The dynamics of the AC voltage control are governed by

$$v_d^{\Delta *} = v_d^{PoC*} + R_a(i_d^{\Delta} - \epsilon_{f_{id}}) \tag{2.34a}$$

$$v_q^{\Delta *} = v_q^{PoC*} + R_a(i_q^{\Delta} - \epsilon_{f_{iq}}) \tag{2.34b}$$

$$\frac{d\epsilon_{f_{i_d^{\Delta}}}}{dt} = \frac{1}{\tau_{tdr}}(i_d^{\Delta} - \epsilon_{f_{id}}) \tag{2.34c}$$

$$\frac{d\epsilon_{f_{i_q^{\Delta}}}}{dt} = \frac{1}{\tau_{tdr}}(i_q^{\Delta} - \epsilon_{f_{iq}}) \tag{2.34d}$$

where v_d^{PoC*} and v_q^{PoC*} are the references for the AC voltage at the AC-PoC, and R_{tdr} is the TDR gain, and τ_{tdr} is the TDR time constant.

From (2.33) and (2.34), the state variables related to the considered implementation of GFM control can be summarized as follows

$$\boldsymbol{x}_{GFM} = \begin{bmatrix} \omega_m & \theta_m & \epsilon_{f_{i_d^{\Delta}}} & \epsilon_{f_{i_q^{\Delta}}} \end{bmatrix}^T \tag{2.35}$$

It should be noted that no PI controllers are utilized to regulate the AC currents $\boldsymbol{i}_{dq}{}^{\Delta}$ in GFM mode, hence no additional states related to the AC current control.

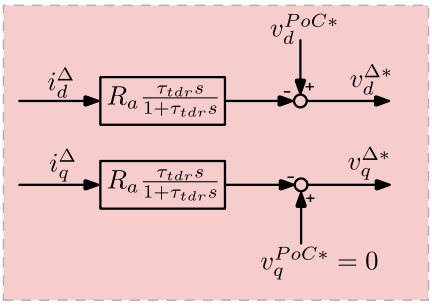

Figure 2.17: AC voltage control structure for GFM strategy with Transient Damping Resistor (TDR).

2.7 Validation of the MMC LTI models

In this section, the accuracy of the derived MMC LTI models is validated against a detailed non-linear MMC-AAM implemented in EMTP-RV. The LTI models, both the AAM and AVM models, are tested under the different control strategies presented in this chapter, see Fig. 2.6. The MMC is connected to an equivalent AC grid using a Thévenin equivalent. The AC grid strength with respect to the MMC is represented by the Short-Circuit Ratio (SCR), defined as the ratio between the AC grid short-circuit power and the rated power of the MMC. An SCR of 5 is considered for all scenarios. The X/R ratio of the AC grid is set to 10.

Two test setups are considered for the validation, differing mainly in the DC-side connection. Setup 1, shown in Fig. 2.18a, employs a stiff DC voltage source connected to the MMC DC terminals. The objective of this setup is to validate the LTI models when operating in constant active power control mode under DC voltage disturbances and active power reference change. Setup 2, shown in Fig. 2.18b, includes a capacitance $C_{dc} = 200\mu$F connected at the MMC DC terminals to evaluate constant DC voltage control mode, under DC power disturbance and DC voltage reference change. Variations in the control modes described in this chapter, such as GFL/GFM and UCM/CM, lead to different *Control*

Settings, as summarized in Table 2.1. The events applied to Setup 1 and Setup 2 are provided in Table 2.2. The combination of GFM control with DC voltage control mode (setup 2) is not considered here as it will be covered in Chapter 3.

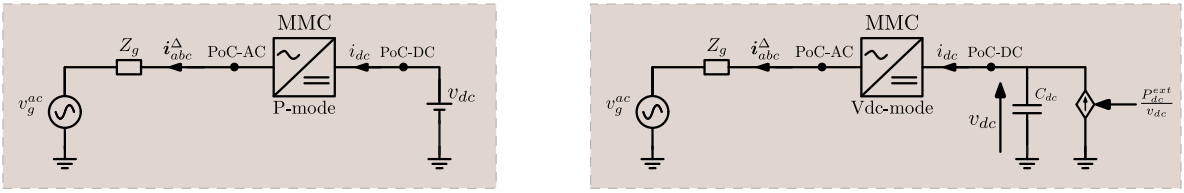

(a) Setup 1

(b) Setup 2

Figure 2.18: MMC validation setups: (a) Setup 1 for constant active power control mode (b) Setup 2 for constant DC voltage control mode.

The MMC and physical and control parameters, alongside the AC grid parameters are summarized in Appendix A.

Table 2.1: MMC LTI model validation scenarios

Control setting	**Description**	**LTI model**
1	GFL + UCM	AAM
2	GFL + CM	AVM
3	GFM + UCM	AAM
4	GFM + CM	AVM

Table 2.2: Step tests for MMC LTI model validation

Setup	**Step variable**	**Step change**	**time**
1	DC voltage disturbance v_{dc}	$\pm$0.05 pu	$t = 2$s and $t = 3$s
1	Active power reference P^*_{ac}	+0.1 pu	$t = 4$ s
2	DC voltage reference v^*_{dc}	$\pm$0.05 pu	$t = 2$s and $t = 3$s
2	DC power disturbance P_{dc}	+0.1 pu	$t = 4$ s

Fig. 2.19 and Fig. 2.20 show the validation results for *Control setting 1*, considering test setup 1. It can be observed that the LTI model accurately captures the dynamic response of the detailed non-linear MMC-AAM model for both DC voltage disturbance and active power reference step changes.

Considering test setup 2, Fig. 2.21 and Fig. 2.22 present the validation results for *Control setting 1*. The results demonstrate that the LTI model effectively replicates the dynamic response of the detailed non-linear MMC-AAM model for both DC voltage reference changes and DC power disturbances.

For conciseness, the validation results related to the remaining scenarios are provided in Appendix C, confirming the accuracy of the derived LTI models.

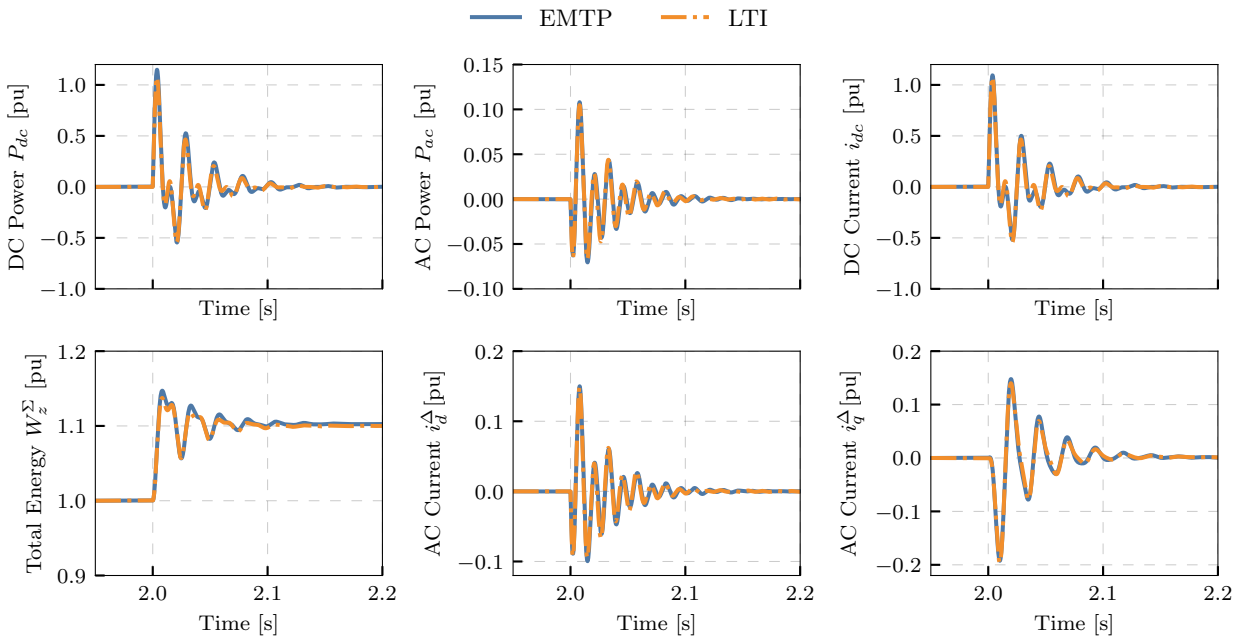

Figure 2.19: Validation of the MMC LTI model under control setting 1 - DC voltage disturbance.

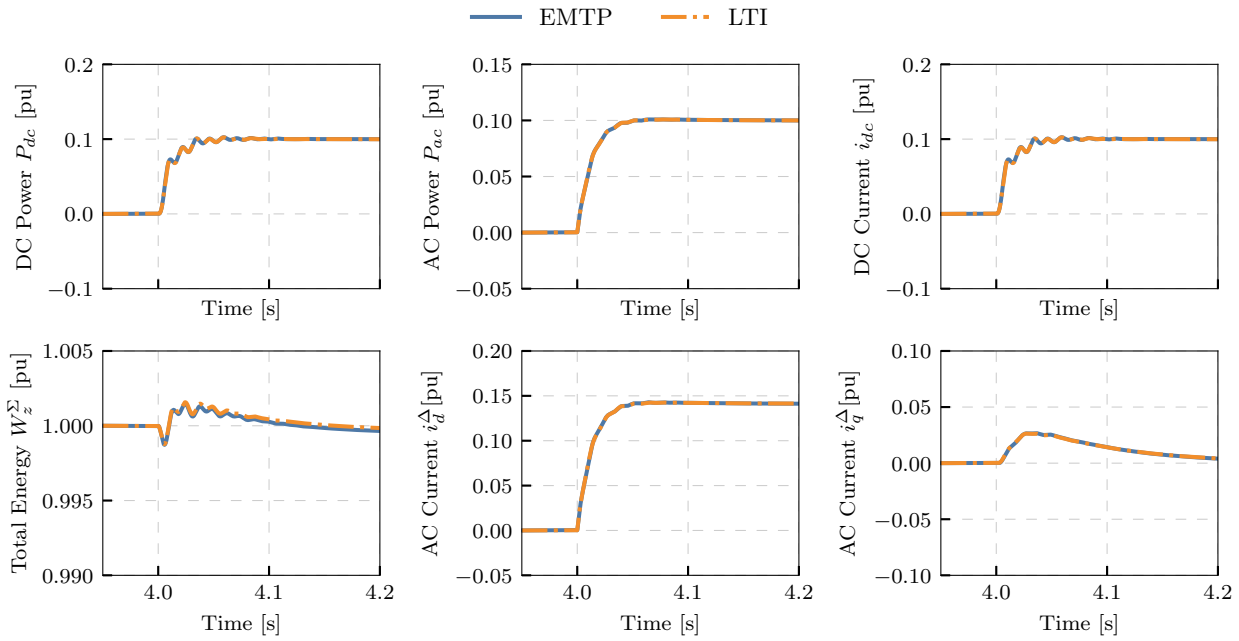

Figure 2.20: Validation of the MMC LTI model under control setting 1 - Active power reference step change.

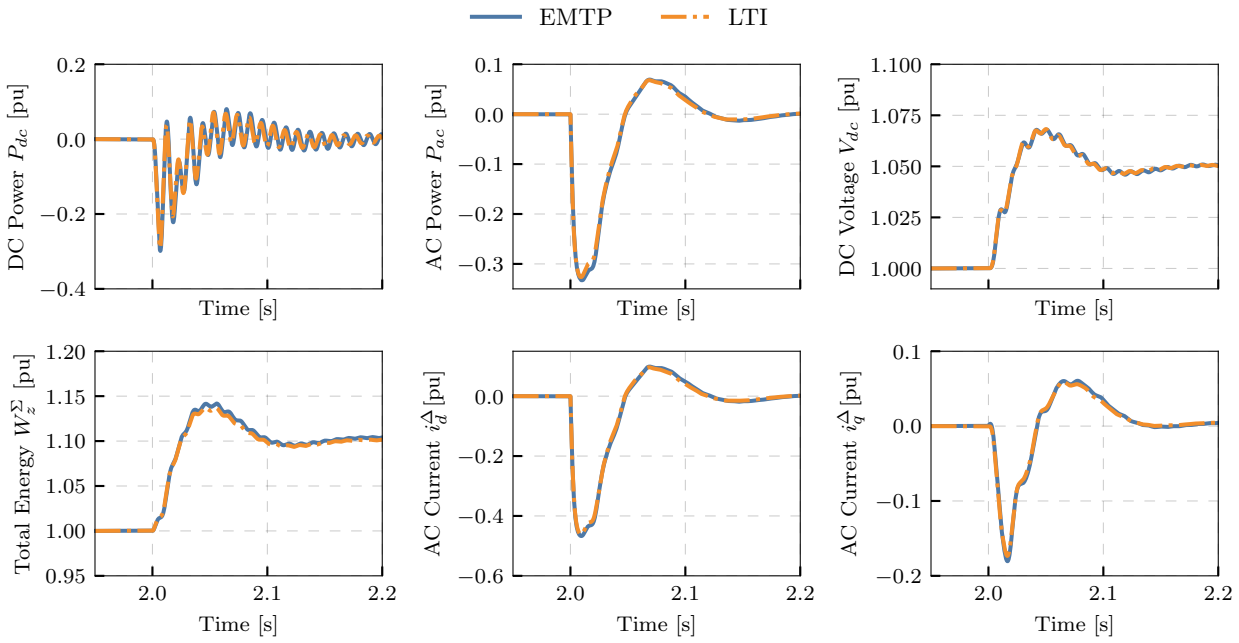

Figure 2.21: Validation of the MMC LTI model under control setting 1 - DC voltage reference change.

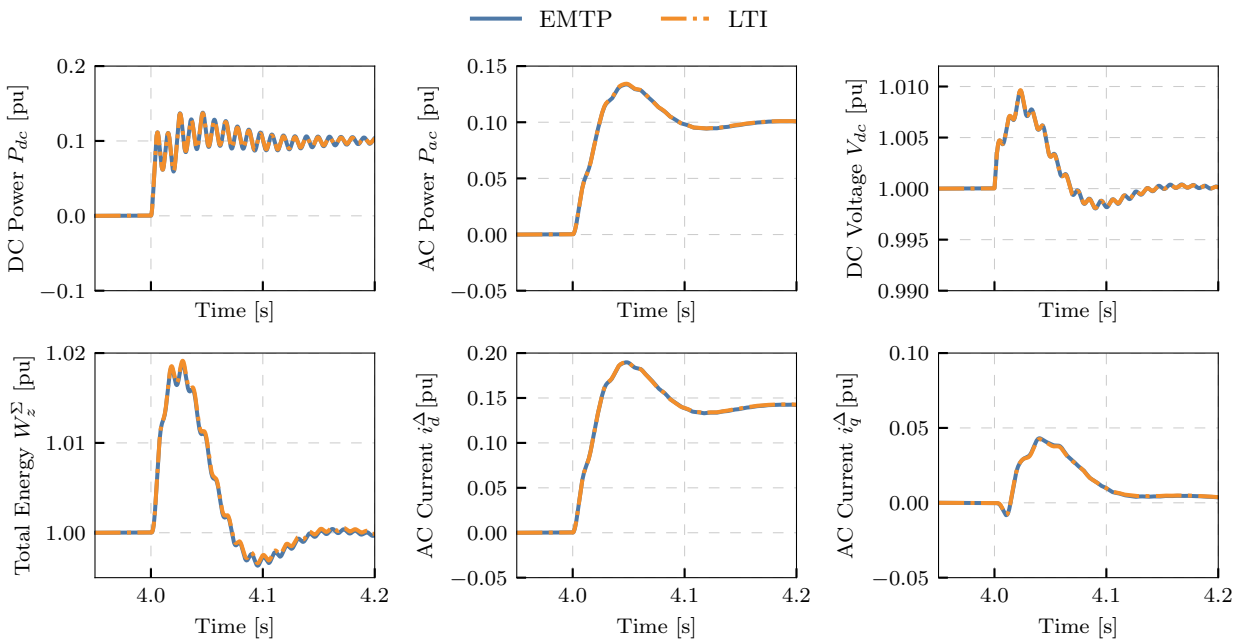

Figure 2.22: Validation of the MMC LTI model under control setting 1 - DC power disturbance.

2.8 Chapter summary

In this chapter, the detailed average model of the MMC has been presented, utilizing the $\Sigma - \Delta$ transformation to isolate the different harmonic components of the MMC variables. The multi-frequency nature of the MMC states in steady-state conditions has been discussed, highlighting the challenges in deriving a steady-state time-invariant solution for small-signal analysis. An overview of various modeling approaches for the MMC has been provided, with a focus on the multi-dq frame transformation approach for deriving a linear time-invariant state-space model. In addition, the MMC-AVM utilized only for a specific control configuration has been adopted and described. Finally, the control structure of the MMC, gathering different controls that will be utilized in the subsequent studies, have been presented in detail with their respective dynamic equations, covering modulation strategies, inner and outer control loops, and synchronization with the AC grid. A validation using time-domain simulations has been conducted for a simple MMC setup under different control strategies to validate the LTI model. The results showed that the models are sufficiently accurate for conducting system level small-signal analysis, or testing specific controls, as will be seen throughout this thesis.

3

Primary DC voltage control in MV-MTDC grids

3.1 Introduction

The operation of Multi-vendor MTDC (MV-MTDC) grids requires a robust and reliable DC voltage control framework to ensure secure and stable grid operation. Primary DC voltage control plays a crucial role in maintaining the DC voltage within acceptable limits, responding to power imbalances, and ensuring stable grid operation.

This chapter, therefore, focuses on the primary DC voltage control functions in MV-MTDC grids. The chapter is divided into two main parts: the first addresses the static aspects of DC voltage droop control, while the second investigates its dynamic behavior and small-signal stability considering different implementation options. Then, it discusses an important constraint regarding converter stations operating in Grid-Forming (GFM) control combined with DC voltage droop control.

The chapter is structured as follows. First, an overview of the operation of MTDC grids is provided, highlighting the hierarchical control structure and the role of primary DC voltage control. Next, the static considerations of DC voltage droop control are discussed, with a focus on multi-segment droop characteristics, which is the droop control form adopted in the InterOPERA project [14]. Next, an introduction to different DC voltage droop implementation options is presented, with their respective stability limitations and interoperability in a three-terminal DC grid under different operational conditions. Finally, the inclusion of GFM control in the MMC stations is considered, and its impact on the stability limitations of the droop gain is analyzed.

3.2 Operation of MTDC grids

The DC voltage acts as the main power-balance indicator in MTDC grids, analogous to frequency in AC systems. Hence, many similarities exist between the operation and control of AC systems and MTDC grids, as will be seen in the following sections. When a change occurs in the power injection or evacuation in the DC grid, such as the outage of a converter station, the DC voltage deviates due

to the charging and discharging of the grid capacitances. This voltage deviation indicates a power imbalance in the DC grid, which must be corrected by adjusting the power output of the converter stations.

In AC systems, the frequency is a global variable, meaning that all generators and loads in the system experience the same frequency deviation in steady-state conditions. In contrast, in an MTDC grid, voltage drops across DC cables exist, with each converter station measuring its own DC voltage at its DC-PoC. DC voltage management in the DC grid therefore represents the main objective of any continuous control framework in order to ensure the grid's secure operation.

DC voltage management involves both centralized and local control functions implemented at different layers of the control hierarchy. Following the guidelines in [14] and [17], the hierarchical control structure of MTDC grids can be classified as shown in Fig. 3.1. This structure consists of different layers operating on different time scales and with different objectives, forming a hierarchy similar to that used in AC power systems. The four main layers are: dispatch-level control, operational-level control, station-level control, and unit-level control. This hierarchical structure enables a clear allocation of roles and responsibilities.

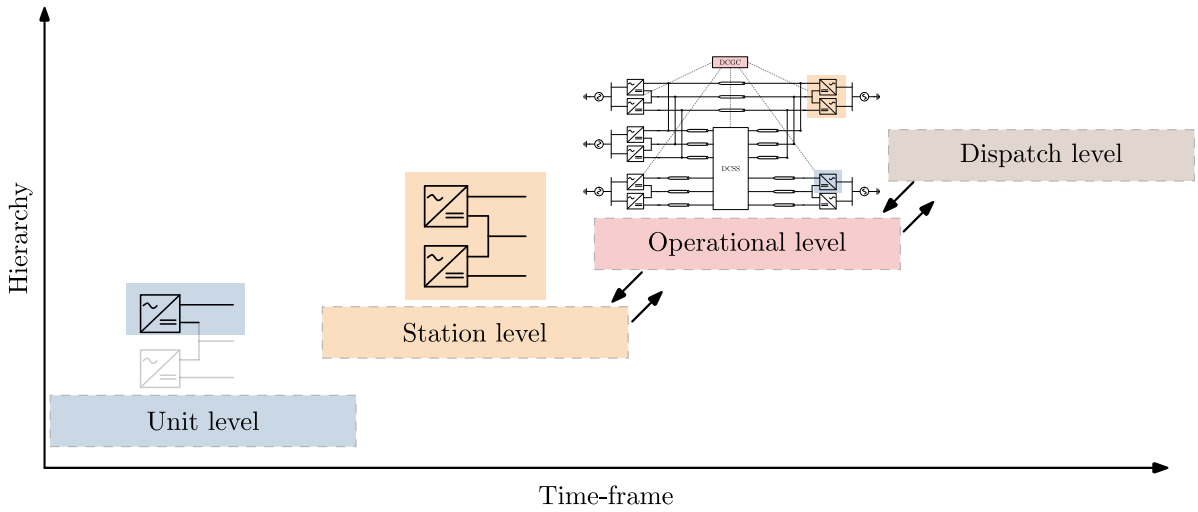

Figure 3.1: Hierarchical control structure of MTDC grids.

3.2.1 Dispatch-level control

The Dispatch-level control is responsible for generating the power setpoints required from the DC grid to support overall AC/DC system operation. It is also referred to as Integrated AC/DC System Control in [17]. It serves as the primary operational interface between the AC and DC grids. This layer is an external entity to the DC grid, providing the necessary power setpoints for each dispatch cycle. For larger grids with more converter stations, this control layer may span several control areas, each managed by a different system operator [14]. This layer is analogous to tertiary control in AC systems. It should be noted that no DC power flow management is performed at this layer, which is the responsibility of the operational-level control. Instead, only power schedules are defined at this layer.

3.2.2 Operational-level control

This layer is governed by the DC-Grid Controller (DCGC), which serves as the interface between dispatch-level and station-level controls. The DCGC coordinates and manages DC grid operations by monitoring grid conditions, including power flows and contingencies, and updating control commands to ensure secure and stable operation.

Its primary objective is to realize the power schedules defined at the dispatch level while respecting the security constraints of DC grid subsystems, including cables and converter stations. To achieve this, it computes the DC power flow and sends active power and DC voltage setpoints to the converter stations.

The DCGC also updates subsystem commands in response to internal or external events, such as the loss of a converter unit or cable. These commands, including active power and DC voltage setpoints, ramp rates, and wind curtailment instructions, may temporarily deviate from the original dispatch-level commands until further instructions are received.

3.2.3 Station-level control

Station-level control is responsible for the local regulation of each converter station, ensuring the tracking of the setpoints provided by the DCGC. This layer includes primary DC voltage control, the focus of this chapter. Additionally, this level transmits necessary measurements and status information back to the DCGC.

In bipolar HVDC grids, this layer may include additional balancing control functions to manage the active power and DC voltage of both positive and negative poles. This ensures that the Dedicated Metallic Return (DMR) conductor is not overloaded and maintains proper power sharing between the poles. The reader is referred to [14, 115, 116], which discuss various balancing control strategies for bipolar DC grids.

3.2.4 Unit-level control

Unit-level control handles the internal regulation of each converter unit within a station, encompassing the internal control functions. Different generic internal control structure for the MMC are presented in Chapter 2.

3.3 Primary DC voltage control in MTDC grids

Before detailing the characteristics of primary DC voltage control, it is essential to recall the requirements from a system operator's perspective. According to [14], the main expectations from the primary DC voltage control in MV-MTDC grids are summarized as follows:

1. Ensuring that the post-contingency steady-state voltages at any system node remain within the continuous operating DC voltage range.

2. Limiting the dynamic voltage overshoot exceeding the continuous operating DC voltage range to no more than the value specified as a percentage of the nominal voltage.

3. Preventing the primary DC voltage control from triggering any unintentional protective actions of any equipment during such events.

4. Converters with the same droop parameter equally contribute dynamically to the extent feasible, provided they are equidistant electrically from the source of the event and connected to AC networks with similar grid strength.

5. The primary DC voltage control shall not render the system unstable in any circumstance.

6. Accessibility to all relevant parameters deemed necessary and mutually agreed upon for ensuring system stability and future expandability.

The above TSO expectations include both static requirements (1 and 4) and dynamic requirements (2, 3 and 5) for primary DC voltage control. Static requirements define the expected steady-state behavior of the DC voltage following a disturbance, while dynamic requirements specify the transient response characteristics, including response speed, damping and stability aspects. The following sections discuss both static and dynamic considerations of primary DC voltage control in MV-MTDC grids.

3.4 Static considerations of primary DC voltage control

3.4.1 DC voltage operating ranges

Following AC system practices, DC voltage operating ranges define the acceptable voltage limits for the continuous operation of a DC grid. The different DC voltage operating ranges are illustrated in Fig. 3.2.

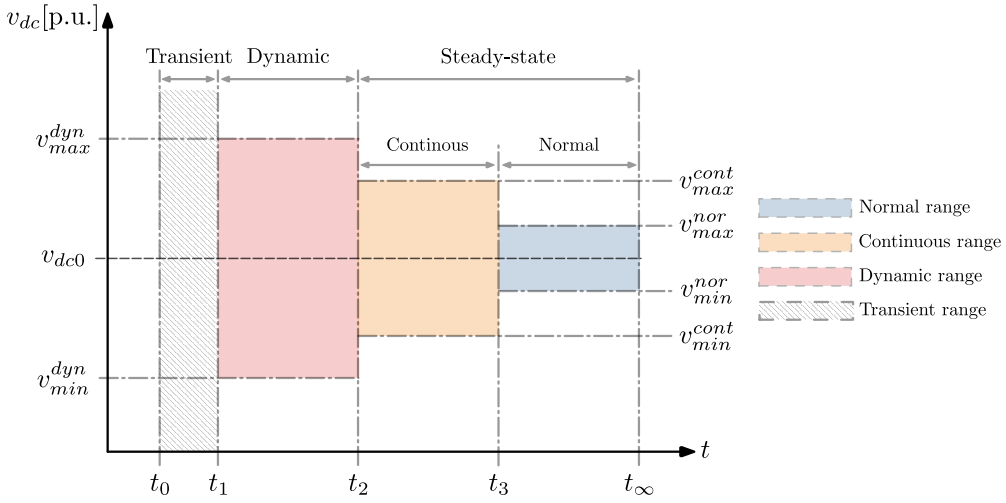

Figure 3.2: Illustration of DC voltage operating ranges in an MTDC grid.

These ranges are typically specified by the system operator and must be adhered to by all converter stations. In general, the upper maximum DC voltage limit is determined by the insulation capabilities of the equipment, including DC cables. The lower DC voltage limit is less straightforward, as this limitation typically depends on the converter modulation [117], which depends on the converter topology and the adopted modulation strategy. Before reaching those maximum limits, the system operator is responsible for defining the acceptable DC voltage operating ranges and their respective time frames, which are classified in [14] as follows:

- *Normal operating range*: This range is defined by the maximum and minimum DC voltage limits [v_{min}^{nor}, v_{max}^{nor}] within which the station is expected to operate under normal conditions, without

any system disturbances such as loss of power generation or evacuation. Consequently, all DC voltage setpoints provided to all converter stations must fall within this range.

- *Continuous operating range*: This range extends beyond the normal operating range and is defined by the maximum and minimum DC voltage limits [v_{min}^{cont}, v_{max}^{cont}] within which the converter stations shall operate continuously, even after power disturbances, and without further modifications by the DCGC. Converter stations must be capable of operating within this range without triggering any protective actions. In the event of a power disturbance, the DC voltage may deviate dynamically outside the normal operating range but must settle within the continuous operating range in steady state, until further corrective actions are taken by the DCGC.

- *Dynamic operating range*: This range defines the maximum DC voltage limits [v_{min}^{dyn}, v_{max}^{dyn}] during disturbance conditions. The DC voltage may temporarily exceed the continuous operating range during dynamic events, such as faults or sudden active power changes. The overshoot or undershoot beyond the continuous operating range should be limited to this dynamic range. If the DC voltage exceeds the upper dynamic limit, a Dynamic Breaking System (DBS) must be activated to protect the equipment.

- *Transient operating range*: This range closely relates to the local protective measures and the adopted DC Fault Ride-Through (DC-FRT) strategy. From a control perspective, this range is less relevant, as it is primarily associated with protection coordination.

3.4.2 DC power flow management

In MTDC grids, DC power flow management is essential to aid in the planning of grid operation and defining power and voltage schedules. This function is typically performed by the DCGC at the operational level, which determines the power setpoints for each converter station based on the overall grid conditions and the requirements from the dispatch level. As the vision towards large MTDCs grids unfolds, DC power flow algorithms have been introduced in the literature [118–124]. In [118], the impact of droop gain selection on the post-contingency DC voltage operating point is studied. Similarly, the work in [119] presented a power flow algorithm incorporating different DC voltage control modes. The system losses were included in the power flow algorithm presented in [121]. However, these studies considered only a single point connection between the AC and DC sides, making the analysis only applicable to monopolar or balanced bipolar configurations.

The authors in [122] considered a bipolar configuration in the DC power flow problem, analyzing the admittance matrix of a true bipolar structure, and different control modes were incorporated. In the case of a bipolar configuration with Dedicated Metallic Return (DMR), the grid shall be able to operate in unbalanced conditions, due to for example the outage of one pole. These cases have been addressed in [124,125], where the DC power flow algorithm is extended to consider unbalanced bipolar operation.

From a system security perspective, DC power flow serves two main purposes. First, an accurate DC power flow calculation is essential for the DCGC to ensure that all pre-contingency operating points are within the defined DC voltage *Normal operating range*. Second, the incorporation of DC voltage droop constraint in the power flow problem allows for the determination of the expected post-contingency DC voltage operating points, ensuring that they remain within the *Continuous operating range*. This is crucial for preventing any protective actions from being triggered. Such considerations

have been considered in multi-vendor context, as presented in [126] and in the InterOPERA 3TDC grid demonstrator [127].

3.4.3 DC voltage static control options

One possible solution for controlling the DC voltage in MTDC grids is fixed DC voltage control (Fig. 3.3a), representing a centralized control solution. Extended from point-to-point systems, this method regulates the DC voltage at a specific station to a fixed setpoint, regardless of power injection or evacuation at that station, subject to its capability limits. This is analogous to the isochronous frequency control of a synchronous generator [43]. While suitable for point-to-point links, applying this control to MTDC grids reduces system security. If the DC-voltage-controlling station is lost, the voltage will collapse due to the loss of the slack converter, unless backup functions are in place. Furthermore, if multiple stations operate in fixed DC voltage control, a hunting effect may occur as they compete to regulate the voltage to their respective references. In general, fixed DC voltage control can only be applied to small MTDC grids with limited redundancy, which restricts its expandability.

Another approach is *DC voltage margin control* (Fig. 3.3b) [128, 129], which combines fixed active power and fixed DC voltage modes. Here, the converter operates in constant power mode within a predefined voltage margin. If the voltage exceeds this margin, the converter switches to fixed voltage control. While this control mode offers more flexibility, the discrete switching can cause undesirable transient responses. Additionally, the hunting effect remains a risk if multiple stations switch modes simultaneously, and coordinating these margins across a large grid presents a control challenge.

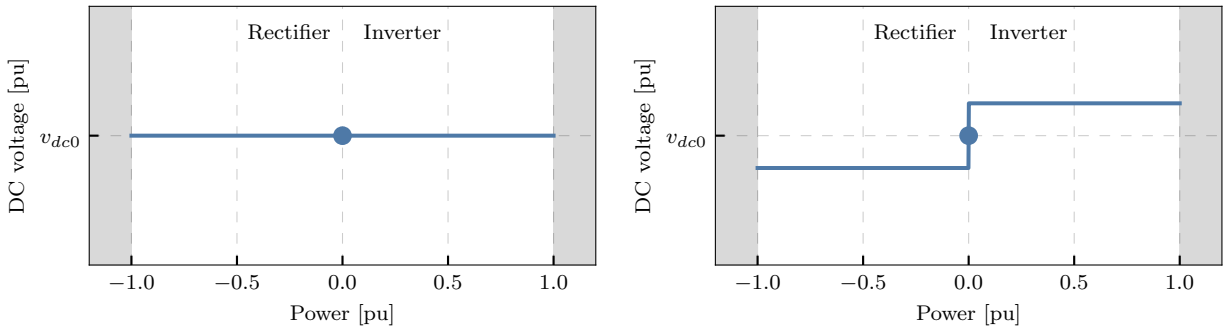

(a) Fixed DC voltage control concept

(b) Voltage margin control concept

Figure 3.3: DC voltage control modes.

DC voltage droop control (Fig. 3.4) is a distributed control solution that allows multiple stations to share the responsibility of DC voltage regulation. Each converter adjusts its power output proportionally to the local DC voltage deviation, similar to frequency droop in AC systems. It enhances reliability because the loss of one droop station does not lead to system collapse; the remaining droop-controlled stations continue to regulate the voltage, with reduced capacity. The droop characteristic of each station is defined by its droop gain k_d, which determines the steady-state deviation of the DC voltage to the change in its active power output. The droop characteristic can be expressed as:

$$k_d = \frac{\Delta v_{dc}}{\Delta P_{ac}} \tag{3.1}$$

where $\Delta v_{dc} = v_{dc} - v_{dc}^{set}$, $\Delta P_{ac} = P_{ac} - P_{ac}^{set}$, v_{dc}^{set} and P_{ac}^{set} are the DC voltage and active power

setpoints[1], respectively. The droop gain k_d is typically expressed in per unit based on the converter's rated power and nominal DC voltage. The positive power direction is defined as power injection from the DC grid to the AC grid.

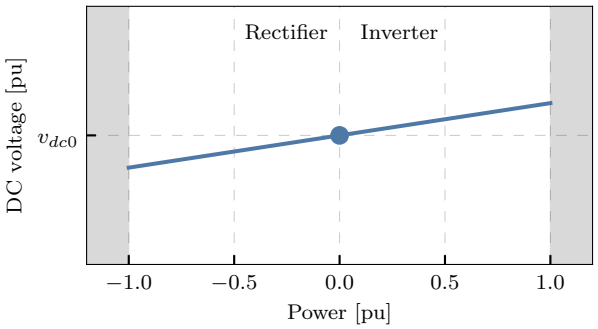

Figure 3.4: DC voltage droop control concept.

The fixed DC voltage droop characteristic shown in Fig. 3.4 has the disadvantage of not accounting for the different DC voltage operating ranges defined earlier. In other words, the droop gain remains constant regardless of the initial operating point. For Frequency Containment Reserve (FCR) in AC systems, the TSO mandates sufficient headroom for frequency regulation [130]. However, in MTDC grids, converter stations are expected to operate close to their rated conditions in order to maximize power transfer to the onshore grid. Consequently, ensuring a sufficient power reserve to support primary DC voltage regulation poses a significant challenge, particularly in small MTDC grids with limited redundancy.

To address this challenge, various methods for selecting the DC voltage droop gain have been proposed in the literature. Selecting the droop gain from a static perspective involves a trade-off between limiting DC voltage deviation and minimizing power deviation from the original setpoint. A smaller droop gain results in tighter voltage regulation but requires larger power adjustments from the converter, which may be constrained by its rated power limits. Conversely, a larger droop gain reduces the required power change but leads to larger voltage deviations. Adaptive droop control has also been explored [131–133], where the droop gain is dynamically adjusted based on system conditions. In [131] and [132], the droop setting is adapted based on the available power headroom of the converter. Conversely, [133] proposes an adaptive droop scheme that adjusts the gain based on the proximity of the DC voltage to its acceptable limits. While adaptive droop control offers improved online adaptability to system conditions, it introduces additional complexity and may pose interoperability challenges in multi-vendor grids.

An intuitive trade-off can be achieved by adopting a *multi-segment droop control* strategy, which defines the droop characteristic as a piecewise linear function. This approach provides additional flexibility by allowing different droop gains in different operating regions. The primary objective of multi-segment droop is to maximize the utilization of converter headroom during normal operation. while maintaining effective grid security. For example, a higher droop gain can be applied near the reference point to avoid excessive power fluctuations, while a smaller droop gain can be activated during larger deviations to minimize DC voltage shifts. These operating segments can be defined in accordance

[1]DC power can also be used as the denominator for the definition of dc voltage droop gain. Without loss of generality, AC power is used throughout this thesis.

with the DC voltage ranges illustrated in Fig. 3.2. This concept is inspired by AC system practices for Frequency Containment Reserve (FCR) [134], where multi-segment frequency droop is used to enhance regulation through modes such as Frequency Sensitive Mode (FSM) and Limited Frequency Sensitive Mode (LFSM). Additionally, the DC voltage droop gains for each controlling station can be pre-set and remain unchanged during the operational cycle, unlike adaptive droop schemes. A schematic illustration of multi-segment DC voltage droop control is shown in Fig. 3.5.

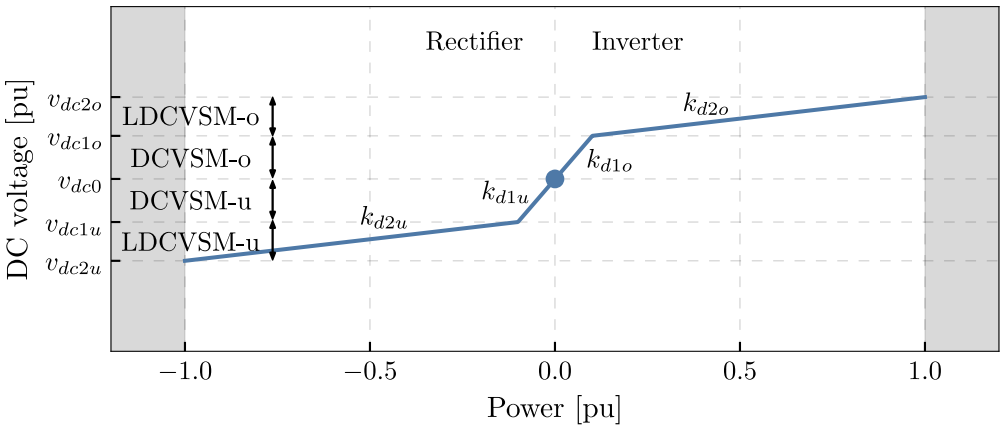

Figure 3.5: Multi-segment DC voltage droop control.

Various forms of multi-segment droop have been proposed in the literature [117, 135–137]. Multi-segment droop can be seen as the most generic form of DC voltage droop control, encompassing other control modes such as fixed DC voltage control and voltage margin control by defining the appropriate droop gains. From Fig. 3.5, the different segments of the droop characteristic can be defined as follows:

- DC voltage sensitive mode (DCVSM): This segment operates within the normal operating range, where droop gains k_{d1o} and k_{d1u} are defined to limit power fluctuations during normal operation.
- Limited DC voltage sensitive mode (LDCVSM): This segment operates within the continuous operating range, where droop gains k_{d2o} and k_{d2u} are defined. These gains are typically smaller than those in the DCVSM to ensure effective voltage regulation during disturbances.

It is observed from Fig. 3.5 that the upper most and lower most segments intersect with the converter rated power limits. In case of a different operating point, this may not be the case. For instance, a positive initial active power setpoint will shift the droop characteristic rightwards, and the LDCVSM-u segment will intersect with the minimum continuous operating DC voltage limit before reaching the rated rectifier power limit. In order to exploit the available converter capacity, another segment, called *DC voltage Limiting Mode* (DCVLM), is defined. The droop gain of this segment k_{d3o} (or k_{d3u} for the lower segment) is typically set sufficiently small to limit further voltage deviation beyond the continuous operating range. An illustration of this case is shown in Fig. 3.6.

In the same case, the LDCVSM-o segment will hit the rated power limit before reaching the maximum continuous operating DC voltage limit. Therefore, another segment is defined, called *Power Limiting Mode* (PLM). This mode ensures that the converter operates within its rated power limits, the implementation of which is the responsibility of each vendor. It can be implemented as a vertical slope ($k_d = \infty$), or a very high droop gain that allows the converter to limit its power output irrespective of the DC voltage variation. The PLM is shown in Fig. 3.6.

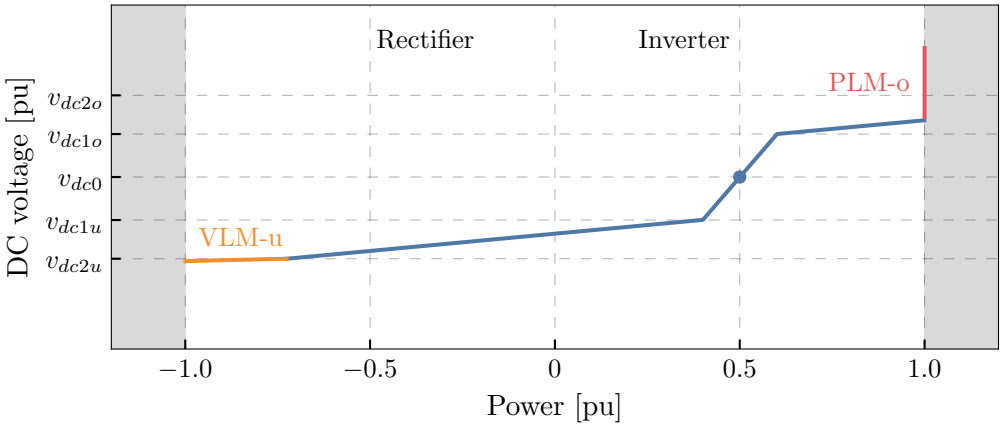

Figure 3.6: Additional Segments of multi-segment droop to account for voltage limitation and power headroom exploitation.

3.5 Dynamic considerations of primary DC voltage control

The previous section discussed the static aspects of DC voltage droop control, which define the expected DC voltage steady-state characteristics under a given disturbance, a setting typically determined by the relevant system operator [14]. From a static perspective, different DC voltage droop implementation options may yield similar steady-state characteristics [138]. On the other hand, from a dynamic perspective, the choice of DC voltage droop implementation can significantly affect the system's small-signal stability and transient response [139–141]. This is shown in Fig. 3.7, where the intuitive distinction between the static and dynamic response of a converter station subject to a disturbance is illustrated. The static response defines the final steady-state operating point, while the dynamic response characterizes the transient behavior. In practice, the implementation of DC voltage droop control functionality lies within the responsibility of each vendor, making it difficult to enforce a specific implementation of DC voltage droop. Therefore, this necessitates the establishment of *dynamic performance requirements* for primary DC voltage control in MV-MTDC grids, which should be considered alongside the static performance requirements [14]. This section provides an overview of the dynamic considerations of primary DC voltage control, highlighting the main challenges and design guidelines to ensure a proper grid operation.

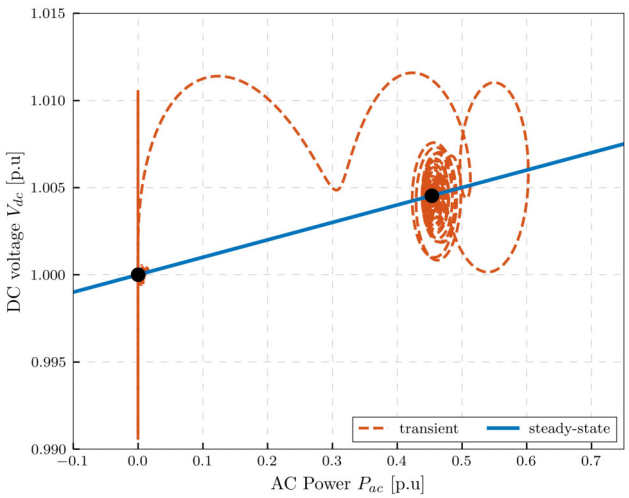

Figure 3.7: Distinction between static and dynamic response of DC voltage droop control.

3.5.1 DC voltage droop implementation options

In contrast to Section 3.4, this section considers a single droop characteristic. The non-linearity of the piecewise multi-segment droop characteristic complicates small-signal analysis; furthermore, the objective here is to analyze the stability limitations of the droop gain in general, rather than focusing on a specific segment of the droop control. Consequently, the stability trends and limitations of the droop gain are examined when different DC voltage droop implementation options are employed within the same DC grid.

Building on the well known fixed DC voltage control and fixed active power control utilized in Point-to-Point systems, two possible implementation options of DC voltage droop are presented, referred to as Scheme A and Scheme B, shown in Fig. 3.8. In Scheme A, the droop gain acts on the DC voltage deviation from its reference to generate an AC power mismatch which is added to the original AC power setpoint, as depicted in Fig. 3.8a, then a PI controller is used to track the AC power reference. This scheme can be seen as an extension of the constant power control mode with a DC voltage droop characteristic. On the other hand, Scheme B changes the DC voltage setpoint in proportion to the AC power deviation. The DC voltage is then regulated by a PI controller as shown in Fig. 3.8b. Droop Scheme B can similarly be seen as an additional active power control layer to the constant DC voltage control mode, previously described in Chapter 2. In both schemes, the output of the PI controller generates the d-axis reference for the inner Δ current control loop.

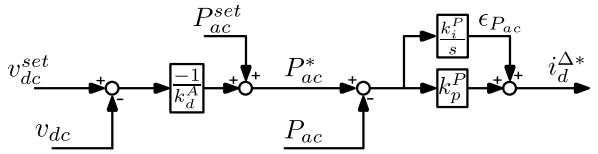

(a) DC voltage droop scheme A

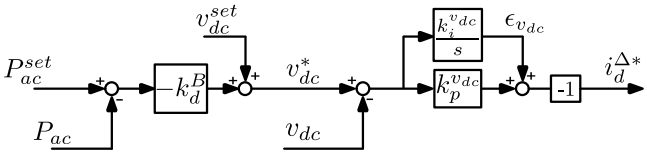

(b) DC voltage droop scheme B

Figure 3.8: DC voltage droop implementation options.

From Fig. 3.8, the integral state of the PI controllers of the respective control schemes for the outer loops is represented by $\epsilon_{P_{ac}}$ for Scheme A and $\epsilon_{v_{dc}}$ for Scheme B. Their dynamics are described by

$$\frac{d\epsilon_{P_{ac}}}{dt} = k_i^P \left(\frac{-1}{k_d}(v_{dc}^{set} - v_{dc}) + P_{ac}^{set} - P_{ac} \right) \tag{3.2a}$$

$$i_d^{\Delta *} = \epsilon_P + k_p^P \left(\frac{-1}{k_d}(v_{dc}^{set} - v_{dc}) + P_{ac}^{set} - P_{ac} \right) \tag{3.2b}$$

if Scheme A is used; or

$$\frac{d\epsilon_{v_{dc}}}{dt} = k_i^{v_{dc}}(-k_d(P_{ac}^{set} - P_{ac}) + v_{dc}^{set} - v_{dc}) \tag{3.3a}$$

$$i_d^{\Delta *} = -\epsilon_{v_{dc}} - k_p^{v_{dc}}(-k_d(P_{ac}^{set} - P_{ac}) + v_{dc}^{set} - v_{dc}) \tag{3.3b}$$

if Scheme B is used.

3.5.2 Three-terminal DC grid under study

To study the interoperability of these two control options and analyze their stability limitations, the three-terminal DC grid in asymmetrical monopole configuration shown in Fig. 3.9 is considered. Three DC cables of 100 km interconnect the three converter stations to a DC switching station (DCSS), which is responsible for establishing the electrical connection between the different HVDC subsystems. It comprises a switching unit, a busbar unit, and a grounding unit [14]. In this study, the DCSS is modeled as an ideal switch. Station 1 operates in fixed active power control mode. Station 2 uses DC voltage droop Scheme A while Station 3 utilizes DC voltage droop Scheme B.

Apart from the adopted droop control, the control of all three stations is identical and follows *Control setting 1*, namely UCM with GFL control, in Chapter 2. The reference for the q-axis current $i_q^{\Delta *}$ is generated by the reactive power controller, which is identical in the three MMC stations. The physical MMC parameters are presented in Appendix A. The main control parameters of the three stations are summarized in Table 3.1. The state-space model of each converter station is derived using the approach presented in Chapter 2 and summarized in Appendix D. The state-space representation of the cable model follows the approach in [142] and is presented in Appendix E.

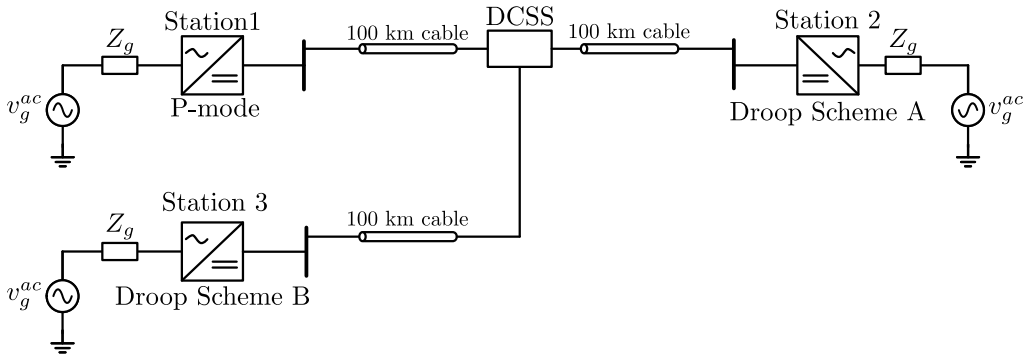

Figure 3.9: Three-terminal HVDC system under study.

Table 3.1: Three-terminal DC grid system parameters

Parameter	**Value**
MMC1 - Fixed P-mode	
Active Power response time [ms]	50
MMC2 - Droop Scheme A	
DC voltage droop gain k_d^A [p.u.]	0.1
Active power control response time τ_r^P [ms]	50
MMC3 - Droop Scheme B	
DC voltage droop gain k_d^B [p.u.]	0.1
DC voltage control response time $\tau_r^{v_{dc}}$ [ms]	50

The full state-space model of the 3TDC grid is obtained by combining the state-space models of the subsystems (converter stations and cables) and linearizing the system around the equilibrium point,

which in this case is defined by zero power setpoints for all three stations.

Before presenting the small-signal stability analysis in the next subsection, a validation step is performed on the linearized model of the 3TDC grid. A comparison with the original non-linear system simulated in EMTP-RV is conducted, where a 0.2 pu step change in the active power setpoint of Station 3 is introduced at $t = 3$ s. As shown in Fig. 3.10, the linearized model captures the dynamics of the non-linear system and is thus validated for the upcoming small-signal analysis.

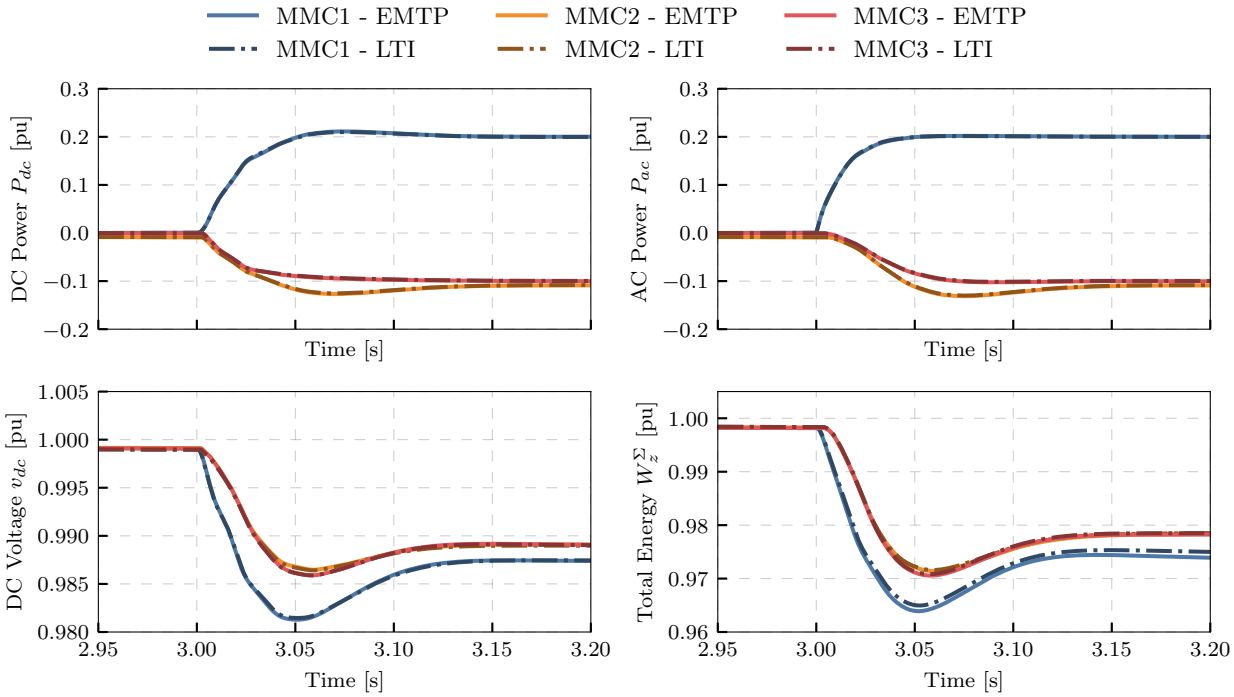

Figure 3.10: Time-domain validation of the linearized 3TDC grid against the non-linear EMT model for the 3TDC system under study.

3.5.3 Small-signal stability analysis

The small-signal stability analysis focuses on the impact of the droop gain of both schemes on the system poles. The droop gains of Station 2 and Station 3, k_d^A and k_d^B, are varied independently to observe their respective impact on the system stability.

Impact of the droop gain of Droop scheme A

This subsection highlights the stability implications of the droop gain for Station 2 operating in DC voltage droop Scheme A. Fig. 3.11 shows the eigenvalue trajectories for different values of k_d^A of Station 2 from 0.002 pu to 0.2 pu with a resolution of 0.010421 p.u. (20 data points are used), while k_d^B of Station 3 is kept constant at 0.1 pu. It can be seen that, as k_d^A decreases, a pair of eigenvalues migrates toward the Right Half Plane (RHP). When $k_d^A = 0.002$ pu, the system becomes unstable, with a damping ratio of -0.0542 and a natural frequency of $f_n = 167$ Hz. It can also be noted that the second lowest value tested in the sensitivity analysis, $k_d^A = 0.0124$ pu, remains stable, with a damping ratio of 0.1 and a natural frequency of $f_n = 101$ Hz. Two observations can be made: first, decreasing the droop gain leads to a higher resonance frequency of the critical eigenvalue; second, the eigenvalue is highly sensitive to small variations of the droop gain in the vicinity of the stability limit.

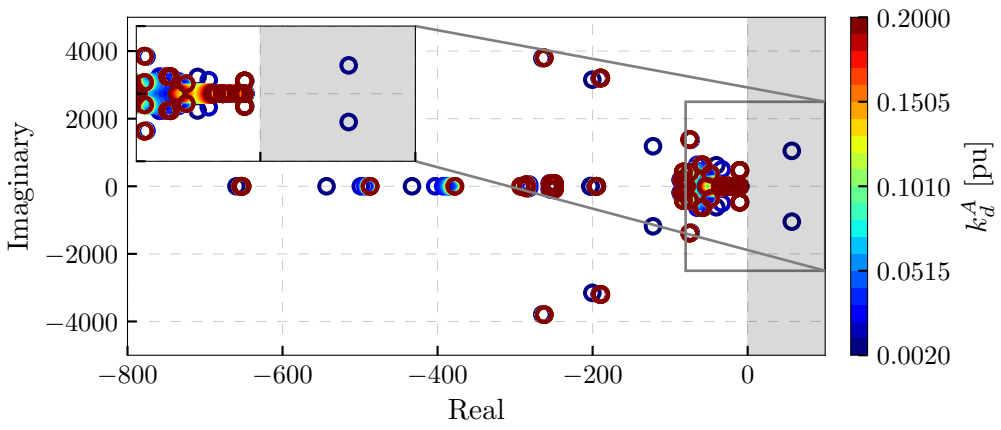

Figure 3.11: Eigenvalue trajectories for different values of k_d^A varying from 0.002 pu to 0.2 pu, while $k_d^B = 0.1$ pu.

Although this initial sweep reveals the instability, the relatively large step size of k_d^A (0.010421 p.u.) does not allow the precise identification of the critical droop gain. Therefore, a second sweep of k_d^A is conducted over a narrower range between 0.002 pu and 0.005 pu, with a finer step of 0.0001 pu. The results shown in Fig. 3.12 indicate that the critical value of k_d^A leading to instability is approximately 0.0025 pu. At this critical point, the unstable eigenvalue exhibits a natural frequency of $f_n = 144.5$ Hz and a damping ratio of -0.001.

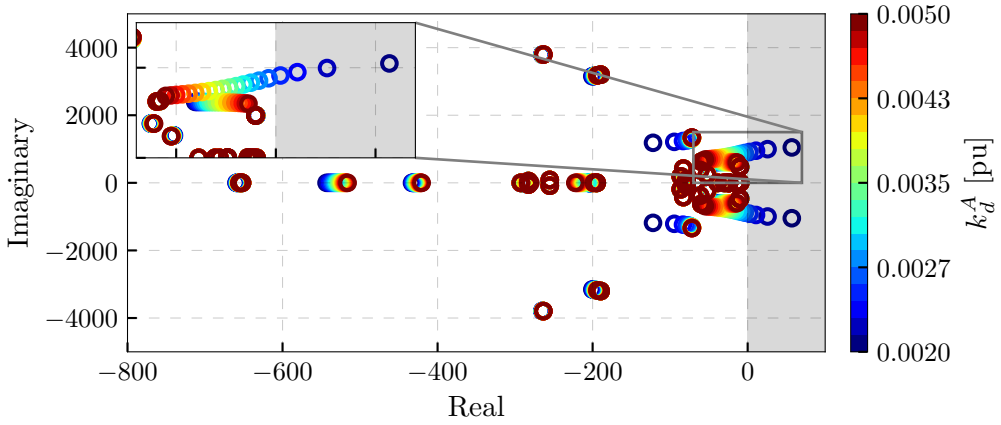

Figure 3.12: Eigenvalues trajectories with different values of k_d^A varying from 0.002 pu to 0.005 pu, while $k_d^B = 0.1$ pu.

A participation factor analysis is conducted on the unstable pair of poles $\lambda = 1.1965 \pm j908.12$, with the results shown in Fig. 3.13. Only states with a participation factor above 0.05 are displayed for conciseness.

The analysis reveals that the states mainly contributing to the unstable poles are related to Station 2, particularly the d component of the Δ current i_{d2}^{Δ}, the d component of the Δ capacitor voltage v_{cd2}^{Δ}, the zero-sequence component of the Σ capacitor voltage v_{cz2}^{Σ}, the integral state of the power controller ϵ_{P2}, and the zero-sequence component of the Σ current i_{z2}^{Σ}. This suggests that the instability is mainly driven by the interaction between the droop control and the internal control loops, including the power control loop and the AC current control loop of Station 2.

To validate this hypothesis, Fig. 3.14 shows the eigenvalue trajectories when varying the active power control response time τ_r^P of Station 2, while keeping $k_d^A = 0.0025$ pu and $k_d^B = 0.1$ pu. It

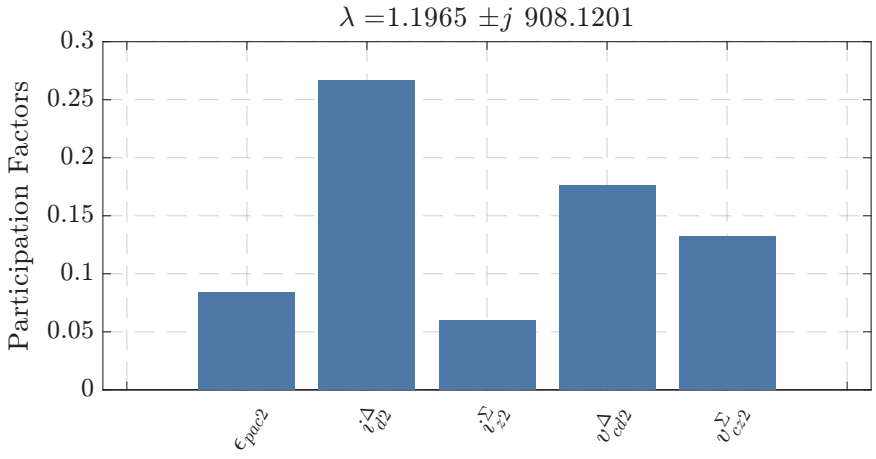

Figure 3.13: Participation factor analysis of the unstable eigenvalues.

can be observed that decreasing the response time shifts the eigenvalues back into the RHP, thereby deteriorating small-signal stability. This confirms that in general a slower outer power control loop improves the system stability.

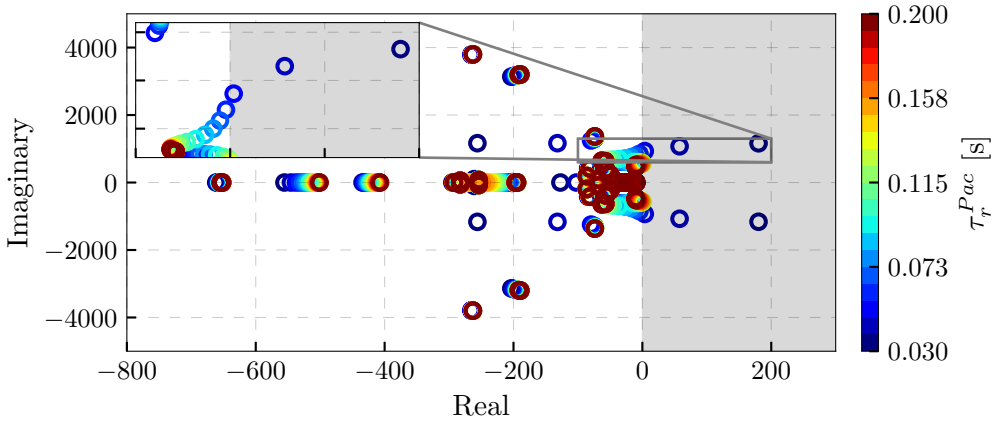

Figure 3.14: Eigenvalues trajectories with different values of τ_r^P varying from 30 ms to 200 ms, while $k_d^A = 0.0025$ pu $k_d^B = 0.1$ pu.

Impact of the droop gain of Droop scheme B

The eigenvalues trajectories obtained when varying k_d^B from 0.002 pu to 0.2 pu with 20 data points, while $k_d^A = 0.1$ pu are shown in Fig. 3.15. The result indicates that all system eigenvalues remain in the Left Half Plane (LHP) for the entire range of k_d^B considered[2]. It can also be noted that the eigenvalues are less sensitive to changes in k_d^B compared to k_d^A. This suggests that droop Scheme B is more robust to droop gain variations compared to Scheme A, especially considering lower values of droop gain, which leads to smaller steady-state DC voltage deviation. It should be noted that stations 2 and 3 are equidistant from the Station 1, hence subject to the same DC voltage variations in case of a power disturbance. Therefore, the different stability behavior observed is attributed to the different implementation of the droop control schemes.

[2]Further variations of the droop gain k_d^B were tested, reaching as low as 0.001 p.u., without resulting in instability.

This can be better explained by observing Fig. 3.8b, where decreasing k_d^B reduces the impact of the AC power mismatch on the DC voltage reference, thus approximating a constant DC voltage control behavior without causing high-gain instability, unlike droop Scheme A.

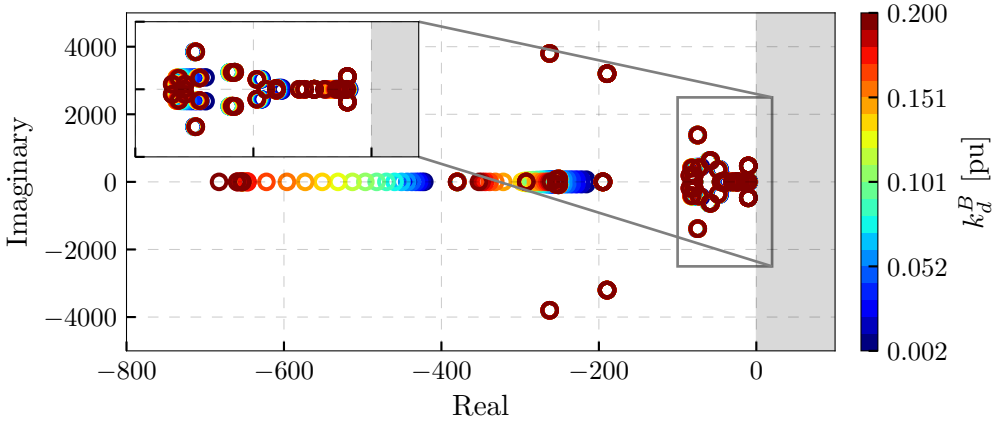

Figure 3.15: Eigenvalues trajectories with different values of k_d^B varying from 0.002 pu to 0.2 pu, while $k_d^A = 0.1$ pu.

3.5.4 Time-domain validation

To validate the small-signal stability analysis results, time-domain simulations are performed on the non-linear EMT model of the 3TDC grid in EMTP-RV. Fig. 3.16 shows the time-domain response of the system for the unstable case identified in the small-signal analysis, where $k_d^A = 0.0025$ pu and $k_d^B = 0.1$ pu. A change in the droop gain of Station 2 is introduced at $t = 3$ s, from a stable value of $k_d^A = 0.1$ pu to the unstable value of $k_d^A = 0.0025$ pu, with $k_d^B = 0.1$ pu. The results confirm the instability predicted by the small-signal analysis, with growing oscillations in both the DC voltage and AC power of Station 2 with an oscillation frequency of approximately 144 Hz, matching the natural frequency of the unstable eigenvalue, identified in Fig. 3.12. It can also be seen that the oscillations at station 2 grow faster than those of the other stations, which is consistent with the participation factor analysis results shown in Fig. 3.13, confirming that it is due to the instability of Station 2.

Another time-domain simulation is performed to validate the impact of the outer AC power control loop response time on the system stability. Fig. 3.17 shows the time-domain response of the system when $k_d^A = 0.002$ pu and $k_d^B = 0.1$ pu, with the outer AC power control loop response time of Station 2 set to $\tau_r^P = 100$ ms. A change in the droop gain of Station 2 is introduced at $t = 3$ s, from a stable value of $k_d^A = 0.1$ pu to the low value of $k_d^A = 0.002$ pu. The results confirm the conclusion drawn from the small-signal analysis, that the choice of a slower AC power control loop ($\tau_r^P = 100$ ms) leads to a stable response with no growing oscillations, and only impacting the steady-state DC voltage deviation. Although the response exhibits some oscillations, they are eventually damped out, confirming the system's stability for this configuration.

The final time-domain simulation is performed to validate the stability of droop Scheme B for low values of droop gain. Fig. 3.18 shows the time-domain response of the system when $k_d^A = 0.1$ pu and $k_d^B = 0.002$ pu. A -0.5 pu step change in the power setpoint of MMC1 is introduced at $t = 3$ s. The results confirm the stability of the system for this configuration, with a stable transient response and no growing oscillations, validating the small-signal analysis findings.

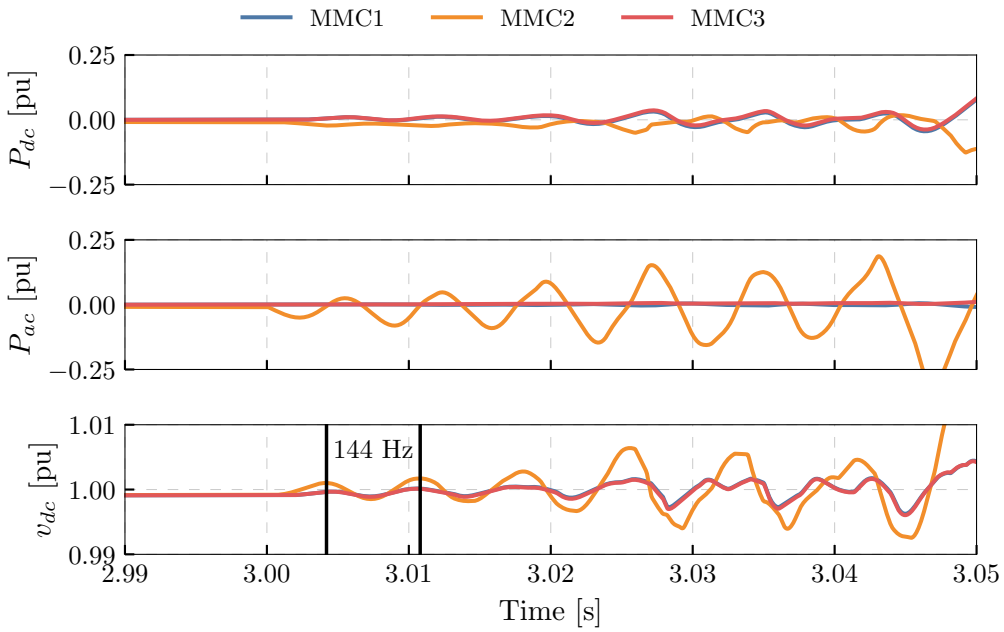

Figure 3.16: Time-domain validation of the unstable case identified in the small-signal analysis, with $k_d^A = 0.0025$ pu and $k_d^B = 0.1$ pu.

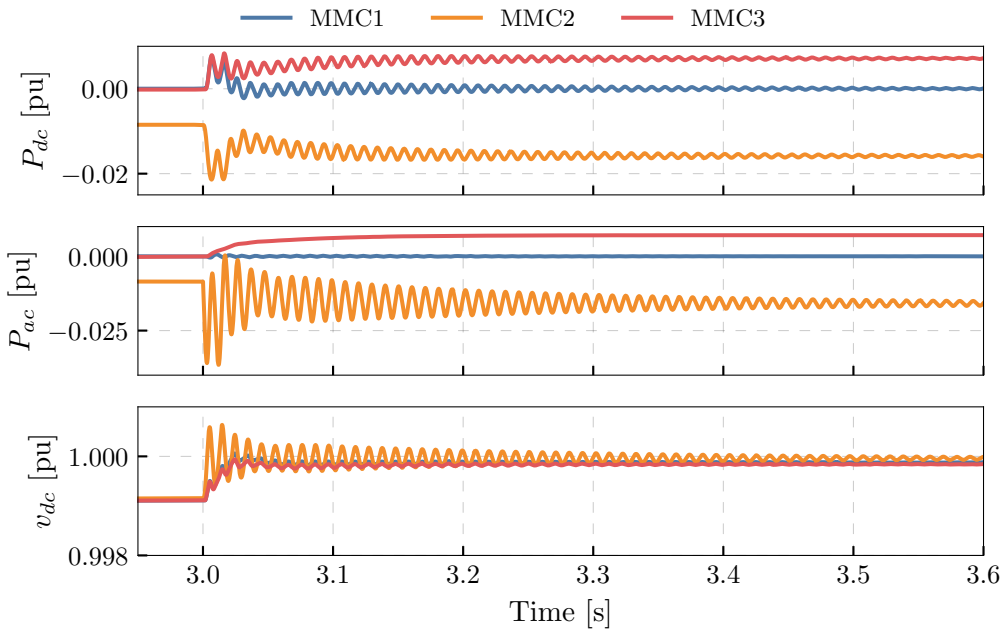

Figure 3.17: Time-domain validation of the stable case with $k_d^A = 0.002$ pu, $k_d^B = 0.1$ pu and $\tau_r^P = 100$ ms.

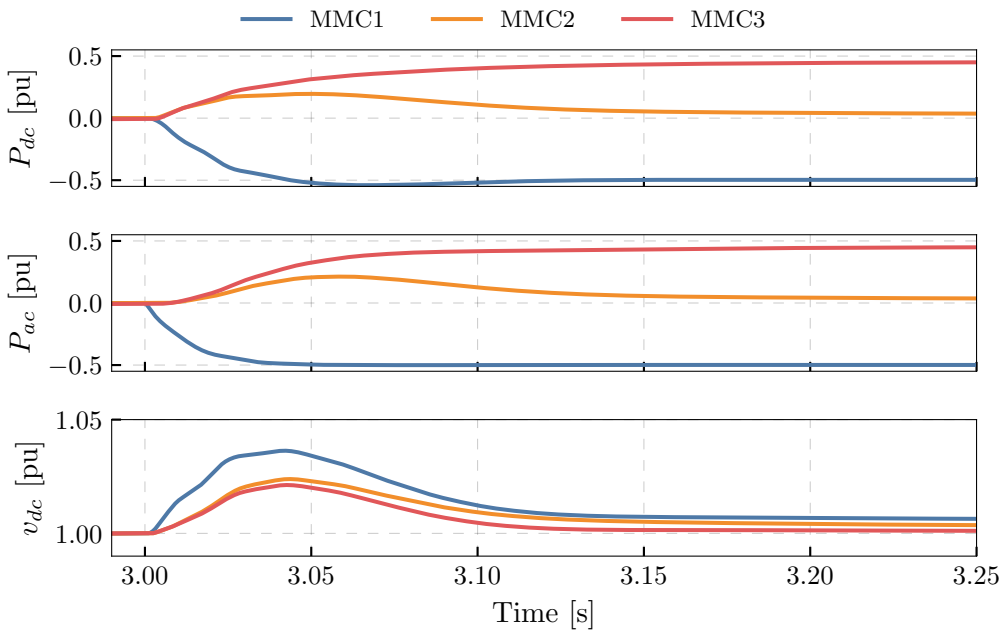

Figure 3.18: Time-domain validation of the stable case with $k_d^A = 0.1$ pu and $k_d^B = 0.002$ pu.

3.5.5 Design space of DC voltage droop in MV-MTDC grids

Fig. 3.19 illustrates the intuitive understanding of the extreme values of DC voltage droop gain for Schemes A and B.

In Scheme A, an infinite droop gain ($k_d^A \to \infty$) results in a fixed power control mode, as the DC voltage deviation from the reference value is multiplied by $1/k_d^A$, which leads to the power control loop being insensitive to DC voltage deviation. In a sense, increasing the droop gain leads to a lower controller loop gain, mitigating the risk of instability; however, this also defeats the purpose of DC voltage droop control, as a high enough droop gain leads to a higher DC voltage deviation in steady state, with an upper limit defined by the static droop requirements. Conversely, a zero droop gain ($k_d^A \to 0$) leads to a fixed DC voltage control mode, as the AC power reference is amplified by the DC voltage deviation from its setpoint. This can be preferred from a static perspective, but as shown in our study, there is always a lower limit defined by high-gain instability, rendering this setting ($k_d^A \to 0$) unfeasible from a dynamic perspective.

In Scheme B, a zero droop gain ($k_d^B \to 0$) results in a fixed DC voltage control mode, as the DC voltage reference is unaffected by the AC power deviation from its setpoint. This setting is feasible from a dynamic perspective, as the controller now converges to a conventional fixed DC voltage control structure. On the other hand, an infinite droop gain ($k_d^B \to \infty$) leads to a fixed power control mode only from a static characteristics perspective, and a similar infeasibility can be expected due to high-gain instability. The same upper limit on the droop gain can be expected on the static behavior of the droop control, before reaching the upper stability limit of the droop gain k_d^B.

3.6 Compatibility with GFM implementations options

One important consideration when analyzing the interoperability of different DC voltage droop control options is their compatibility with different grid-forming (GFM) implementations. GFM control has been recently viewed as a mandatory requirement for converter stations in MTDC grids. In [143],

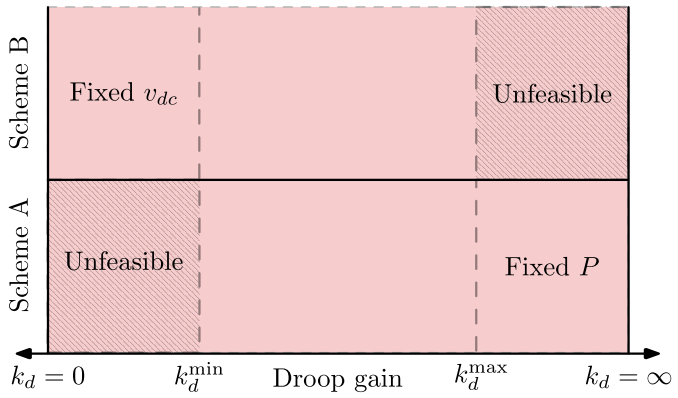

Figure 3.19: Design space for the two DC voltage droop control options.

the requirements for GFM control in MV-MTDC grids are outlined and classified into three main categories: *Mandatory functions*, *optional functions*, and *withstand capabilities*. A summary of these requirements is presented in Table 3.2.

Table 3.2: GFM functional requirements proposed in [143]

Mandatory functions	**Optional functions**	**Withstand capabilities**
Self-synchronization	Black start	Maximum step change of SCR at PoC
Phase jump active power	Sink for voltage unbalances	Maximum phase jump
Inertial active power	Sink for harmonics	Maximum RoCoF
Positive damping power		Temporary islanding of PPMs
Inherent reactive power		

3.6.1 Literature review of GFM control structures

The objective of this section is to include GFM control functionalities while maintaining compatibility with primary DC voltage control. As discussed in Chapter 2, the concept of GFM control can be summarized as the ability of the device to emulate a voltage source behavior behind an impedance, allowing it to establish and regulate the voltage at its point of connection to the grid [110]. A review of the main power synchronization-related GFM structures is presented below. AC voltage magnitude control aspects are intentionally excluded. Next, the combination of DC voltage droop control with GFM functionalities is discussed.

Droop-Based GFM Control

Droop-based GFM control is one of the earliest and most intuitive grid-forming strategies. It relies on obtaining the synchronization angle by integrating the frequency obtained from the active power/frequency (P–ω) relationship. In its simplest form, droop-based GFM control provides a static response to frequency deviations, corresponding to primary frequency control.

This basic implementation does not inherently provide inertial behavior [144, 145] as shown in Fig. 3.20a. However, virtual inertia can be introduced by applying a low-pass filter to the active power measurement, which results in dynamics analogous to those of synchronous machines.

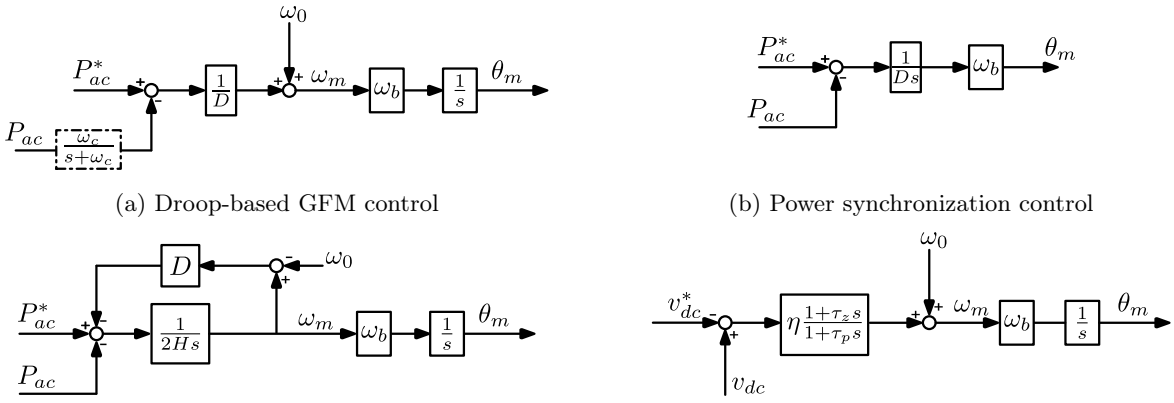

(a) Droop-based GFM control

(b) Power synchronization control

(c) VSM GFM control

(d) Matching GFM control

Figure 3.20: Different GFM control strategies found in the literature.

Power Synchronization Control

Power Synchronization Control (PSC) is fundamentally equivalent to droop-based GFM control from a synchronization perspective. PSC establishes synchronization by directly linking the active power mismatch to the voltage angle at the AC point of connection (AC-PoC) [146, 147]. Similar to Droop-based GFM control, PSC originally does not provide inertial support to the connected AC grid, see Fig. 3.20b.

Virtual Oscillator Control

Virtual oscillator control (VOC) was originally introduced for grid-forming inverters operating in islanded systems and was subsequently adapted for grid-connected scenarios. VOC-based methods introduce nonlinear oscillator dynamics to enable synchronization without relying on a phase-locked loop [148].

Within the family of VOC strategies, dispatchable virtual oscillator control (dVOC) has attracted considerable interest in grid-forming applications because of its robustness and dependable dynamic behavior [149]. One of the main strengths of dVOC is its capacity to explicitly characterize achievable performance limits based on both converter dynamics and power transfer constraints of the transmission network [149, 150].

Virtual Synchronous Machine GFM Control

Virtual synchronous machine (VSM) GFM control is one of the most widely adopted GFM strategies in the literature. Its structure is essentially based on emulating the swing equation of a synchronous generator, enabling an intuitive synchronization mechanism. VSM-based GFM control provides inertial response, damping, and frequency droop functionalities [151–153]. These features are tuned through the virtual inertia constant H and damping coefficient D in the control loop (see Fig. 3.20c).

While grid codes generally do not dictate specific implementation details, VSM-GFM control is introduced as a representative GFM approach in ENTSO-E documentation [110], highlighting its practical relevance.

Although droop-based and VSM GFM controls are typically classified as distinct approaches, it can be shown that appropriate tuning of droop-based GFM parameters allows the same dynamic behavior as VSM implementations [154]. In fact, if the low-pass filter is applied to the error signal between the

active power reference and measurement in droop-based GFM control, Fig. 3.20a leads to the same swing equation as in VSM GFM control shown in Fig. 3.20c by choosing $\omega_c = D/2H$.

Another variation of the control structure shown in Fig. 3.20c involves replacing the nominal frequency ω_0 with a frequency measured by a dedicated Phase-Locked Loop (PLL) at the AC Point of Connection (PoC). The purpose of this modification is to decouple the power-frequency droop from the inertial support. By doing so, inertial support is provided solely by the VSM block, allowing a dedicated frequency droop to be added separately to the active power reference [155].

Matching-GFM Control

Matching GFM control is a more recent GFM strategy that utilizes the structural similarity between power converters and synchronous machines to achieve grid-forming capabilities [156–158]. The core concept of matching GFM control is to adjust the converter's angle based on DC-side voltage dynamics instead of active power measurements, effectively *matching* the converter's behavior to that of a synchronous machine. This approach leverages the energy stored in the DC-side capacitor to provide GFM support to the AC grid, as illustrated in Fig. 3.20d.

The reviewed GFM control strategies differ primarily in their synchronization mechanisms rather than in their steady-state power-sharing objectives. Droop-based, PSC, and VSM-based approaches can be shown to be dynamically equivalent under appropriate parameter tuning, whereas VOC and matching-based controls introduce fundamentally different synchronization mechanisms based on nonlinear oscillators and DC-side dynamics, respectively.

DC voltage control and GFM control are potentially conflicting control objectives, since both rely on the same degree of freedom, namely the active power of the converter. Therefore, the combination of the two control objectives requires careful consideration of their interoperability. Recent literature has studied the combination of DC voltage droop control and GFM control [159, 160].

3.6.2 Combining DC voltage droop with GFM control

The analysis presented in this section studies the interoperability of two possible control structures combining GFM and DC voltage droop control. These two structures follow a logical extension from the two DC voltage droop schemes presented in Section 3.5.1. The two retained GFM control structures are: VSM-GFM and matching-GFM.

- VSM-GFM control is combined with the DC voltage droop Scheme A, which adjusts the AC power reference proportionally to the DC voltage deviation as seen in Fig. 3.21a.
- Matching-GFM control is combined with the DC voltage droop Scheme B, which adjusts the DC voltage reference proportionally to the AC power deviation, see Fig. 3.21b.

This pairing is logical because the output of droop Scheme A (the AC power reference) is the input for VSM-GFM, while the output of droop Scheme B (the DC voltage reference) is the input for matching-GFM.

As mentioned earlier, the VSM-GFM control emulates the swing equation of a synchronous machine to provide inertial and primary frequency support to the connected AC grid. The frequency dynamics of VSM-GFM without considering DC voltage droop is described by Fig. 3.20c and can be expressed as:

$$\frac{d\omega_m}{dt} = \frac{1}{2H}\left(P_{ac}^{*} - P_{ac} - D(\omega_m - \omega_0)\right) \tag{3.4}$$

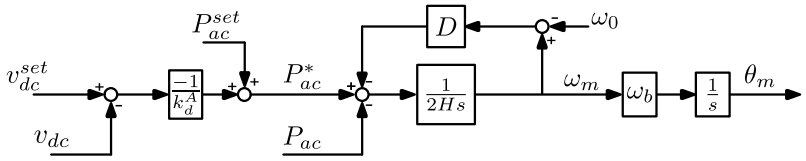

(a) DC voltage droop Scheme A with VSM-GFM control

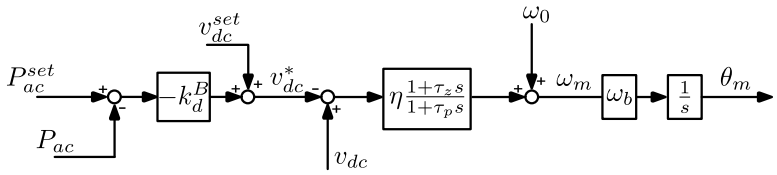

(b) DC voltage droop Scheme B with matching-GFM control

Figure 3.21: DC voltage droop implementation options with GFM control.

where P_{ac}^* is the active power reference provided to the VSM-GFM control, P_{ac} is the active power injected to the AC grid, ω_m is the frequency generated by the VSM-GFM control, ω_0 is the nominal grid frequency, H is the tuned inertial constant and D is the tuned damping coefficient. The transfer function from the active power deviation to the frequency deviation can be derived from (3.4) as:

$$G_{P\omega}^{\text{VSM}}(s) = \frac{\Delta\omega(s)}{\Delta P_{ac}(s)} = \frac{1}{2Hs + D} \tag{3.5}$$

with $\Delta\omega(s) = \omega_m(s) - \omega_0$ and $\Delta P_{ac}(s) = P_{ac}^*(s) - P_{ac}(s)$.

When combined with DC voltage droop Scheme A, the active power reference P_{ac}^* is modified according to the DC voltage deviation from its setpoint, as shown in Fig. 3.21a. The frequency dynamics of the VSM-GFM control with DC voltage droop Scheme A can thus be modified as:

$$\frac{d\omega_m}{dt} = \frac{1}{2H}\left(\frac{-1}{k_d^A}(v_{dc}^{set} - v_{dc}) + P_{ac}^{set} - P_{ac} - D(\omega_m - \omega_0)\right) \tag{3.6}$$

where P_{ac}^{set} is the active power setpoint. The transfer function from the DC voltage mismatch to the frequency deviation can be derived from (3.6) as:

$$G_{V\omega}^{\text{VSM}}(s) = \frac{\Delta\omega(s)}{\Delta V_{dc}(s)} = \frac{1}{k_d^A(2Hs + D)} \tag{3.7}$$

where $\Delta V_{dc}(s) = V_{dc}(s) - V_{dc}^{set}(s)$. Two observations can be made from (3.7): first, the inertial constant H and damping coefficient D directly influence the dynamic response of the converter to DC voltage deviations; second, the droop gain k_d^A inversely affects the gain of the transfer function, indicating that a lower droop gain leads to higher sensitivity of the frequency to DC voltage deviations.

The matching-GFM control adjusts the converter's frequency in response to DC voltage variations to achieve synchronization with the AC grid. Specifically, and inspecting Fig. 3.21b, the transfer function from the DC voltage deviation to the frequency deviation is given by

$$G_{V\omega}^{\text{mat}}(s) = \frac{\Delta\omega(s)}{\Delta V_{dc}(s)} = \eta\frac{1 + \tau_z s}{1 + \tau_p s} \tag{3.8}$$

where η defines the static relationship between the DC voltage deviation and the frequency deviation, τ_z is the lead time constant and τ_p is the lag time constant. Following the structure in Fig. 3.21b, the

transfer function from the AC power deviation to the frequency deviation can be derived as:

$$G_{P\omega}^{\text{mat}}(s) = \frac{\Delta\omega(s)}{\Delta P_{ac}(s)} = k_d^B \eta \frac{1+\tau_z s}{1+\tau_p s} \tag{3.9}$$

with $\Delta P_{ac}(s) = P_{ac}^{set}(s) - P_{ac}(s)$. Comparing the transfer function in (3.9) with that of the VSM-GFM in (3.5) shows that the difference in dynamics arises from the presence of a zero in the numerator of (3.9), which introduces a lead behavior. This lead behavior can enhance the dynamic response of the converter to active power deviations, potentially improving stability and transient performance. While VSM-GFM control, with its implementation in Fig. 3.21a, acts as a low-pass filter from active power to frequency, matching-GFM control can introduce a phase lead if $\tau_z > \tau_p$.

For a GFM control law, it is important to be able to tune the inertial and damping response. Such tuning is straightforward in VSM-GFM control through the parameters H and D, which have a physical meaning due to the resemblance to the parameters of a conventional synchronous machine. In matching-GFM control, the inertial and damping response can be adjusted through the compensator parameters τ_z, τ_p and η. Specifically, and by analogy between (3.5) and (3.9), the inertia is proportional to $\frac{\tau_p}{\eta k_d^B}$ and the damping is proportional to $\frac{1}{\eta k_d^B}$. τ_z is an extra degree of freedom and shall be chosen smaller than τ_p to ensure a lead behavior.

3.6.3 Study of a standalone MMC operating with DC voltage droop and GFM control

To verify the above notions, the simple test setup 2 presented in Chapter 2 is considered, recalled in Fig. 3.22, where a GFM-MMC is connected to an AC grid with SCR = 2 and a capacitor in parallel with a power source on the DC side. The two combinations of DC voltage droop and GFM control are studied separately. Initially, the MMC is transferring zero active power between the two grids. In both cases, the droop gain is set to a value of 0.2 pu, and the impact of the GFM control parameters on the system response is studied.

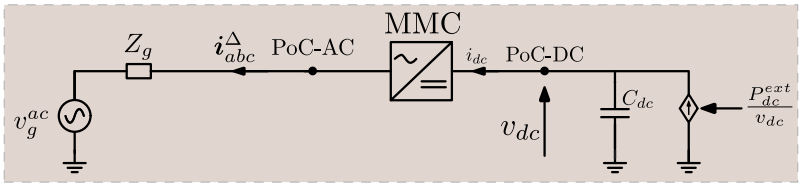

Figure 3.22: Test setup 2 used to study GFM control and DC voltage droop.

VSM-GFM control with DC voltage droop Scheme A

First, VSM-GFM control combined with DC voltage droop Scheme A is studied. The system response to a step change in the MMC active power setpoint from 0 MW to 200 MW is shown in Fig. 3.23, with H varying between 0.5 s and 2 s. The results show that increasing the inertia constant H leads to a slower dynamic response of both the DC voltage and AC power, with the value of $H = 2$s leading to system instability.

Next, the impact of the damping coefficient D on the system response is studied, with results shown in Fig. 3.24, when D is varied from 50 to 200 p.u. For the responses of the active power, frequency and DC voltage, increasing D leads to a slower system response. An interesting observation is that

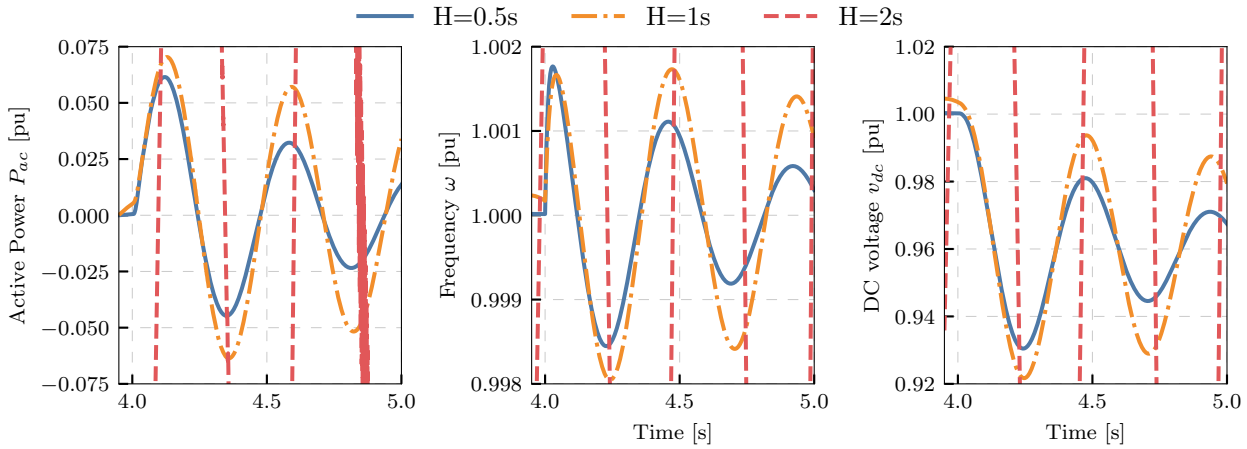

Figure 3.23: Time-domain response of the MMC with VSM-GFM control and DC voltage droop Scheme A, for different values of inertia constant H.

increasing the damping coefficient D leads to a better damped response of both the frequency and AC power responses, as expected. However, increasing D also leads a less damped DC voltage response.

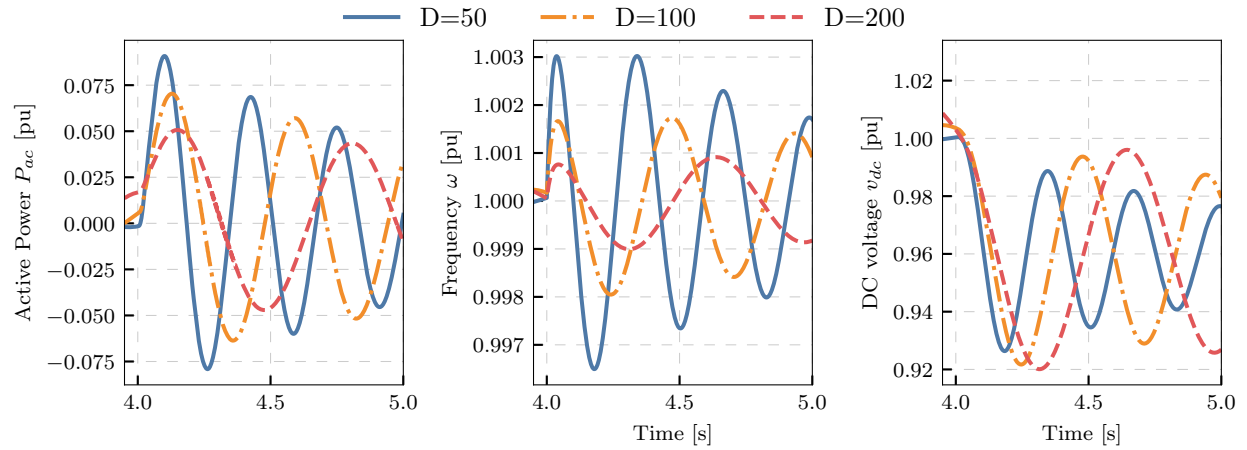

Figure 3.24: Time-domain response of the MMC with VSM-GFM control and DC voltage droop Scheme A, for different values of damping coefficient D.

Matching-GFM control with DC voltage droop Scheme B

The response of the MMC operating in matching-GFM control combined with DC voltage droop Scheme B is now studied. The system response to a step change in active power setpoint from 0 MW to 100 MW is shown in Fig. 3.25, with η varied between 0.025 to 0.1 p.u. Increasing η leads to a better damped response for the low-frequency oscillations, although it leads to a higher maximum frequency and AC power overshoot.

Next, the impact of the lag time constant τ_p on the system response is studied, with results shown in Fig. 3.26, where the lag time constant τ_p is varied from 5 ms to 20 ms in the simulations. The results show that varying τ_p does not significantly impact the dynamic response of the system, except for a lower maximum frequency overshoot for higher values of τ_p.

Finally, the impact of the lead time constant τ_z on the system response is studied, with results shown in Fig. 3.27, where the lead time constant τ_z is varied from 20 ms to 100 ms. The results show

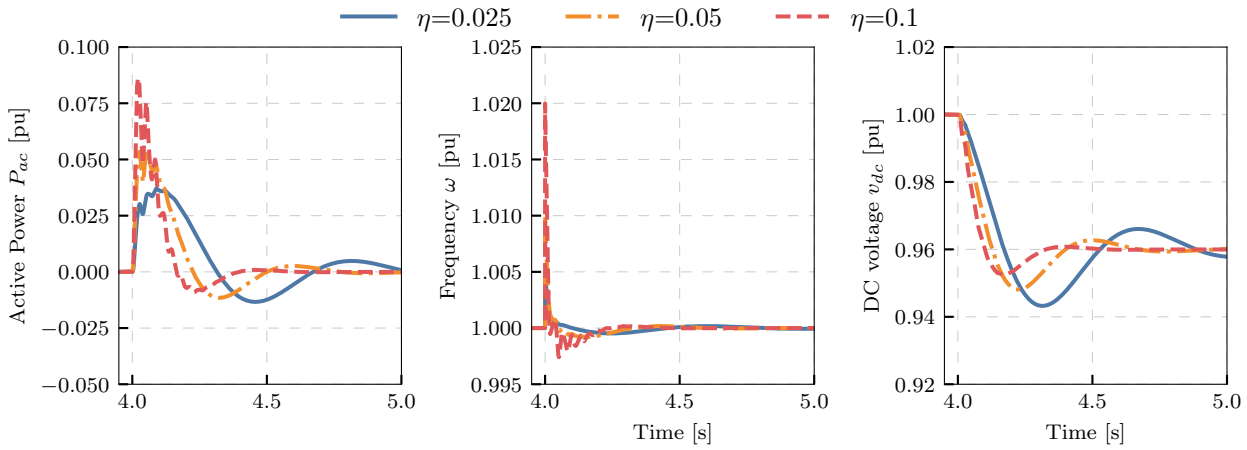

Figure 3.25: Time-domain response of the MMC with matching-GFM control and DC voltage droop Scheme B, for different values of η.

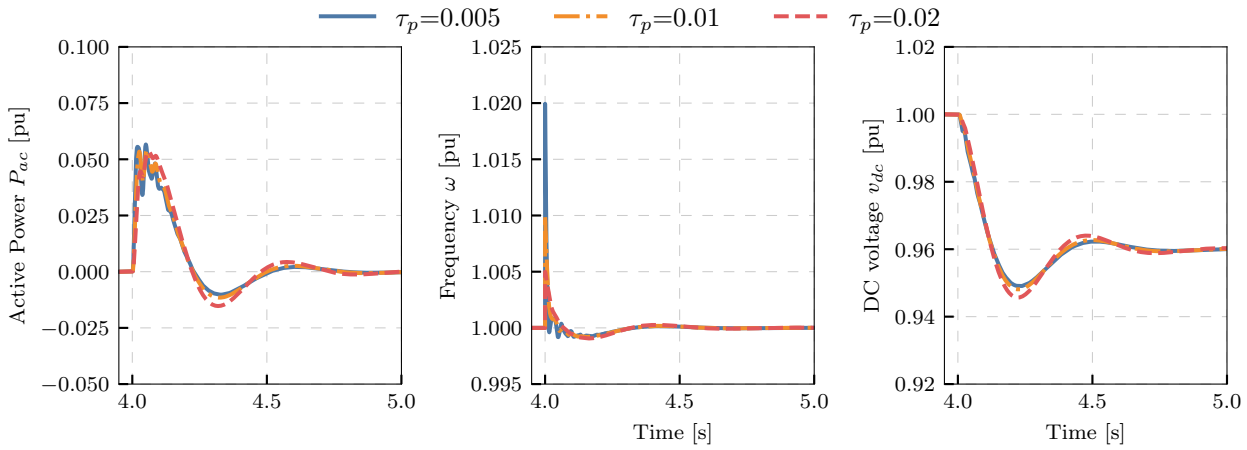

Figure 3.26: Time-domain response of the MMC with matching-GFM control and DC voltage droop Scheme B, for different values of lag time constant τ_p.

that increasing τ_z leads to a better damped response for all the three variables.

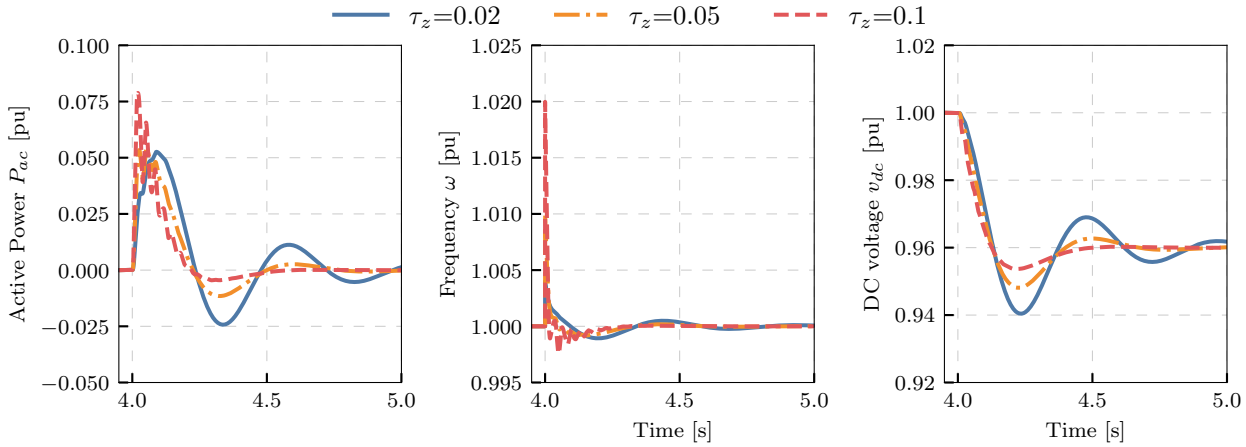

Figure 3.27: Time-domain response of the MMC with matching-GFM control and DC voltage droop Scheme B, for different values of lead time constant τ_z.

As shown in Section 3.6.2, the inertia and frequency damping response of the matching-GFM control can be adjusted through the parameters η, τ_p, and τ_z to yield the same dynamic behavior as the VSM-GFM control. The only modification required for the matching-GFM control in this comparison is neglecting the zero by setting $\tau_z = 0$. This equivalence is confirmed by the time-domain results presented in Fig. 3.28, where the matching-GFM parameters are selected to reproduce the same inertial and damping response as the VSM-GFM control with $H = 0.5$ s and $D = 100$ p.u. The results show that both GFM implementations lead to similar dynamic responses in terms of DC voltage, frequency, and AC power.

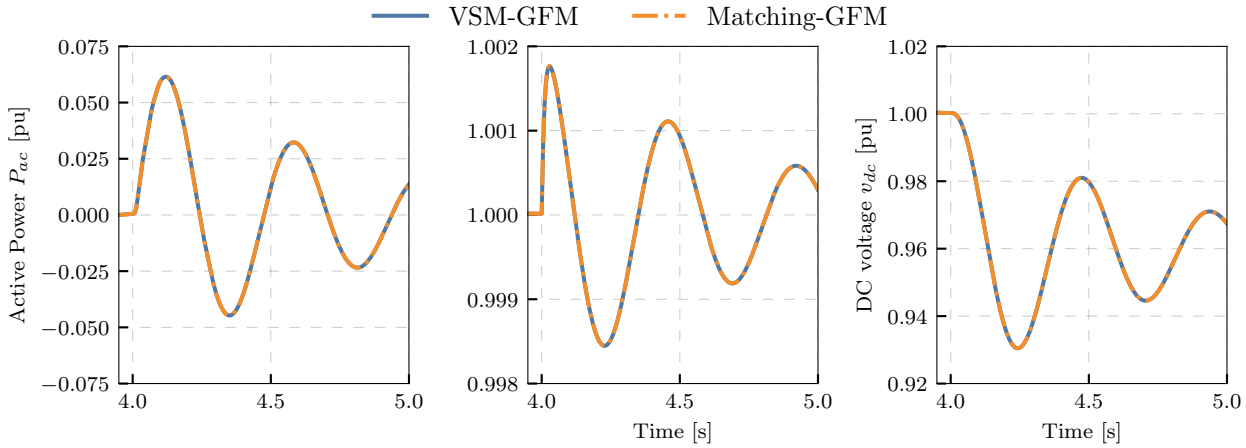

Figure 3.28: Time-domain response comparison between matching-GFM control and VSM-GFM control with equivalent inertial and damping response.

3.6.4 Three-terminal DC grid with the two combinations of droop schemes and GFM controls

In order to study the interoperability of the two DC voltage droop schemes combined with GFM control in a multi-terminal DC grid from a small-signal stability perspective, the previously studied three-terminal DC (3TDC) system is revisited, now with two MMCs operating with GFM control.

A schematic of the grid under study is shown in Fig. 3.29. Station 1 uses GFL control and fixed AC power mode. Station 2 uses droop Scheme A combined with VSM-GFM control, Station 3 uses droop Scheme B combined with matching-GFM control. In both GFM structures of Stations 2 & 3, a constant AC voltage reference is used for the modulation of the internal AC voltage, as described in Chapter 2. The physical and control parameters of the system are outlined in Table 3.3.

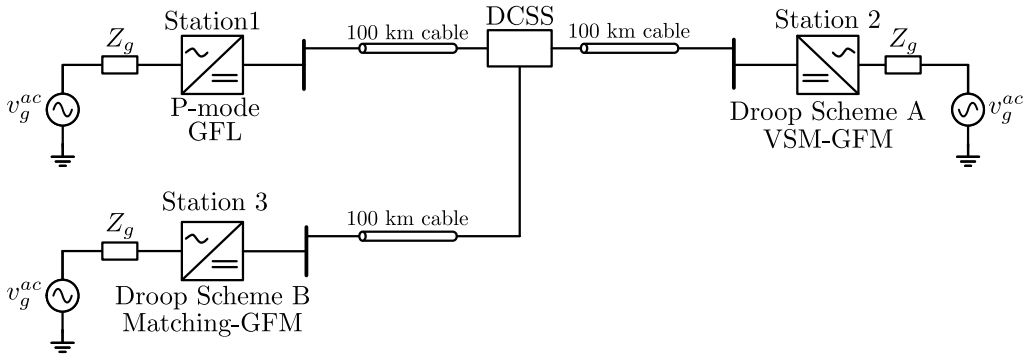

Figure 3.29: Three-terminal HVDC system under study with GFM control and DC voltage droop.

Table 3.3: Three-terminal DC grid system parameters with GFM control

Parameter	**Value**
MMC1 - Fixed P-mode with GFL	
Active Power response time [ms]	50
PLL response time [ms]	10
MMC2 - Droop Scheme A with VSM-GFM	
DC voltage droop gain k_d^A [p.u.]	0.1
Inertia constant H [s]	0.5
Damping coefficient D [p.u.]	100
MMC3 - Droop Scheme B with Matching-GFM	
DC voltage droop gain k_d^B [p.u.]	0.1
η [p.u.]	0.1
lead time constant τ_z [ms]	50
lag time constant τ_p [ms]	10

First, the validation of the linearized model of the 3TDC grid with GFM control is performed by comparing its response to that of the non-linear EMT model simulated in EMTP-RV. A step change in the power setpoint of Station 3 is introduced at $t = 3$ s. As shown in Fig. 3.30, the linearized model captures the dynamics of the non-linear system and is thus validated for the upcoming small-signal analysis.

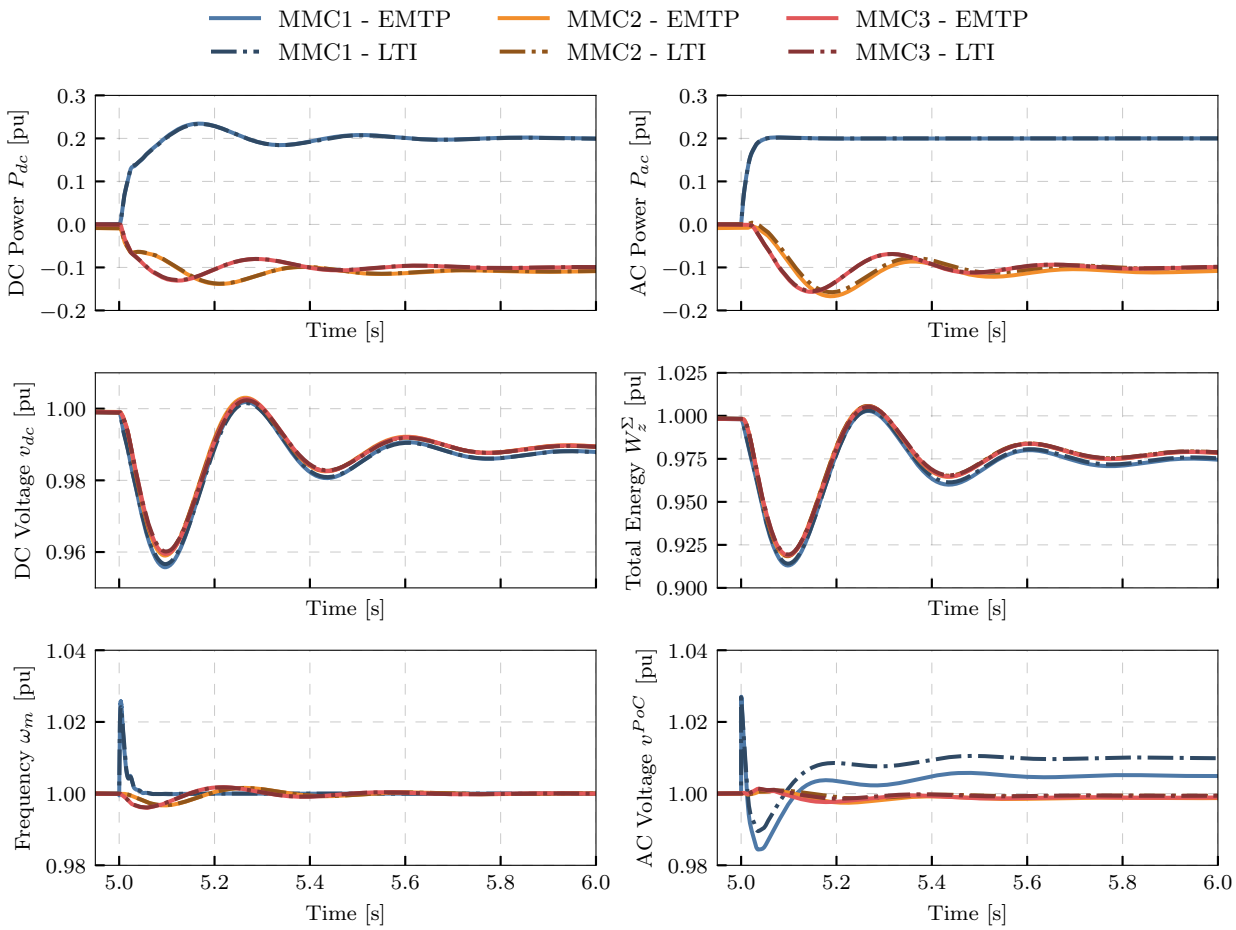

Figure 3.30: Time-domain validation of the linearized model against the non-linear EMT model.

Small-signal analysis

The next step is to analyze the small-signal stability dependencies of the 3TDC system with GFM control and DC voltage droop. The eigenvalues of the system are computed for the operating point where all MMCs are transferring zero active power. Unless otherwise specified, apart from the varied parameters, all system parameters are kept constant as in Table 3.3. The focus of the study is the impact of the droop gains of the Stations 2 & 3. For both stations, the droop gain is varied from 0.01 p.u to 0.2 p.u, while the other parameters are kept constant as in Table 3.3.

Figure 3.31 illustrates the variation in system eigenvalues as k_d^A varies while k_d^B remains constant at 0.1 pu. The results indicate that reducing k_d^A below 0.02 pu renders the system unstable at the specified operating point.

The primary explanation is that high inertial support for the AC grid slows down AC power dynamics, which conflicts with the requirement for a fast MMC response in DC voltage regulation. In this scenario, even with a low inertia constant for MMC1 ($H_1 = 1$ s), instability occurs when the DC voltage support is enhanced by reducing k_d^A to 0.03 pu. This confirms the findings in [159], which highlighted the interaction mechanism between VSM-GFM control and DC voltage droop Scheme A and proposed a phase compensator within the droop control loop to mitigate this low-frequency instability.

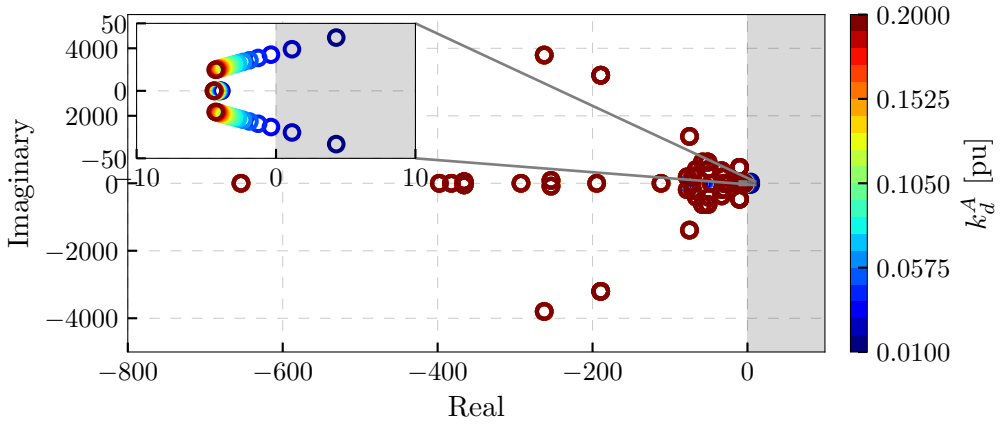

Figure 3.31: System poles when varying the droop gain of MMC2 k_d^A from 0.01 pu to 0.2 pu, while $k_d^B = 0.1$ pu.

For a droop gain of $k_d^A = 0.02$ p.u, the unstable eigenvalue $\lambda = 1.1446 \pm j30.8279$ indicate a negatively damped oscillation with a frequency of 4.9 Hz. To further investigate the nature of this instability, the participation factor analysis in Fig. 3.32 shows that the highest state participating in the unstable eigenvalue is the GFM angle θ_{m2} of MMC2 and also the GFM frequency generated by the synchronization loop, followed by the Σ capacitor voltages of the three MMCs, indicating a high interaction between the three stations on the DC side through the DC grid. Finally, the angle of the matching GFM of MMC3 also has a non-negligible participation in the unstable eigenvalue, indicating a strong coupling between the two GFM MMC stations through the DC grid.

The impacts of the inertia constant H and damping coefficient D of MMC2 on the system stability are also analyzed. Figure 3.33 illustrates the eigenvalues when varying H from 0.5 s to 5 s and D from 0.1 pu to 1 pu, with $k_d^A = 0.03$ pu and $k_d^B = 0.1$ pu. It can be observed that increasing the inertia constant H reduces the damping of the critical eigenvalues, as the pair of eigenvalues shift toward the RHP. Conversely, increasing the damping coefficient D improves the damping of these critical

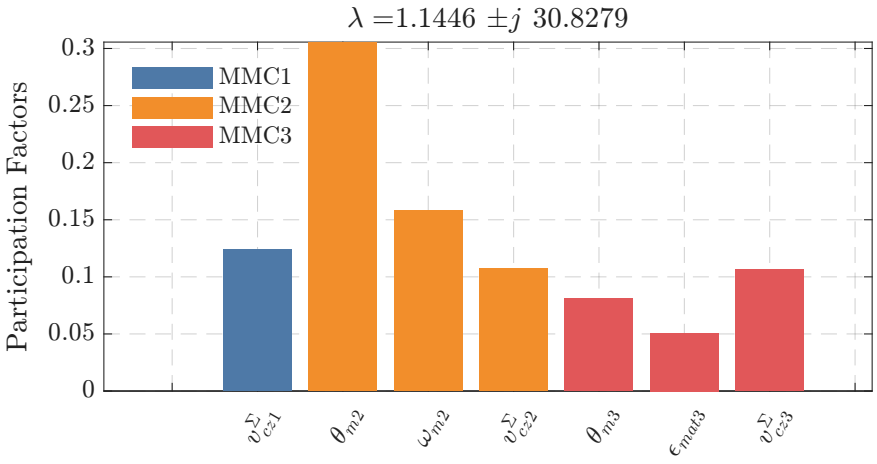

Figure 3.32: Participation factor analysis of the unstable eigenvalues.

eigenvalues, hence enhancing overall system stability.

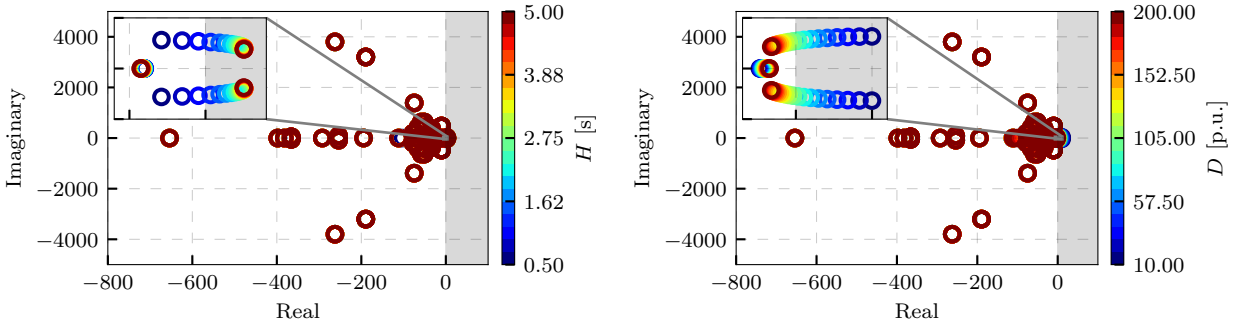

(a) Variation of the inertial constant H

(b) Variation of the damping coefficient D

Figure 3.33: Variation of : (a) the inertial constant H from 0.5 s to 5 s, (b) the damping coefficient D from 0.1 pu to 1 pu of MMC2, while $k_d^A = 0.03$ pu and $k_d^B = 0.1$ pu.

The same variation is applied to the droop gain of MMC3, k_d^B, to analyze its impact on system stability. The results, illustrated in Fig. 3.34, indicate that the system remains stable as k_d^B varies from 0.01 p.u. to 0.2 p.u. However, decreasing the droop gain causes the critical eigenvalues to move closer to the imaginary axis, without rendering the system unstable.

Simulation results

Time-domain simulations are conducted on the same three-terminal DC grid shown in Fig.3.29 using the non-linear EMT model in EMTP-RV to validate the small-signal analysis results. The first considered case involves decreasing the droop gain of MMC2, k_d^A, from its original value 0.1 p.u. to 0.02 p.u., while keeping $k_d^B = 0.1$ p.u. Other control parameters are kept constant according to Table 3.3. The results in Fig. 3.35 show that the system becomes unstable, with the same oscillation frequency of 4.9 Hz as predicted by the small-signal analysis. This confirms the findings from the small-signal analysis, where decreasing the droop gain k_d^A below a certain threshold leads to system instability.

In the second case, the droop gain of MMC3, k_d^B, is set to the minimal value considered for the variation in Fig. 3.34, i.e., $k_d^B = 0.01$ p.u., while $k_d^A = 0.1$ p.u. A step change of the AC power setpoint of MMC1 from 0 pu to -0.5 pu is applied at $t = 5$ s. The system response in Fig. 3.36 shows that the system remains stable, confirming the small-signal analysis results. Due to the low droop gain of

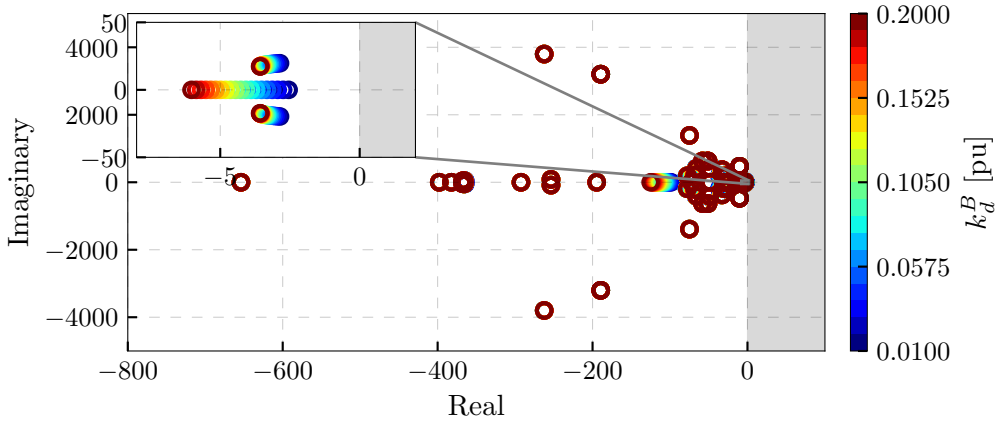

Figure 3.34: System poles with varying the droop gain of MMC3 k_d^B from 0.01 pu to 0.2 pu, while $k_d^A = 0.1$ pu.

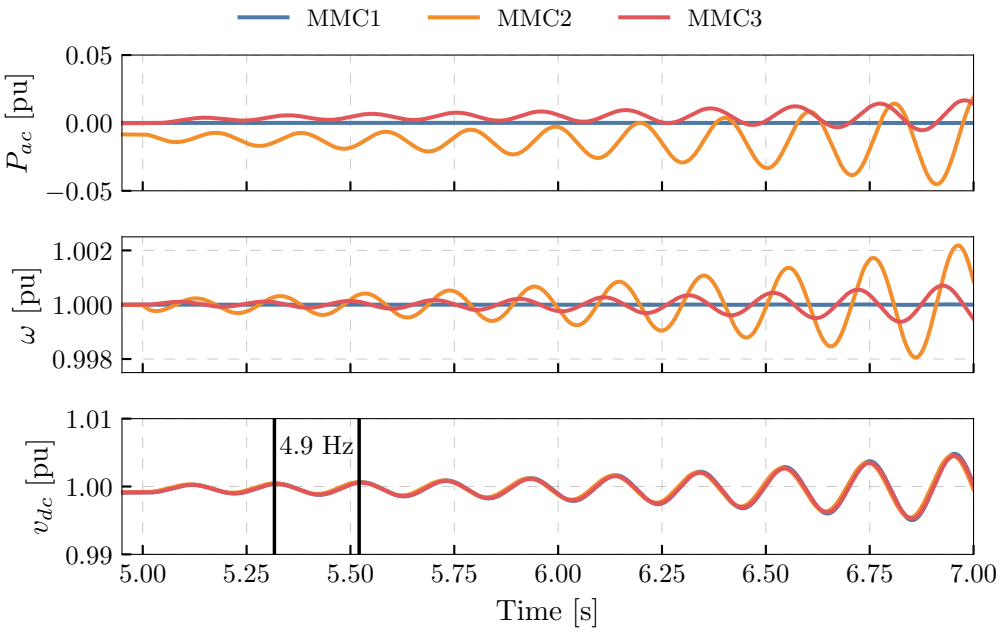

Figure 3.35: System response when k_d^A is changed to 0.02 pu at t=5 s and $k_d^B = 0.1$ pu.

MMC3, the steady-state power extracted from the AC grid by MMC3 is higher than MMC2, with a value of approximately 0.455 pu compared to 0.045 pu for MMC2.

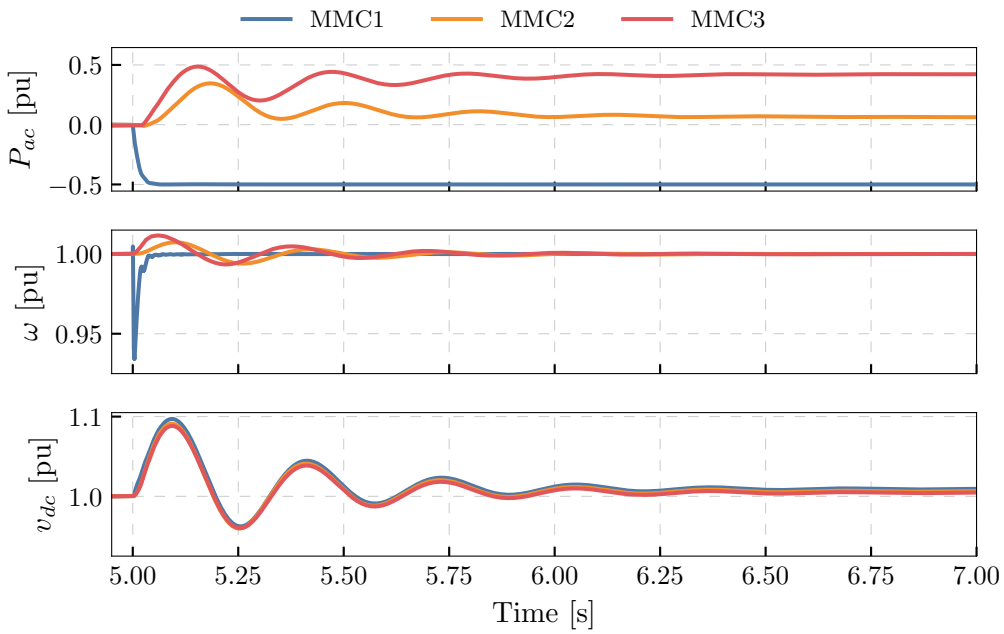

Figure 3.36: System response to a -0.5 pu step change in MMC3 AC power setpoint at t=5 s, with $k_d^B = 0.01$ pu and $k_d^A = 0.1$ pu.

3.7 Considerations on the design space for DC voltage droop with GFM control

Section 3.5.5 presented a design space for DC voltage droop control in multi-terminal DC grids with GFL-controlled MMCs. Given the considered three-terminal DC grid, it was shown that a dynamic lower limit on the droop gain exists when DC voltage droop Scheme A is used, while no such limit exists for Scheme B. However, when GFM control is introduced alongside DC voltage droop, as studied in this section, the design space needs to be revised.

The small-signal analysis and time-domain simulations in Section 3.6.4 showed that, when DC voltage droop Scheme A is combined with VSM-GFM control, the lowest feasible droop gain is increased compared to the GFL-controlled case. This is due to the interaction between the inertial response of the VSM-GFM control and the DC voltage droop, which can lead to low-frequency instability if the droop gain is lower (in our case below 0.03 p.u.). Scheme B combined with matching-GFM control does not exhibit such a limitation, since, intuitively, the lead action provided by the matching-GFM control increase the phase margin at the low frequency range.

Table 3.4 summarizes the differences between the two DC voltage droop schemes, with respective considerations for their design space.

3.8 Conclusion

This chapter has introduced the fundamental concepts of managing the DC voltage in multi-terminal DC grids through droop control mechanisms. First, the overall hierarchical control structure of the

Table 3.4: Design space considerations for DC voltage droop with GFM control

Aspect	**Droop Scheme A**	**Droop Scheme B**
Input/output	$\Delta v_{dc} \rightarrow \Delta P_{ac}$	$\Delta P_{ac} \rightarrow \Delta v_{dc}$
Stability limit	High-gain instability at low k_d	Stable with low k_d
Extreme value feasibility	$k_d = 0$ is not feasible	$k_d = 0$ is fixed DC voltage mode
GFM compatibility	Compatible with VSM-GFM	Compatible with matching-GFM

DC voltage control was presented, highlighting the objective of each control layer. Then, a focus on primary DC voltage control was given, since it is the first non-communication based reaction to grid disturbances. The static requirements for DC voltage droop control were presented, focusing on multi-segment droop as an efficient way to improve system security by exploiting the available capacity of the MMC stations. A description of different DC voltage droop segments was provided, along with the necessary consideration for their choice.

Then, the second part of the chapter focused on the dynamic aspects of DC voltage droop control. Two implementation options for DC voltage droop were presented, each adjusting a different control reference within the MMC control structure. The feasibility of co-existence of using these two droop control scheme in an MTDC grid was proven, with an additional focus on their small-signal stability limitations.

Finally, the interoperability of DC voltage droop control combined with grid-forming control strategies was studied. A review of the main GFM control strategies was provided, followed by an analysis of their combination with DC voltage droop control. Two combinations were studied: VSM-GFM control with DC voltage droop Scheme A, and matching-GFM control with DC voltage droop Scheme B. The dynamic interactions between the DC voltage droop and GFM controls were analyzed through small-signal analysis and time-domain simulations, revealing a risks of low-frequency instability when the droop gain of Scheme A is set too low. The chapter concluded with considerations on the design space for DC voltage droop control in MTDC grids with GFM-controlled MMCs.

4

Impact of passive elements on the dynamic performance and stability of MTDC grids

4.1 Introduction

The previous chapter focused on stability performance studies related to primary DC voltage control in MTDC grids. However, other factors can also significantly influence the dynamic interactions between the converters and the grid, as well as the overall stability of MTDC systems. In particular, passive elements such as DC reactors (DCRs) and the internal control strategies implemented in the MMC play crucial roles in shaping individual impedance characteristics, which in turn affect overall system stability.

This chapter first presents a literature review of the possible causes of small-signal stability in MTDC grids, with a focus on the impact of DCRs in Section 4.2. A simplified low-frequency DC-side impedance model of the MMC is derived in Section 4.3, which captures the influence of the outer control loop and the operating point on the impedance shape. Subsequently, a stability analysis is performed using the impedance-based stability criterion to identify the key factors affecting system stability within the considered frequency range.

In Section 4.4, the findings from the simplified model are validated using a more detailed MMC model in a standalone setup, allowing for a comprehensive analysis of the impact of DCR size, operating point, and control strategies on system stability. Furthermore, additional insights into the combined effects of these factors are provided through a stability map. In Section 4.5, the MMC impedance is reshaped by a dedicated active damping solution based on a lead compensator to mitigate instability issues caused by large DCR values. A case study of a four-terminal meshed DC grid is presented in Section 4.6 to demonstrate the impact of generalizing the standalone results under various operating conditions. Finally, the impact of DCRs on DC voltage support and coupling among converter stations is investigated in Section 4.7. The main conclusions of this chapter are summarized in Section 4.8.

4.2 Literature review

The problem of stability in MTDC grids has gained increasing attention, building on the literature review of stability studies presented in Chapter 1. One of the primary factors contributing to stability issues in MTDC grids is the presence of DC reactors (DCRs).

From a protection perspective, DC faults can trigger rapid current rises reaching several tens of kiloamperes within a few milliseconds, necessitating fast fault interruption through DC circuit breakers (DCCBs) [161,162]. DC reactors (DCRs), placed next to DCCBs or at converter terminals, are used to limit fault currents, and their sizing or placement depend on the protection philosophy, cable lengths, and grid configuration [14, 163, 164].

On the dynamic performance side, however, DCRs introduce additional dynamics that affect DC voltage stability and damping performance. Several studies have investigated such effects. In [165], large inductance values are shown to reduce the damping and controllability of the DC voltage at the low frequency-range. A dedicated outer-loop controller, called DC-PSS, is proposed to mitigate the instability. Similarly, in [166], an outer controller is proposed to modify the active power setpoint of the MMC according to the derivative of the DC voltage. In [167], DCRs were shown to limit the power transfer capability of the MMC, and the active power control loop is tuned to narrow its bandwidth in order to improve the DC voltage response. In [46], a Power-Flow Controller (PFC)-based active damping is introduced to improve the transient performance of a two-level-VSC-based DC grid with large DCRs. In recent multi-vendor related projects [14, 126], such impacts have been investigated, showing that the DCR may impact the dynamic response speed and damping of the DC voltage.

While these studies provide valuable insights into the impact of DCRs on small-signal stability, most of them rely on outer-loop controllers to mitigate their negative effects. However, research remains limited regarding inner control strategies that leverage the inherent controllability and available degrees of freedom of the MMC to address these issues. This is one of the contributions of this thesis, presented in detail in Section 4.5.

Beyond their impact on DC voltage damping, DCRs also influence the coupling between converter stations. In order to investigate the global MTDC grid behavior, previous studies model the DC grid by an equivalent DC-side capacitance [168, 169], an assumption that is valid particularly when cables are short and electrical distances are small. This assumption implies that the DC voltages of different MMC stations are dynamically coupled, even during fast transient responses.

This simplification has guided extensive research on the system-level impact of MMC internal energy control structures, from Uncompensated Modulation (UCM), which exhibits inherent DC-side capacitance, to Compensated Modulation (CM), where the internal energy must be explicitly regulated, significantly reducing the effective DC-side inertia [72, 169–171]. To compensate for this reduction, various virtual-capacitance strategies have been developed to enhance the DC voltage dynamic response [48, 108, 172].

However, with the introduction of DCCBs and associated large DCRs, this equivalent-capacitance assumption needs to be revisited to correctly assess the electrostatic inertial support between stations under realistic grid assumptions. To the best of the author's knowledge, the impact of DCRs on the coupling effects and the sharing of electrostatic inertia among converter stations has not been thoroughly investigated in the literature.

This motivates a broader reassessment of how DCRs shape the overall dynamic behavior of MTDC grids. Despite the aforementioned advances in the literature, a unified understanding of how DCRs

affect (i) DC voltage damping and (ii) the sharing of electrostatic inertia among converter stations is still lacking.

This chapter builds upon the existing literature by focusing on the frequency range where DCRs significantly influence grid dynamics. Previous research indicates that low-frequency interactions are dominated by passive grid elements and the converter's outer control loops, such as DC voltage control. Therefore, this chapter uses these findings as a starting point for the analysis in the following sections.

4.3 Low-frequency MMC DC-side impedance

From the literature review presented in Section 4.2, it is evident that DCRs impact the low frequency range of MMC dynamics. Therefore, this section focuses on deriving a simplified low-frequency DC-side impedance model of the MMC, which captures the influence of outer-loop control and operating point. This model serves as a basis for preliminary stability analysis using the impedance-based stability criterion. All findings are then verified using a more detailed MMC model in Section 4.4.

To derive this impedance, we begin with the Average Value Model (AVM) described in Chapter 2 [75,79]. Fig. 4.1 illustrates the DC-side MMC-AVM used for this analysis. Beyond the simplifications inherent in the AVM, we further simplify the model by neglecting AC-side dynamics; consequently, AC-side controls, such as the Phase-Locked Loop (PLL) and AC current control are neglected. A key distinction between the model in Fig. 4.1 and the one in Chapter 2 is that the DC current is not explicitly controlled, which is consistent with the UCM assumptions. In Fig. 4.1, L_{dc} and R_{dc} represent the equivalent DC-side inductance and resistance of the MMC, calculated as $L_{dc} = \frac{2}{3}L_{arm}$ and $R_{dc} = \frac{2}{3}R_{arm}$. The capacitor C_{mmc} represents the equivalent MMC capacitance, defined as $C_{mmc} = 6C_{arm}$.

The outer control behavior is represented by a controlled current source connected in parallel to C_{mmc}, as depicted in Fig. 4.2. In the general case, the MMC operates under DC voltage droop control[1].

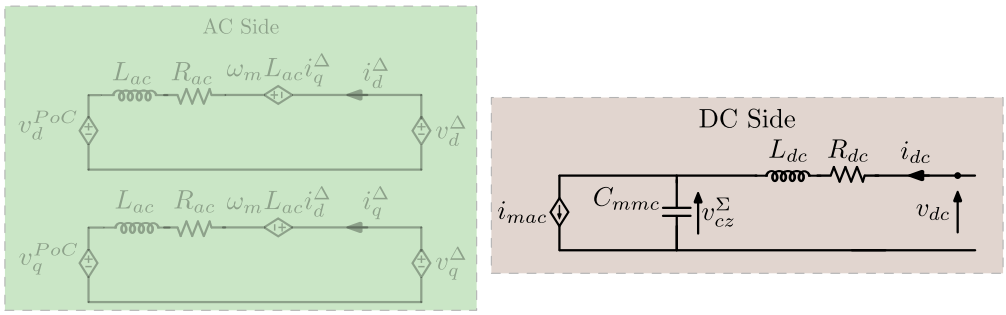

Figure 4.1: MMC-AVM model for low-frequency DC-side impedance derivation, simplified by neglecting AC-side dynamics.

The impedance of the simplified model in Fig. 4.2 is derived starting from the capacitor voltage dynamics. The voltage across the equivalent capacitor C_{mmc} is denoted by v_{cz}^{Σ} and satisfies

$$C_{mmc}\frac{dv_{cz}^{\Sigma}}{dt} = i_{dc} - i_{mmc}. \tag{4.1}$$

[1]Only DC voltage droop Scheme A is considered in this chapter.

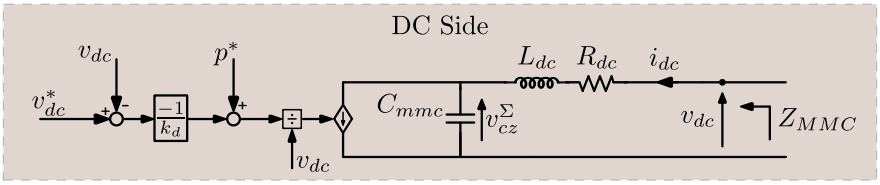

Figure 4.2: Outer control representation of the DC-side MMC-AVM.

where i_{mmc} is the current of the controlled source, defined as:

$$i_{mmc} = \frac{P}{v_{dc}} \tag{4.2}$$

Linearizing (4.2) around the operating point (v_{dc0}, P_0) yields:

$$\Delta i_{mmc} = \frac{\Delta P}{v_{dc0}} - \frac{P_0}{v_{dc0}^2}\Delta v_{dc} \tag{4.3}$$

The Δ terms represent perturbations around the respective operating points. Considering the DC voltage droop control,

$$\Delta P = \frac{1}{k_d}\Delta v_{dc} \tag{4.4}$$

where k_d denotes the droop gain. Inserting (4.4) into (4.3) gives

$$\Delta i_{mmc} = \left(\frac{1}{k_d v_{dc0}} - \frac{P_0}{v_{dc0}^2}\right)\Delta v_{dc} \tag{4.5}$$

Linearizing the capacitor voltage in (4.1) and taking into account Δi_{mmc} results in:

$$C_{mmc}\frac{d\Delta v_{cz}^{\Sigma}}{dt} = \Delta i_{dc} - \left(\frac{1}{k_d v_{dc0}} - \frac{P_0}{v_{dc0}^2}\right)\Delta v_{dc} \tag{4.6}$$

In the Laplace domain, this becomes:

$$sC_{mmc}\Delta V_{cz}^{\Sigma}(s) = \Delta I_{dc}(s) - \left(\frac{1}{k_d v_{dc0}} - \frac{P_0}{v_{dc0}^2}\right)\Delta V_{dc}(s) \tag{4.7}$$

From Kirchhoff's voltage law applied to Fig. 4.2, the relationship between v_{dc} and v_{cz}^{Σ} is given by:

$$v_{dc} = v_{cz}^{\Sigma} + R_{dc}i_{dc} + L_{dc}\frac{di_{dc}}{dt}. \tag{4.8}$$

Linearizing and transforming (4.8) into the Laplace domain yields

$$\Delta V_{cz}^{\Sigma}(s) = \Delta V_{dc}(s) - (R_{dc} + sL_{dc})\,\Delta I_{dc}(s). \tag{4.9}$$

Inserting (4.9) into (4.7) and solving for the DC-side MMC impedance

$$Z_{\mathrm{MMC}}(s) = \frac{\Delta V_{dc}(s)}{\Delta I_{dc}(s)}$$

yields

$$Z_{\text{MMC}}(s) = \frac{L_{dc}C_{mmc}s^2 + R_{dc}C_{mmc}s + 1}{sC_{mmc} + \frac{1}{k_d v_{dc0}} - \frac{P_0}{v_{dc0}^2}}. \tag{4.10}$$

This simplified model captures the low-frequency influence of the outer-loop control (P-mode and DC voltage droop) via k_d, the operating point P_0, and the MMC capacitance C_{mmc}. While it neglects higher-frequency dynamics and detailed internal controller parameters, its accuracy is sufficient for the preliminary stability studies presented in the following subsections.

4.3.1 Constant power mode operation

When the MMC operates in constant power mode ($k_d \to \infty$), the impedance in (4.10) simplifies to:

$$Z_{\text{MMC}}^{Pmode}(s) = \frac{L_{dc}C_{mmc}s^2 + R_{dc}C_{mmc}s + 1}{sC_{mmc} - \frac{P_0}{v_{dc0}^2}} \tag{4.11}$$

Equation (4.11) shows that $Z_{\text{MMC}}^{Pmode}(s)$ contains a real pole at $s = \frac{P_0}{C_{mmc}v_{dc0}^2}$. Given that C_{mmc} is a fixed design parameter and assuming v_{dc0} remains near its nominal values, the open-loop behavior is primarily determined by P_0. Specifically, in inverter mode ($P_0 > 0$), the pole is located in the right-half plane (RHP), introducing non-passive behavior. In rectifier mode ($P_0 < 0$), the pole moves to the left-half plane (LHP), contributing positive damping. This highlights the significant impact of the operating point on the converter behavior.

To evaluate the frequency range of validity for (4.11), a comparison is made with a frequency scan of a detailed MMC Arm Average Model (AAM) simulated in EMTP-RV. The MMC parameters are provided in Appendix B, and correspond to the low-frequency DC-side impedance parameters in (4.11). In the considered validation test, the operating point is set to $P_0 = 0$ p.u.

The frequency scan is conducted using the setup shown in Fig. 4.3, where a small AC voltage signal $v_p(t) = \hat{v}_p \sin(\omega_p t)$ is superimposed on the DC voltage source v_{dc}^{nom}, and the resulting DC current $i_{dc}(t)$ is measured at the DC-PoC. A total of 210 frequency scanning points are logarithmically spaced from 1 Hz to 1 kHz, with a perturbation amplitude of $\hat{v}_p = 0.01$ p.u. For each perturbation frequency ω_p tested, Fast Fourier Transform (FFT) is applied to the measured current signals to extract the magnitude and phase information and the DC-side admittance at that frequency is then calcuated as $Y_{\text{MMC}}(\omega_p) = \frac{I_{dc}(\omega_p)}{V_{dc}(\omega_p)}$. The DC-side impedance is obtained as the inverse of the admittance, i.e., $Z_{\text{MMC}}(\omega_p) = \frac{1}{Y_{\text{MMC}}(\omega_p)}$.

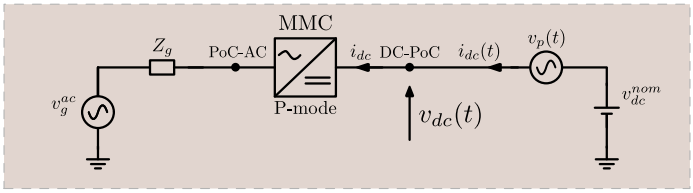

Figure 4.3: Test setup for frequency scan of the MMC-DC side impedance using the MMC-AAM model.

Fig. 4.4 shows the frequency response of both models. Comparing the two frequency responses, the following observations can be made:

- Up to around 25 Hz, the simplified model in (4.11) accurately captures the low-frequency behavior, which is dominated by the MMC capacitance.

- In the mid-frequency range (25 Hz to 100 Hz), discrepancies arise due to neglected AC current controller dynamics and CCSC in the low-frequency model. In the AVM, the series resonance around 55 Hz is a natural outcome of the LC components of the MMC DC side; however, in the detailed MMC-AAM model, this resonance is influenced by the circulating current dynamics and AC-side control loops.
- Beyond 100 Hz, where the dynamics are dominated by the DC side inductance $L_{dc} = \frac{2}{3}L_{arm}$, the low-frequency AVM provides a good representation of the MMC behavior.

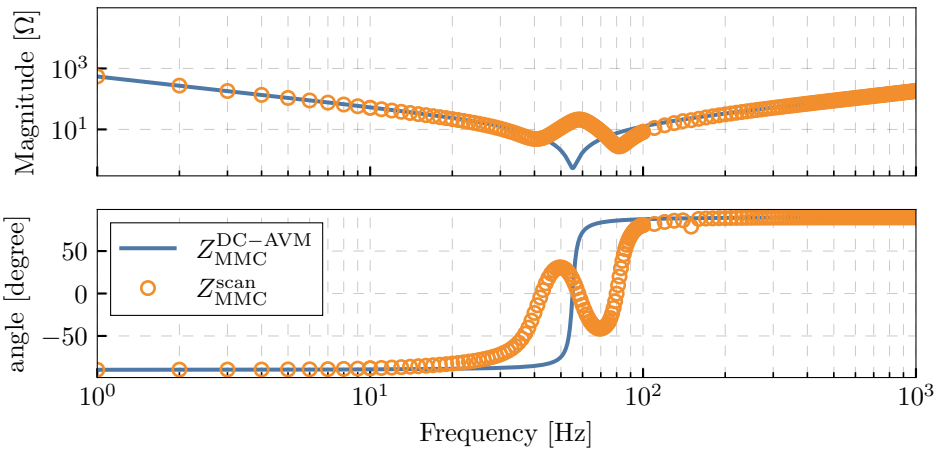

Figure 4.4: Comparison of the DC-side impedance frequency response between the DC-side AVM in constant power mode and a frequency scan of the MMC-AAM. The simplified model accurately captures low-frequency behavior up to around 25 Hz.

To perform a preliminary stability analysis on the DC-side MMC-AVM under constant P-mode operation considering the impact of the DC reactor, we add an inductance L_{dcr} connected in series with the MMC DC terminal, as shown in Fig. 4.5. The impedance-based stability criterion [50], previously outlined in Chapter 1, is applied, where the grid impedance is represented solely by the DC reactor: $Z_g(s) = sL_{dcr}$. The stability of the system is determined by the return ratio $\mathcal{L}(s) = \frac{Z_{\text{MMC}}(s)}{Z_g(s)}$, which is given by

$$\mathcal{L}(s) = \frac{L_{dc}C_{mmc}s^2 + R_{dc}C_{mmc}s + 1}{sL_{dcr}\left(sC_{mmc} - \frac{P_0}{v_{dc0}^2}\right)} \tag{4.12}$$

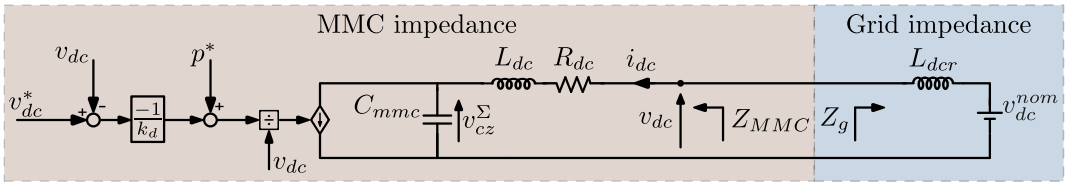

Figure 4.5: DC-side MMC-AVM with DC reactor for stability analysis using impedance-based criterion.

From (4.12), L_{dcr} influences the magnitude of $\mathcal{L}(s)$, while the phase is determined by the physical parameters and the operating point. This is illustrated in Fig. 4.6 for $P_0 = 1$ p.u. (rated inverter power). In this case, increasing L_{dcr} reduces the magnitude of $\mathcal{L}(s)$, shifting the gain crossover frequency to lower values where the phase is more negative due to the RHP pole. This reduction in phase margin increases the risk of instability.

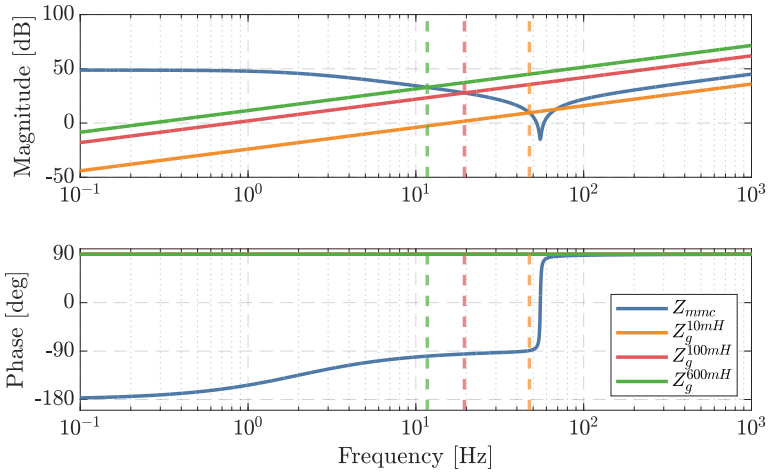

Figure 4.6: Impedance frequency response of the DC-side MMC AVM in constant power mode versus inductive grid impedance. Increasing L_{dcr} reduces the gain crossover frequency, decreasing the phase margin and potentially causing instability.

4.3.2 DC-voltage droop control

When the converter operates with DC voltage droop control, the impedance in (4.10) incorporates the droop gain k_d. For a positive droop gain, the typical practical case, the pole in (4.11) shifts leftward in the complex plane, thereby enhancing system stability. This effect is illustrated in Fig. 4.7, which compares the low-frequency impedance of the MMC-AVM in constant power mode against droop control ($k_d = 0.1$ p.u.) at $P_0 = 0$ p.u.. The results demonstrate that droop control significantly improves the phase response at low frequencies.

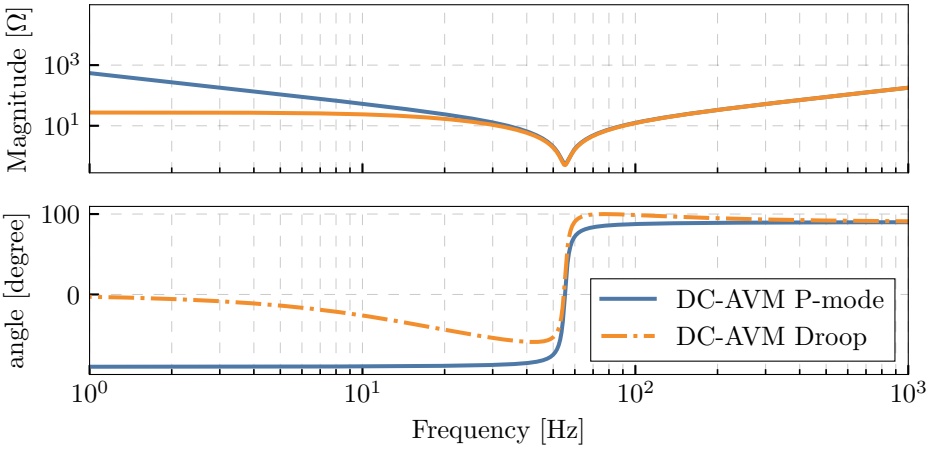

Figure 4.7: Comparison of the DC-side impedance frequency response between the MMC-AVM in constant power mode and with DC voltage droop control ($k_d = 0.1$ p.u.)

Under DC voltage droop control ($k_d < \infty$), the return ratio becomes:

$$\mathcal{L}(s) = \frac{L_{dc}C_{mmc}s^2 + R_{dc}C_{mmc}s + 1}{sL_{dcr}\left(sC_{mmc} + \frac{1}{k_d v_{dc0}} - \frac{P_0}{v_{dc0}^2}\right)} \tag{4.13}$$

A similar impact of L_{dcr} on the magnitude of $\mathcal{L}(s)$ is observed as in constant power mode. However, the phase behavior is now influenced by both the droop gain k_d and the operating point P_0. This is

depicted in Fig. 4.8, which shows the frequency response of $\mathcal{L}(s)$ for a droop gain of $k_d = 0.1$ p.u., considering $L_{dcr} = 600$ mH and $P_0 = 1$ p.u, a condition that rendered the P-mode converter unstable, see Fig. 4.6. The results shown in Fig. 4.8 indicate that for such a high DCR value, the phase margin remains positive, suggesting that droop control can effectively mitigate instability risks associated with large DCRs.

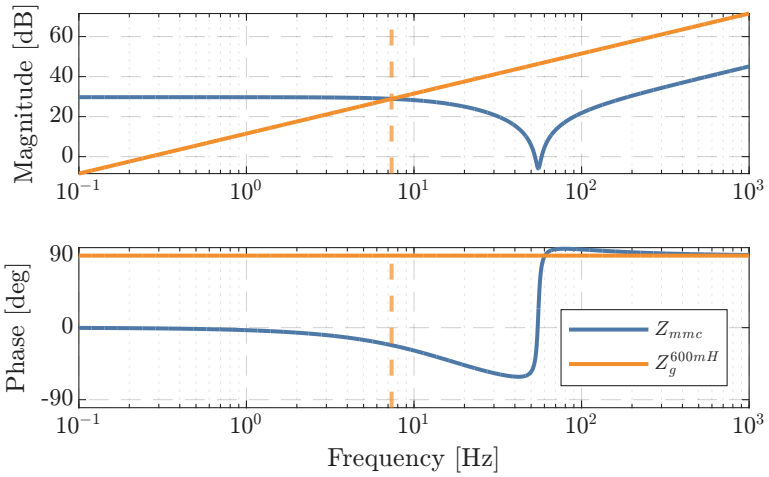

Figure 4.8: Impedance frequency response of the DC-side MMC AVM with DC voltage droop control versus the DCR impedance of 600 mH.

4.4 Full MMC impedance

In order to verify the analysis conducted in Section 4.3 using the simplified low-frequency MMC model, a test setup shown in Fig. 4.9 is presented, similar to the one in Fig. 4.5, but with the more detailed MMC-AAM representation explained in Chapter 2. The Arm Average Model (AAM) is utilized to represent each MMC arm by an equivalent capacitor. The control strucutre for the considered AAM in this section follows *control setting 1* with UCM and GFL operation mode (see Chapter 2). Unlike the simplified model, the AC-side control loops, including the PLL and AC current control, are included in the MMC-AAM. Moreover, the AC grid is represented by its Thévenin equivalent with an SCR of 5.

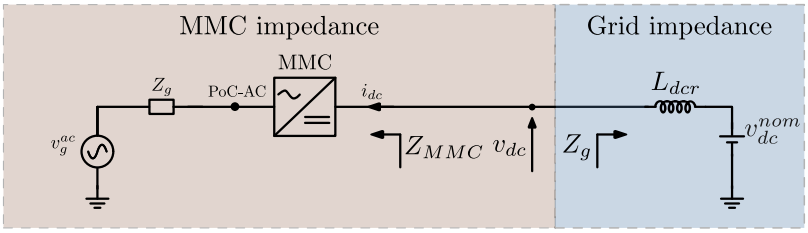

Figure 4.9: Standalone MMC test setup with DC reactor for validation of the low-frequency MMC impedance analysis and performing further studies.

The process of obtaining the MMC-DC side impedance is described here. The starting point is the state-space model of the MMC-AAM presented in Chapter 2. On the DC side, the MMC is connected to a DC voltage source, considered as an external input to the state-space model, and the DC current is

the output to be measured. The transfer function from the DC voltage to the DC current is obtained by linearizing the state-space model around the operating point. The DC-side impedance is then calculated as the inverse of this transfer function. This process is schematically depicted in Fig. 4.10.

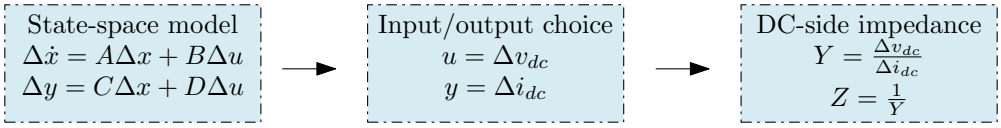

Figure 4.10: Process of deriving the DC-side impedance at the DC-PoC from the corresponding state-space representation.

Although the MMC-AAM was verified against time-domain simulations in Chapter 2, the derived small-signal impedance must also be compared to a frequency scan of the MMC simulation model using identical parameters. The results are shown in Fig. 4.11, where the MMC operates in constant power mode at $P_0 = 0$ p.u. The comparison shows good agreement between the two models in both magnitude and phase across the frequency range of 1 Hz to 1000 Hz, validating the accuracy of the derived impedance from the state-space model for further analysis. Comparing Figures 4.4 and 4.11, it can be observed that the MMC-AAM impedance captures additional dynamics in the mid-frequency range (25 Hz to 100 Hz) compared to the simplified AVM model.

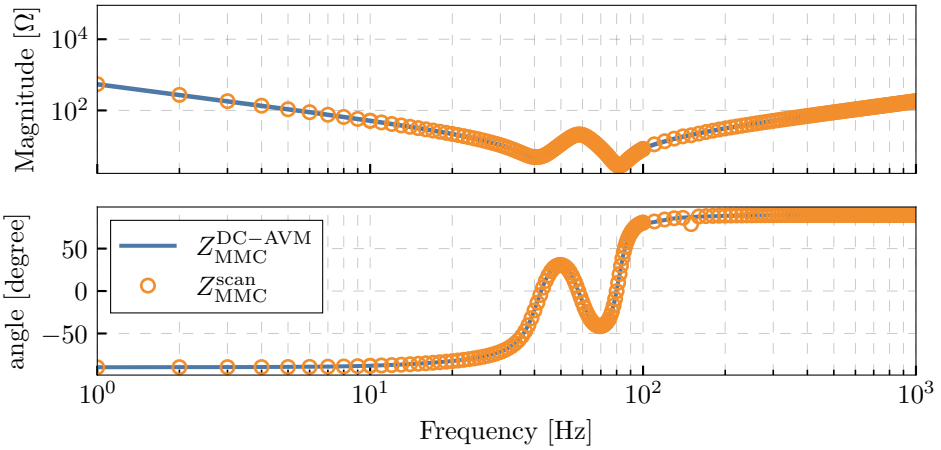

Figure 4.11: Comparison of the DC-side impedance frequency response between the MMC-AAM frequency scan and the derived MMC-DC side impedance from the state-space model. The results show good agreement in both magnitude and phase across the frequency range of 1 Hz to 1k Hz.

Similar to the analysis in Section 4.3, the return ratio $\mathcal{L}(s)$ is calculated using the derived MMC-DC-side impedance and the DCR impedance. The following subsections analyze the impact of various factors on the frequency response of $\mathcal{L}(s) = \frac{Z_{\text{MMC}}(s)}{sL_{dcr}}$, including the operating point, the DCR size, and the outer control strategies. The choice of analyzing the return ratio $\mathcal{L}(s)$ instead of the individual MMC impedance is due to the ability of the return ratio to directly reflect the system's stability margins, as per the impedance-based stability criterion.

4.4.1 Impact of the operating point

As discussed in Section 4.3.1, the operating point has a significant impact on the damping behavior at low frequencies. Fig. 4.12 shows the variation of the operating point P_0 from –1 p.u. to 1 p.u., while keeping the DCR value constant at 400 mH. The results indicate that increasing the power transfer

from the AC to the DC side (rectifier direction) increases the phase margin, thereby improving the damping response. In fact, when a P-mode station operates in inverter direction, a Constant Power Load (CPL) behavior can be observed on the DC side [173]. It can also be observed that the variation of the operating point has little impact on resonances in the mid- to high-frequency range of the return ratio, which is dominated by the internal dynamics of the MMC.

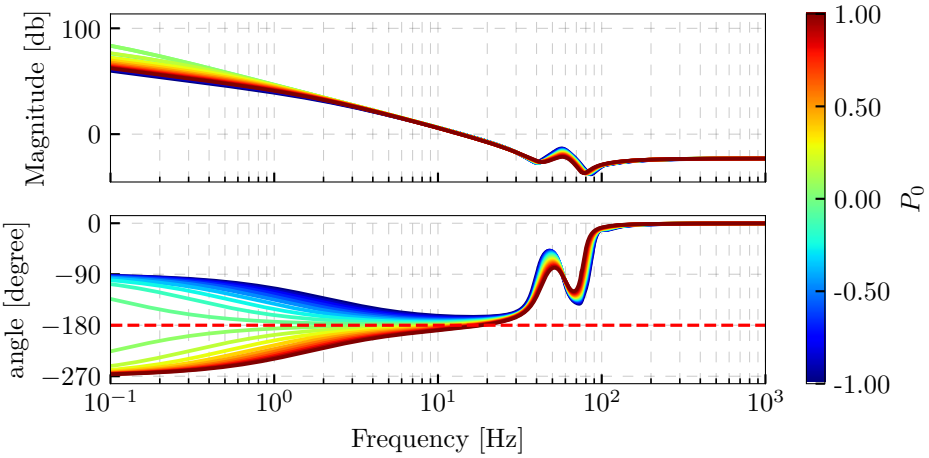

Figure 4.12: Frequency response of the return ratio for different MMC operating points P_0 with $L_{dcr} = 400$ mH. The phase margin decreases as the power increases in inverter direction (positive P_0).

4.4.2 Impact of the DCR size

Fig. 4.13 shows the frequency response of the return ratio $\mathcal{L}(s)$ for different values of L_{dcr} from 10 mH to 400 mH, considering the MMC operating in constant power mode with $P_0 = 1$ p.u, which represent the worst case condition obtained in the previous subsection. The results show that, as L_{dcr} increases, the magnitude of $\mathcal{L}(s)$ decreases, while the phase remains unchanged. This confirms the analysis conducted in Section 4.3. Above a critical value $L_{dcr}^{cr} = 198$ mH, the phase margin becomes negative, indicating that the system is unstable.

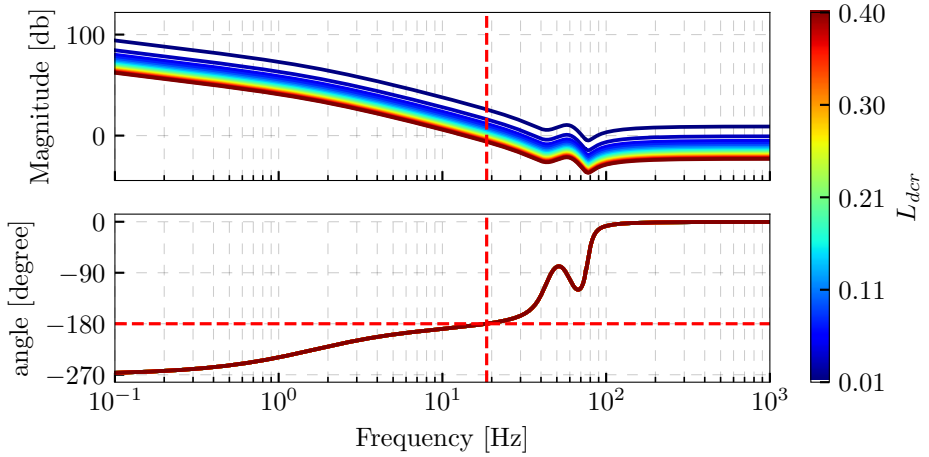

Figure 4.13: Frequency response of the return ratio for the standalone MMC operating in constant power mode $\mathcal{L}(s)$ for different values of L_{dcr}. Increasing L_{dcr} reduces the magnitude without affecting the phase, leading to instability above a critical value $L_{dcr}^{cr} = 198$ mH.

4.4.3 Impact of outer control

In this subsection, the effect of outer control variation on the return ratio frequency response is analyzed. Fig. 4.14 compares three different outer control strategies: constant power mode, DC voltage droop control with $k_d = 0.1$ p.u., and constant DC voltage control mode with a PI controller tuned to a closed-loop bandwidth of 10 Hz. The DCR value is set to 400 mH, and the operating point is $P_0 = 1$ p.u. The results indicate that both droop control and DC voltage control mode enhance the phase margin compared to constant power mode. This confirms that outer control strategies that regulate the DC voltage can effectively improve system damping in the presence of large DCRs.

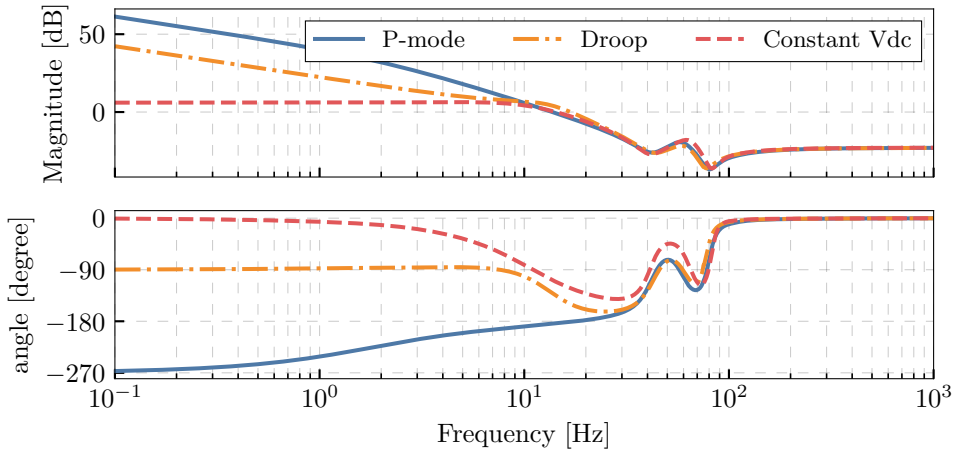

Figure 4.14: Frequency response of the return ratio for different outer control strategies with $L_{dcr} = 400$ mH and $P_0 = 1$ p.u. Both DC voltage droop control and DC voltage control mode improve the phase margin compared to constant power mode.

Next, the impact of DC voltage droop gain on the frequency response of the return ratio is shown in Fig. 4.15, with the droop gain k_d varying from 0.05 to 0.5 p.u./p.u (note that a lower droop gain means higher droop-control action). It can be seen that decreasing the droop gain further improves the phase margin of the system. As explained in Chapter 3, droop control modifies the power output of the MMC in response to variations in the DC voltage, which may not be desirable for a P-mode station, where the power output is expected to be equal to the setpoint. Nevertheless, DC voltage droop control can be used to mitigate the instability issues caused by the DCR and the inverter operating point. On the other hand, according to the conclusions drawn from Chapter 3, the droop gain should be selected carefully to avoid the high-gain instability that arises for extremely low droop gains. Therefore, such a trade-off should be considered when selecting the droop gain to mitigate the impact of DCRs.

4.4.4 Stability map

After analyzing the impact of the individual system parameters, whether control or passive elements, it is important to understand the combined impact of the DCR size and the operating point. For this, the operating point P_0 is varied from -1 to 1 p.u. for different values of L_{dcr} ranging from 10 mH to 400 mH , and the system stability is assessed using the phase margin. The resulting stability map is shown in Fig. 4.16, where the unstable region corresponds to a negative phase margin. It can be seen that, below the critical DCR value $L_{dcr}^{cr} = 198\,\text{mH}$, the system remains stable across all considered operation power values. However, as L_{dcr} increases, the stable operating region gradually narrows, particularly when the inverter power increases (positive P_0). This confirms that a larger DCR value

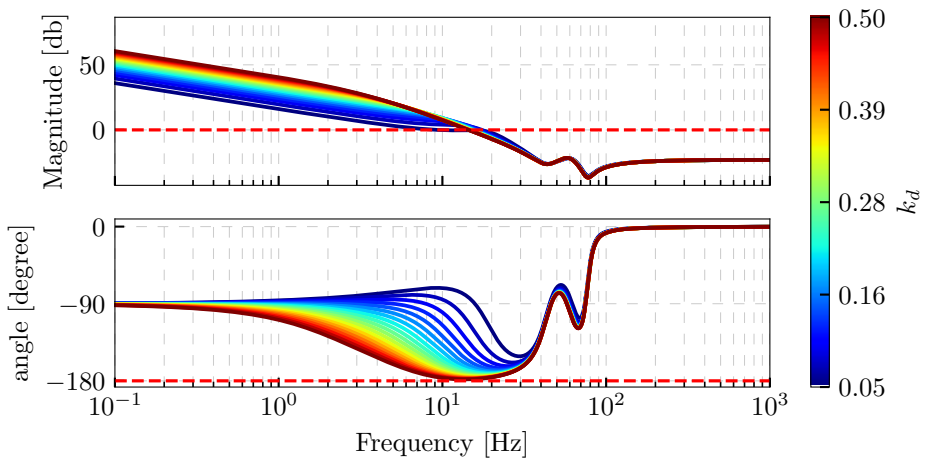

Figure 4.15: Effect of DC voltage droop control on the return ratio for $L_{dcr} = 400$ mH. A higher droop action (lower k_d) increases the phase margin and improves damping in the low-frequency range.

increases the risk of instability, especially when the MMC operates in inverter mode. It can also be observed that the system remains stable for negative P_0 values (rectifier mode), even for large DCR values. In fact, for the considered L_{dcr} values, the system remains stable for all operating points below the critical value $P_0^{cr} = 0.402$ p.u.

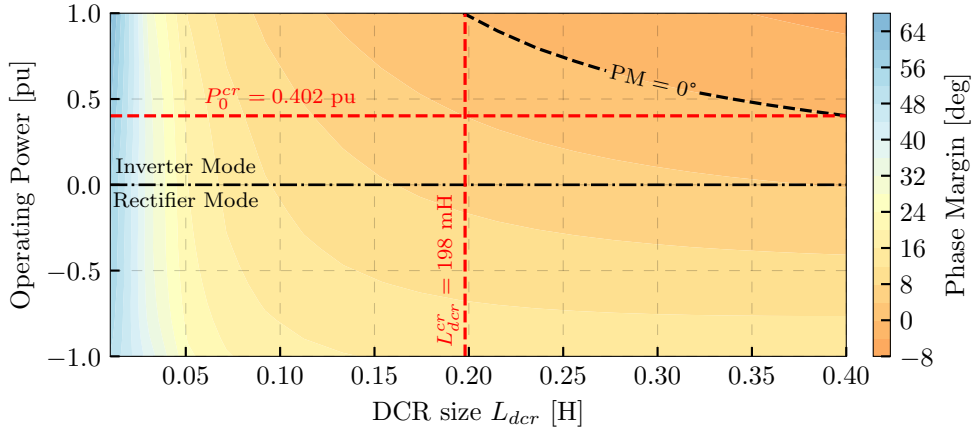

Figure 4.16: Stability map of the standalone MMC operating in constant power mode, showing the stable and unstable regions for different values of L_{dcr} and operating points P_0. Larger L_{dcr} values reduce the stable operating region, especially in inverter mode (positive P_0).

4.5 Mitigation solution for the impact of DCR

As established in the previous sections in this chapter, the instability arising from large DCR values is linked to a negative phase margin within the low-frequency range. To mitigate this instability, the MMC impedance can be reshaped in this range to introduce positive damping. As illustrated in Fig. 4.17, this is achieved by introducing a voltage source v_{lead} that reacts to variations in the DC current i_{dc}, effectively acting as a virtual impedance.

While DC voltage droop control serves as a form of proportional damping, where v_{lead} is proportional to DC current variations, the droop modifies the power output of the MMC. This shift in power may be undesirable for a station operating in P-mode. Consequently, an alternative approach is to

implement active damping via a lead compensator. This method improves the phase margin at the desired frequency range without significantly changing the steady-state response.

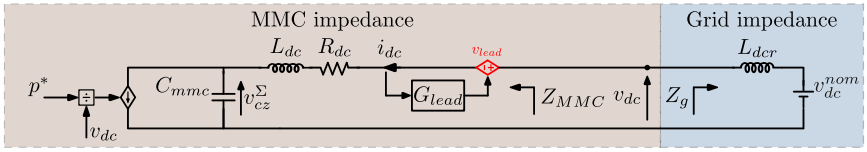

Figure 4.17: Principle of active damping: a lead compensator generates a voltage signal v_{lead} in response to DC current variations, which can be considered as a virtual impedance.

In this thesis, the damping action is applied to the zero-sequence circulating current i_z^{Σ}, because it is directly related to the DC current by $i_{dc} = 3i_z^{\Sigma}$. A lead compensator is added to the MMC control structure (Fig. 4.18) to improve the phase margin around the original crossover frequency. The transfer function of the lead compensator is given by:

$$G_{lead}(s) = \eta \frac{Ts + 1}{\alpha Ts + 1} \tag{4.14}$$

where η is the gain of the compensator. The lead compensator has a zero at $s = \frac{-1}{T}$ and a pole at $s = -\frac{1}{\alpha T}$.

For the considered L_{dcr} values between 10 mH and 400 mH, the phase crossover frequency of the original system is about 18.1 Hz (see Fig. 4.13). Following the approach in [42], achieving a 30° positive phase margin requires $\alpha = 0.0334$. The lowest gain crossover frequency within the studied range of L_{dcr} is 14 Hz, corresponding to $L_{dcr} = 400$ mH. Therefore, a value of $T = 15.9$ ms is chosen, which, with the above value of α, corresponds to a zero at 10 Hz and a pole at 30 Hz.

The gain η should be chosen sufficiently small to avoid adding an excessive DC offset to the MMC capacitor voltage v_{cz}^{Σ}, as the compensator output $v_z^{\Sigma *}$ directly affects it (See (D.9) in Appendix D). In this study, $\eta = 0.05$ is chosen, which leads to a phase margin of 23.39°, though below the 30° target, while adding a minimal v_{cz}^{Σ} offset.

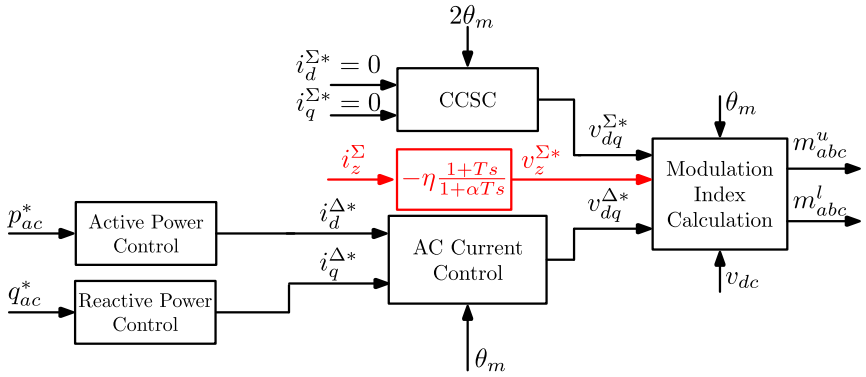

Figure 4.18: Integration of the lead compensator into the MMC control structure, acting on the zero-sequence circulating current i_z^{Σ}.

Fig. 4.19 shows the frequency response of the return ratio $\mathcal{L}(s)$ with and without the lead compensator, considering $L_{dcr} = 400$ mH and $P_0 = 1$ p.u, representing the worst case conditions for system stability (see Fig. 4.16). It can be seen that the lead compensator indeed improves the phase margin at the critical frequency range, leading to better damping characteristics. It can further be noted that the lead compensator does not alter either the low-frequency range (below 10 Hz) or the high-frequency

range (above 200 Hz). Unlike switching to DC voltage droop control mode, the lead compensator does not affect the steady-state DC voltage response.

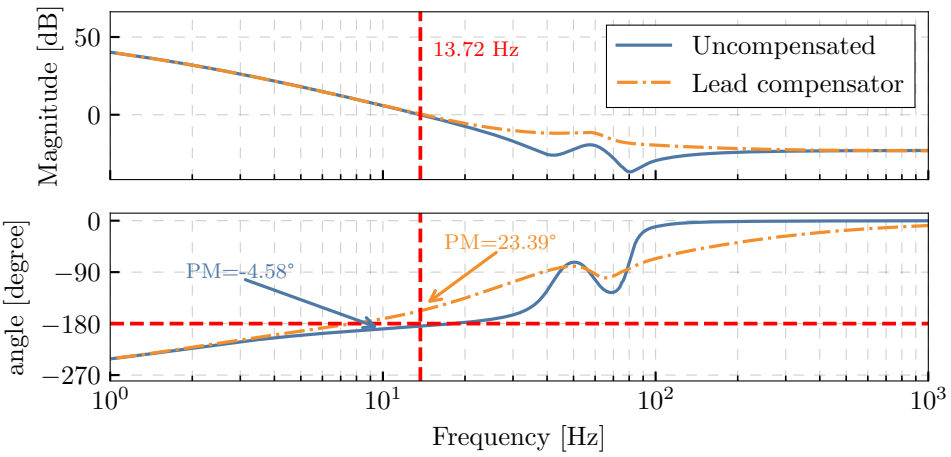

Figure 4.19: Return ratio with and without lead compensation for $L_{dcr} = 400$ mH and $P_0 = 1$ p.u. Lead compensation improves the phase margin from -5° to 28°, thus stabilizing the system.

A time-domain simulation is conducted to verify the performance of the lead compensator. It compares the response of the MMC in the test setup shown in Fig. 4.9 under a step DC voltage disturbance of 0.05 p.u., without and with the lead compensator applied. The results presented in Fig. 4.20 demonstrate that the lead compensator effectively stabilizes the system. The DC voltage response remains stable, even when $L_{dcr} = 400$ mH.

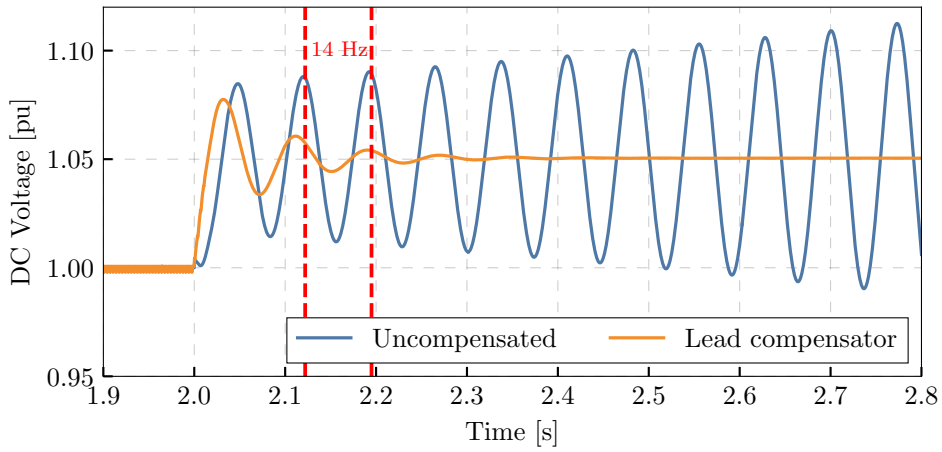

Figure 4.20: DC voltage response of the MMC to a step disturbance comparing uncompensated and lead-compensated systems with $P_0 = 1$ p.u. and $L_{dcr} = 400$ mH.

4.6 Case study 1: small-signal stability analysis of a four-terminal DC grid with DCRs

In this section, small-signal stability is assessed for a four-terminal DC grid with DCRs at the MMC terminals, shown in Fig. 4.21. The objective is to validate the findings from the previous sections in a full MTDC system. A symmetrical monopolar configuration is considered. Each of the four MMCs is connected to an AC grid with an SCR of 5, representing a strong AC grid. The MMC parameters are

the same as in Appendix B. Four cables of length 100 km interconnect the MMC stations, creating a meshed topology. The DCRs are placed at the terminals of the MMC stations.

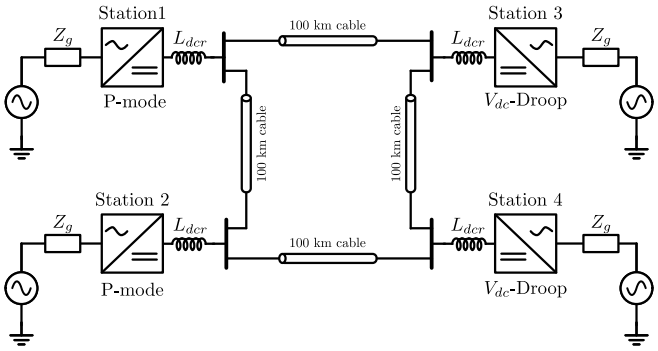

Figure 4.21: Four-terminal meshed DC grid under study.

As explained in Chapter 2, all subsystem state-space models are first obtained individually and then interconnected by their respective inputs and outputs to form the global state-space model. The small-signal model of the 4TDC grid is subsequently obtained by linearizing the system around the operating point, which is defined by the power flow and the converter control mode.

In this case study, detailed modeling of the offshore wind-side dynamics is not included, as the objective is to focus on DC-side dynamics induced by the presence of large DCRs. In addition, the four MMC stations follow *control setting 1*, with GFL and UCM operation modes. The DC cable model follows the π-model representation, as explained in Appendix E [142].

Four scenarios are defined to analyze the impact of the operating point, the control mode, and the lead compensator on the small-signal stability of the 4TDC grid, defined as:

- Scenario 1: Operating point 1 with St1 and St2 in inverter mode (Table 4.1).
- Scenario 2: Operating point 2 with St1 and St2 in rectifier mode (Table 4.2).
- Scenario 3: Operating point 1 but with St2 switched to DC voltage droop control.
- Scenario 4: Operating point 1 but with lead compensator applied to St1 and St2.

Table 4.1: Operating point 1 of the 4T DC grid.

Converter	Control Mode	v_{dc}^{set} [pu]	p_{ac}^{set} [pu]
Station 1	P-mode (inverter)	N/A	0.95
Station 2	P-mode (inverter)	N/A	0.95
Station 3	DC voltage droop	1	-0.925
Station 4	DC voltage droop	1.007	-1

4.6.1 Impact of the DCR size

To analyze the impact of the DCR size on the small-signal stability of the 4TDC grid, the system eigenvalues are computed for different DCR values under under the operational scenarios defined above.

Table 4.2: Operating point 2 of the 4T DC grid.

Converter	Control Mode	v_{dc}^{set} [pu]	p_{ac}^{set} [pu]
Station 1	P-mode (rectifier)	N/A	-0.95
Station 2	P-mode (rectifier)	N/A	-0.95
Station 3	DC voltage droop	1	0.855
Station 4	DC voltage droop	0.996	1

Considering Scenario 1, the eigenvalues of the linearized 4TDC grid are plotted as a function of the DCR value, based on operating point 1 as defined in Table 4.1. The results are shown in Fig. 4.22, where the DCR values for all stations are varied from 10 mH to 500 mH.

It can be observed that, as the DCR values increase, a pair of eigenvalues moves toward the right-half plane (RHP). When the DCR value exceeds 358 mH, these eigenvalues move into the RHP, indicating that the system becomes unstable. The natural frequency of these unstable eigenvalues is 13.6 Hz, which is close to the frequency where instability was observed in the simplified MMC model in Section 4.3 and verified by the standalone MMC behavior in Section 4.4.

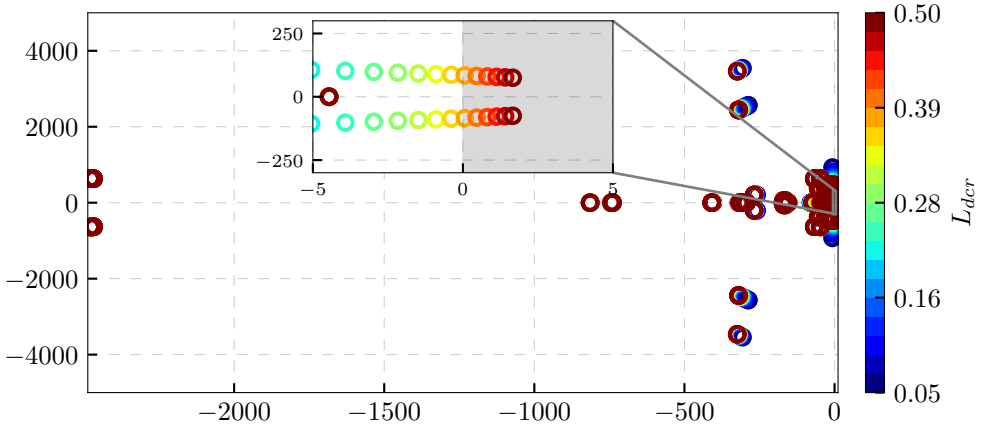

Figure 4.22: Eigenvalues of the 4T DC grid at operating point 1 with St1&2 in inverter mode, showing instability as DCR values increase.

For a DCR value of 400 mH (unstable value), a participation factor analysis is performed to find that the unstable eigenvalues (λ_{71} and λ_{72}) are mainly influenced by the states i_{dcr1}, i_{dcr2}, v_{cz1}^{Σ}, and v_{cz2}^{Σ}, which correspond to the DC current of Stations 1 and 2, and the zero-sequence components of the capacitor voltages of Stations 1 and 2, respectively. This confirms that the instability is primarily driven by the interaction between the DCRs and the MMC stations operating in P-mode. The participation factor results are illustrated in Fig. 4.23.

For scenario 2, the operating point is defined by Table 4.2, where the P-mode MMC stations (St1&2) operate in rectifier mode. Fig. 4.24 shows that, with the same range of DCR variation, all the system eigenvalues lie on the LHP, which is a sufficient condition for system stability. This shows the considerable impact of the operating point on the system dynamics, especially when large DCRs are present in the grid. It should be noted that this operational scenario is more likely to occur in practical applications, as P-mode stations are generally expected to operate in rectifier mode to transfer power from the offshore grid to the MTDC. While the system remains stable for all DCR values in

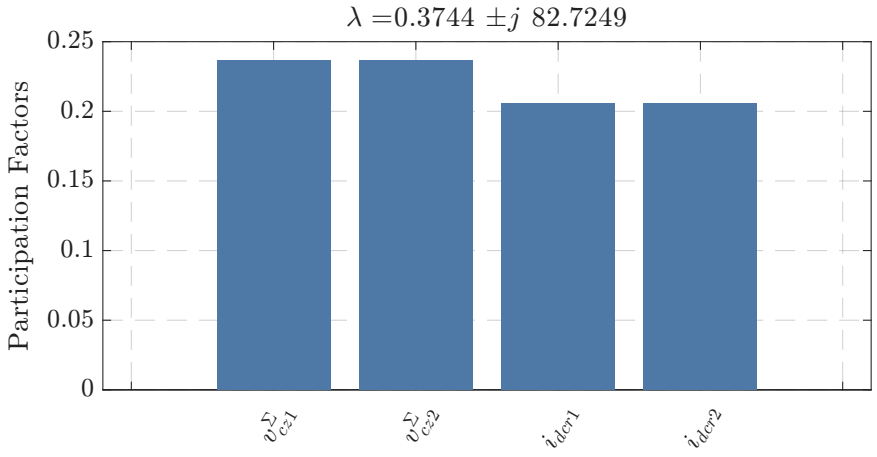

Figure 4.23: Participation factor analysis of the unstable eigenvalues of the 4TDC grid at operating point 1, showing the main contributing states.

this scenario, it is observed that the damping of the critical eigenvalues decreases as the DCR values increase, indicating a trend toward reduced stability margins.

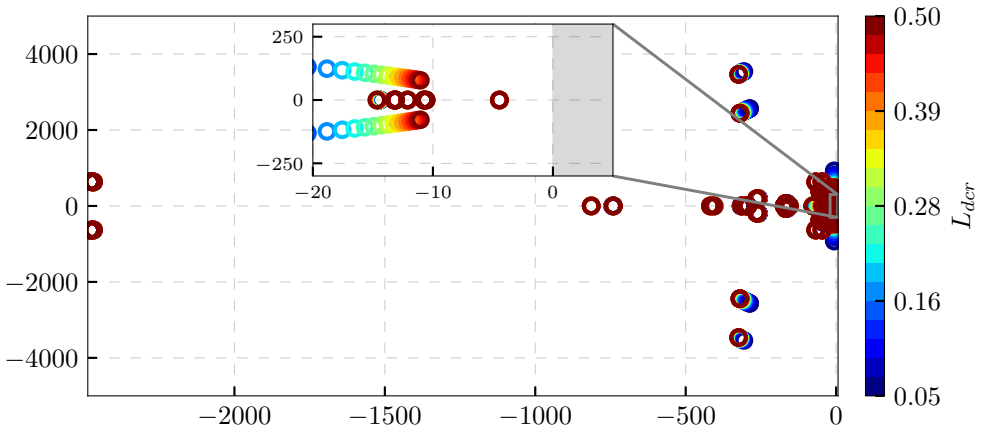

Figure 4.24: Eigenvalues of the 4T DC grid at operating point 2 with St1&2 in rectifier mode, the system remains stable for all DCR values.

Scenario 3 considers the impact of DC voltage droop control on the system dynamics, the closed-loop system poles are plotted in Fig. 4.25 for the case where the system is at operating point 1 but with St2 control mode switched to DC voltage droop. The results indicate that the system remains stable for all values of DCR. This demonstrates that the DC voltage droop control introduces positive damping to the system.

Finally, the impact of the active damping provided by the proposed lead compensator is analyzed by applying it to St1 and St2 at operating point 1. The parameters of the compensator correspond to the design criterion in Section 4.5. The results presented in Fig. 4.26 show that the lead compensator effectively mitigates the instability caused by the large DCR values, even with St1 and St2 operating in inverter mode, with no poles moving to the RHP.

The above small-signal analysis of the 4TDC grid is consistent with the analytical predictions conducted in Section 4.3 and the standalone MMC results in Section 4.4. Moreover, the same design parameters of the lead compensator presented in Section 4.5 are utilized on the 4TDC grid case, showing the effectiveness of the active damping controller.

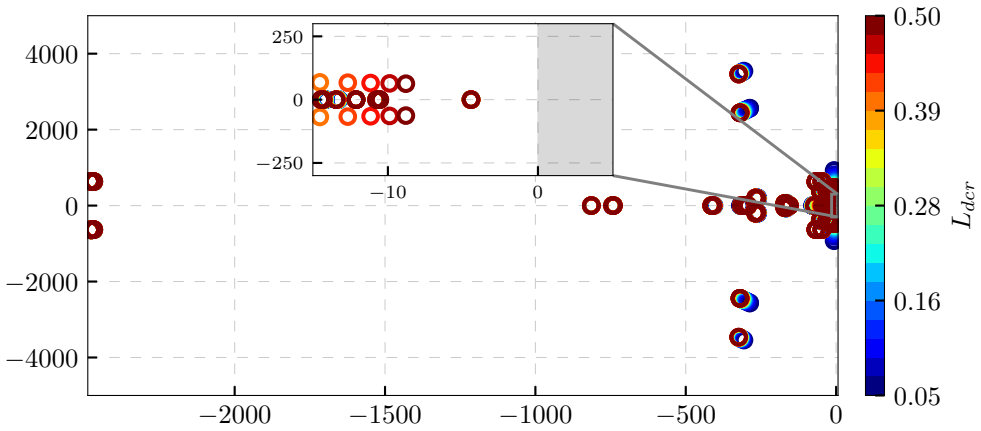

Figure 4.25: Eigenvalues of the 4T DC grid at operating point 1 but with St2 switched to DC voltage droop control, showing system stability for all DCR values.

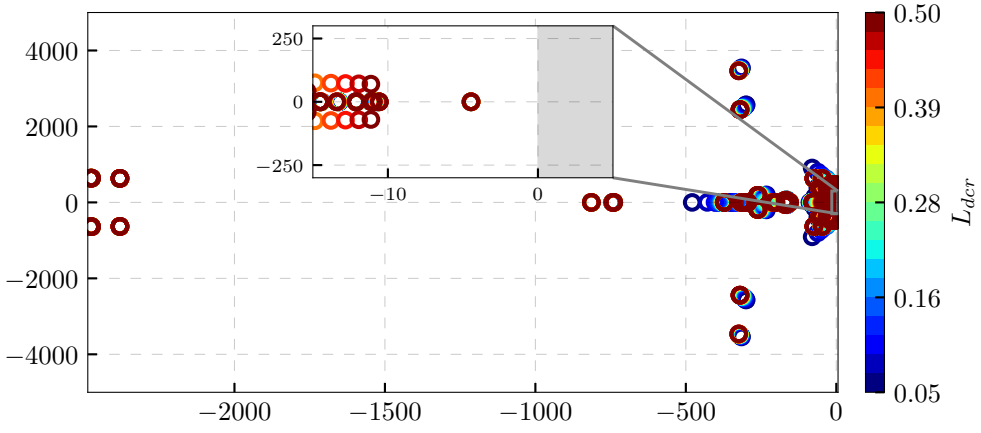

Figure 4.26: Eigenvalues of the 4T DC grid at operating point 1 with lead compensator applied to St1&2, showing system stability for all DCR values.

4.6.2 Time-domain validation of the 4T DC grid

Time-domain simulations are conducted in EMTP-RV to verify the small-signal analysis results in Section 5.2. The same control and physical parameters are utilized for consistency. The AAM is used for the MMC stations. The wideband cable models are used to represent the DC cables. In all simulations in this part, the DCR values are set to 400 mH for all stations, which is higher than the critical value obtained in the small-signal analysis of the 4TDC grid, i.e. 358 mH. The same operational scenarios defined in the small-signal analysis are considered here.

The first scenario considers operating point 1. From Fig. 4.27, growing oscillations can be observed in the DC voltage of St1 and St2. The oscillation frequency is about 14 Hz, which is close to the natural frequency of the unstable eigenvalues obtained in the small-signal analysis (13.6 Hz). It can also be seen that the growing oscillations are reflected in the DC voltages of St3 and St4, but slowly growing compared to St1 and St2, which is expected since St3 and St4 operate in droop control mode providing better damping compared to P-mode.

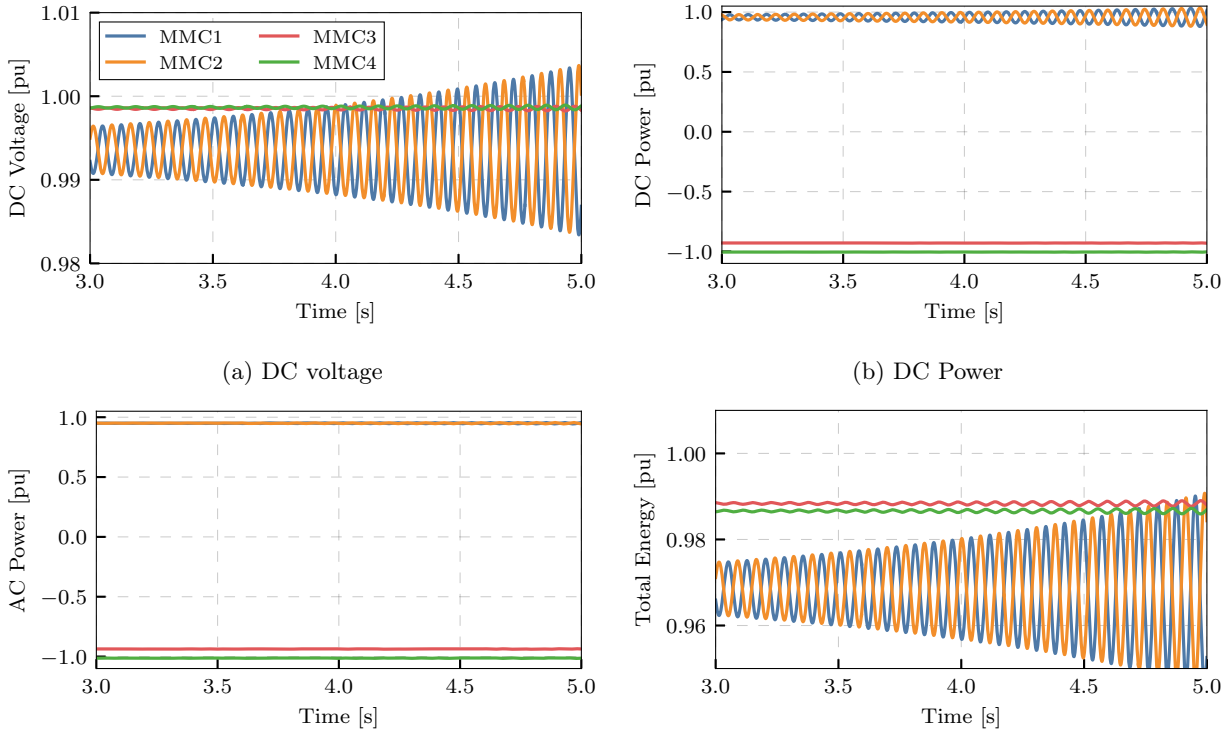

(a) DC voltage

(b) DC Power

(c) AC Power

(d) Total Energy

Figure 4.27: Time-domain response of the 4TDC grid considering Case 1; St1 and St2 in inverter mode, with 400 mH DCRs.

In Fig. 4.28, at operating point 2 but with St1 and St2 in rectifier mode, the system remains stable after a 500 MW step decrease in St1 AC power setpoint at $t = 4\,\text{s}$. While all DC voltages reach steady state, St1 and St2 (P-mode) exhibit more oscillations compared to St3 and St4 (droop control), indicating that, regardless of the operating point, the DC voltages of P-mode stations are generally less damped than those of stations operating under DC voltage droop control.

In Fig. 4.29, for operating point 1, DC voltage droop is activated at $t = 5\,\text{s}$. It can be observed that switching St2 control mode from constant P-mode to DC voltage control restores system stability. It can also be seen that the steady-state operating point is slightly changed. This behavior is expected since DC voltage droop control changes the active power output of the station.

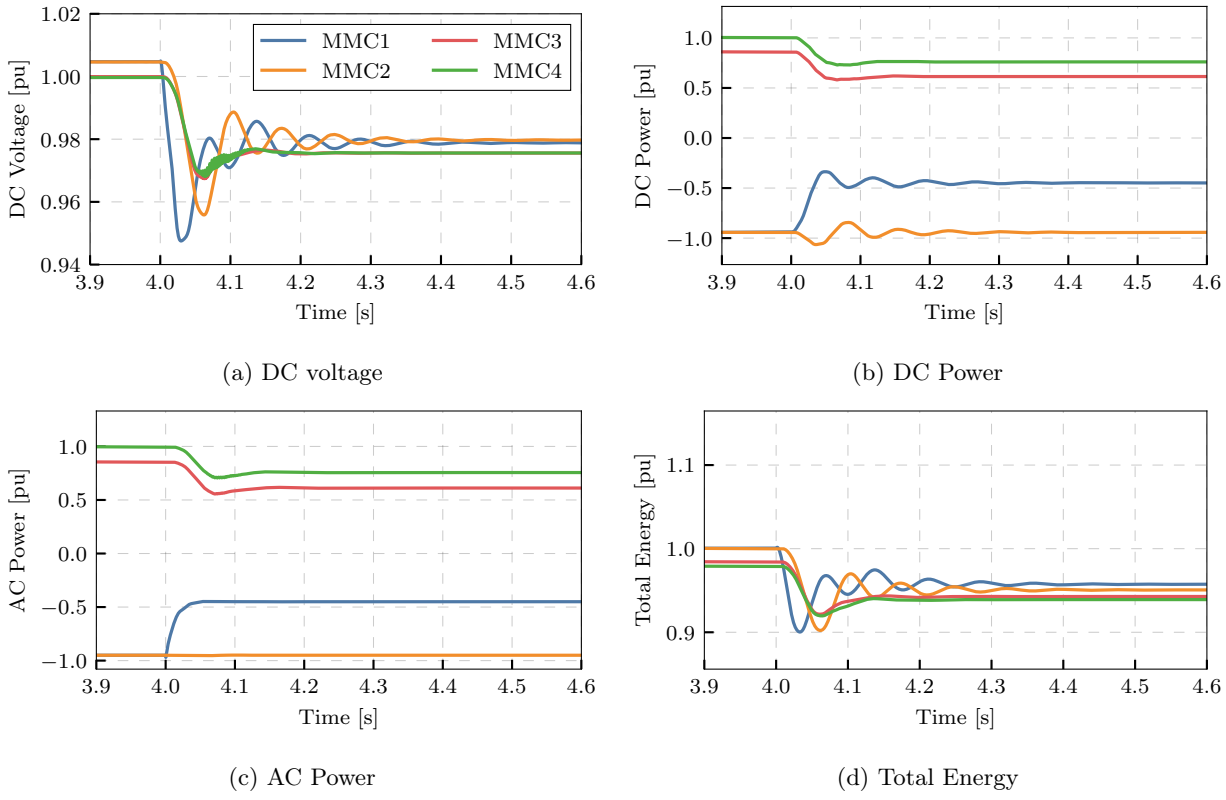

(a) DC voltage

(b) DC Power

(c) AC Power

(d) Total Energy

Figure 4.28: Time-domain response of the 4TDC grid considering Case 2; St1 and St2 in rectifier mode, with 400 mH DCRs.

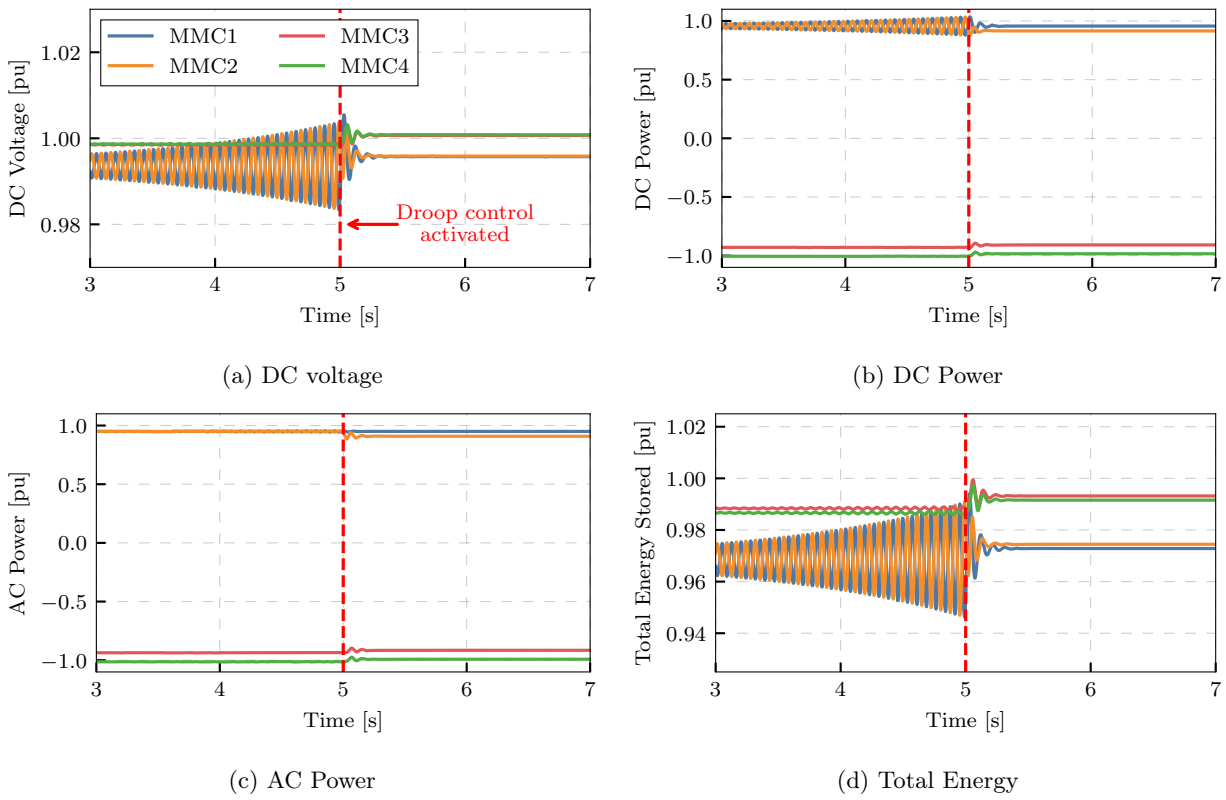

(a) DC voltage

(b) DC Power

(c) AC Power

(d) Total Energy

Figure 4.29: Time-domain response of the 4TDC grid considering Case 3; droop control is applied to St2 at $t = 5$ s, with 400 mH DCRs.

In Fig. 4.30, for operating point 1, applying the lead compensator to St1 and St2 at $t = 5$ s stabilizes the system. The DC voltage responses exhibit well-damped behavior, even with St1 and St2 operating in inverter mode, confirming the effectiveness of the lead compensator. We also observe that after applying the lead compensator, the steady-state behavior of the DC voltages of St3 and St4 remains unchanged; this verifies that the damping controller does not alter the steady-state DC voltage response. However, a small offset can be observed in the total energy of St1 and St2, which is attributed to the DC component introduced by the lead compensator output, as discussed in Section 4.5.

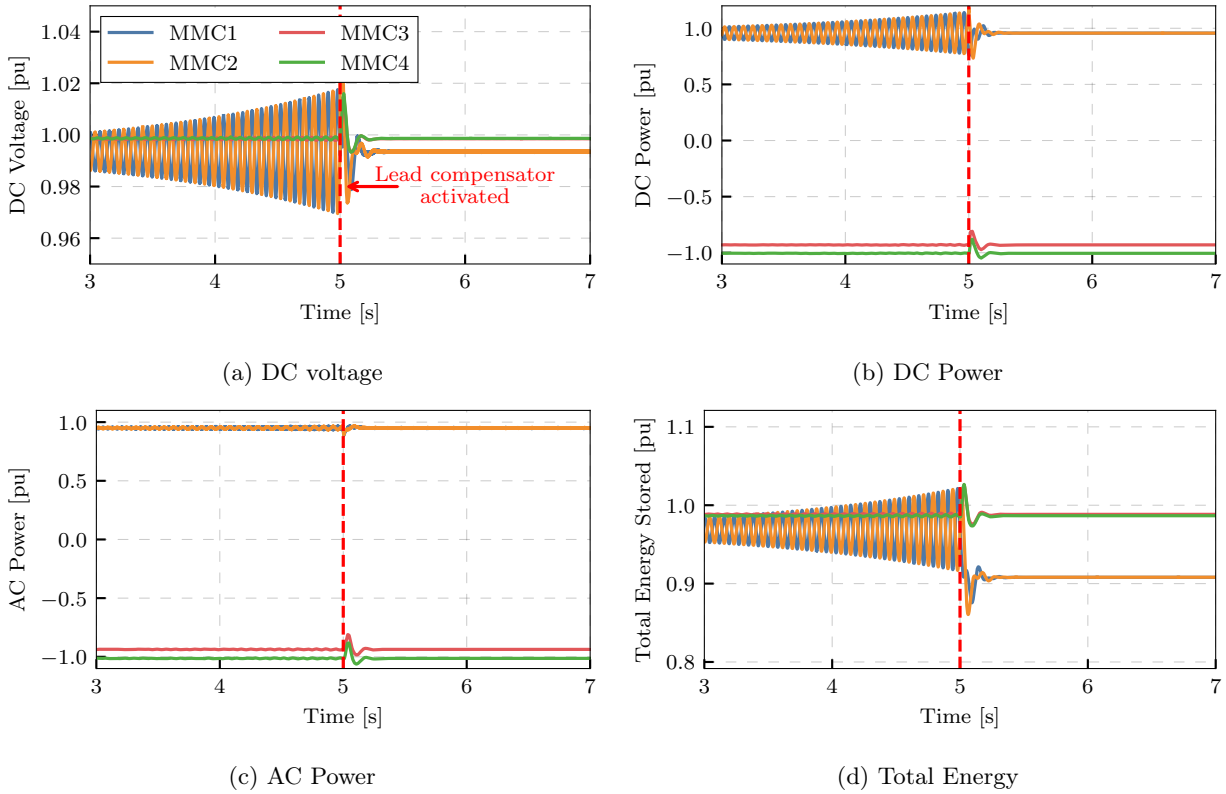

(a) DC voltage

(b) DC Power

(c) AC Power

(d) Total Energy

Figure 4.30: Time-domain response of the 4TDC grid considering Case 4; lead compensator is applied to St1 and St2 at $t = 5$ s, with 400 mH DCRs.

Table 4.3 summarizes the discussed mitigation measures to the stability issues introduced by the DCRs in the 4T DC grid, with the respective practical considerations for each solution.

4.7 Case study 2: DCR impact on DC voltage support in MTDC grid

In this section, we examine another implication of introducing DCRs in DC grids, specifically, their impact on converter coupling and DC voltage support. We consider the same 4T DC grid presented in Section 4.6, using operating point 2 as defined in Table 4.2, where St1 and St2 operate in rectifier mode. We now consider two different internal MMC control structures, namely *control setting 1* and *control setting 2*, previously defined in Chapter 2. In *control setting 1*, UCM is utilized, where the circulating currents are suppressed and no explicit energy regulation is applied. In *control setting 2*, CM is applied, where the circulating currents are used to regulate the internal energy of the MMC, limiting the inherent capacitive support provided by the MMC submodule capacitances.

One of the motivations behind the choice between these two control settings is their influence on

Table 4.3: Mitigation measures to the stability issues introduced by DCRs in the 4T DC grid, with practical considerations for each solution.

Mitigation solution	Practical considerations
Increasing the number of DC voltage droop stations	• Adding more droop stations can enhance damping and improve dynamic stability. • For small and sparse grid configurations, the number of droop-controlled stations is often dictated by the system's steady-state voltage regulation needs. • Less flexibility in DC grid planning.
Operating P-mode stations only in rectifier mode	• For offshore stations, rectifier operation is realistic. • For onshore stations, however, constraining P-mode operation to rectifier mode imposes limitations on power flow direction. • Proper system-level design is needed.
Active damping by lead compensation	• Offers improvement in system damping without restricting operational flexibility. • Requires careful design and testing to evaluate the impact on other transient response considerations (e.g. high-frequency dynamics, system response time).

the maximum transient DC voltage deviation following a disturbance. Our objective is to investigate whether the presence of DCRs affects this metric and whether the different stations exhibit similar dynamic behavior. To analyze this impact, four case scenarios are considered and described below, with Stations 3 and 4 controlling the DC voltage and using *Control setting 1* in all cases.

- Case 1: St1&2 in UCM, with no DCRs.
- Case 2: St1&2 in CM, with no DCRs.
- Case 3: St1&2 in UCM, with DCRs of 300 mH.
- Case 4: St1&2 in CM, with DCRs of 300 mH.

The transfer function used for the frequency response evaluation is defined from the AC power reference of St1 to the DC voltages at each station. Fig 4.31 shows that, for cases 1 and 2, the frequency responses of the four DC voltages in the grid are quite similar. This indicates that the DC voltage at each station is, in transient, similarly sensitive to changes in the AC power reference of St1; this is due to the short electrical distances between them, as the stations are interconnected using 100 km cables. However, higher resonant peaks are observed in the high-frequency range (above 100 Hz) in Case 2 compared to Case 1, suggesting that larger DC voltage excursions are expected when St1 and St2 operate in CM mode.

When DCRs are introduced in Cases 3 and 4, the frequency response of St1 voltage exhibits a different behavior compared to the other stations, indicating that the remaining stations are less responsive to the disturbance introduced by St1, as shown in Fig. 4.32. It is also clear that the high-frequency responses of St3 and St4 are significantly worse, exhibiting higher resonant peaks, when CM is used (Case 4) compared to UCM (Case 3). This suggests that the decoupling effect among converter DC voltages caused by the introduction of DCRs worsens the DC voltage response when CM is utilized.

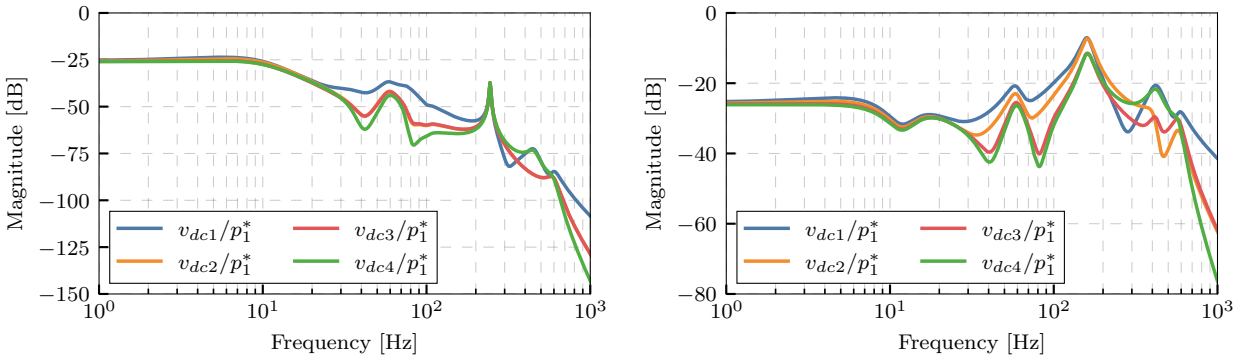

(a) Case 1 (b) Case 2

Figure 4.31: Magnitude frequency response from AC power reference of St1 to DC voltages at each station, for Cases 1 and 2. St1 and St2 in UCM and CM respectively, with no DCRs in the grid.

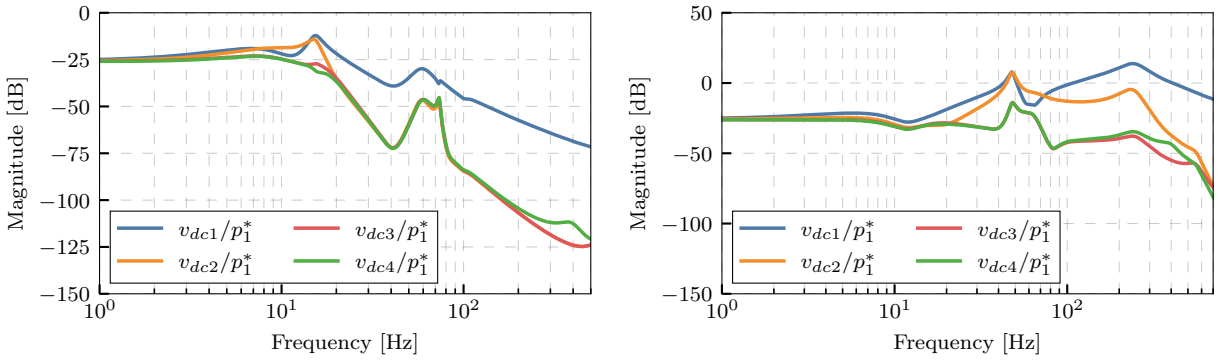

(a) Case 3 (b) Case 4

Figure 4.32: Magnitude frequency response from AC power reference of St1 to DC voltages at each station, for Cases 3 and 4. St1 and St2 in UCM and CM respectively, with DCRs of 300 mH at each station.

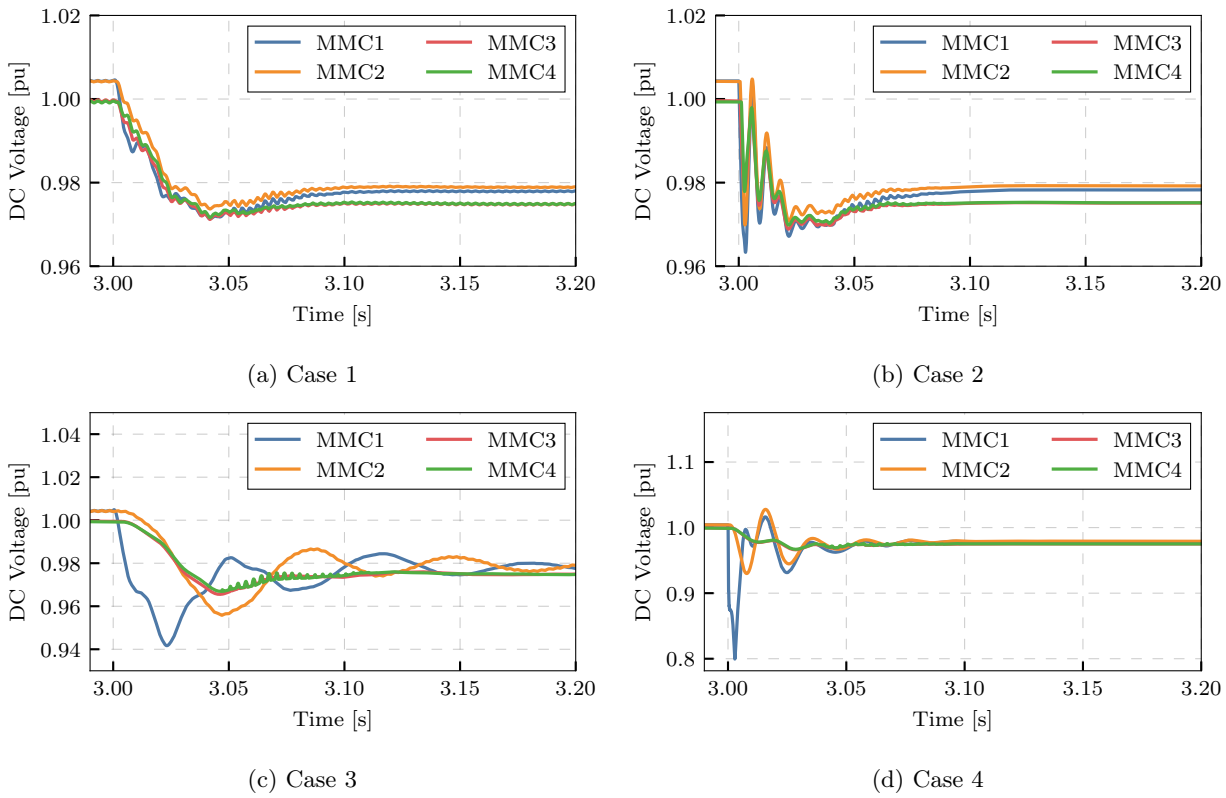

(a) Case 1

(b) Case 2

(c) Case 3

(d) Case 4

Figure 4.33: Time-domain DC voltage responses to a power step at St1 for the four cases considered. Without DCRs, DC voltages respond similarly; with DCRs, responses are decoupled, and CM increases voltage deviation at the station closest to the disturbance (St1).

EMT simulations are performed on the 4T DC grid to verify the results obtained from the small-signal analysis. For consistency with the small-signal analysis conditions, a step change in the active power reference of St1 is introduced at $t = 3$ s, and the DC voltage responses of all stations are shown for the four cases previously described.

Figs 4.33a and 4.33b show that, when no DCRs are present, the time-domain responses of the DC voltages of all stations are similar, supporting the equivalent capacitor assumption of the grid. In Case 2, due to the increase of the number of energy control stations, the DC voltage response exhibits higher transient excursions.

The results of Cases 3 and 4, shown in Figs. 4.33c and 4.33d, indicate that, since the DC voltage of St1 is closer to the original disturbance, its maximum DC voltage deviation is higher than the other stations, with an even higher deviation in Case 4, where CM is used.

The results shown in Fig. 4.33 reveal that the choice of energy control structure for MMC stations primarily affects the response of the individual stations where it is implemented. Increasing the number of stations acting as capacitors has no significant impact on the overall system response, as the presence of DCRs decouples the DC voltage dynamics between stations. For faster transient responses, each converter behaves independently, and no inertial support is exchanged or shared among stations when DCRs are present. Nonetheless, the individual testing of each station should be conducted, in order for the DC voltage not to exceed the maximum allowed deviation with respect to the time-frame of interest [14].

4.8 Conclusion

This chapter has investigated the influence of passive DC reactors (DCRs) on the small-signal stability and dynamic performance of MMC-based MTDC grids. By utilizing both simplified low-frequency impedance models and detailed state-space representations, several key insights were established:

- It was demonstrated that while DCRs are essential for fault current limitation, large inductance values can compromise small-signal stability. Specifically, MMCs operating in constant power (P-mode) exhibit non-passive behavior in the low-frequency range. In inverter operation, this leads to a reduction in phase margin that can trigger instability once a critical DCR threshold is exceeded.
- The analysis revealed a high sensitivity to the power flow direction. Rectifier operation inherently provides more damping, whereas inverter operation narrows the stable region. This suggests that operational conditions can be made use of to mitigate stability risks associated with large DCRs.
- To address these stability risks without sacrificing protection performance or changing steady-state power flow, a lead-compensator-based active damping solution was proposed. This solution effectively reshapes the MMC impedance in the critical frequency range, providing robust stability across a wide range of DCR values and operating points. In addition, the lead compensator does not affect other frequency ranges, thus avoiding unintended consequences on other transient response characteristics.
- At the MTDC grid level, the introduction of large DCRs was found to decouple the electrostatic inertial support between converter stations. This limits the applicability of the common equivalent capacitance assumption for fast transients, meaning that the choice of internal energy control (CM vs. UCM) becomes a localized design concern rather than a system-wide consideration.

In conclusion, the design of MTDC grids requires a coordinated approach to DCR sizing that reconciles protection requirements with small-signal stability constraints. The findings emphasize that active damping strategies are essential for ensuring robust performance in the presence of large DCRs.

5

Development of DC grid equivalent models for standalone converter compliance and stability assessment

5.1 Introduction

The previous chapters have presented the various aspects impacting MTDC grid dynamic performance and small-signal stability, ranging from primary DC voltage control implementation to the influence of DC grid components and operational conditions. The findings highlighted the complexity of accurately representing the DC grid dynamics, which is crucial for the proper design and assessment of converter controls. In fact, in a multi-vendor MTDC grid, each converter station may be designed and tested independently, often without full knowledge of the DC grid configuration and parameters. This situation raises concerns about interoperability when connecting different converters to the same DC grid.

To address these challenges, this chapter focuses on developing equivalent models for representing the DC grid dynamics at the DC Point of Connection (DC-PoC). These equivalent models are constructed based on validated assumptions and analytical results. The goal is to provide simplified yet accurate representations of the DC grid that can be used for converter control design and dynamic performance assessment, even when detailed information about the grid is not available.

The chapter is organized as follows: Section 5.2 provides a literature review on existing approaches for DC grid representation and highlights the need for equivalent models. Section 5.3 presents the methodology for deriving the DC grid impedance at the DC-PoC, considering its dependencies on different elements in Section 5.4. Building on this analysis and the observations drawn from previous chapters, Section 5.5 proposes two equivalent models for representing the DC grid: a simplified RLC model and a frequency-dependent model, with their validation in a test setup. Section 5.6 presents the time-domain validation of the proposed equivalent models. Section 5.7 presents a case study to test the applicability of both models in performing small-signal stability analysis of a three-terminal DC grid, comparing the results with those obtained from the full grid model. The advantages, disadvantages,

and key applications of each model are discussed in Section 5.8. Finally, Section 5.9 provides concluding remarks and insights.

5.2 Literature review

To analyze the dynamic performance of MTDC grids, time-domain simulations are commonly conducted to evaluate performance metrics, such as reference tracking and disturbance rejection of converter stations. Instability issues may arise due to interactions between converter controls and DC grid dynamics. This has motivated research in time-domain behavior and small-signal stability analysis of MTDC grids. In a multi-vendor MTDC grid, TSOs do not have access to vendors' detailed converter models, making small-signal stability assessment particularly challenging. One possible way to mitigate control interoperability issues is to test different variants of control strategies and grid configurations through extensive time-domain simulations and small-signal analysis. This approach has been adopted in Chapter 3, where different control strategies were presented and tested on the same DC grid. A similar approach was adopted in [63], where variants of linear and nonlinear MMC controllers were tested on the same grid. However, this method is time-consuming and may not cover all possible configurations, particularly in a multi-vendor MTDC grid where each converter is designed by a different vendor and the control design is protected by intellectual property. Several stability studies of MTDC grids reported in the literature are based on eigenvalue analysis [166, 174, 175]. A primary shortcoming of this approach is the requirement for full knowledge of the system configuration, including the DC grid elements and detailed converter models.

To address these challenges, frequency-domain stability studies have gained significant attention [59, 61, 176]. These studies involve performing frequency scans of different subsystems and applying the Generalized Nyquist Criterion (GNC) [59]. The advantage of this approach is that it focuses on the terminal behavior of converters and the DC grid by using their respective impedances. This allows for stability assessment without requiring detailed proprietary information of the converter models, as long as their frequency response can be obtained through measurements or provided by the vendors.

Another challenge regarding small-signal stability in multi-vendor MTDC grids is identifying the origin of instability. Since converter models are often provided as black boxes, it is difficult to pinpoint the source of instability when it occurs. To address this, sensitivity analysis using the identification of the frequency response of different subsystems has been proposed in [59].

Despite these advancements, major challenges remain. Even when converters are treated as black boxes, stability analysis can typically only be performed at an advanced stage of an MTDC project once the grid configuration and parameters are finalized. However, converter vendors must begin designing their controls well before the final grid configuration is available. This increases the importance of performing standalone compliance testing of converter stations before connecting them to the actual grid. These tests must rely on valid and acceptable assumptions regarding DC grid behavior to justify qualifying or disqualifying a specific converter's performance.

In a standalone compliance test, converter stations are connected to an AC grid equivalent at the AC Point of Connection (AC-PoC) and a DC grid equivalent at the DC Point of Connection (DC-PoC), as illustrated in Fig. 5.1. If both AC and DC grid equivalents are designed to accurately represent the actual grid behavior at their respective PoCs, the converter's dynamic performance can be properly assessed, mitigating possible control interoperability issues when connecting to the actual grid.

Regarding AC grid representation, a simple Thévenin equivalent is typically utilized, consisting

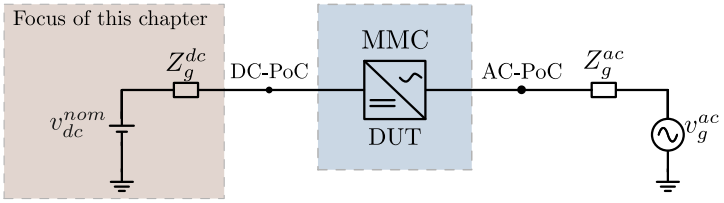

Figure 5.1: Concept of AC and DC grid equivalents for standalone compliance and stability assessment of converter stations.

of an ideal AC voltage source v_g^{ac} behind an impedance Z_g^{ac}. This provides an indication of the AC system's strength via the Short-Circuit Ratio (SCR). While the Thévenin equivalent is effective when assuming that synchronous machines are the primary sources in an AC grid, the increasing penetration of power electronics and the subsequent new converter-driven interactions [27] reduced the reliability of traditional SCR-based metrics [177–183].

Consequently, modified versions of the SCR have been proposed. The Weighted Short Circuit Ratio (WSCR) [177] and Composite Short Circuit Ratio (CSCR) [184] account for interactions between multiple converters. In [179], the Site-Dependent Short Circuit Ratio (SDSCR) was proposed to account for the grid strength at respective AC-PoCs and the electrical distances between nodes. Additionally, the Generalized Short Circuit Ratio (gSCR) was introduced in [180] to address small-signal stability aspects.

Other studies has focused on frequency-dependent impedance network equivalents [181, 185–189] to capture grid impedance behavior over wider frequency ranges. This concept has taken various forms, such as the Impedance-based SCR [181] and the Frequency-Averaged Grid Impedance Metric (FAGIM) [189]. Vector fitting techniques have been utilized in [190] to identify frequency-dependent AC network equivalents. In addition, the need for an accurate AC grid representation has driven industry standards to account for such dependencies. According to [191], system operators are required to provide representative AC network equivalents that describe grid behavior at the AC-PoC, in order to simplify both control design and the compliance process.

On the DC grid side, however, there is a lack of clear guidelines and established practices for representing the grid at the DC-PoC. In the literature, DC system representation has often relied on oversimplified hypotheses [168, 170, 174, 175, 192, 193]. For instance, an ideal DC voltage source is typically used when testing active power response [92,96], while an ideal DC current source is often used for DC voltage control tests, paired with a parallel capacitor to approximate cable dynamics [194–196]. Such simplifications fail to capture the complexity of an actual MTDC grid, potentially leading to converter responses in the reality that differ significantly from design-stage results. In addition, the dynamics of the DC grid has a strong dependency on control strategies, operating points, and grid components, as demonstrated in previous chapters. These dependencies are even less clear in a multi-vendor MTDC grids, where each converter may be designed and tested independently.

To the author's knowledge, only [197] has investigated different DC system models for proper control design, focusing on the risks of model reduction. However, the study did not provide deeper insights into other factors impacting impacting DC grid behavior, such as operating points and DC reactor size.

From the above review, there is a lack of standardized and validated approaches for representing DC grids at the DC-PoC to be used in standalone compliance testing of converter stations. This chapter addresses this gap by providing insights into DC grid behavior, exploiting the observations

from previous chapters. Then, two equivalent models for a given DC grid are proposed, following a structure similar to the AC grid representation in Fig. 5.1. The first equivalent is a simplified model capturing dominant low-frequency dynamics, while the second is a detailed model capturing the frequency-dependent nature of the grid impedance. The frequency-dependent equivalent model exploits vector fitting techniques and state-space identification to represent the grid impedance across a wider frequency range than the low-frequency RLC-based equivalent. Furthermore, the frequency-dependent equivalent is implemented in the time domain, bridging the gap between frequency-domain and time-domain stability analyses, significantly reducing the system order for more efficient simulations. These models are designed to capture various operational conditions and grid dependencies. They are validated against a reference three-terminal DC grid model with detailed MMC dynamics. Finally, their respective advantages, disadvantages, and key applications are discussed.

5.3 System modeling and DC grid impedance derivation

Consider the three-terminal DC grid shown in Fig. 5.2, which consists of three MMC converter stations connected by two DC cables. All three converter stations are connected to AC grids with an SCR of 5. The parameters of the converter stations are similar to those adopted in previous chapters and provided in Appendix A. The MMCs are modeled using the Average Arm Model (AAM) presented in Chapter 2, while the DC cables are represented by their wideband models, as described in Appendix E. Regarding the internal control of the MMCs, initially, all stations are considered to operate in *control setting 1*, with UCM and GFL control, as explained in Section 2.7.

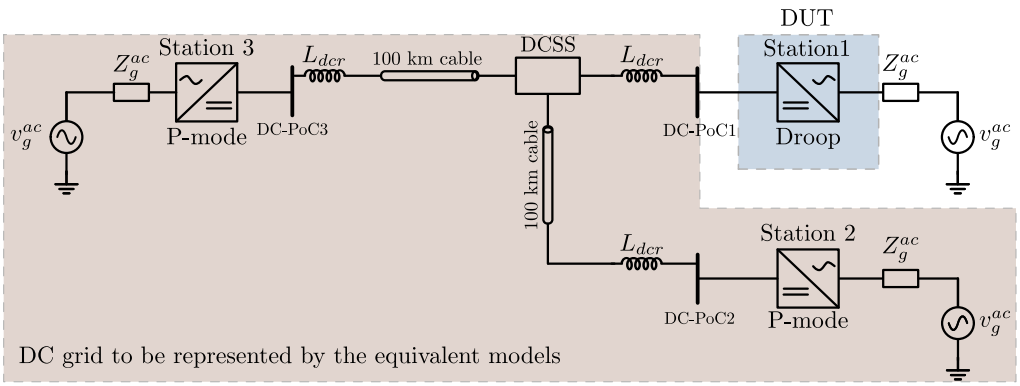

Figure 5.2: Three-terminal DC grid under study.

Station 1 is considered as the Device Under Test (DUT), while Stations 2 and 3 are remote stations operating initially in constant P-mode. The DC reactors (DCRs) connected on the DC side of each station have an initial size of 200 mH. The objective is to derive the DC grid impedance at DC-PoC1 and analyze its dependencies on various parameters, including the DC reactor size, operating points, and control modes of the remote stations. To achieve this, Station 1 and its AC side are replaced by a constant DC voltage source, and the state-space model of the system shown in Fig. 5.3 is constructed, following the methodology presented in Chapter 2 for the MMC and in Appendix E for the cable. Then, the linearized DC-grid impedance at DC-PoC1 is obtained by considering v_{dc} as the system input and the DC current flowing to the grid i_{dc} as the output. The DC-grid impedance is thus given by $Z_g^{dc}(s) = \frac{V_{dc}(s)}{I_{dc}(s)}$. This methodology is similar to the one followed in Chapter 4 to obtain the individual MMC impedance, recalled in Fig. 5.4.

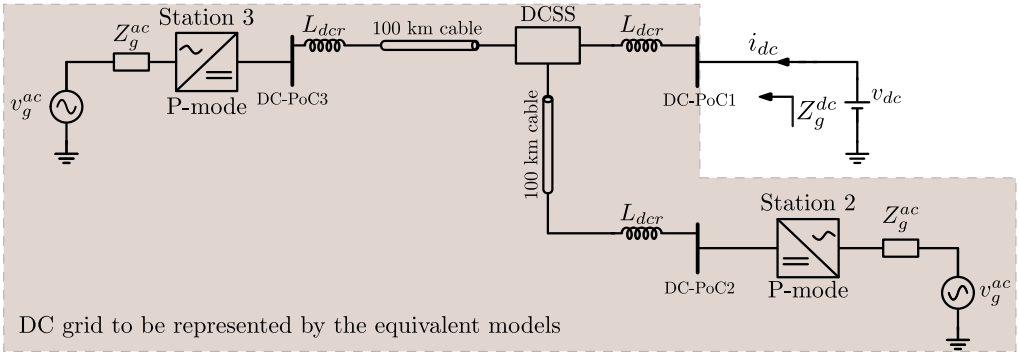

Figure 5.3: Three-terminal DC-grid model for deriving the grid impedance at DC-PoC1.

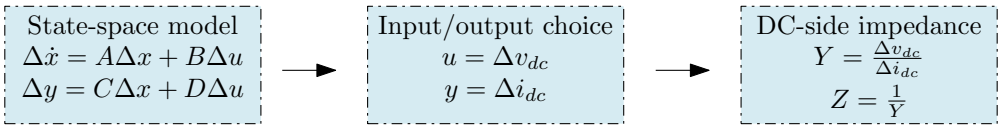

Figure 5.4: Methodology to derive the DC-grid impedance at the DC-PoC from the corresponding state-space representation.

To validate the impedance model derived for the grid in Fig. 5.2, a frequency scan is also conducted using the nonlinear model in EMTP-RV with the same grid parameters. The scanning process follows the approach presented in Chapter 4. Fig. 5.5 shows that the scanned grid impedance is accurately represented by the analytical linearized model, which reflects the different resonances observed in the frequency scan results. In particular, in the very low-frequency range below 10 Hz, the grid exhibits capacitive behavior, characterized by a decreasing magnitude and a phase angle of -90°. This behavior, previously explained in Chapter 4, is primarily attributed to the MMC capacitance under zero power flow conditions combined with the cable capacitance. Around 10 Hz, a series resonance occurs when the grid impedance magnitude reaches a minimum. In the high-frequency range above 110 Hz, the grid impedance is dominated by inductive behavior, represented by an increasing magnitude and a phase angle of 90°. The mid-frequency resonances result from the combined dynamics of the cable and the internal MMC control.

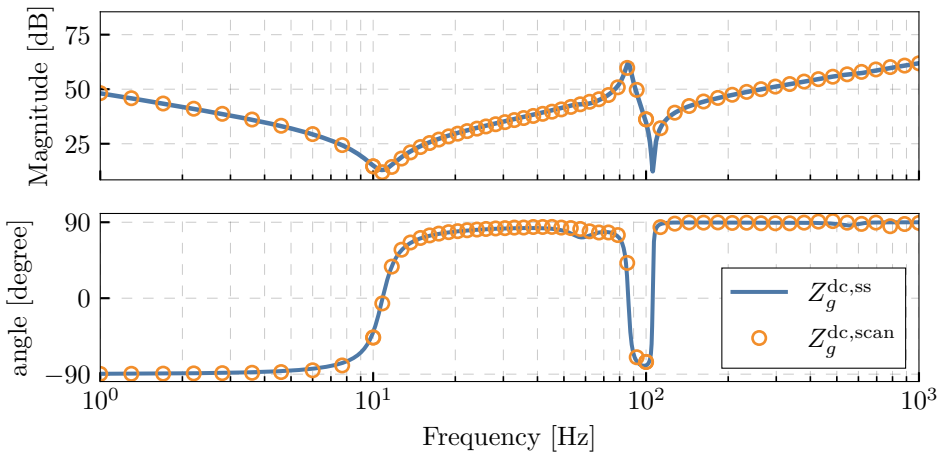

Figure 5.5: Comparison between the analytically derived grid impedance and the frequency scan result.

A time-domain simulation is also conducted to investigate how the different grid resonances manifest in the time domain. A disturbance is applied at DC-PoC1 by introducing a 0.05 p.u. step change in

the DC voltage source at $t = 2$ s. The response of the DC current flowing to the grid is shown in Fig. 5.6. The results indicate that the low-frequency resonance around 10 Hz is the dominant one. The mid-frequency series resonance around 100 Hz is also visible in the time-domain response, but its impact is less pronounced compared to the dominant low-frequency resonance.

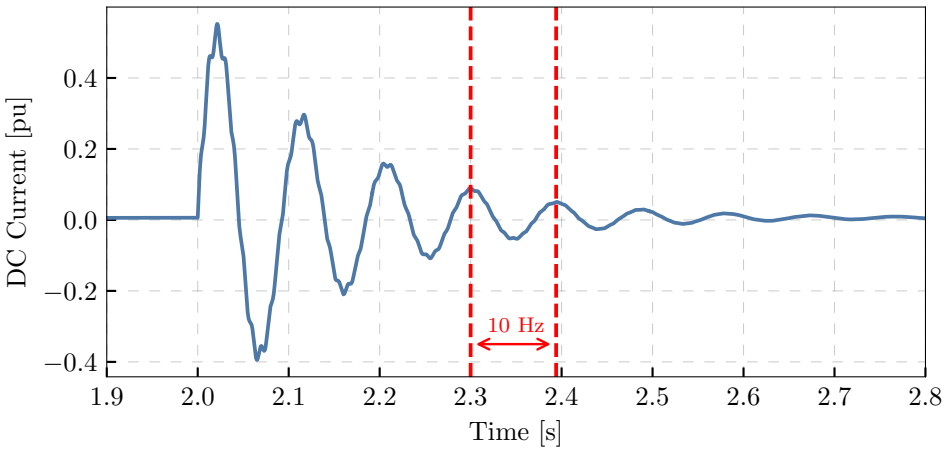

Figure 5.6: Time-domain response of the DC current at DC-PoC1 to a step change in the DC voltage source.

5.4 DC-grid impedance dependencies

In this section, a sensitivity analysis is conducted to investigate the parameters impacting the DC-grid impedance at the DC-PoC. To thoroughly capture the behavior of the grid impedance, we investigate the influence of both the DC-grid passive components and the outer control mode of the remote MMC stations. Although all the sensitivity analyses are performed using the developed analytical model, similar analyses can also be conducted using frequency scans. The insights drawn from this analysis are crucial for developing accurate equivalent models for representing the DC grid at the DC-PoC, as will be presented in Section 5.5.

The focus of this section is on the impact of the DC reactor size, operating points, and control modes of the remote stations. The impact of the grid strength and the GFM control of the remote stations is also analyzed, as they are expected to have an impact on the grid impedance at DC-PoC1.

5.4.1 Impact of the DC reactor size

The impact of the DCR on MTDC dynamics and stability was extensively presented in Chapter 4. In this subsection, a variation of the DCR size of all three stations is considered to analyze its effect on the grid impedance seen at DC-PoC1. The results are shown in Fig. 5.7 for different values of DC reactors varying from 200 mH to 400 mH. As observed, the DCR variation influences the resonances at different frequency ranges. For the dominant low-frequency resonance around 10 Hz, the impedance magnitude is lower for larger DCRs, indicating lower damping for this resonance, which is in line with the conclusions in Chapter 4. For the mid-frequency resonances around 100 Hz, the DCR increase shifts the series and parallel resonance frequencies to lower values. As the frequency increases beyond 100 Hz, the grid impedance is dominated by the inductive behavior of the DCRs, where the impedance magnitude increases with the DCR size. These observations confirm that the DCR size has a significant

impact on the grid impedance across a wide frequency range, which must be considered when developing equivalent models for representing the DC grid at the DC-PoC.

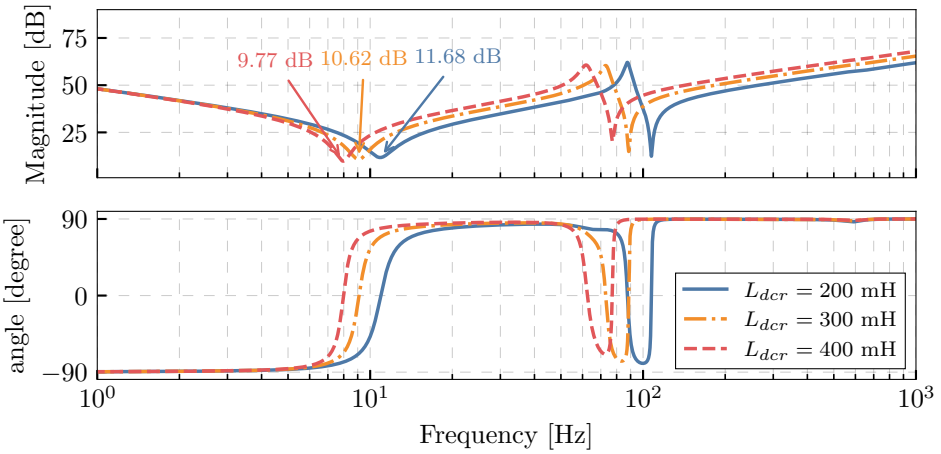

Figure 5.7: Impact of DCR size on the grid impedance seen at DC-PoC1.

To distinguish the impact of the DCR in the vicinity of DC-PoC1 from that of the DCRs installed at a considerable distance from the DUT, we first change only the size of the DCR directly connected to DC-PoC1, and then only the size of the DCR connected to DC-PoC2 and DC-PoC3. The results in Fig. 5.8 indicate that the impact of the nearby DCR is noticable in low-frequency resonance around 10 Hz and the high-frequency magnitude above 100 Hz. In the mid-frequency range, resonance, the nearby DCR has little impact on the resonance frequency.

On the other hand, the effect of the remote DCRs of remote stations is less pronounced in the low frequency resonance compared to the nearby DCR. However, the remote DCRs have a significant impact on the the resonance frequency around 100 Hz. Finally, the remote DCRs have no impact on the high-frequency range above 100 Hz, where the nearby DCR dominates the grid impedance. This last observation leads to the conclusion that high-frequency dynamics are primarily a local phenomenon, with the nearby DCR filtering out high-frequency dynamics originating from distant stations. This also supports the findings in Chapter 4, where fast transients were observed to be limited to the disturbance location due to the filtering effect of the DCRs.

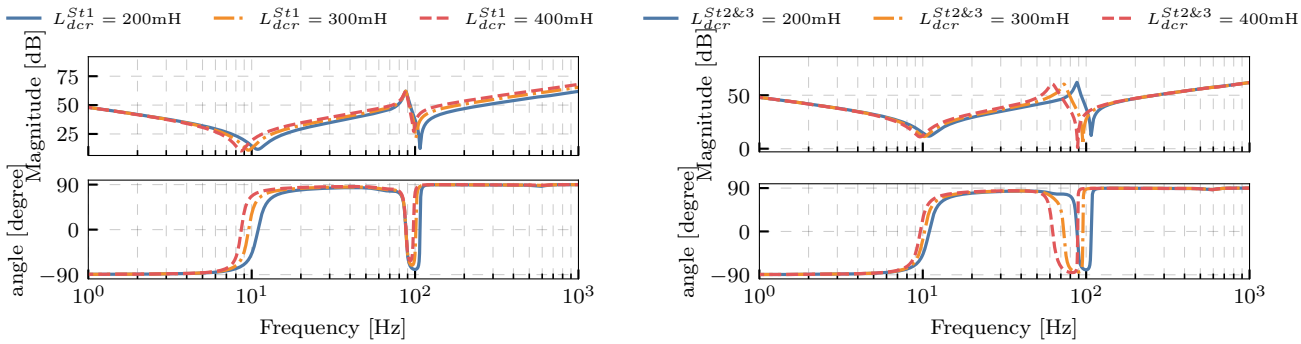

Figure 5.8: Impact of the DCR size: (a) Changing only L_{dcr}^{St1}, with L_{dcr}^{St2} and L_{dcr}^{St3} maintained at 200 mH and (b) Changing only L_{dcr}^{St2} and L_{dcr}^{St3}, with L_{dcr}^{St1} maintained at 200 mH.

5.4.2 Impact of the operating point

The impact of the operating point on the MMC impedance was discussed in Chapter 4, where it was shown that the MMC has negative impedance behavior when operating in inverter mode, positive impedance behavior in rectifier mode, and capacitive behavior at zero power flow. These observations were shown to apply to the low-frequency range below 10 Hz.

In this part, this behavior is tested on the grid impedance seen at DC-PoC1. Three operating points are considered for Stations 2 and 3, as follows:

1. At op1, $P_2 = P_3 = 0$ pu.
2. At op2, $P_2 = P_3 = -0.5$ pu, i.e. both stations in rectifier mode.
3. At op3, $P_2 = P_3 = 0.5$ pu, i.e. both stations in inverter mode.

The results in Fig. 5.9 indicate that the grid impedance at low frequencies is primarily influenced by the operating point of the distant MMCs. In particular, at op1, where both remote stations operate at zero power, the grid impedance exhibits capacitive behavior at low frequencies. At op2, where both remote stations operate in rectifier mode, the grid impedance shows resistive behavior with a constant magnitude and a phase angle of 0°. Finally, at op3, where both remote stations operate in inverter mode, the grid impedance displays negative resistive behavior with a constant magnitude and a phase angle of 180°.

On the other hand, neither the mid-frequency resonances around 100 Hz nor the high-frequency grid behavior is impacted by the operating point; the impedance responses at the three operating points are nearly identical.

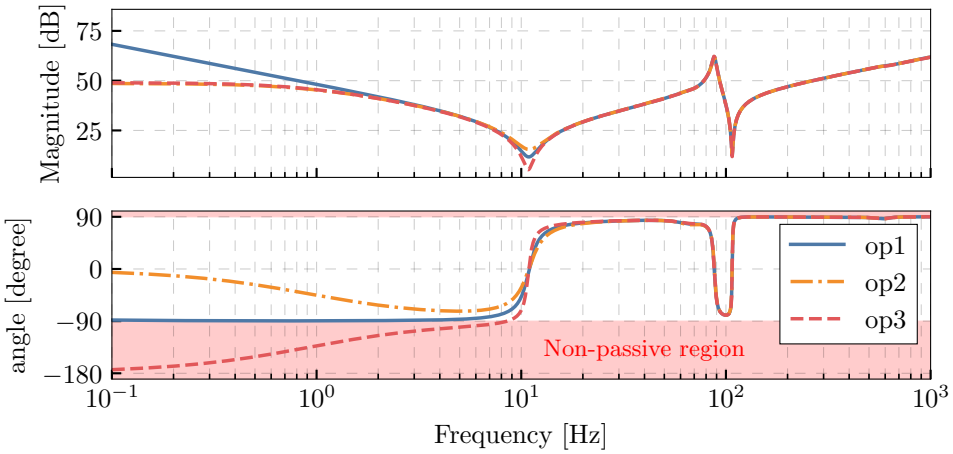

Figure 5.9: Grid impedance seen at DC-PoC1 for different operating points considering P-mode operation of the remote stations.

5.4.3 Impact of the control mode of remote stations

The participation of remote stations in regulating the DC voltage can alter the grid impedance observed at the DC-PoC. We consider two cases of control modes for the remote stations. In Case 1, both Stations 2 and 3 are in P-mode, while in Case 2, Station 2 operates in Vdc-droop control mode with a droop gain $k_d = 0.1$ pu, and Station 3 remains in P-mode. In both cases, the zero power operating point is considered (op1 in Section 5.4.2).

The results in Fig. 5.10 show that applying droop control to Station 2 leads to higher impedance magnitude at the resonance frequency around 10 Hz compared to the case with P-mode. In addition, the phase angle . This indicates that the droop control mimics a resistive behavior in the low-frequency range, improving the damping of the DC voltage. This impact will be further analyzed in Section 5.5. However, since DC voltage droop control is a higher-level control whose bandwidth is constrained to frequencies below approximately 20 Hz, it does not significantly affect the grid impedance at higher frequencies compared to Case 1, where Station 2 operates in P-mode.

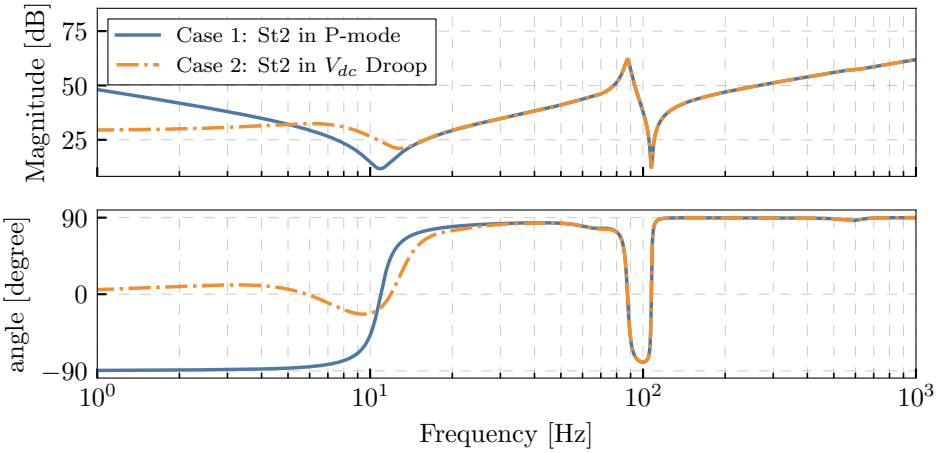

Figure 5.10: Impact of the control mode of Station 2 on the grid impedance at DC-PoC1.

Recall that the droop gain k_d used for the results in Fig. 5.10 is set to a practical value typically used in DC voltage droop control. However, the impact of the droop gain on the grid impedance can be further analyzed by varying k_d and observing the frequency range over which the droop control influences the grid impedance. Such a variation is provided in Fig. 5.11, where the droop gain is varied from 0.001 pu to 0.2 pu.

As depicted in the figure, the droop gain has a significant impact on the grid impedance at low frequencies, with lower droop gains (stronger droop action) resulting in a higher impedance magnitude and improved damping around the resonance frequency of 10 Hz. Additionally, a significantly low value of k_d lowers the magnitude of the series resonance around 100 Hz, which can even lead to instability if this resonance magnitude drops below 0 dB. This confirms the high-gain instability observed in Chapter 3 where the droop gain is set to a very low value[1]. This indicates that, unlike the common perception that droop control only affects low-frequency dynamics, when the droop gain is sufficiently low, its impact can extend to higher frequencies.

Consequently, care must be taken when designing the droop control to ensure k_d is not set so low that it interacts poorly with mid-frequency resonance, while still providing sufficient damping at low frequencies.

To analyze the combined impact of the operating point and the DC voltage droop control applied to Station 2, the same three operating points as in Section 5.4.2 are considered while the droop gain is kept at $k_d = 0.1$ pu. Unlike the case of P-mode operation of Station 2 in Fig. 5.9, where the low-frequency grid impedance is significantly influenced by the operating point, with the droop control of Station 2, the low-frequency grid impedance becomes less sensitive to the operating point. The impedance

[1]It should be noted that this phenomenon is observed only with Droop Scheme A, see Chapter 3.

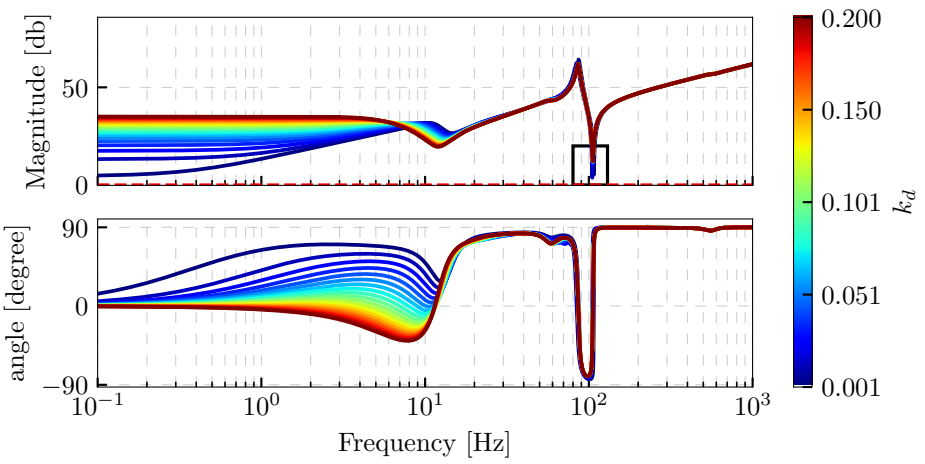

Figure 5.11: Impact of the droop gain k_d of Station 2 on the grid impedance at DC-PoC1.

converges to a constant magnitude with a phase angle close to 0° for all operating points, indicating predominantly resistive behavior. This confirms that DC voltage droop control improves low-frequency damping. Nevertheless, the operating point still slightly affects the low-frequency resonance, with op3 exhibiting a marginally lower impedance magnitude at the resonance frequency around 10 Hz. In contrast, the high-frequency impedance remains unaffected by the operating point, consistent with the results in Section 5.4.2.

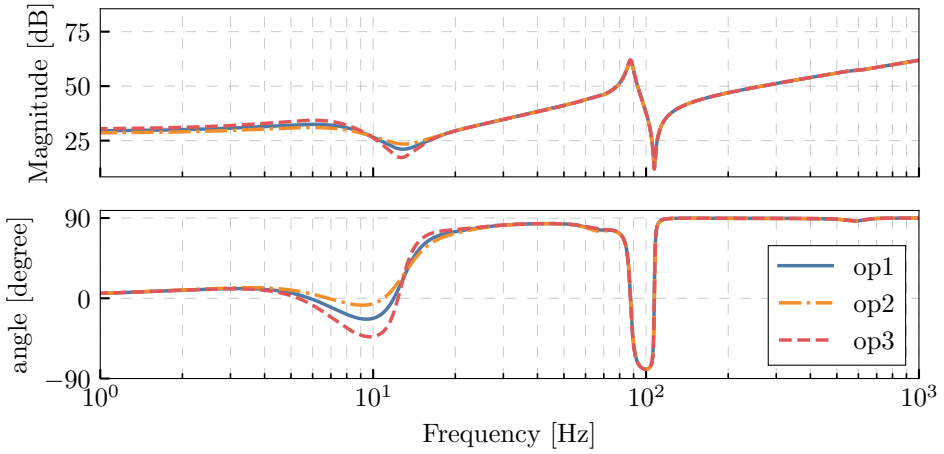

Figure 5.12: Impact of the operating point on the grid impedance at DC-PoC1 when Station 2 operates in Vdc-droop control mode.

5.4.4 Impact of the grid strength of the remote stations

It is well established in the literature that the AC-grid strength connected to the AC-PoC of a converter stations has an impact on the stability of the converter, especially with GFL control where the PLL might lead to adverse interactions, and even to instability [198].

The objective here is to analyze if the variation in the AC-grid strength of the remote stations has an impact on the grid impedance seen at DC-PoC1. To achieve this, the SCRs of the AC grids connected to Station 2 and 3 are varied from 1 to 10. The results in Fig. 5.13 indicate that the grid strength of the remote stations has no impact on the grid impedance at DC-PoC1 across the entire frequency range. This observation is consistent with the fact that the AC grid strength primarily affects

the dynamics of the converter station at the local AC-PoC, and does not impact the other DC-PoCs in the grid.

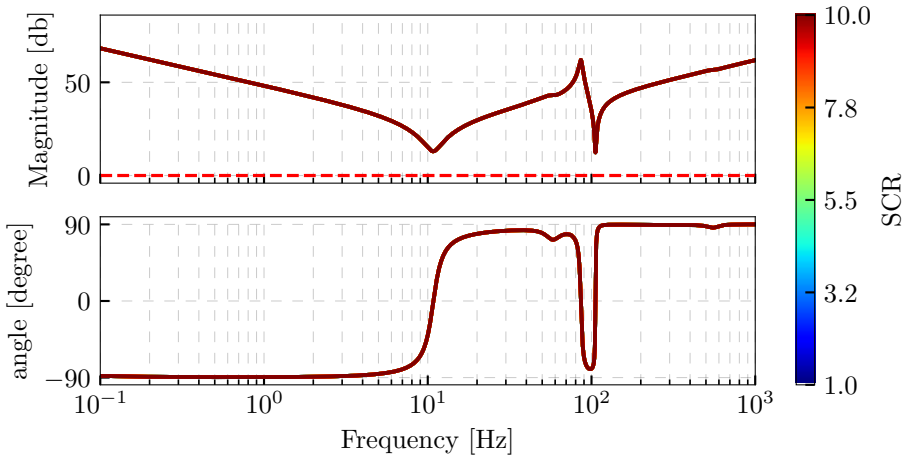

Figure 5.13: Impact of the grid strength of the remote stations on the grid impedance at DC-PoC1.

5.4.5 Impact of the GFM control strategy of the remote stations

The different control strategies of the remote stations can also influence the grid impedance at DC-PoC1. To analyze this impact, Stations 2 and 3 are switched to *control setting 3* defined in Chapter 2, in which both stations operate under GFM control with UCM. VSM-GFM control is applied using the parameters provided in Appendix A.

The results shown in Fig. 5.14 indicate that the change from GFL to GFM control of the remote stations has only a minor effect on the frequency response of the grid impedance at DC-PoC1, except for a slight increase in the resonance frequency around 10 Hz. This behavior can be explained by the fact that the GFM control of the remote stations mainly influences their local dynamics.

It should be emphasized that this result does not imply that potential instability caused by the GFM control of the remote stations would not be observable at DC-PoC1. Rather, it indicates that, as long as the GFM control of the remote stations is properly designed, whether they operate in GFL or GFM mode does not significantly affect the grid impedance at DC-PoC1. However, if the GFM control is poorly designed, it may lead to instability that becomes visible at DC-PoC1. This aspect have been demonstrated in Chapter 3.

5.5 Development of the equivalent grid model

The findings from the previous section highlight that the grid impedance is influenced by various factors across different frequency ranges. These dependencies must be considered when developing equivalent models for the DC grid to ensure an accurate representation of its behavior.

In this section, we investigate two possible approaches yielding two different models for representing the grid impedance at the DC-PoC. The design philosophy of the proposed models is the balance between simplicity and accuracy. Hence, the choice between the two would depend on the required level of accuracy and the available grid information. The first model is a simple RLC equivalent model, while the second model is a frequency-dependent equivalent model that can accurately capture the DC-grid dynamics across wider frequency ranges.

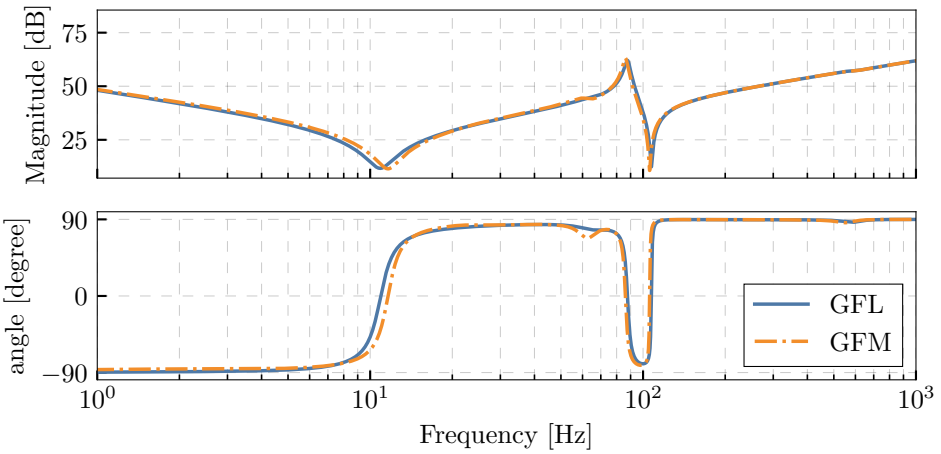

Figure 5.14: Impact of the GFM control of the remote stations on the grid impedance at DC-PoC1.

5.5.1 Low-frequency RLC-based equivalent model

The results from Section 5.4 showed a series resonance around 10 Hz in the grid impedance at the DC-PoC1. Therefore, an RLC equivalent model is proposed to capture the low-frequency dynamics of the grid impedance, particularly around this resonance frequency. This model is intended to provide a simplified representation of the grid for preliminary control design and standalone dynamic studies. From Fig. 5.15, the model combines a series resistance R, inductance L, and capacitance C. The equivalent impedance can be expressed as

$$Z_{eq1}^{dc}(s) = R + sL + \frac{1}{sC - \frac{P_0}{v_{dc0}^2}} \tag{5.1}$$

where C represents the aggregated capacitance of the DC grid, L the inductance present in the DC grid, and R the resistive losses in the grid, which also provides damping to the system. Notice that the impedance expression in (5.1) is similar to the one derived for the MMC-AVM in P-mode in Chapter 4, where the third term represents the capacitive behavior of the MMC at low frequencies, which is dependent on the operating point (P_0, v_{dc0}).

To select the RLC parameters, the capacitor C is chosen to represent the aggregated capacitance of the grid, which is expressed as

$$C = \sum_{i=1}^{N_{\text{mmc}}} C_{\text{mmc},i} + \sum_{i=1}^{N_{\text{cable}}} C_{\text{cable},i} \tag{5.2}$$

With two MMC stations ($N_{\text{mmc}} = 2$) and two cables ($N_{\text{cable}} = 2$) connected to the DC grid at DC-PoC1, and considering the MMC parameters in Appendix A and the cable parameters in Appendix E, the total capacitance is calculated as $C = 596.65$ μF.

Similarly, the equivalent inductance is obtained by combining the cable inductance and the DCR inductance, taking into account their series/parallel connection in the considered DC grid in Fig. 5.2. The DC inductance of each terminal is 200 mH, and the per-kilometer cable inductance at the low frequency range is 0.4 mH/km, resulting in a total inductance seen at DC-PoC1 of $L = 320$ mH.

The resistance R is selected to reflect the resistive losses in the DC grid, which are mainly attributed to the cable resistance. From Appendix E, the per-kilometer resistance of the cable at the low frequency

range is 0.04 Ω/km, yielding a total resistance of $R = 2$ Ω.

Finally, P_0 is set according to the initial power of the DUT.

It should be noted that, to account for the variations in grid configurations and parameters, a feasible range of the parameters of $Z^{dc}_{eq1}(s)$ can be obtained, and hence a similar calculation procedure can be followed to select the RLC parameters for different DC-grid conditions. An approach of obtaining such ranges is presented in [14].

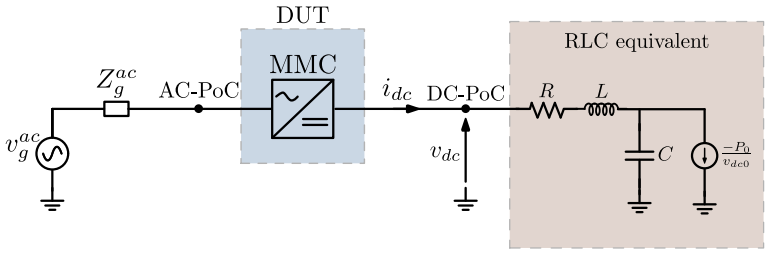

Figure 5.15: RLC equivalent model connected to the converter station.

Fig. 5.16 compares the RLC model to the full grid model obtained in Section 5.3 for the three operating points defined in Section 5.4.2. The result confirms the capability of the RLC model to represent the grid impedance at DC-PoC1 in a simplified form, for different DC-grid operating points. This equivalent representation can be used for the design of the converter control, and for the preliminary testing of the converter low-frequency dynamic performance before connecting to the actual DC grid.

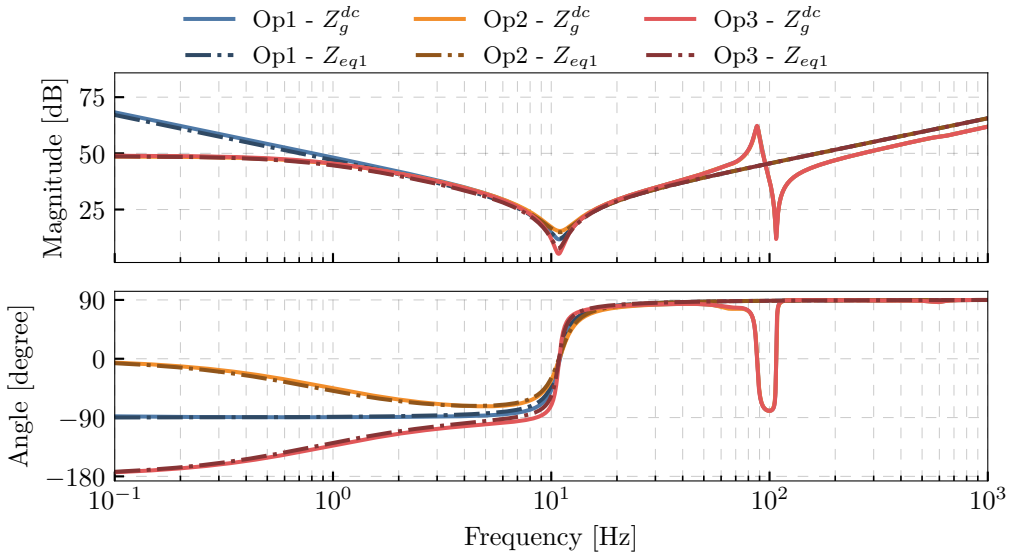

Figure 5.16: Validation of the RLC model against the full grid impedance when both remote stations are in P-mode following (5.1), with different operating points for St 2&3.

To account for the outer control mode of the remote stations under DC voltage droop control, the RLC model in (5.1) can be extended to incorporate the droop control dynamics. In Fig. 5.16, the remote stations are considered to operate in P-mode. If Station 2 operates in DC voltage droop control mode instead, then a DC voltage source in series with an RL element should be added in parallel with the capacitor of the RLC model in Fig. 5.15. This extended RLC equivalent model is illustrated in Fig. 5.17. This addition emulates the positive damping effect introduced by droop control in the low-frequency range, as discussed in Section 5.4.2. The impedance of the extended model can therefore

be expressed as

$$Z_{eq2}^{dc}(s) = R + sL + \frac{1}{sC - \frac{P_o}{v_{dc0}^2} + \frac{1}{sL_{droop}+R_{droop}}} \tag{5.3}$$

with R_{droop} being the parallel resistance representing the droop action provided by other converter stations in the DC grid. In fact, in steady state (i.e., $s = j0$), the grid impedance given in (5.3) reduces to

$$Z_{eq2}^{dc}(0) = R + \frac{R_{droop}}{1 - \frac{P_o R_{droop}}{v_{dc0}^2}}$$

which shows the steady-state impact of R_{droop} and the series resistance R, the latter representing the resistive losses in the DC grid.

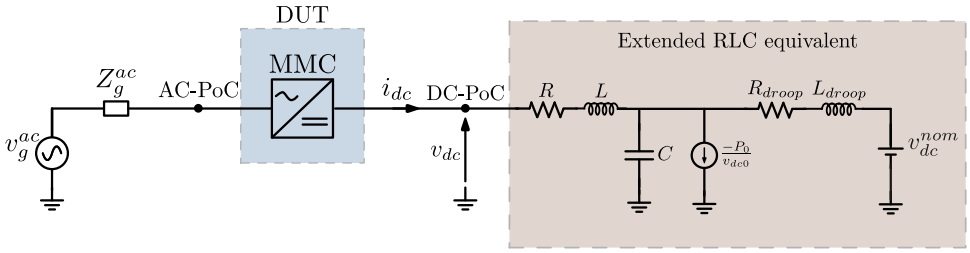

Figure 5.17: Extended RLC equivalent to cover droop control mode of station 2.

To choose the parameters in (5.3), the values of R, L, and C are selected as previously described for the simple RLC model of (5.1). R_{droop} is chosen to represent the droop action provided by Station 2. In this case, a droop gain of $k_d = 0.1$ pu is considered. Using the nominal DC voltage and power, the droop resistance is calculated as $R_{droop} = \frac{k_d v_{dc0}^2}{P_{nom}} = 27.656\ \Omega$. The value of L_{droop} is selected to capture the dynamic effect of the droop control. It should be emphasized that L_{droop} does not necessarily represent a physical inductance in the grid. Instead, it is a dynamic term introduced to reflect the impedance magnitude around the low-frequency resonance, which is known to occur near 10 Hz. Based on this consideration, L_{droop} is set to 538 mH. If multiple droop-controlling stations are present in the grid, the value of R_{droop} can be adapted to reflect the aggregated effect of multiple droop controllers, following the principles of DC voltage droop characteristics, as discussed in [14, 137].

To verify this model, the extended RLC equivalent is compared to the actual grid impedance of Case 2 where Station 2 operates in DC voltage droop control mode, while Station 3 operates in P-mode. The results, depicted in Fig. 5.18, show that the RLC model accurately captures the low-frequency dynamics of the grid impedance, including the impact of the droop control mode of Station 2.

In summary, depending on the operating conditions of the converters in the grid and their respective control modes, the simplified RLC models developed so far accommodate two configurations for the remote stations:

- All stations in P-mode: A simple RLC equivalent, as shown in Fig. 5.15, can be used.

- One or more stations in droop control mode: An extended RLC equivalent, as shown in Fig. 5.17 can be applied, where R_{droop} and L_{droop} are chosen to represent both the steady-state and dynamic impacts of the droop control mode.

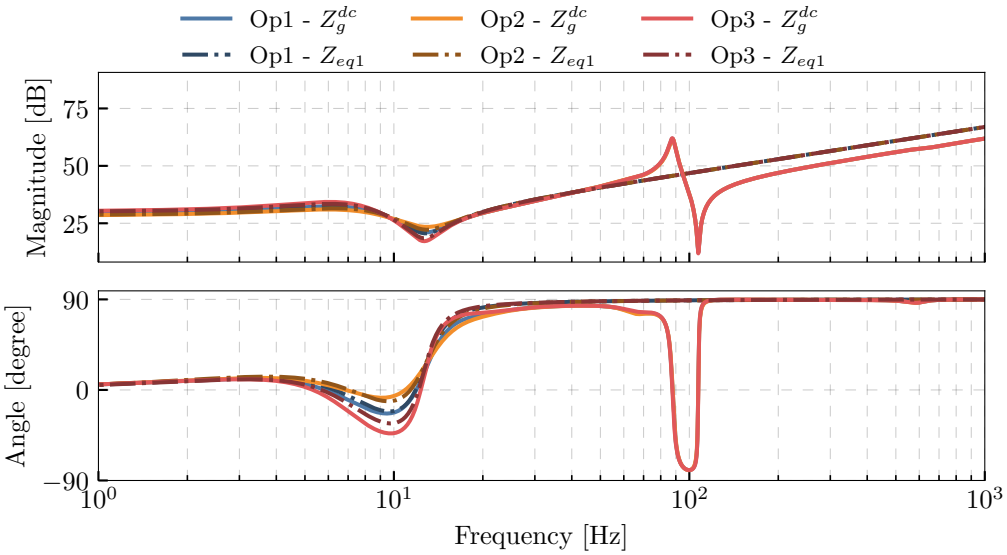

Figure 5.18: Validation of the extended RLC model against the full grid impedance when St 2 operates in DC voltage droop following (5.3), with different operating points for St 3.

5.5.2 Frequency-dependent equivalent model

As more information becomes available during the planning of an HVDC project, driven by the need to accurately represent grid impedance for reliable standalone compliance testing of converter control functionalities, it becomes increasingly difficult to represent all grid resonances using concatenated passive elements.

To achieve higher accuracy across a wider frequency range, an alternative modeling approach is required at the DC-PoC. This is particularly important for small-signal analysis. Consequently, a frequency-dependent equivalent model is proposed. This equivalent is obtained by fitting the actual grid impedance, whether derived analytically or via a frequency scan, to a transfer function. For this, the vector fitting method in [199] is used. The order of the model can be selected based on the complexity of the grid impedance frequency response and the desired accuracy of the equivalent model.

To investigate the reliability of this approach, Fig. 5.19 shows the approximation of the full grid impedance using a 5th-order transfer function. The results show that the frequency-dependent model can accurately capture the grid impedance dynamics across a wide frequency range, including the low-frequency resonance around 10 Hz, the mid-frequency resonances around 100 Hz, and the high-frequency behavior above 100 Hz. It is important to note that the original DC-side impedance of the grid at the DC-PoC is of order 47, which is significantly reduced through the fitting process. This order reduction offers the advantage of allowing the equivalent model to be easily implemented in time-domain simulations, enabling it to capture the frequency-dependent grid dynamics while significantly reducing the computational burden associated with simulating the full grid model. This process will be further illustrated in the case study presented in the next section.

The grid impedance of Case 2 (Station 2 operating in DC voltage droop control mode) is also fitted to a 5th-order transfer function. The results in Fig. 5.20 show that the frequency-dependent model can accurately capture the grid impedance dynamics while Station 2 operates in droop control mode. This is true for the three different grid operating points considered for Station 3, previously defined in Section 5.4.2.

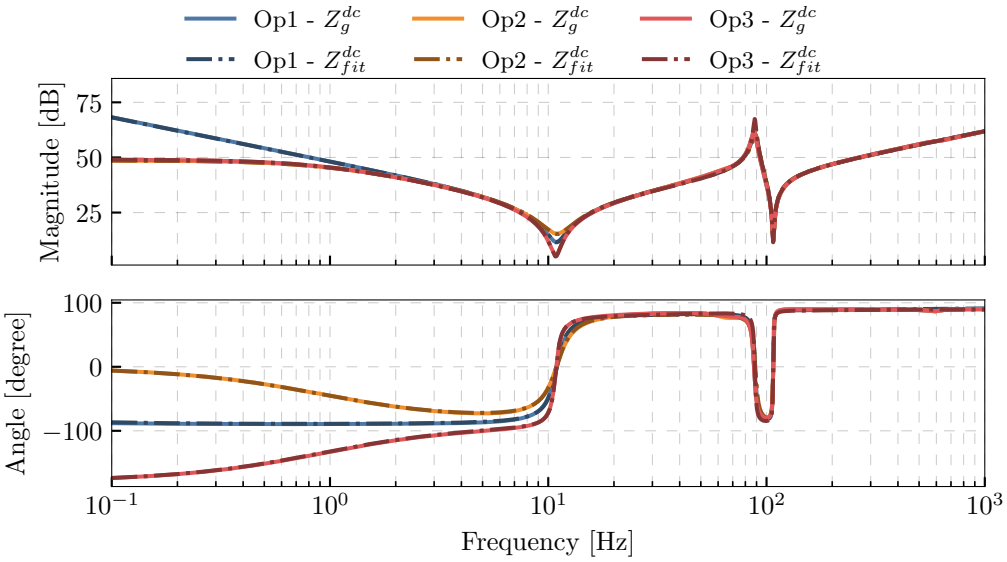

Figure 5.19: Comparison between the fitted grid impedance and the actual grid impedance when both remote stations are in P-mode, with different operating points for St 2&3.

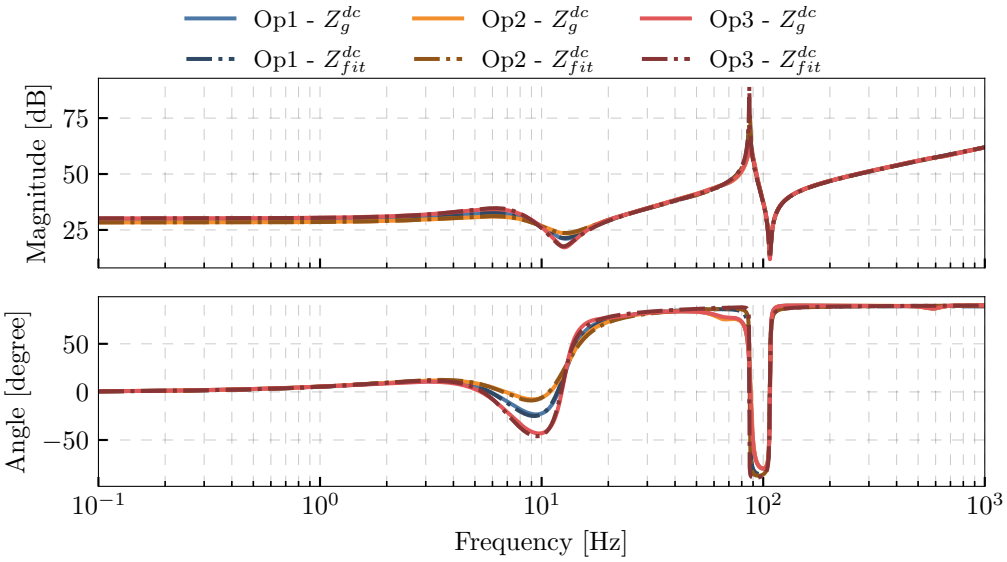

Figure 5.20: Comparison between the fitted grid impedance and the actual grid impedance for Case 2 (Station 2 operating in DC voltage droop control mode), with different operating points for St 3.

5.6 Time-domain validation of the equivalent models

In this section, the two equivalent models developed in Section 5.5 are validated through time-domain simulations, and compared against the reference response of the full 3TDC grid model.

For the low-frequency RLC equivalent model, the setup in Fig. 5.15 is used. For the frequency-dependent model, the setup shown in Fig. 5.21 is proposed, where the fitted transfer function is implemented in the time-domain simulation, to capture the frequency-dependent behavior of the grid impedance. The considered disturbance is +0.05 pu step reference change in the DC voltage of Station 1 (DUT). Station 1 (DUT) operates in DC voltage droop control mode. The droop gain k_d is set to 0.05 pu, while for Stations 2 and 3, different control modes are considered, as described in the following

- Case 1: Both Stations 2 and 3 operate in constant P-mode.
- Case 2: Station 2 operates in DC voltage droop control mode, while Station 3 operates in constant P-mode.

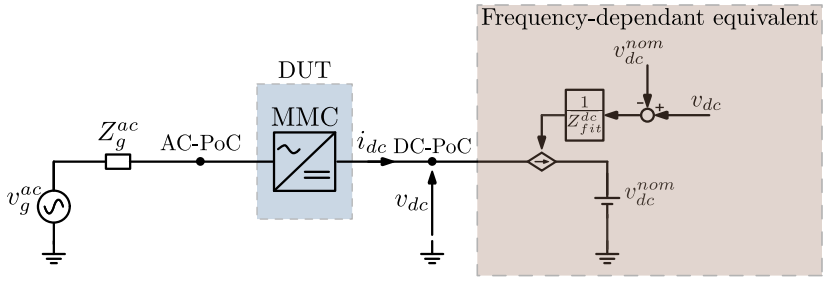

Figure 5.21: Implementation of the frequency-dependent grid impedance in time-domain simulation.

Case 1

For Case 1, the results in Fig. 5.22 show that both the RLC equivalent model and the frequency-dependent model can adequately represent the full grid dynamics in the low-frequency range, with the frequency-dependent model offering a more precise representation than the RLC model. This is true for all three operating points considered in Section 5.4.2.

Regarding the computational burden in the considered time-domain simulation, the full grid model requires approximately 2 minutes to simulate 5 seconds of operation, while both the RLC equivalent model and the fitted frequency-dependent model take around 19 seconds to simulate the same duration of operation[2].

This demonstrates the significant computational efficiency of utilizing the equivalent models compared to simulating the full grid model.

Case 2

In Case 2 shown in Fig. 5.10, Station 2 operates in DC voltage droop control mode. The results presented in Fig. 5.23 demonstrate that both the extended RLC equivalent and the frequency-dependent model accurately capture the static and dynamic responses of the full grid to the step change. The impact of the droop control of Station 2 is also well captured.

[2]The simulations were performed on a computer equipped with an Intel Core i7 CPU (1.3 GHz) and 16 GB of RAM.

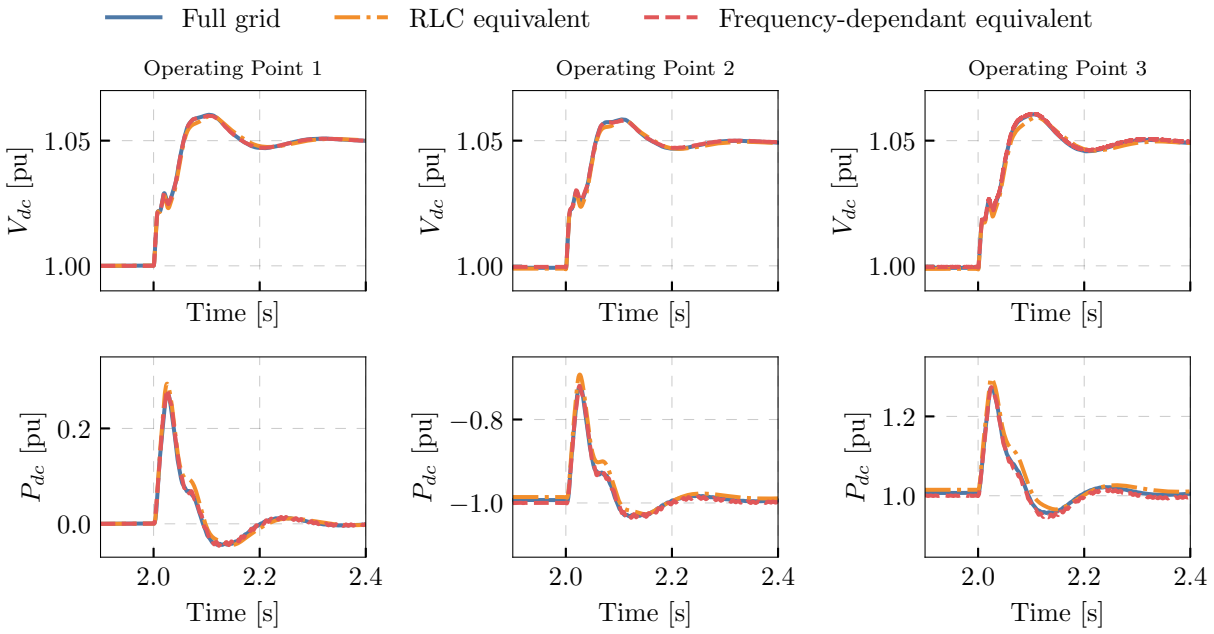

Figure 5.22: Step reference response of the DC voltage of Station 1 for the 3T grid model, the RLC model, and the frequency-dependent model.

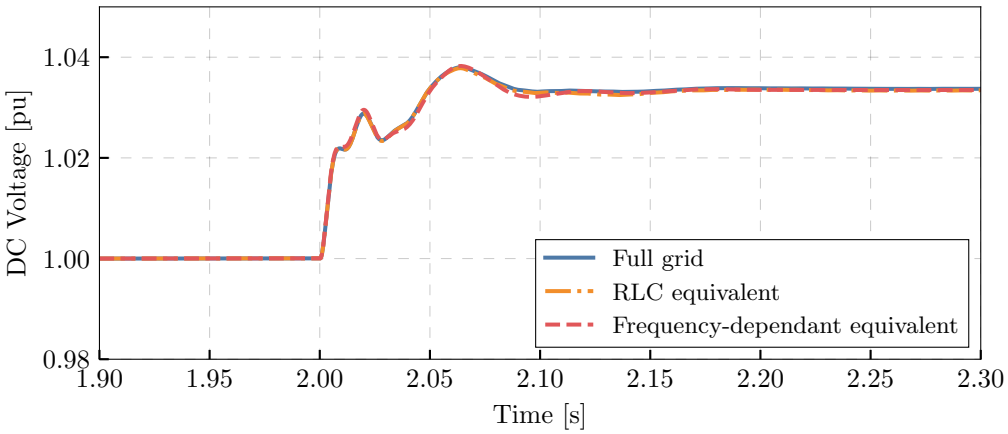

Figure 5.23: Step reference response of the DC voltage of Station 1 for the 3T grid model, the extended RLC model, and the frequency-dependent model.

5.7 Case study: small-signal stability analysis using the equivalent models

To evaluate the small-signal interactions between the DUT and the connected grid represented by the two proposed models, the impedance-based stability criterion is employed [50], which applies the Nyquist criterion on the open-loop transfer function to assess the stability of the closed-loop system in the frequency domain.

In Chapter 3, it has been shown that a potential source of instability in DC networks is the high-gain instability of DC voltage Droop scheme A. In this case study, we consider Station 1 (DUT) operating in DC voltage droop control mode using Droop scheme A, with a low droop gain of $k_d = 0.005$ pu. Both Stations 2 and 3 operate in constant P-mode at zero power (op1 in Section 5.4.2). The DCR inductance of all stations is set to 200 mH, as in previous sections.

Fig. 5.24 presents the Bode plot of the Station 1 impedance Z_{MMC}, the equivalent RLC model Z^{dc}_{eq1}, and the return ratio defined as $\mathcal{L} = \frac{Z_{MMC}}{Z^{dc}_{eq1}}$. Recall that the return ratio represents the loop transfer function of the system, providing an indication of the system's closed-loop stability. The results show no intersection between the two impedances, indicating system stability. Furthermore, the Nyquist plot of $\mathcal{L}$, depicted in Fig. 5.25, shows no encirclement of the -1 point, further confirming the stability of the system when the RLC model is utilized.

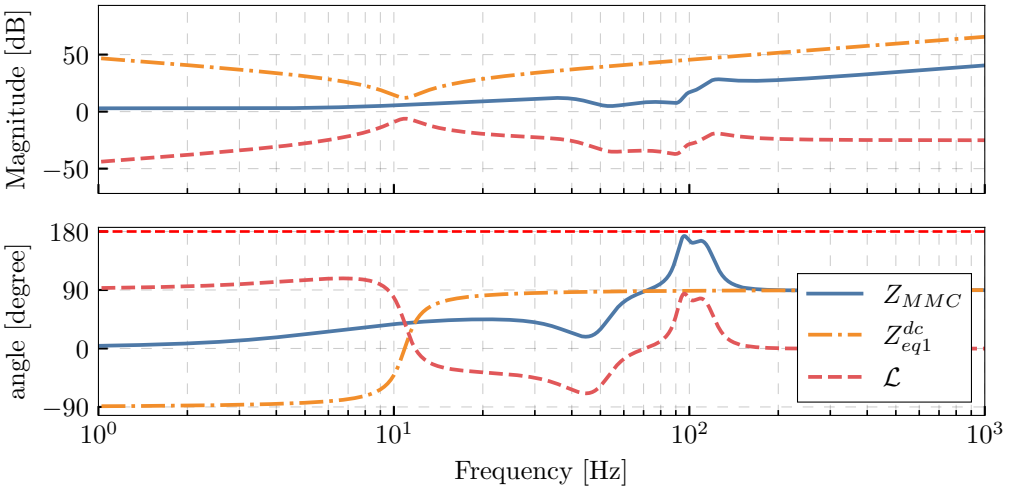

Figure 5.24: Bode plot of Z_{MMC}, Z_{eq1}, and the return ratio $\mathcal{L} = \frac{Z_{MMC}}{Z^{dc}_{eq1}}$.

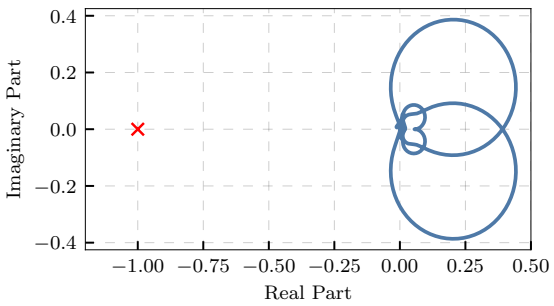

Figure 5.25: Nyquist plot of the return ratio $\mathcal{L} = \frac{Z_{MMC}}{Z^{dc}_{eq1}}$.

The same analysis is performed on the fitted frequency-dependent equivalent impedance, denoted

by Z_{fit}^{dc}, and the loop gain is redefined as $\mathcal{L} = \frac{Z_{MMC}}{Z_{fit}^{dc}}$. The Bode plots are presented in Fig. 5.26, and the Nyquist plot of $\mathcal{L}$ is shown in Fig. 5.27. The results demonstrate that the system is unstable, with a phase angle exceeding 180° at the gain crossover frequency $f_c = 110$ Hz in the Bode plot (Fig. 5.26) and a clockwise encirclement of the -1 point in the Nyquist plot (Fig. 5.27).

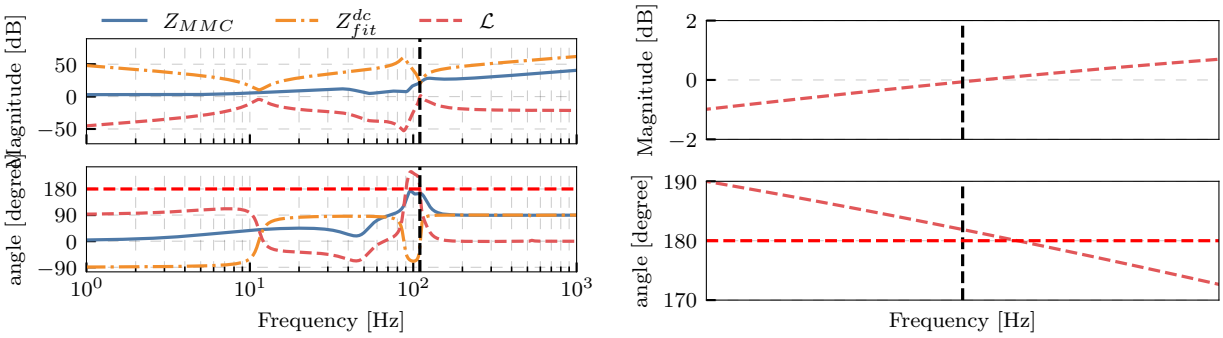

(a) (b)

Figure 5.26: Bode plot of the Z_{MMC}, Z_{fit}^{dc}, and the return ratio $\mathcal{L} = \frac{Z_{MMC}}{Z_{fit}^{dc}}$ (a) Full plot (b) Zoomed plot.

To further validate the impedance analysis results, the poles of the closed-loop system are compared for three cases: when Station 1 is connected to the full grid model, the RLC model, and the frequency-dependent fitted grid model. The results, shown in Fig. 5.28, indicate that both the full grid model and the frequency-dependent model reveal the presence of a pair of unstable poles, $\lambda = 4.1 \pm j691$, corresponding to a resonance frequency of 110 Hz. In contrast, the RLC model fails to capture this pair of unstable poles. This frequency coincides with the gain crossover observed in the Bode plot in Fig. 5.26, confirming that the instability is caused by the resonance around 110 Hz. This phenomenon is accurately captured by the frequency-dependent model but not by the RLC model.

It can also be observed that, although the fitted frequency-dependent model successfully captures the unstable poles, it does not represent all the poles of the system. This is expected due to the order reduction from 47 to 5 in the grid model. Nevertheless, the fitted model captures all the dominant poles of the system, which is sufficient for a reliable stability analysis.

The case study results reveal that the RLC model reflects the grid behavior only in the low-frequency range. In contrast, the frequency-dependent model accurately captures both low- and high-frequency dynamics, which is critical for a thorough stability analysis. This is intuitive since the frequency-dependent model serves as a data-driven behavioral representation, whereas the RLC model is a simplified model that captures only dominant low-frequency characteristics.

A time-domain simulation is conducted for the same case study to validate the small-signal analysis results, by using the same physical and control parameters for consistency. The results with the full grid impedance, depicted in Fig. 5.29, confirm that the system is indeed unstable, and exhibits growing oscillations in the DC voltage at $f_c = 110$ Hz. This instability is reproduced with the frequency-dependent model, yielding oscillations at the same frequency, but not with the RLC model. These findings align with the predictions made by the small-signal analysis, and prove that the frequency-dependent model is suitable for a reliable small-signal stability assessment on a standalone test bench, while the RLC model can only provide a preliminary indication of the system behavior in the low-frequency range.

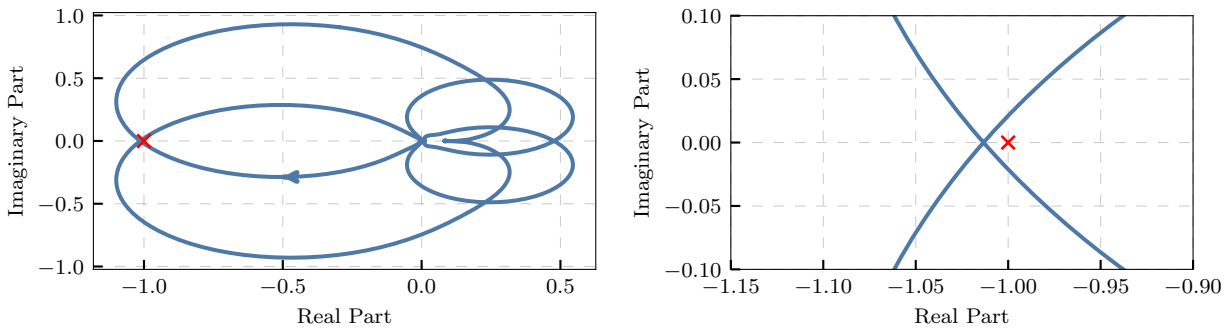

(a) (b)

Figure 5.27: (a) Nyquist plot of the return ratio $\mathcal{L} = \frac{Z_{MMC}}{Z_{fit}^{dc}}$ (b) Zoomed plot.

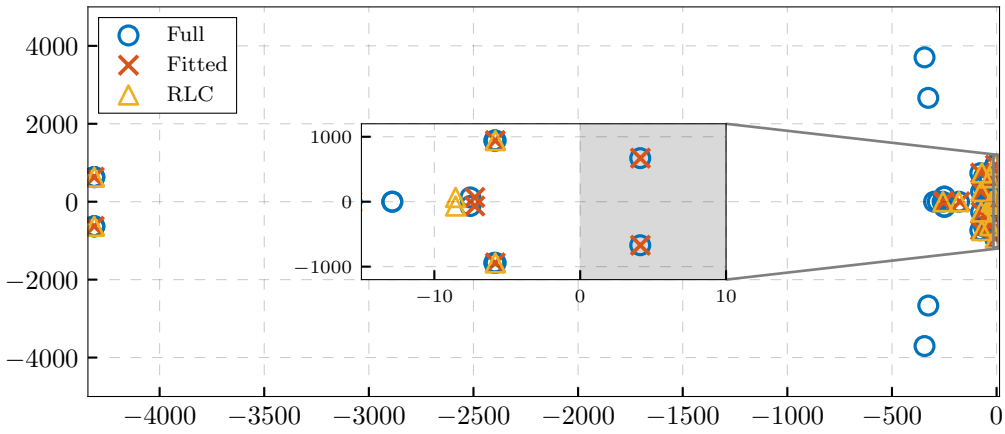

Figure 5.28: Comparison of the closed-loop poles obtained with the full grid model, the RLC model, and the frequency-dependent fitted model.

5.8 Guidelines for the application of the proposed equivalent models in a multi-vendor compliance testing process

To demonstrate the applications of the two proposed models, Table 5.1 provides a comparison in terms of the required grid information, the order of the equivalent system, and the intended use of the two models.

In a multi-vendor HVDC project, from a converter control design perspective, the project can be divided into three stages [14]: (1) specification stage, in which functional and performance requirements are defined; (2) design stage in which each converter manufacturer develops the control system for its respective converter station to meet the specified requirements; and (3) integration stage, in which all converter stations are integrated and tested together to ensure that the overall MTDC system behavior complies with the defined requirements.

The focus of this chapter is the design stage, during which parallel converter control design and testing are expected. For this purpose, the two proposed equivalent models can serve to define a common standalone testing framework for the converter manufacturers. This can be applied according to the flowchart shown in Fig. 5.30. In the early design phase, when detailed grid information is not yet available, the simplified RLC model can be used to verify basic control functionalities and to gain insight into the low-frequency grid dynamics.

Once this preliminary testing for each converter station is successfully completed, and as the project

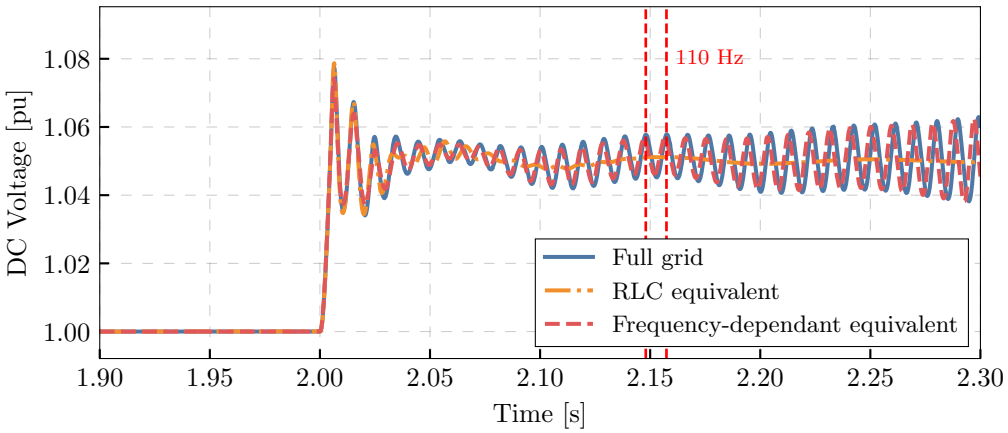

Figure 5.29: DUT response to a 0.05 step change in the DC voltage setpoint at $t = 2$s.

Table 5.1: Comparison between the two proposed DC equivalent models.

	RLC equivalent	**Frequency-dependent equivalent**
Required grid information	Minimal information needed, such as number of connected stations, DCR values, and cable length	The exact grid impedance at the DC-PoC, derived or scanned, is required to capture the response over the whole frequency range
Frequency range	Valid for dominant low-frequency dynamics	Valid for the entire frequency range 1-1000 Hz
Equivalent system order	second-order system	5th-order system (in the current grid configuration)
Application	Preliminary converter control design and testing.	Detailed stability analysis and final converter compliance testing.

advances, the DC-grid impedance at each DC-PoC can be obtained. This impedance should be provided to the converter manufacturers for implementation in the frequency-dependent equivalent model, which can then be used in time-domain simulations for detailed stability assessment and final standalone compliance testing. The advantage of using the frequency-dependent model is that it can be considered a behavioral model of the grid, which can be implemented in time-domain simulations instead of the full grid model, while still capturing the frequency-dependent dynamics.

Then, if compliance is not achieved, the converter manufacturer can refine the control design and repeat the testing using the frequency-dependent model until the required performance is met. Subsequently, the DC-grid impedance can be updated to reflect any changes following control refinement, with a maximum number of iterations defined in the project specifications.

This procedure helps mitigate potential control interoperability issues during the design stage. As a result, fewer issues are expected to arise during the integration stage, when all converter stations are integrated and tested together.

5.9 Conclusions

In this chapter, the dynamic behavior of a 3-terminal DC grid was investigated, with a focus on how various grid elements influence the impedance at the DC point of connection (DC-PoC). Through a comparative analysis, it was shown that DC reactors, operating points, and the control modes of remote stations all have a significant impact on the grid's dynamic response across different frequency ranges.

To address the need for accurate yet practical representations of DC-grid dynamics, two equivalent grid models were proposed. The first one, an RLC-based equivalent, provides a simple and effective method for capturing low-frequency behavior. It is particularly suitable for preliminary converter control design and low-frequency response testing thanks to its low computational burden. The second one, a frequency-dependent equivalent reduced from a higher-order model, captures both low- and high-frequency dynamics, offering a more comprehensive tool for detailed stability analysis.

Validation through frequency-domain impedance scans and comparison with nonlinear time-domain simulations confirmed the accuracy and reliability of both models. The results emphasize the importance of selecting the appropriate impedance representation based on the intended application and required accuracy. Furthermore, the frequency-dependent equivalent was successfully implemented in time-domain simulations, enabling the evaluation of small-signal stability conditions directly in the time domain.

Importantly, these equivalent models can also serve as a foundational step toward mitigating control interoperability challenges in MTDC systems by providing standardized and representative models for converter testing and control development in a multi-vendor environment.

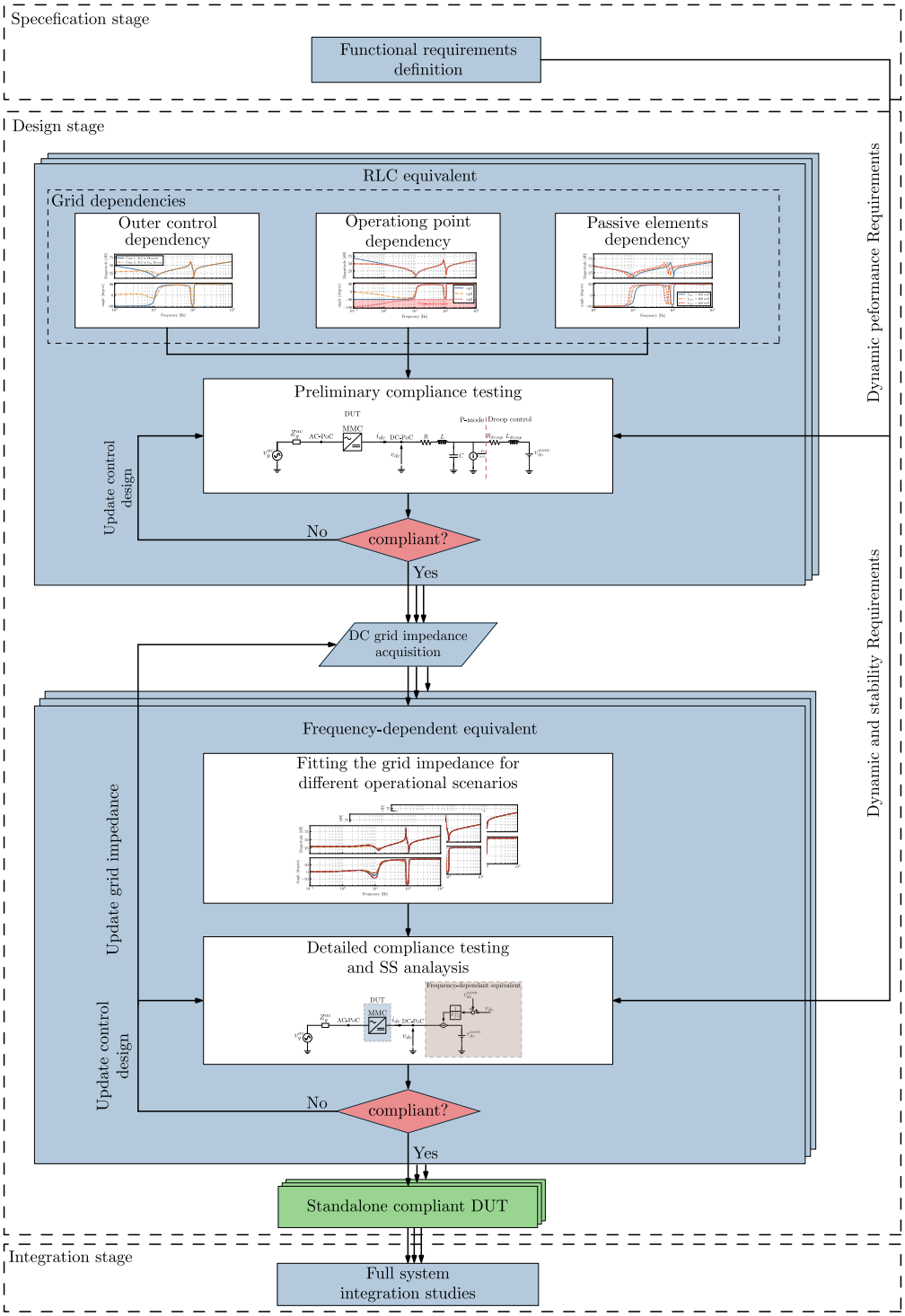

Figure 5.30: Flowchart for the application of the proposed equivalent models in a multi-vendor compliance testing procedure.

6

Conclusions and Perspectives

This chapter summarizes the main conclusions and contributions of this thesis and outlines perspectives for future research directions. The work addressed key challenges related to the stability, dynamic behavior, and interoperability of multivendor MTDC grids based on MMCs. Section 6.1 provides a summary of the main conclusions from each chapter, while Section 6.2 outlines potential avenues for extending the research presented in this thesis.

6.1 Main conclusions

With the increasing interest in multi-terminal DC grids to enhance the optimal utilization of transmission assets for integrating offshore wind, a deep understanding of the dynamic interactions and stability phenomena in these systems has become increasingly critical. In addition, these systems are expected to consist of equipment from multiple vendors, making interoperability a key concern. The interoperability challenges are particularly pronounced in the context of control design, where a dedicated framework for defining functional requirements and performance specifications is essential to ensure that different control implementations can coexist and operate stably within the same grid, and that these implementations do not lead to stability issues.

This thesis focused on topics related to the stability of multi-vendor DC grids, including the design of DC voltage droop control, the impact of passive DC reactors, and the development of accurate DC grid equivalent models to enable standalone converter testing and preliminary interoperability validation. The main conclusions from each chapter are summarized below, excluding Chapters 1 and 2, which primarily provide background and modeling frameworks for the subsequent analysis.

Chapter 3

Chapter 3 focused on the analysis of DC voltage droop control in MTDC grids with multiple implementation options. The chapter first provided an overview of the hierarchical control structure of MTDC grids, highlighting the critical role of DC voltage droop control in providing local response to power

disturbances, such as the loss of a converter station or a change in the wind production. The multi-segment droop characteristic was analyzed, showing its importance in exploiting converter capacity to enhance system security while maintaining acceptable DC voltage deviations from the original setpoint.

The chapter emphasized that droop design is not only a steady-state power-sharing problem but also a key determinant of dynamic behavior. Two droop implementation options were analyzed, Scheme A and Scheme B, each modifying a different outer-control loop reference within the MMC control. It was shown that both implementations can coexist within the same MTDC grid by different converter stations, which is an important result for multi-vendor interoperability. However, their impact under extreme droop gains differs, implying that a feasible design space for droop gains must be defined, encompassing the stability limits of both implementations when combined. It has also been shown that internal MMC control tuning can significantly impact the stability limitations of DC voltage droop control.

The combination of DC voltage droop and GFM controls constitutes an important challenge of MTDC grid stability. Through small-signal analysis and time-domain simulations, it was shown that the DC voltage droop control and GFM control represent two conflicting control objectives, since they both dominate the low-frequency behavior of the converter. Stability margins combining Droop Scheme A and VSM-GFM were found to be significantly low, limiting the feasible droop gain range when inertial support is provided to the interconnected AC grid.

As a solution to the identified stability challenges, the combination of Droop scheme B and matching GFM control was proposed. This combination was shown to provide significantly improved stability margins, enabling the use of lower DC voltage droop gains (higher droop action) and simultaneously provide inertial support to the connected AC grid. This scheme was validated through time-domain simulations, demonstrating its effectiveness in maintaining system stability under various operating conditions and disturbances. Special attention was given to the impact of matching control parameters on the overall system stability, showing that careful tuning is required to ensure optimal GFM and DC voltage droop performance.

Finally, the chapter highlighted the importance of coordinated design of DC voltage droop and GFM controls, particularly in multi-vendor environments where different implementations may coexist.

Chapter 4

Chapter 4 examined the control and passive elements impacting the stability and dynamic performance of MMC-based MTDC grids. Using the Linear time-invariant models developed in Chapter 2, the MMC impedance was analyzed under various operating conditions, revealing that the converter can exhibit non-passive behavior at low frequencies when operating in fixed power mode in the inverter direction. This non-passivity is a key factor contributing to small-signal instability in MTDC grids in the low-frequency range.

The impedance-based stability analysis was further applied to a simplified MMC representation and full MMC model, with a focus on DC reactor size. The results showed that while increasing the DC reactor size can improve fault current limiting capability, it can also lead to reduced phase margins and potential instability. The critical reactor value beyond which instability occurs was identified for a standalone MMC setup. Its dependence on operating conditions and power flow direction was highlighted. More specifically, rectifier operation for constant P-mode stations was found to pose no risk of instability considering large DCRs. In addition, it was shown that droop control can naturally

mitigate the negative impact of large DC reactors on stability by providing damping at the low-frequency range.

As a solution to the identified instability risk, a lead-compensator-based active damping method was proposed. This method reshapes the converter impedance in the low-frequency range without affecting steady-state operation or DCR size, enabling stable operation across wide DCR ranges. The proposed solution was validated through time-domain simulations, demonstrating its effectiveness in maintaining system stability.

At the system level, large DCRs were confirmed to negatively impact the overall stability of MTDC grids, particularly under inverter operation. The identified mitigation measures, such as applying droop control or avoiding using inverter direction for constant P-mode stations, were shown to be effective in restoring stability even with large DCRs. In addition, the proposed lead compensator was applied to the constant P-mode stations, showing that it can effectively restore stability even with large DCRs.

The analysis also revealed that the presence of large DCRs can significantly reduce transient coupling between converters, limiting the validity of common equivalent capacitance assumption during fast dynamics. Consequently, internal MMC energy control strategies become local design choices rather than global system properties.

This chapter demonstrated that passive component sizing cannot be treated independently from converter control design, highlighting the need for considering the grid configuration and the existence of passive elements in the control design process.

Chapter 5

Chapter 5 addressed the challenge of representing the DC grids at the DC-PoC, in order to enable standalone converter dynamic performance evaluation and accurate small-signal stability validation. The chapter first analyzed the elements impacting the DC grid impedance seen at the DC-PoC, identifying the key role of DC reactors, operating conditions, and remote converter control modes. The analysis also identified the frequency ranges where the DC grid impedance is dominated by different elements.

Next, two equivalent models were proposed. The first one, an RLC-based equivalent, provides a compact representation capturing dominant low-frequency dynamics and is well suited for preliminary controller design and early-stage testing. The model was extended to represent the outer control mode of the remote stations with different operating points. The second model, a frequency-dependent reduced-order equivalent, preserves both low- and high-frequency behavior, enabling detailed stability assessments considering the full frequency range.

Validation against impedance scans and nonlinear time-domain simulations demonstrated the accuracy and robustness of both models. Importantly, the frequency-dependent equivalent was successfully implemented in time-domain simulations, allowing small-signal stability phenomena to be evaluated using conventional EMT simulation environments while significantly reducing the computational burden compared to full grid simulations.

The proposed equivalent models provide a pathway toward standardized DC grid representations, facilitating converter testing and reducing early control interoperability risks in multi-vendor environments.

6.2 General recommendations and perspectives for future work

There are various challenges associated with the development of future multi-vendor HVDC grids. This thesis attempted to answer certain questions regarding the stability, dynamic performance, and compliance testing of these networks. However, further work can be envisioned as an extension of this research. Below are several ideas on how the studies conducted in this thesis could be expanded, along with some general perspectives to ensure the proper operation of multi-vendor HVDC grids.

Extension of the analysis to bipolar HVDC grid configurations

All the grid studies conducted in this thesis assumed an asymmetrical monopolar configuration. This approach was chosen to focus on the fundamental interaction phenomena between the MMC control and the connected DC grid, without the additional complexity and possible redundancy introduced by the presence of a second pole. However, bipolar configurations are now more commonly considered for future MTDC systems, particularly in the context of offshore wind integration. Recent literature has shown that bipolar-specific phenomena can arise, such as possible interactions between the positive and negative poles [200,201], which may impact the overall system stability and dynamic performance. In addition, even under steady-state conditions, the outage of a converter pole or cable can lead to a combination of monopolar and bipolar configurations, rendering DC voltage control a challenging task.

As future work, the analysis conducted in this thesis, although generally applicable to bipolar systems, should be extended to explicitly consider bipolar configurations and the possible interactions between the two poles. For instance, the extension of the developed DC grid equivalent models to bipolar systems would be of great interest, as the presence of two poles may introduce new dynamic interactions and affect the validity of the proposed equivalent models. Another direction is to develop DC voltage control strategies that can effectively manage voltage regulation in bipolar configurations, particularly under the outage of one pole or under unbalanced conditions.

Detailed modeling of the AC system

Most investigations relied on a Thévenin equivalent representation of the connected AC grids. While suitable for DC-side analysis, more detailed AC network models would enable deeper investigation of AC–DC interaction mechanisms, including electromechanical modes and grid-forming dynamics under weak-grid conditions.

Extension of the DC grid equivalent models to test DC fault conditions

As stated in Chapter 3, the DC voltage must be regulated within acceptable limits depending on the time scale. In this thesis, the focus was on the small-signal representation of the DC grid, which is suitable for analyzing stability and dynamic performance. It would be useful to consider extending the proposed equivalent models to include large disturbances, such as DC faults. This involves examining how the grid should be represented at the DC-PoC during a fault, which varies depending on the fault location and other grid parameters.

A possible vision for such an approach is to develop a grid representation that can be used to simultaneously test converter control, dynamic performance, and DC fault ride-through capabilities under different conditions. This would reduce the need for separate testing of control and protection, allowing vendors to co-design control and DC-FRT capabilities. Since converter impedance has already

been considered for testing DC-FRT capabilities in [202], a logical next step is to extend the grid representation to include the impact of DC faults on the grid impedance.

Functional specifications using Model Based Systems Engineering (MBSE) approaches

Future multi-vendor HVDC grids are expected to be large and complex. For such large-scale systems, the use of Model Based Systems Engineering (MBSE) could be highly beneficial for defining functional specifications and performance requirements in a structured and systematic way. MBSE can facilitate the integration of different subsystems, including control and protection, and help manage the complexity of multi-vendor environments by providing a clear framework for requirement definition, traceability, and validation. A first idea of utilizing MBSE approaches for multi-vendor MTDC systems is presented in [203].

The analysis conducted in Chapter 3 showed that different implementation options of DC voltage droop control and GFM control can coexist in the same HVDC grid. Based on this observation, MBSE could be used to formulate behavioral requirements at both the AC-PoC and DC-PoC, independently of specific control implementations. In addition, the utilization of the developed DC-grid equivalent models could fit in the process of testing the requirements set by the MBSE framework.

Quantitative dynamic performance requirements

While the thesis focused on studying the underlying interaction phenomena between MMC control and the connected DC grid, a natural extension is to make efforts toward establishing grid-code-ready requirements based on quantitative limits for dynamic performance and stability. Currently, such specifications are often defined on a per-project basis and rely on specific configurations and non-exhaustive operational scenarios. Approaching multi-vendor challenges from a subsystem-requirement perspective could lead to a more modular development process. Although these quantitative requirements should remain open to future extension, experience gained from upcoming projects will be highly valuable. Nevertheless, the approach should move toward detailed specifications. The developed equivalent models could serve as a first step in this direction, enabling the definition of standardized test cases and performance-checking criteria.

Machine learning for DC-grid equivalent generation

The development of machine learning models trained on large datasets of grid configurations and operating conditions could enable fast and accurate data-driven DC grid equivalent generation. The proposed frequency-dependent equivalent model provides a reduced-order representation of the grid dynamics, which limits the number of parameters required to describe the DC-PoC behavior. This reduced parameter space is particularly suitable for machine learning, as it allows efficient training using a manageable number of grid scenarios.

A first step would consist of defining representative grid scenarios and scanning the grid impedance at the DC-PoC to build a dataset linking reduced-order model parameters to operating conditions. The results of the stability analysis, including the obtained stability margins, could then be used as labels for training the machine learning model.

Once trained, the model could predict stability margins for unseen configurations and identify operating regions where stability is most critical. In this way, machine learning would guide the

selection of the most critical scenarios to be tested, thereby reducing the number of required simulations while maintaining coverage of the most relevant operating conditions.

Tool development for multi-vendor interoperability testing

Building on the above perspectives, the development of dedicated automated tools for multi-vendor interoperability testing could be highly beneficial. These tools could integrate the developed equivalent models, machine learning–based predictions, and standardized test cases to provide a comprehensive platform for testing converter control and protection. In harmony with these tests, the tool could also be used to perform integration and interaction testing during the integration phase of a project. One major advantage of such a future tool is the *standardization* of test cases and performance criteria, which is a key objective for multi-vendor interoperability.

A

System parameters

This appendix provides the physical MMC and default control parameters used throughout the thesis, in Tables A.1 and A.2, respectively. The AC grid parameters are provided in Table A.3.

Table A.1: MMC physical parameters

Parameter	**Value**
Rated power [MVA]	1000
Rated DC voltage [kV]	525
Rated AC-PoC L-L voltage [kV]	400
Number of submodules per arm	400
Submodule capacitance [mF]	19.348
Arm inductance [mH]	43
Arm resistance [Ω]	0.8
Transformer reactance [pu]	0.18
Transformer resistance [pu]	0.005

Table A.2: MMC control parameters

Parameter	**Value**
Outer loop controllers	
Active/reactive power controller response time [ms]	50
DC voltage controller response time [ms]	50
Horizontal Energy controller response time [ms]	50
Vertical Energy controller response time [ms]	200
Total energy controller response time [ms]	50
Inner loop controllers	
i^{Δ} controller response time [ms]	10
i_{Σ} controller response time [ms]	5
CCSC response time [ms]	5
PLL response time [ms]	10
GFM control	
Inertial constant [s]	1
Damping coefficient [p.u.]	100
TDR gain [p.u.]	0.2
TDR time constant [ms]	3.2
Matching GFM control	
η [p.u.]	0.1
lead time constant τ_z [ms]	50
lag time constant τ_p [ms]	10

Table A.3: AC grid parameters

Parameter	**Value**
Short-circuit ratio (SCR)	5
X/R ratio	10

B

Definitions

B.1 Base values and per-unit system

Throughout this thesis, all the physical MMC and grid parameters are modelled in SI units. However, all the control structures and the corresponding control parameters are designed in the per-unit system. The base values used for the per-unit system are given in Table B.1.

Table B.1: Base values for the per-unit system

Parameter	**Value**
Base power S_b [MVA]	1000
Base DC voltage V_{dcb} [kV]	525
Base AC voltage V_{acb} [kV]	173.2
Base DC current I_{dcb} [kA]	1.9048
Base AC current I_{acb} [kA]	1.9245
Base frequency f_b [Hz]	50
Base angular frequency ω_b [rad/s]	314.16
Base energy W_b [MJ]	40

B.2 Park transformation

The Park transformation is used to convert three-phase quantities from the *abc* frame to the rotating *dq* frame. The amplitude-invariant Park transformation [204] is considered throughout this thesis. The

transformation matrix is given by:

$$\boldsymbol{P_\theta} = \frac{2}{3}\begin{bmatrix} \cos(\theta) & \cos(\theta - \frac{2\pi}{3}) & \cos(\theta + \frac{2\pi}{3}) \\ -\sin(\theta) & -\sin(\theta - \frac{2\pi}{3}) & -\sin(\theta + \frac{2\pi}{3}) \\ \frac{1}{2} & \frac{1}{2} & \frac{1}{2} \end{bmatrix} \tag{B.1}$$

with d axis lagging q axis by 90 degrees. A visualization of the Park transformation is shown in Figure B.1. The dq frame rotates at an angular frequency of ω.

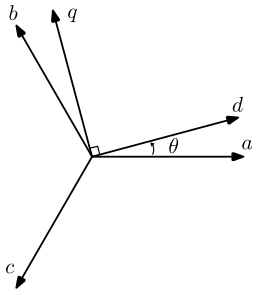

Figure B.1: Park transformation

B.3 Clarke transformation

The Clarke transformation is used to transform three-phase quantities from the abc frame to the stationary $\alpha\beta z$ frame. The amplitude-invariant transformation matrix [204] is given by:

$$\boldsymbol{C} = \frac{2}{3}\begin{bmatrix} 1 & -\frac{1}{2} & -\frac{1}{2} \\ 0 & \frac{\sqrt{3}}{2} & -\frac{\sqrt{3}}{2} \\ \frac{1}{2} & \frac{1}{2} & \frac{1}{2} \end{bmatrix} \tag{B.2}$$

In this thesis, the Clarke transformation is only used in the non-linear EMTP models, more specifically in the horizontal and vertical energy balancing control loops, where the $\alpha\beta$ components of the capacitor voltages are used to calculate the horizontal and vertical energy imbalances. A visualization of the Clarke transformation is shown in Figure B.2.

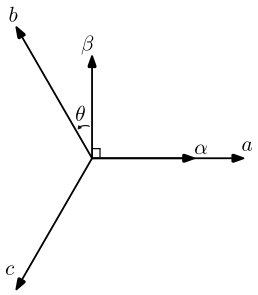

Figure B.2: Clarke transformation.

C

Validation of the MMC-LTI models

This appendix presents the remaining validation results of the MMC-LTI models developed in Chapter 2. The validation setups and scenarios are repeated here for convenience. The validation scenarios are summarized in Table C.1, where the control settings are defined.

Table C.1: MMC LTI model validation scenarios

Control setting	**Description**	**LTI model**
1	GFL + UCM	AAM
2	GFL + CM	AVM
3	GFM + UCM	AAM
4	GFM + CM	AVM

Table C.2: Step tests for MMC LTI model validation

Setup	**Step variable**	**Step change**	**time**
1	DC voltage disturbance v_{dc}	± 0.05 pu	$t = 2 - 3$ s
1	Active power reference P^*_{ac}	$+0.05$ pu	$t = 4$ s
2	DC voltage reference v^*_{dc}	± 0.05 pu	$t = 2 - 3$ s
2	DC power disturbance P_{dc}	$+0.05$ pu	$t = 4$ s

For each control setting, two setups are considered, as shown in Fig. C.1. The step tests conducted for each setup are described in Table C.2. The validation results for the remaining scenarios are shown in Figs. C.2 to C.9. The results for control setting 1 are already shown in Chapter 2. For Scenarios 3 and 4, which correspond to GFM control, only setup 1 is considered for validation, since the combination of GFM control and DC voltage control is discussed in detail in Chapter 3.

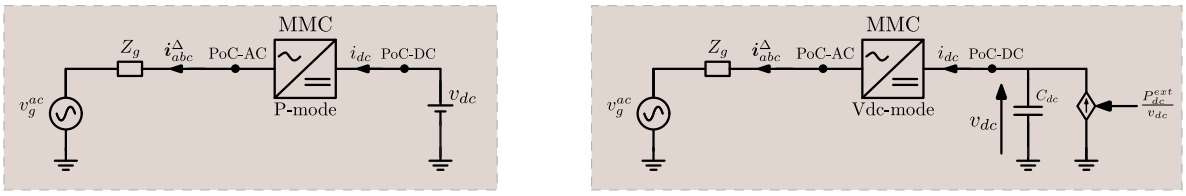

(a) Setup 1 (b) Setup 2

Figure C.1: MMC validation setups: (a) Setup 1 for constant active power control mode (b) Setup 2 for constant DC voltage control mode.

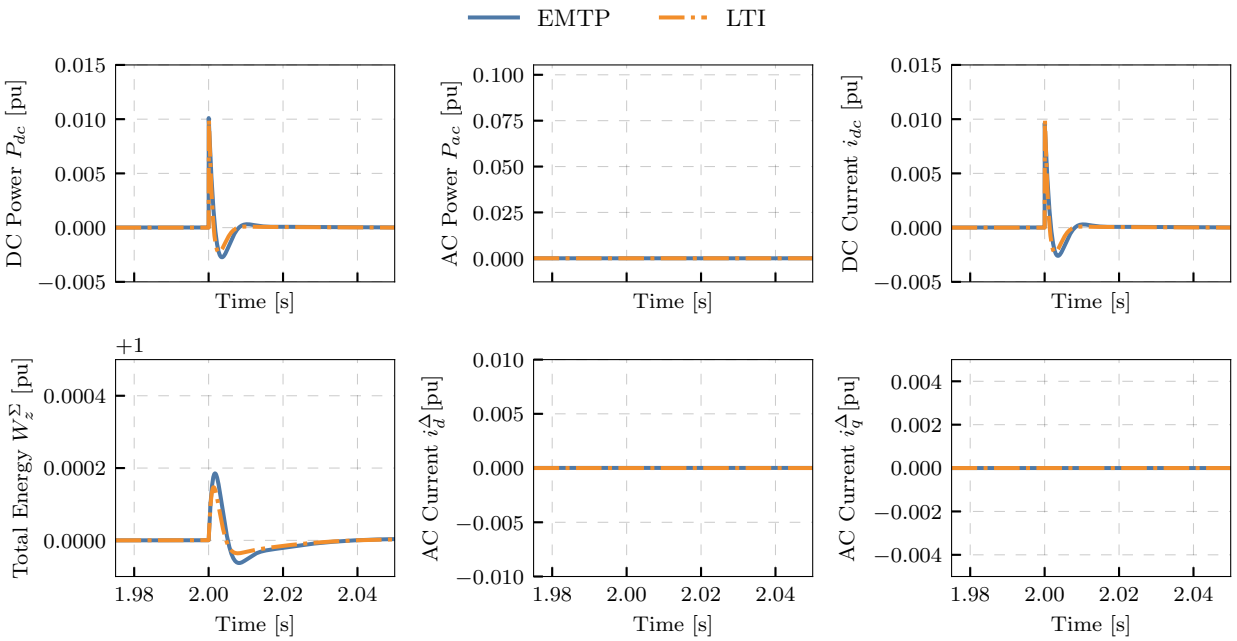

Figure C.2: Validation of the MMC-LTI model under control setting 2 - CM and GFL control - Setup 1 - DC voltage disturbance

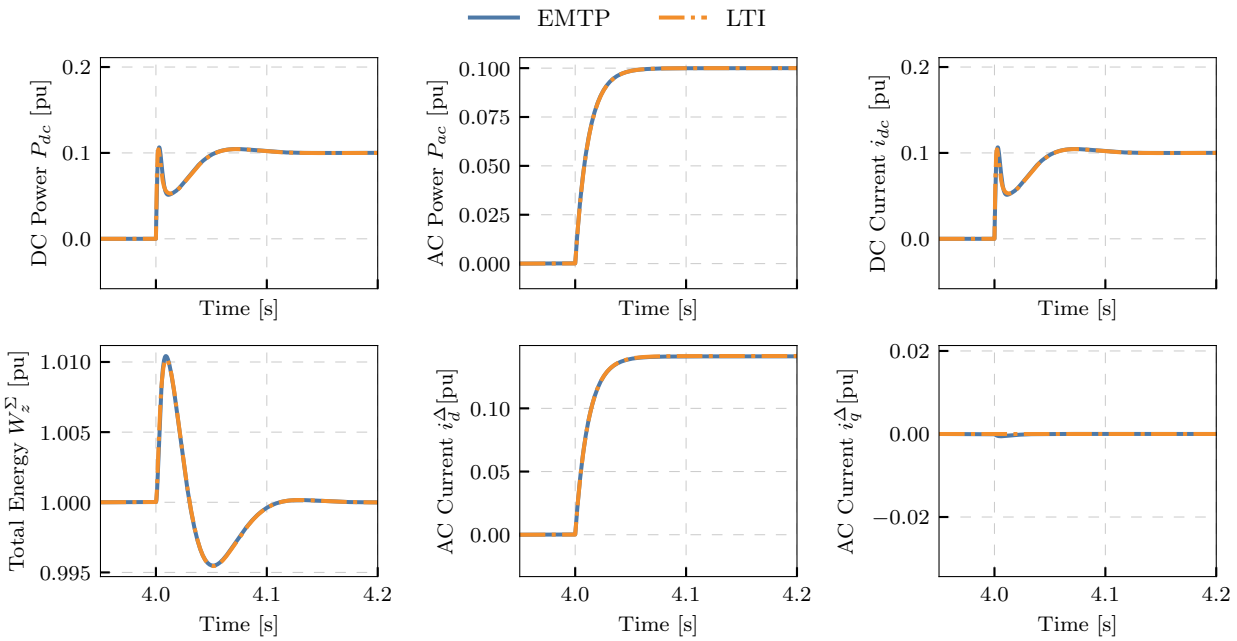

Figure C.3: Validation of the MMC-LTI model under control setting 2 - CM and GFL control - Setup 1 - AC active power reference step change.

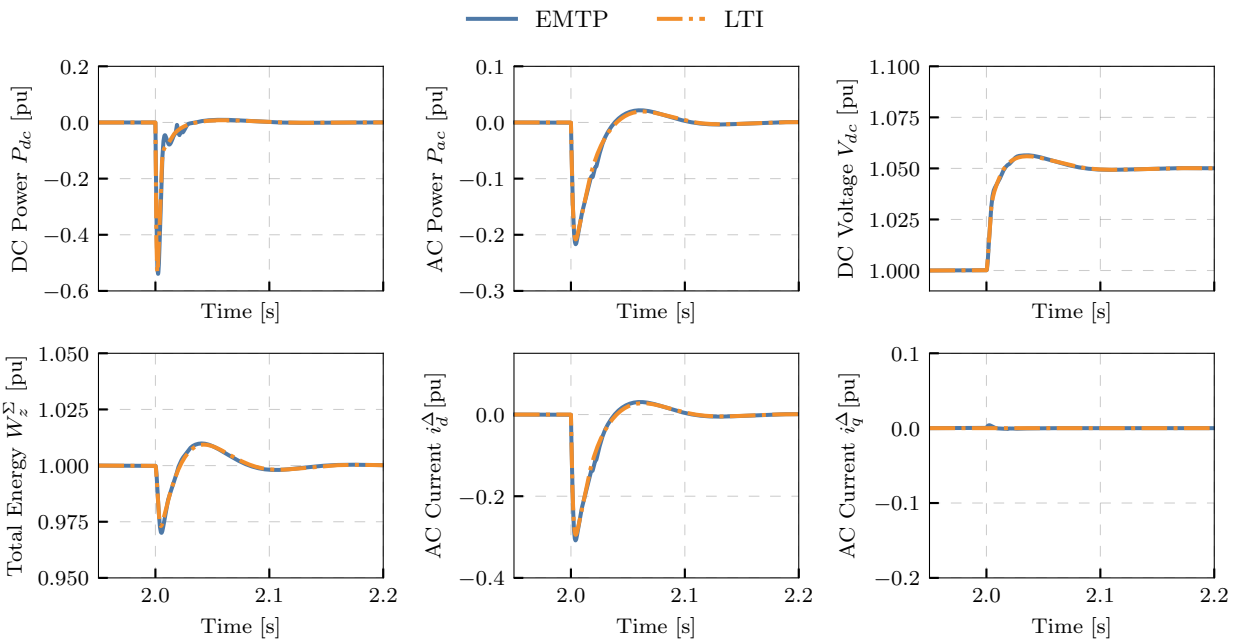

Figure C.4: Validation of the MMC-LTI model under control setting 2 - CM and GFL control - Setup 2 - DC voltage reference change 3 - DC voltage reference change.

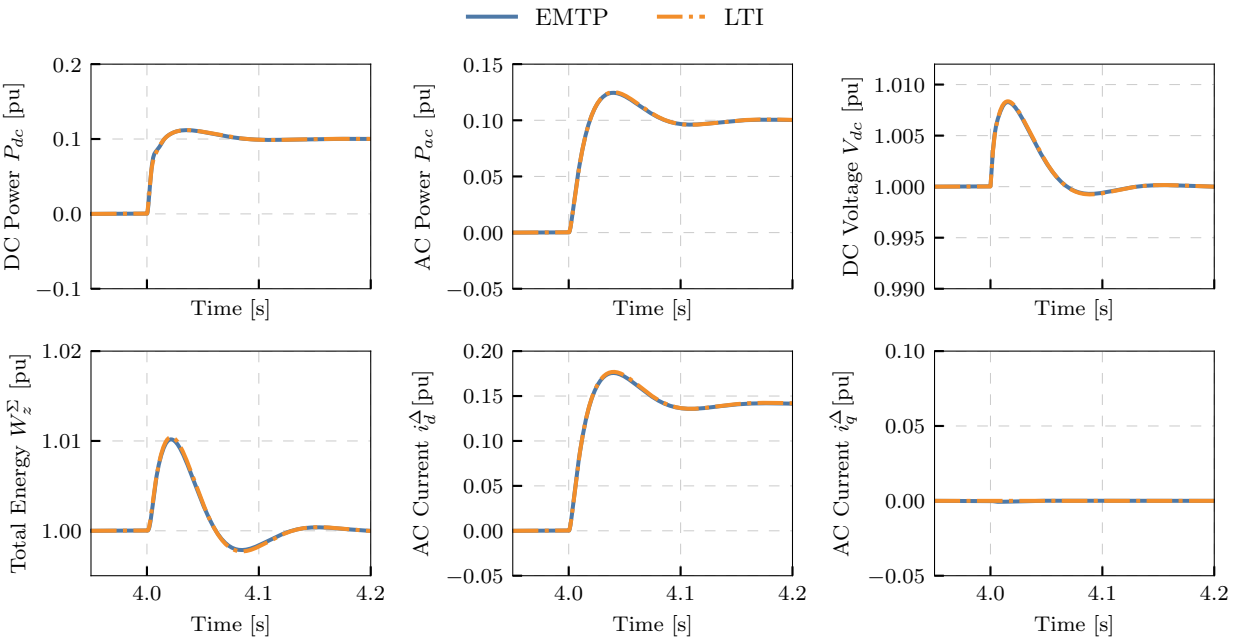

Figure C.5: Validation of the MMC-LTI model under control setting 2 - CM and GFL control - Setup 2 - Active power reference step change.

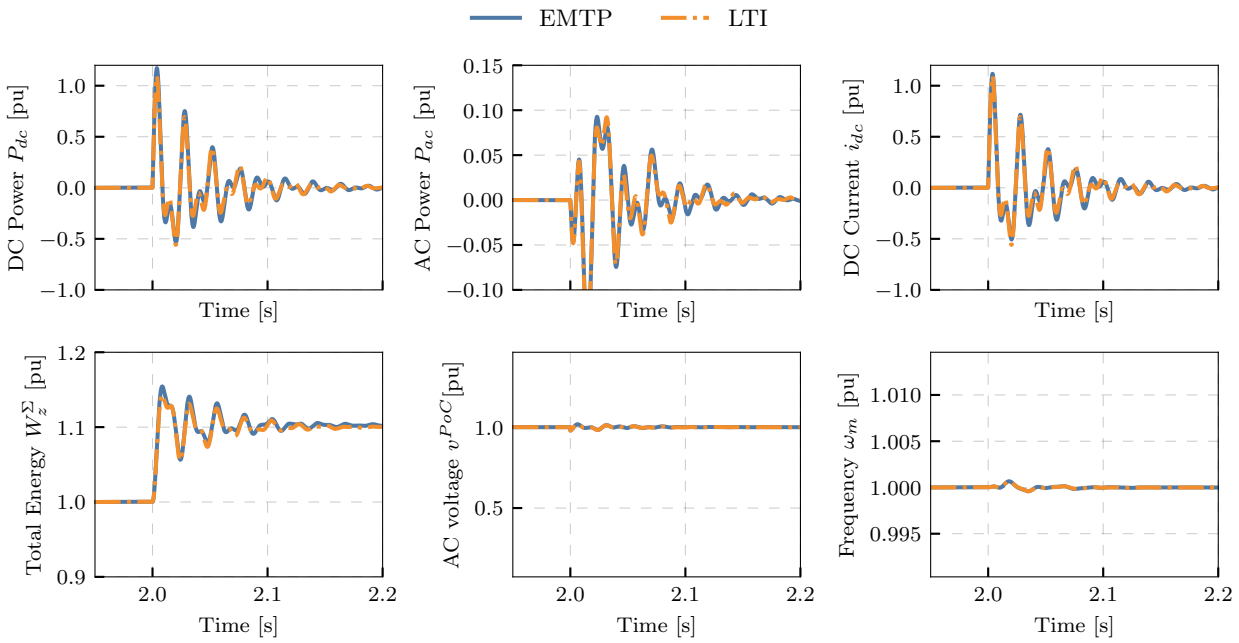

Figure C.6: Validation of the MMC-LTI model under UCM and GFM control - Setup 1 - DC voltage disturbance.

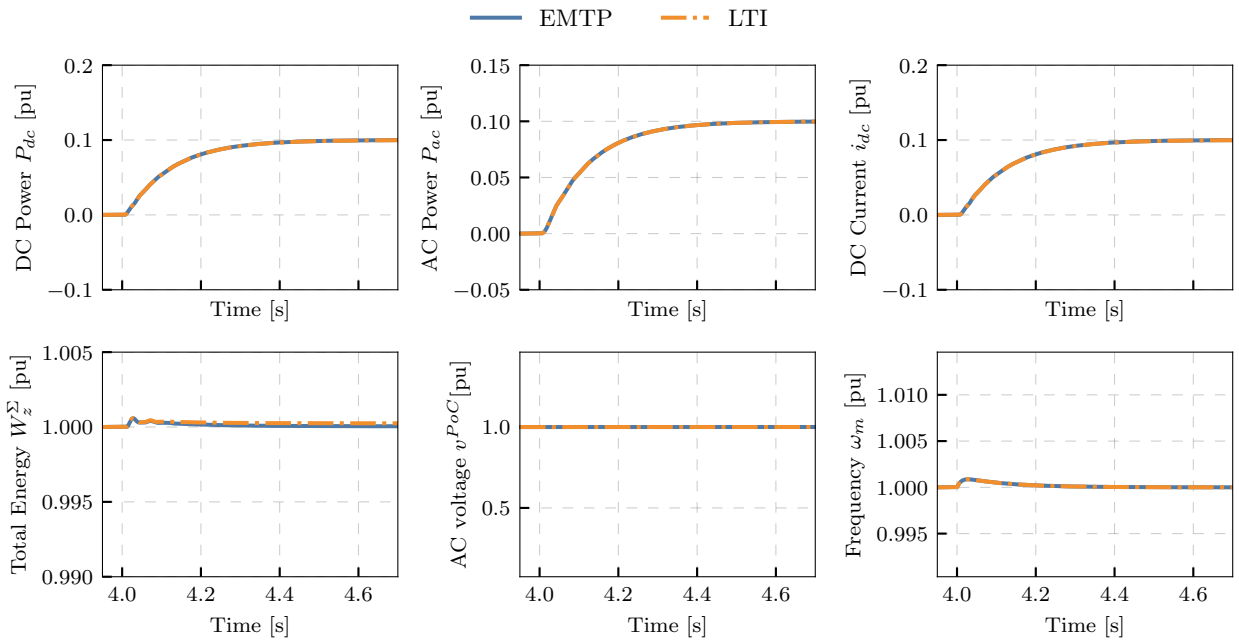

Figure C.7: Validation of the MMC-LTI model under UCM and GFM control - Setup 1 - AC active power reference step change.

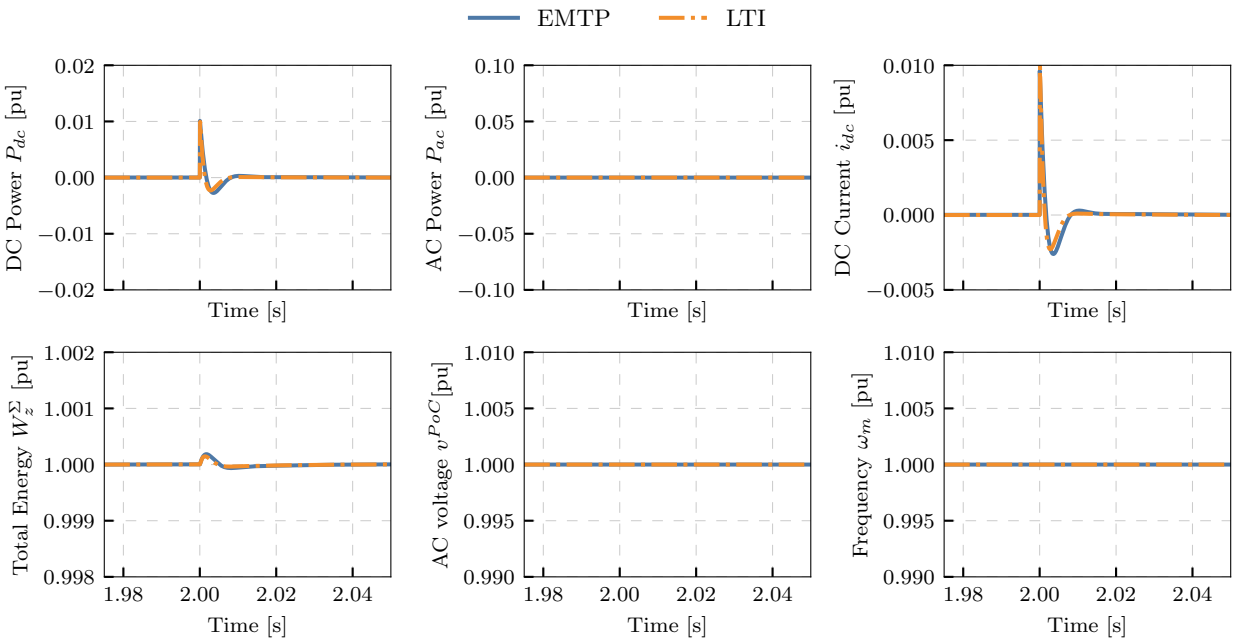

Figure C.8: Validation of the MMC-LTI model under CM and GFM control - Setup 1 - DC voltage disturbance.

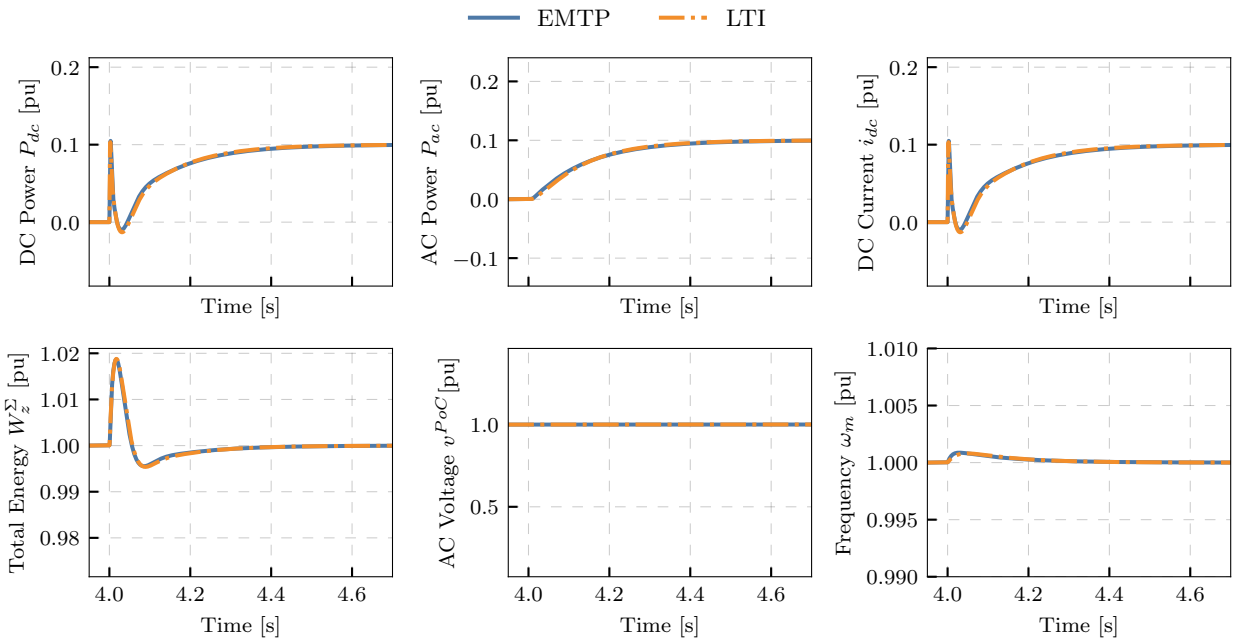

Figure C.9: Validation of the MMC-LTI model under CM and GFM control - Setup 1 - AC active power reference step change.

The following observations can be made for the validation results:

- The MMC-LTI models show good accuracy with the non-linear EMT simulations in all the scenarios, which validates the developed models and the assumptions adopted in their derivation.
- In Fig. C.2, the DC voltage disturbance is directly fed to the output of the i_z^{Σ} current control loop, leading to the DC current controller being insensitive to the disturbance. The small transient response observed in the DC current (and consequentially the DC power) is only due to the delay of the modulation step, which in the LTI model is represented by a first-order delay with a time constant of 10 μs. This confirms the DC voltage disturbance rejection characteristics of the CM. It can also be noted that this transient response is not observed in the AC side variables, which indicate the transient decoupling between the AC and DC side states of the MMC with CM.
- In Fig. C.3, There is no observed 100 Hz oscillation in the response of the AC active power, which indicates that the 100 Hz oscillation in the DC current, compared to UCM. This is because of the explicit control of the zero-sequence current in the CM, which leads to the suppression of the 100 Hz oscillations. Only low frequency response is observed with an AC power control loop tuned for a response time of 50 ms. This is also true for Figs. C.4 and C.5, which correspond to DC voltage control mode.
- For the combination of GFM control with UCM, Fig. C.6 shows that the DC voltage disturbance still induces 100 Hz oscillations in the DC current. This resonance is also observed in the AC power, total energy, AC voltage and frequency responses. This confirms that UCM couples the AC and DC side dynamics, which leads to the propagation of the 100 Hz oscillations to the AC side variables. On the other hand, the step active power reference change in Fig. C.7 does not induce 100 Hz oscillations, which is because of the slow response of the AC power control loop, which is not able to excite the 100 Hz resonance.
- Finally, for the combination of GFM control with CM, Fig. C.8 show similar DC voltage disturbance rejection characteristics as in the GFL control case with CM. Moreover, the 100 Hz oscillations are also suppressed in the DC current response. The step active power reference change in Fig. C.9 show the first order characteristics of the expected inertial response of the GFM control, with no higher-frequency oscillations observed in the response.

D

LTI model of the MMC

The derivation of the LTI representation of the MMC-AAM in the dq frame is presented in this appendix. It is based on the work in [34][1]. The starting point is the set of equations given in (2.14), which are restated below for convenience.

$$\underbrace{2C_{arm}\frac{d}{dt}(\boldsymbol{P_{\theta}^{-1}}\boldsymbol{v}_{cdqz}^{\Delta})}_{\text{LHS}} = \underbrace{\boldsymbol{P_{\theta}^{-1}}\boldsymbol{m}_{dqz}^{\Delta} \circ \boldsymbol{P_{-2\theta}^{-1}}\boldsymbol{i}_{dqz}^{\Sigma} + \frac{1}{2}\boldsymbol{P_{-2\theta}^{-1}}\boldsymbol{m}_{dqz}^{\Sigma} \circ \boldsymbol{P_{\theta}^{-1}}\boldsymbol{i}_{dqz}^{\Delta}}_{\text{RHS}} \tag{D.1a}$$

$$\underbrace{2C_{arm}\frac{d}{dt}(\boldsymbol{P_{-2\theta}^{-1}}\boldsymbol{v}_{cdqz}^{\Sigma})}_{\text{LHS}} = \underbrace{\boldsymbol{P_{-2\theta}^{-1}}\boldsymbol{m}_{dqz}^{\Sigma} \circ \boldsymbol{P_{-2\theta}^{-1}}\boldsymbol{i}_{dqz}^{\Sigma} + \frac{1}{2}\boldsymbol{P_{\theta}^{-1}}\boldsymbol{m}_{dqz}^{\Delta} \circ \boldsymbol{P_{\theta}^{-1}}\boldsymbol{i}_{dqz}^{\Delta}}_{\text{RHS}} \tag{D.1b}$$

$$\boldsymbol{P_{\theta}^{-1}}\boldsymbol{v}_{dqz}^{\Delta} = \frac{-1}{2}\left(\boldsymbol{P_{\theta}^{-1}}\boldsymbol{m}_{dqz}^{\Delta} \circ \boldsymbol{P_{-2\theta}^{-1}}\boldsymbol{v}_{cdqz}^{\Sigma} + \boldsymbol{P_{-2\theta}^{-1}}\boldsymbol{m}_{dqz}^{\Sigma} \circ \boldsymbol{P_{\theta}^{-1}}\boldsymbol{v}_{cdqz}^{\Delta}\right) \tag{D.1c}$$

$$\boldsymbol{P_{-2\theta}^{-1}}\boldsymbol{v}_{dqz}^{\Sigma} = \frac{1}{2}\left(\boldsymbol{P_{-2\theta}^{-1}}\boldsymbol{m}_{dqz}^{\Sigma} \circ \boldsymbol{P_{-2\theta}^{-1}}\boldsymbol{v}_{cdqz}^{\Sigma} + \boldsymbol{P_{\theta}^{-1}}\boldsymbol{m}_{dqz}^{\Delta} \circ \boldsymbol{P_{\theta}^{-1}}\boldsymbol{v}_{cdqz}^{\Delta}\right) \tag{D.1d}$$

$$\underbrace{L_{ac}\frac{d}{dt}(\boldsymbol{P_{\theta}^{-1}}\boldsymbol{i}_{dqz}^{\Delta})}_{\text{LHS}} = \underbrace{\boldsymbol{P_{\theta}^{-1}}\boldsymbol{v}_{dqz}^{\Delta} - \boldsymbol{P_{\theta}^{-1}}\boldsymbol{v}_{dqz}^{PoC} - R_{ac}\boldsymbol{P_{\theta}^{-1}}\boldsymbol{i}_{dqz}^{\Delta}}_{\text{RHS}} \tag{D.1e}$$

$$\underbrace{L_{arm}\frac{d}{dt}(\boldsymbol{P_{-2\theta}^{-1}}\boldsymbol{i}_{dqz}^{\Sigma})}_{\text{LHS}} = \underbrace{\frac{v_{dc}}{2}\mathbf{1} - \boldsymbol{P_{-2\theta}^{-1}}\boldsymbol{v}_{dqz}^{\Sigma} - R_{arm}\boldsymbol{P_{-2\theta}^{-1}}\boldsymbol{i}_{dqz}^{\Sigma}}_{\text{RHS}} \tag{D.1f}$$

For each of the above equations, the following sections will detail its derivation considering two main assumptions:

- Neglecting the 6ω harmonics that appear in the equations.
- Considering that $i_z^{\Delta} = 0$ due to Δ connection of the MMC transformer (no path for the zero-sequence component).

[1] Some sign differences exist compared to the final expressions in [34], which are due to the choice of the Park transformation, specifically, we consider the q axis leading the d axis by 90 degrees.

D.1 Capacitor voltages dynamics - Δ capacitor voltages

Starting from equation D.1a, we multiply both sides by $\boldsymbol{P_\theta}$ from the left. The LHS is written separately as:

$$\boldsymbol{P_\theta}\text{LHS} = 2C_{arm}\boldsymbol{P_\theta}\boldsymbol{P_\theta^{-1}}\frac{d}{dt}(\boldsymbol{v}^{\Delta}_{cdqz}) + 2C_{arm}\boldsymbol{P_\theta}\frac{d\boldsymbol{P_\theta^{-1}}}{dt}\boldsymbol{v}^{\Delta}_{cdqz} \tag{D.2a}$$

$$= 2C_{arm}\frac{d}{dt}(\boldsymbol{v}^{\Delta}_{cdqz}) + 2C_{arm}\begin{bmatrix} 0 & -\omega & 0 \\ \omega & 0 & 0 \\ 0 & 0 & 0 \end{bmatrix}\boldsymbol{v}^{\Delta}_{cdqz} \tag{D.2b}$$

A similar multiplication by $\boldsymbol{P_\theta}$ is performed on the RHS of (D.1a). We consider $m_z^{\Delta} \overset{\text{def}}{=} m_{zd}^{\Delta}\cos(3\omega t) + m_{zq}^{\Delta}\sin(3\omega t)$. This definition will be useful when the zero-sequence component dynamics are addressed. The RHS components are obtained as:

$$\begin{aligned}
\text{RHS}_d = &\left(\frac{m_d^{\Sigma}}{4} + \frac{m_z^{\Sigma}}{2}\right) i_d^{\Delta} - \frac{m_q^{\Sigma}}{4} i_q^{\Delta} + \left(\frac{m_d^{\Sigma}\cos(3\omega t)}{2} + \frac{m_q^{\Sigma}\sin(3\omega t)}{2}\right) i_z^{\Delta} \\
&+ \left(\frac{m_d^{\Delta}}{2} + \frac{m_{zd}^{\Delta}}{2} + \frac{m_{zd}^{\Delta}\cos(6\omega t)}{2} + \frac{m_{zq}^{\Delta}\sin(6\omega t)}{2}\right) i_d^{\Sigma} \\
&+ \left(\frac{m_{zq}^{\Delta}}{2} - \frac{m_q^{\Delta}}{2} - \frac{m_{zq}^{\Delta}\cos(6\omega t)}{2} + \frac{m_{zd}^{\Delta}\sin(6\omega t)}{2}\right) i_q^{\Sigma} \\
&+ m_d^{\Delta} i_z^{\Sigma}
\end{aligned} \tag{D.3a}$$

$$\begin{aligned}
\text{RHS}_q = &-\frac{m_q^{\Sigma}}{4} i_d^{\Delta} + \left(\frac{m_z^{\Sigma}}{2} - \frac{m_d^{\Sigma}}{4}\right) i_q^{\Delta} + \left(\frac{m_q^{\Sigma}\cos(3\omega t)}{2} - \frac{m_d^{\Sigma}\sin(3\omega t)}{2}\right) i_z^{\Delta} \\
&+ \left(\frac{m_{zq}^{\Delta}\cos(6\omega t)}{2} - \frac{m_{zq}^{\Delta}}{2} - \frac{m_q^{\Delta}}{2} - \frac{m_{zd}^{\Delta}\sin(6\omega t)}{2}\right) i_d^{\Sigma} \\
&+ \left(\frac{m_{zd}^{\Delta}}{2} - \frac{m_d^{\Delta}}{2} + \frac{m_{zd}^{\Delta}\cos(6\omega t)}{2} + \frac{m_{zq}^{\Delta}\sin(6\omega t)}{2}\right) i_q^{\Sigma} \\
&+ m_q^{\Delta} i_z^{\Sigma}
\end{aligned} \tag{D.3b}$$

$$\begin{aligned}
\text{RHS}_z = &\left(\frac{m_d^{\Sigma}\cos(3\omega t)}{4} + \frac{m_q^{\Sigma}\sin(3\omega t)}{4}\right) i_d^{\Delta} + \left(\frac{m_q^{\Sigma}\cos(3\omega t)}{4} - \frac{m_d^{\Sigma}\sin(3\omega t)}{4}\right) i_q^{\Delta} + \frac{m_z^{\Sigma}}{2} i_z^{\Delta} \\
&+ \left(\frac{m_d^{\Delta}\cos(3\omega t)}{2} - \frac{m_q^{\Delta}\sin(3\omega t)}{2}\right) i_d^{\Sigma} + \left(\frac{m_q^{\Delta}\cos(3\omega t)}{2} + \frac{m_d^{\Delta}\sin(3\omega t)}{2}\right) i_q^{\Sigma} \\
&+ \left(m_{zd}^{\Delta}\cos(3\omega t) + m_{zq}^{\Delta}\sin(3\omega t)\right) i_z^{\Sigma}
\end{aligned} \tag{D.3c}$$

The components RHS_d and RHS_q directly lead to a an LTI representation if the two main assumptions are considered regarding the 6ω harmonics and i_z^{Δ}. However, RHS_z still contains 3ω harmonics. To solve this, an approach presented in [34] is followed, where the zero-sequence component v_{cz}^{Δ} is modelled in a fictitious α-β frame. Analyzing (D.3c), and grouping terms with $\cos(3\omega t)$ and $\sin(3\omega t)$, respectively, we write $\text{RHS}_z = \text{RHS}_{zd}\cos(3\omega t) + \text{RHS}_{zq}\sin(3\omega t)$. The α component of the fictitious

frame is defined as $\alpha = \mathrm{RHS}_z$, exactly the same as (D.3c), while the β component is 90 degrees shifted clockwise as $\beta = \mathrm{RHS}_{zd}\sin(3\omega t) - \mathrm{RHS}_{zq}\cos(3\omega t)$. These can be expressed in matrix form as:

$$\begin{bmatrix}\alpha\\ \beta\end{bmatrix} = \underbrace{\begin{bmatrix}\cos(3\omega t) & \sin(3\omega t)\\ \sin(3\omega t) & -\cos(3\omega t)\end{bmatrix}}_{\boldsymbol{T_{3\omega}^{-1}}} \begin{bmatrix}\mathrm{RHS}_{zd}\\ \mathrm{RHS}_{zq}\end{bmatrix} \tag{D.4}$$

By only considering the zero-sequence dynamics of the Δ capacitor voltage, it can be written in terms of the α component and the *fictitious* β component as:

$$2C_{arm}\frac{d}{dt}\begin{bmatrix}v_{cz\alpha}^{\Delta}\\ v_{cz\beta}^{\Delta}\end{bmatrix} = \begin{bmatrix}\alpha\\ \beta\end{bmatrix} = \underbrace{\begin{bmatrix}\cos(3\omega t) & \sin(3\omega t)\\ \sin(3\omega t) & -\cos(3\omega t)\end{bmatrix}}_{\boldsymbol{T_{3\omega}^{-1}}} \begin{bmatrix}\mathrm{RHS}_{zd}\\ \mathrm{RHS}_{zq}\end{bmatrix} \tag{D.5}$$

where we define $v_{cz}^{\Delta} \overset{\text{def}}{=} [\ v_{cz\alpha}^{\Delta} \quad v_{cz\beta}^{\Delta}\ ]^T$. Multiplying both sides of (D.5) by $\boldsymbol{T_{3\omega}}$ from the left, we get:

$$2C_{arm}\frac{d}{dt}\begin{bmatrix}v_{czd}^{\Delta}\\ v_{czq}^{\Delta}\end{bmatrix} + 2C_{arm}\begin{bmatrix}0 & 3\omega\\ -3\omega & 0\end{bmatrix}\begin{bmatrix}v_{czd}^{\Delta}\\ v_{czq}^{\Delta}\end{bmatrix} = \begin{bmatrix}\mathrm{RHS}_{zd}\\ \mathrm{RHS}_{zq}\end{bmatrix} \tag{D.6}$$

where v_{czd}^{Δ} and v_{czq}^{Δ} are the d and q components of the zero-sequence capacitor voltage. $\boldsymbol{T_{3\omega}}$ can be seen as the transformation matrix from the α-β frame to a dq frame rotating at 3ω. The final formulations of the d, q, zd, zq components of the Δ capacitor voltages are obtained by equating the LHS obtained in (D.2) and the RHS components in (D.3) and (D.6), which lead to:

$$\begin{aligned}2C_{arm}\frac{dv_{cd}^{\Delta}}{dt} &= +2\omega C_{arm}v_{cq}^{\Delta} + \left(m_d^{\Sigma} + 2m_z^{\Sigma}\right)\frac{i_d^{\Delta}}{4} - m_q^{\Sigma}\frac{i_q^{\Delta}}{4}\\ &\quad + \left(m_d^{\Delta} + m_{zd}^{\Delta}\right)\frac{i_d^{\Sigma}}{2} + \left(m_{zq}^{\Delta} - m_q^{\Delta}\right)\frac{i_q^{\Sigma}}{2} + m_d^{\Delta}i_z^{\Sigma} \qquad \text{(D.7a)}\\ 2C_{arm}\frac{dv_{cq}^{\Delta}}{dt} &= -2\omega C_{arm}v_{cd}^{\Delta} - m_q^{\Sigma}\frac{i_d^{\Delta}}{4} + \left(2m_z^{\Sigma} - m_d^{\Sigma}\right)\frac{i_q^{\Delta}}{4}\\ &\quad - \left(m_{zq}^{\Delta} + m_q^{\Delta}\right)\frac{i_d^{\Sigma}}{2} + \left(m_{zd}^{\Delta} - m_d^{\Delta}\right)\frac{i_q^{\Sigma}}{2} + m_q^{\Delta}i_z^{\Sigma} \qquad \text{(D.7b)}\\ 2C_{arm}\frac{dv_{czd}^{\Delta}}{dt} &= -6\omega C_{arm}v_{czq}^{\Delta} + \frac{m_d^{\Sigma}}{4}i_d^{\Delta} + \frac{m_q^{\Sigma}}{4}i_q^{\Delta} + \frac{m_d^{\Delta}}{2}i_d^{\Sigma} + \frac{m_q^{\Delta}}{2}i_q^{\Sigma} + m_{zd}^{\Delta}i_z^{\Sigma} \qquad \text{(D.7c)}\\ 2C_{arm}\frac{dv_{czq}^{\Delta}}{dt} &= +6\omega C_{arm}v_{czd}^{\Delta} + \frac{m_q^{\Sigma}}{4}i_d^{\Delta} - \frac{m_d^{\Sigma}}{4}i_q^{\Delta} + -\frac{m_q^{\Delta}}{2}i_d^{\Sigma} + \frac{m_d^{\Delta}}{2}i_q^{\Sigma} + m_{zq}^{\Delta}i_z^{\Sigma} \qquad \text{(D.7d)}\end{aligned}$$

D.2 Inserted voltages dynamics - Δ inserted voltages

Starting from equation D.1c, both sides are multiplied by $\boldsymbol{P_\theta}$ from the left. The LHS directly gives $\boldsymbol{v}^{\Delta}_{dqz}$. The RHS is simplified and obtained as:

$$\begin{aligned}
v_d^{\Delta} = &-\frac{1}{4}\left(m_d^{\Delta}+m_{zd}^{\Delta}\right)v_{cd}^{\Sigma}+\frac{1}{4}\left(m_q^{\Delta}-m_{zq}^{\Delta}\right)v_{cq}^{\Sigma}-\frac{1}{2}m_d^{\Delta}v_{cz}^{\Sigma}\\
&-\frac{1}{4}\left(m_d^{\Sigma}+2m_z^{\Sigma}\right)v_{cd}^{\Delta}+\frac{1}{4}m_q^{\Sigma}v_{cq}^{\Delta}-\frac{1}{4}m_d^{\Sigma}v_{czd}^{\Delta}-\frac{1}{4}m_q^{\Sigma}v_{czq}^{\Delta}\\
&-\frac{1}{4}\left(m_{zd}^{\Delta}v_{cq}^{\Sigma}+m_{zq}^{\Delta}v_{cd}^{\Sigma}+m_d^{\Sigma}v_{czq}^{\Delta}+m_q^{\Sigma}v_{czd}^{\Delta}\right)\sin(6\omega t)\\
&+\frac{1}{4}\left(m_{zq}^{\Delta}v_{cq}^{\Sigma}-m_{zd}^{\Delta}v_{cd}^{\Sigma}+m_q^{\Sigma}v_{czq}^{\Delta}-m_d^{\Sigma}v_{czd}^{\Delta}\right)\cos(6\omega t) \qquad \text{(D.8a)}\\
v_q^{\Delta} = &\frac{1}{4}\left(m_d^{\Delta}-m_{zd}^{\Delta}\right)v_{cq}^{\Sigma}+\frac{1}{4}\left(m_q^{\Delta}+m_{zq}^{\Delta}\right)v_{cd}^{\Sigma}-\frac{1}{2}m_q^{\Delta}v_{cz}^{\Sigma}\\
&+\frac{1}{4}m_q^{\Sigma}v_{cd}^{\Delta}+\frac{1}{4}\left(m_d^{\Sigma}-2m_z^{\Sigma}\right)v_{cq}^{\Delta}+\frac{1}{4}m_d^{\Sigma}v_{czq}^{\Delta}-\frac{1}{4}m_q^{\Sigma}v_{czd}^{\Delta}\\
&+\frac{1}{4}\left(m_{zd}^{\Delta}v_{cd}^{\Sigma}-m_{zq}^{\Delta}v_{cq}^{\Sigma}+m_d^{\Sigma}v_{czd}^{\Delta}-m_q^{\Sigma}v_{czq}^{\Delta}\right)\sin(6\omega t)\\
&-\frac{1}{4}\left(m_{zd}^{\Delta}v_{cq}^{\Sigma}+m_{zq}^{\Delta}v_{cd}^{\Sigma}+m_d^{\Sigma}v_{czq}^{\Delta}+m_q^{\Sigma}v_{czd}^{\Delta}\right)\cos(6\omega t) \qquad \text{(D.8b)}\\
v_z^{\Delta} = &-\frac{1}{4}\left(m_d^{\Delta}\cos(3\omega t)-m_q^{\Delta}\sin(3\omega t)\right)v_{cd}^{\Sigma}-\frac{1}{4}\left(m_q^{\Delta}\cos(3\omega t)-m_d^{\Delta}\sin(3\omega t)\right)v_{cq}^{\Sigma}\\
&-\frac{1}{2}\left(m_{zd}^{\Delta}\cos(3\omega t)+m_{zq}^{\Delta}\sin(3\omega t)\right)v_{cz}^{\Sigma}\\
&-\frac{1}{4}\left(m_d^{\Sigma}\cos(3\omega t)+m_q^{\Sigma}\sin(3\omega t)\right)v_{cd}^{\Delta}-\frac{1}{4}\left(m_q^{\Sigma}\cos(3\omega t)-m_d^{\Sigma}\sin(3\omega t)\right)v_{cq}^{\Delta}\\
&-\frac{1}{2}\left(m_z^{\Sigma}\cos(3\omega t)v_{czd}^{\Delta}+m_z^{\Sigma}\sin(3\omega t)v_{czq}^{\Delta}\right) \qquad \text{(D.8c)}
\end{aligned}$$

A similar procedure is followed for the zero-sequence component as in Section D.1, which is modelled in a dq frame rotating at 3ω, yielding v_{zd}^{Δ} and v_{zq}^{Δ}. The process is omitted for brevity, and the final expressions for the inserted voltages are obtained as:

$$\begin{aligned}
v_d^{\Delta} = &-\frac{1}{4}\left(m_d^{\Delta}+m_{zd}^{\Delta}\right)v_{cd}^{\Sigma}+\frac{1}{4}\left(m_q^{\Delta}-m_{zq}^{\Delta}\right)v_{cq}^{\Sigma}-\frac{1}{2}m_d^{\Delta}v_{cz}^{\Sigma}\\
&-\frac{1}{4}\left(m_d^{\Sigma}+2m_z^{\Sigma}\right)v_{cd}^{\Delta}+\frac{1}{4}m_q^{\Sigma}v_{cq}^{\Delta}-\frac{1}{4}m_d^{\Sigma}v_{czd}^{\Delta}-\frac{1}{4}m_q^{\Sigma}v_{czq}^{\Delta} \qquad \text{(D.9a)}\\
v_q^{\Delta} = &\frac{1}{4}\left(m_d^{\Delta}-m_{zd}^{\Delta}\right)v_{cq}^{\Sigma}+\frac{1}{4}\left(m_q^{\Delta}+m_{zq}^{\Delta}\right)v_{cd}^{\Sigma}-\frac{1}{2}m_q^{\Delta}v_{cz}^{\Sigma}\\
&+\frac{1}{4}m_q^{\Sigma}v_{cd}^{\Delta}+\frac{1}{4}\left(m_d^{\Sigma}-2m_z^{\Sigma}\right)v_{cq}^{\Delta}+\frac{1}{4}m_d^{\Sigma}v_{czq}^{\Delta}-\frac{1}{4}m_q^{\Sigma}v_{czd}^{\Delta} \qquad \text{(D.9b)}\\
v_{zd}^{\Delta} = &-\frac{1}{4}m_d^{\Delta}v_{cd}^{\Sigma}-\frac{1}{4}m_q^{\Delta}v_{cq}^{\Sigma}-\frac{1}{2}m_{zd}^{\Delta}v_{cz}^{\Sigma}-\frac{1}{4}m_d^{\Sigma}v_{cd}^{\Delta}-\frac{1}{4}m_q^{\Sigma}v_{cq}^{\Delta}-\frac{1}{2}m_z^{\Sigma}v_{czd}^{\Delta} \qquad \text{(D.9c)}\\
v_{zq}^{\Delta} = &\frac{1}{4}m_q^{\Delta}v_{cd}^{\Sigma}-\frac{1}{4}m_d^{\Delta}v_{cq}^{\Sigma}-\frac{1}{2}m_{zq}^{\Delta}v_{cz}^{\Sigma}-\frac{1}{4}m_q^{\Sigma}v_{cd}^{\Delta}+\frac{1}{4}m_d^{\Sigma}v_{cq}^{\Delta}-\frac{1}{2}m_z^{\Sigma}v_{czq}^{\Delta} \qquad \text{(D.9d)}
\end{aligned}$$

D.3 Capacitor voltage dynamics - Σ capacitor voltages

We start with equation D.1b and multiply both sides by $\boldsymbol{P_{-2\theta}}$ from the left. The LHS is written as:

$$\boldsymbol{P_{-2\theta}}\text{LHS} = 2C_{arm}\boldsymbol{P_{-2\theta}}\boldsymbol{P_{-2\theta}^{-1}}\frac{d}{dt}(\boldsymbol{v}_{cdqz}^{\Sigma}) + 2C_{arm}\boldsymbol{P_{-2\theta}}\frac{d\boldsymbol{P_{-2\theta}^{-1}}}{dt}\boldsymbol{v}_{cdqz}^{\Sigma} \tag{D.10a}$$

$$= 2C_{arm}\frac{d}{dt}(\boldsymbol{v}_{cdqz}^{\Sigma}) + 2C_{arm}\begin{bmatrix} 0 & 2\omega & 0 \\ -2\omega & 0 & 0 \\ 0 & 0 & 0 \end{bmatrix}\boldsymbol{v}_{cdqz}^{\Sigma} \tag{D.10b}$$

Similarly multiplying the RHS by $\boldsymbol{P_{-2\theta}}$ from the left, while considering $m_z^{\Delta} = m_{zd}^{\Delta}\cos(3\omega t) + m_{zq}^{\Delta}\sin(3\omega t)$, yields:

$$\begin{aligned}
\text{RHS}_d = &\left(\frac{m_d^{\Delta}}{4} + \frac{m_{zd}^{\Delta}}{2}\left(\frac{\cos(6\omega t)}{2} + \frac{1}{2}\right) + \frac{m_{zq}^{\Delta}\sin(6\omega t)}{4}\right) i_d^{\Delta} \\
&+ \left(\frac{m_{zq}^{\Delta}}{2}\left(\frac{\cos(6\omega t)}{2} + \frac{1}{2}\right) - \frac{m_{zq}^{\Delta}}{2} - \frac{m_q^{\Delta}}{4} - \frac{m_{zd}^{\Delta}\sin(6\omega t)}{4}\right) i_q^{\Delta} \\
&+ \left(\frac{m_d^{\Delta}\cos(3\omega t)}{2} - \frac{m_q^{\Delta}\sin(3\omega t)}{2}\right) i_z^{\Delta} \\
&+ \left(m_z^{\Sigma} + \frac{m_d^{\Sigma}\cos(6\omega t)}{2} + \frac{m_q^{\Sigma}\sin(6\omega t)}{2}\right) i_d^{\Sigma} \\
&+ \left(\frac{m_d^{\Sigma}\sin(6\omega t)}{2} - \frac{m_q^{\Sigma}\cos(6\omega t)}{2}\right) i_q^{\Sigma} \\
&+ m_d^{\Sigma} i_z^{\Sigma}
\end{aligned} \tag{D.11a}$$

$$\begin{aligned}
\text{RHS}_q = &\left(\frac{m_{zq}^{\Delta}}{2} - \frac{m_q^{\Delta}}{4} - \frac{m_{zq}^{\Delta}}{2}\left(\frac{\cos(6\omega t)}{2} + \frac{1}{2}\right) + \frac{m_{zd}^{\Delta}\sin(6\omega t)}{4}\right) i_d^{\Delta} \\
&+ \left(\frac{m_{zd}^{\Delta}}{2}\left(\frac{\cos(6\omega t)}{2} + \frac{1}{2}\right) - \frac{m_d^{\Delta}}{4} + \frac{m_{zq}^{\Delta}\sin(6\omega t)}{4}\right) i_q^{\Delta} \\
&+ \left(\frac{m_q^{\Delta}\cos(3\omega t)}{2} + \frac{m_d^{\Delta}\sin(3\omega t)}{2}\right) i_z^{\Delta} \\
&+ \left(\frac{m_d^{\Sigma}\sin(6\omega t)}{2} - \frac{m_q^{\Sigma}\cos(6\omega t)}{2}\right) i_d^{\Sigma} \\
&+ \left(m_z^{\Sigma} - \frac{m_d^{\Sigma}\cos(6\omega t)}{2} - \frac{m_q^{\Sigma}\sin(6\omega t)}{2}\right) i_q^{\Sigma} \\
&+ m_q^{\Sigma} i_z^{\Sigma}
\end{aligned} \tag{D.11b}$$

$$\begin{aligned}
\text{RHS}_z = &\frac{m_d^{\Delta}}{4} i_d^{\Delta} + \frac{m_q^{\Delta}}{4} i_q^{\Delta} + \left(\frac{m_{zd}^{\Delta}\cos(3\omega t)}{2} + \frac{m_{zq}^{\Delta}\sin(3\omega t)}{2}\right) i_z^{\Delta} \\
&+ \frac{m_d^{\Sigma}}{2} i_d^{\Sigma} + \frac{m_q^{\Sigma}}{2} i_q^{\Sigma} + m_z^{\Sigma} i_z^{\Sigma}
\end{aligned} \tag{D.11c}$$

Considering the neglection of the 6ω harmonics and considering that $i_z^{\Delta} = 0$, and equating the LHS and RHS components in (D.10) and (D.11), we get the final expressions for $\boldsymbol{v}_{dqz}$dynamics as:

$$2C_{arm}\frac{dv_{cd}^{\Sigma}}{dt} = -4\omega C_{arm}v_{cq}^{\Sigma} + \left(m_d^{\Delta} + m_{zd}^{\Delta}\right)\frac{i_d^{\Delta}}{4} + \left(-m_q^{\Delta} - m_{zq}^{\Delta}\right)\frac{i_q^{\Delta}}{4} + m_z^{\Sigma}i_d^{\Sigma} + m_d^{\Sigma}i_z^{\Sigma} \tag{D.12a}$$

$$2C_{arm}\frac{dv_{cq}^{\Sigma}}{dt} = +4\omega C_{arm}v_{cd}^{\Sigma} + \left(m_{zq}^{\Delta} - m_q^{\Delta}\right)\frac{i_d^{\Delta}}{4} + \left(-m_d^{\Delta} + m_{zd}^{\Delta}\right)\frac{i_q^{\Delta}}{4} + m_z^{\Sigma}i_q^{\Sigma} + m_q^{\Sigma}i_z^{\Sigma} \tag{D.12b}$$

$$2C_{arm}\frac{dv_{cz}^{\Sigma}}{dt} = \frac{m_d^{\Delta}}{4}i_d^{\Delta} + \frac{m_q^{\Delta}}{4}i_q^{\Delta} + \frac{m_d^{\Sigma}}{2}i_d^{\Sigma} + \frac{m_q^{\Sigma}}{2}i_q^{\Sigma} + m_z^{\Sigma}i_z^{\Sigma} \tag{D.12c}$$

D.4 Inserted voltages dynamics - Σ inserted voltages

The dynamics of the Σ inserted voltages in dq representation are obtained by considering D.1d, and multiplying both sides by $\boldsymbol{P_{-2\theta}}$. The LHS leads to $\boldsymbol{v}_{dqz}^{\Sigma}$ and the RHS is simplified as:

$$\begin{aligned}
v_d^{\Sigma} = {} & \frac{1}{4}\left(m_d^{\Delta}v_{cd}^{\Delta} - m_q^{\Delta}v_{cq}^{\Delta} + m_d^{\Delta}v_{czd}^{\Delta} + m_{zd}^{\Delta}v_{cd}^{\Delta} - m_q^{\Delta}v_{czq}^{\Delta} - m_{zq}^{\Delta}v_{cq}^{\Delta}\right) \\
& + \frac{1}{2}\left(m_d^{\Sigma}v_{cz}^{\Sigma} + m_z^{\Sigma}v_{cd}^{\Sigma}\right) \\
& + \frac{1}{4}\Big(m_d^{\Delta}v_{czd}^{\Delta} + m_{zd}^{\Delta}v_{cd}^{\Delta} + m_q^{\Delta}v_{czq}^{\Delta} + m_{zq}^{\Delta}v_{cq}^{\Delta} + m_d^{\Sigma}v_{cd}^{\Sigma} - m_q^{\Sigma}v_{cq}^{\Sigma}\Big)\cos(6\omega t) \\
& + \frac{1}{4}\Big(m_d^{\Delta}v_{czq}^{\Delta} - m_q^{\Delta}v_{czd}^{\Delta} - m_{zd}^{\Delta}v_{cq}^{\Delta} + m_{zq}^{\Delta}v_{cd}^{\Delta} + m_d^{\Sigma}v_{cq}^{\Sigma} + m_q^{\Sigma}v_{cd}^{\Sigma}\Big)\sin(6\omega t)
\end{aligned} \tag{D.13a}$$

$$\begin{aligned}
v_q^{\Sigma} = {} & \frac{1}{4}\left(m_d^{\Delta}v_{czq}^{\Delta} - m_q^{\Delta}v_{cd}^{\Delta} - m_d^{\Delta}v_{cq}^{\Delta} + m_q^{\Delta}v_{czd}^{\Delta} + m_{zd}^{\Delta}v_{cq}^{\Delta} + m_{zq}^{\Delta}v_{cd}^{\Delta}\right) \\
& + \frac{1}{2}\left(m_q^{\Sigma}v_{cz}^{\Sigma} + m_z^{\Sigma}v_{cq}^{\Sigma}\right) \\
& + \frac{1}{4}\Big(m_d^{\Delta}v_{czd}^{\Delta} + m_{zd}^{\Delta}v_{cd}^{\Delta} + m_q^{\Delta}v_{czq}^{\Delta} + m_{zq}^{\Delta}v_{cq}^{\Delta} + m_d^{\Sigma}v_{cq}^{\Sigma} - m_q^{\Sigma}v_{cd}^{\Sigma}\Big)\sin(6\omega t) \\
& + \frac{1}{4}\Big(-m_d^{\Delta}v_{czq}^{\Delta} + m_q^{\Delta}v_{czd}^{\Delta} + m_{zd}^{\Delta}v_{cq}^{\Delta} - m_{zq}^{\Delta}v_{cd}^{\Delta} - m_d^{\Sigma}v_{cd}^{\Sigma} - m_q^{\Sigma}v_{cq}^{\Sigma}\Big)\cos(6\omega t)
\end{aligned} \tag{D.13b}$$

$$\begin{aligned}
v_z^{\Sigma} = {} & \frac{1}{4}\left(m_d^{\Delta}v_{cd}^{\Delta} + m_q^{\Delta}v_{cq}^{\Delta} + m_{zd}^{\Delta}v_{czd}^{\Delta} + m_{zq}^{\Delta}v_{czq}^{\Delta} + m_d^{\Sigma}v_{cd}^{\Sigma} + m_q^{\Sigma}v_{cq}^{\Sigma}\right) + \frac{1}{2}m_z^{\Sigma}v_{cz}^{\Sigma} \\
& + \frac{1}{4}\left(m_{zd}^{\Delta}v_{czq}^{\Delta} + m_{zq}^{\Delta}v_{czd}^{\Delta}\right)\sin(6\omega t) \\
& + \frac{1}{4}\left(m_{zd}^{\Delta}v_{czd}^{\Delta} - m_{zq}^{\Delta}v_{czq}^{\Delta}\right)\cos(6\omega t)
\end{aligned} \tag{D.13c}$$

The 6ω harmonics are neglected as per the main assumption of this LTI model. The final expressions

for the inserted voltages are summarized as:

$$v_d^{\Sigma} = \frac{1}{4}\left[m_d^{\Delta}\left(v_{cd}^{\Delta} + v_{czd}^{\Delta}\right) - m_q^{\Delta}\left(v_{cq}^{\Delta} + v_{czq}^{\Delta}\right) + m_{zd}^{\Delta} v_{cd}^{\Delta} - m_{zq}^{\Delta} v_{cq}^{\Delta}\right] + \frac{1}{2}\left(m_d^{\Sigma} v_{cz}^{\Sigma} + m_z^{\Sigma} v_{cd}^{\Sigma}\right) \tag{D.14a}$$

$$v_q^{\Sigma} = \frac{1}{4}\left[m_d^{\Delta}\left(v_{czq}^{\Delta} - v_{cq}^{\Delta}\right) + m_q^{\Delta}\left(v_{czd}^{\Delta} - v_{cd}^{\Delta}\right) + m_{zd}^{\Delta} v_{cq}^{\Delta} + m_{zq}^{\Delta} v_{cd}^{\Delta}\right] + \frac{1}{2}\left(m_q^{\Sigma} v_{cz}^{\Sigma} + m_z^{\Sigma} v_{cq}^{\Sigma}\right) \tag{D.14b}$$

$$v_z^{\Sigma} = \frac{1}{4}\left(m_d^{\Delta} v_{cd}^{\Delta} + m_q^{\Delta} v_{cq}^{\Delta} + m_{zd}^{\Delta} v_{czd}^{\Delta} + m_{zq}^{\Delta} v_{czq}^{\Delta} + m_d^{\Sigma} v_{cd}^{\Sigma} + m_q^{\Sigma} v_{cq}^{\Sigma}\right) + \frac{1}{2} m_z^{\Sigma} v_{cz}^{\Sigma} \tag{D.14c}$$

D.5 Δ currents dynamics

Starting from (D.1e), we multiply both sides by $\boldsymbol{P_\theta}$ from the left. The LHS gives:

$$\boldsymbol{P_\theta}\text{LHS} = L_{eq}\boldsymbol{P_\theta}\boldsymbol{P_\theta^{-1}}\frac{d}{dt}(\boldsymbol{i}_{dqz}^{\Delta}) + L_{eq}\boldsymbol{P_\theta}\frac{d\boldsymbol{P_\theta^{-1}}}{dt}\boldsymbol{i}_{dqz}^{\Delta} = L_{eq}\frac{d}{dt}(\boldsymbol{i}_{dqz}^{\Delta}) + L_{eq}\begin{bmatrix} 0 & -\omega & 0 \\ \omega & 0 & 0 \\ 0 & 0 & 0 \end{bmatrix}\boldsymbol{i}_{dqz}^{\Delta} \tag{D.15}$$

Multiplying the RHS by $\boldsymbol{P_\theta}$ from the left and simplifying we get:

$$\boldsymbol{P_\theta}\text{RHS} = \boldsymbol{v}_{dqz}^{\Delta} - \boldsymbol{v}_{dqz}^{PoC} - R_{eq}\boldsymbol{i}_{dqz}^{\Delta} \tag{D.16}$$

Since the i_z^{Δ} component is ignored in this derivation, only the d and q components are considered. Equating the LHS and RHS components in (D.15) and (D.16), we get the final expressions for the dynamics of $\boldsymbol{i}_{dq}^{\Delta}$ as:

$$L_{eq}\frac{di_d^{\Delta}}{dt} = +\omega L_{eq} i_q^{\Delta} + v_d^{\Delta} - v_d^{PoC} - R_{eq} i_d^{\Delta} \tag{D.17a}$$

$$L_{eq}\frac{di_q^{\Delta}}{dt} = -\omega L_{eq} i_d^{\Delta} + v_q^{\Delta} - v_q^{PoC} - R_{eq} i_q^{\Delta} \tag{D.17b}$$

The inserted voltages v_d^{Δ} and v_q^{Δ} are respectively obtained in (D.9a) and (D.9b).

D.6 Σ currents dynamics

The Σ currents dynamics are obtained by multiplying both side of (D.1f) by $\boldsymbol{P_{-2\theta}}$ from the left. The LHS is hence written as:

$$\boldsymbol{P_{-2\theta}}\text{LHS} = L_{eq}\boldsymbol{P_{-2\theta}}\boldsymbol{P_{-2\theta}^{-1}}\frac{d}{dt}(\boldsymbol{i}_{dqz}^{\Sigma}) + L_{eq}\boldsymbol{P_{-2\theta}}\frac{d\boldsymbol{P_{-2\theta}^{-1}}}{dt}\boldsymbol{i}_{dqz}^{\Sigma} = L_{eq}\frac{d}{dt}(\boldsymbol{i}_{dqz}^{\Sigma}) + L_{eq}\begin{bmatrix} 0 & 2\omega & 0 \\ -2\omega & 0 & 0 \\ 0 & 0 & 0 \end{bmatrix}\boldsymbol{i}_{dqz}^{\Sigma} \tag{D.18}$$

Similarly multiplying the RHS by $\boldsymbol{P_{-2\theta}}$ from the left, and simplifying, we get:

$$\boldsymbol{P_{-2\theta}}\text{RHS} = \begin{bmatrix} 0 & 0 & \frac{v_{dc}}{2} \end{bmatrix}^T - \boldsymbol{v}_{dqz}^{\Sigma} - R_{eq}\boldsymbol{i}_{dqz}^{\Sigma} \tag{D.19}$$

Equating the LHS and RHS components in (D.18) and (D.19), we get the final expressions for the dynamics of $\boldsymbol{i}_{dqz}^{\Sigma}$ as:

$$L_{eq}\frac{di_d^{\Sigma}}{dt} = -2\omega L_{eq}i_q^{\Sigma} - v_d^{\Sigma} - R_{eq}i_d^{\Sigma} \tag{D.20a}$$

$$L_{eq}\frac{di_q^{\Sigma}}{dt} = +2\omega L_{eq}i_d^{\Sigma} - v_q^{\Sigma} - R_{eq}i_q^{\Sigma} \tag{D.20b}$$

$$L_{eq}\frac{di_z^{\Sigma}}{dt} = \frac{v_{dc}}{2} - v_z^{\Sigma} - R_{eq}i_z^{\Sigma} \tag{D.20c}$$

where the inserted voltages $\boldsymbol{v}_{dqz}^{\Sigma}$ are given in (D.14).
This completes the derivation of the MMC average model in multiple dq frames.

E

DC Cable state-space model

This appendix describes the procedure from which the state-space model of a DC cable is obtained. It is then linearized for small signal analysis.

The starting point is cable wideband model shown in Fig. E.1. The models contains frequency dependent series and shunt elements, which accurately represent the cable behavior in a wide frequency range.

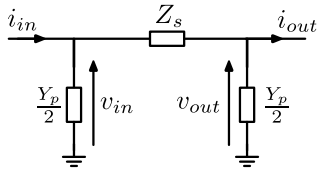

Figure E.1: General representation of the wideband cable model.

The series and shunt elements are described as follows [142]:

$$Z_s = zl\frac{\sinh(\gamma\ell)}{\gamma\ell} \tag{E.1}$$

$$Y_p = yl\frac{\tanh(\frac{\gamma\ell}{2})}{\frac{\gamma\ell}{2}} \tag{E.2}$$

where z and y are the per-length series impedance and shunt admittance, respectively, ℓ is the cable length, $\gamma = \sqrt{zy}$ is the propagation constant. z and y can be described as:

$$z = r(\omega) + j\omega l(\omega) \tag{E.3}$$

$$y = g(\omega) + j\omega c(\omega) \tag{E.4}$$

where r, l, g, c are respectively the series resistance, inductance, and the shunt conductance and capacitance. As can be noticed from equations (E.3) and (E.4), two characteristics limit the derivation of a state space model for the DC cable:

- The hyperbolic correction factors in (E.1) and (E.2), which differentiate the nominal model from the equivalent model. As the cable length decreases, the terms $\frac{\sinh(\gamma l)}{\gamma l}$ and $\frac{\tanh(\frac{\gamma l}{2})}{\frac{\gamma l}{2}}$ approach 1.
- The frequency dependence of the per-length parameters. Fig. 2 shows the frequency dependence of the parameters of the wideband cable with its physical parameters described in Table 1.

To address these challenges, two main simplifications are adopted in [142]. The first simplification is representing the hyperbolic correction factors by cascaded sections. The second simplification is neglecting the frequency dependence of the shunt elements g and c. As can be seen from Fig. 2d, the shunt capacitance does not change with frequency and hence can be considered a constant value. Furthermore, the conductance value is almost constant until a frequency of approximately 100 Hz. On the other hand, the frequency dependence of the series elements is quite more visible from frequencies as low as 10 Hz. Hence, their dependencies cannot be neglected.

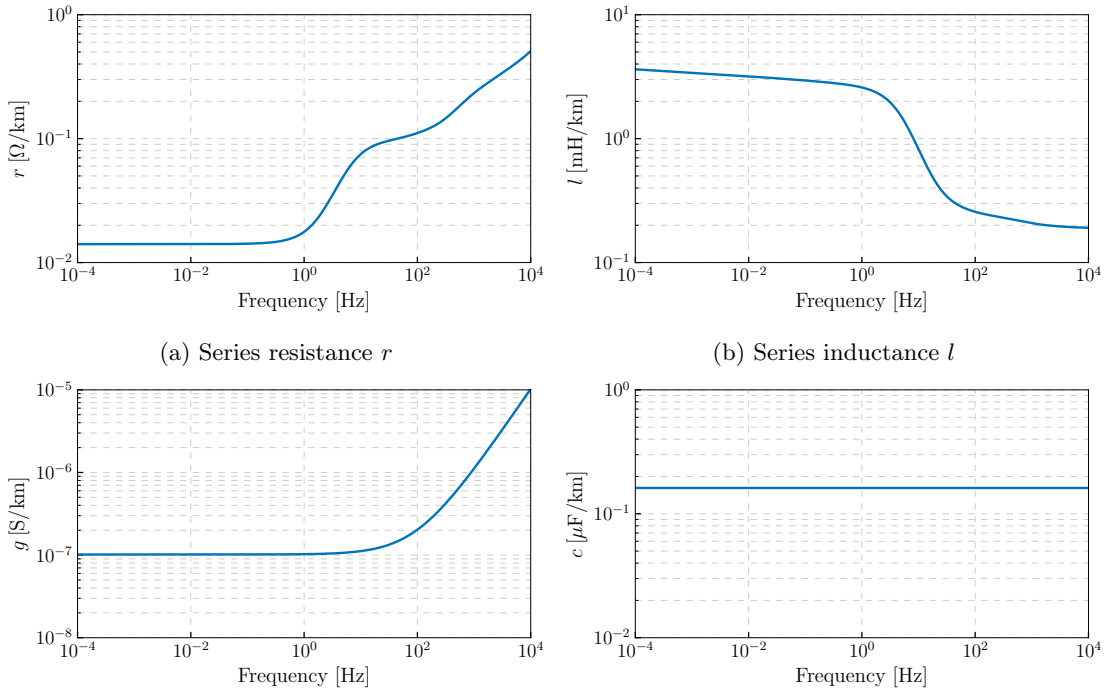

(a) Series resistance r

(b) Series inductance l

(c) Shunt conductance g

(d) Shunt capacitance c

Figure E.2: Frequency dependence of the per-length cable parameters.

Frequency-dependent variables cannot be directly represented in a state space model. Hence, an approximation method is required to represent the series impedance in a state space form, hence the series impedance z is approximated by parallel RL branches, as depicted in Fig. E.3.

It should be noted that increasing the number of both the π sections and the parallel branches will lead to better approximation to the wideband model. However, this comes at the cost of obtaining a high order system with additional computational complexity. In [142], a single section with three parallel branches were identified as sufficient to approximate the wideband model, as shown in Fig. E.4.

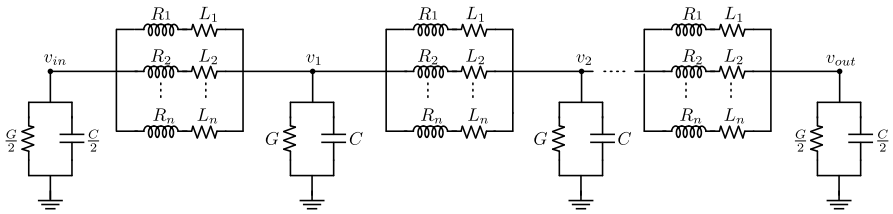

Figure E.3: Equivalent π model with parallel branches.

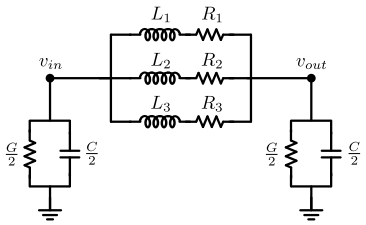

Figure E.4: Equivalent π model with three parallel branches.

In order to obtain the corresponding R and L values, the vector fitting method in [199] is adopted, where we only consider the series impedance of the cable since the frequency dependence of the shunt elements has been neglected. Fig. E.5 shows a comparison between the original series impedance of the wideband model and the fitted data based on three parallel branches. The fitted series impedance can accurately represent the original one with slight mismatch at higher frequencies. The values obtained from the fitting result are described in Table E.2.

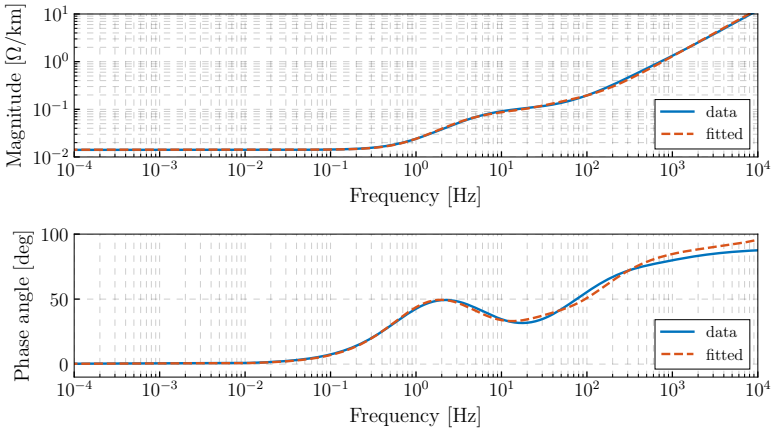

Figure E.5: Vector fitting of the series impedance per km z with three branches.

Combined with the shunt capacitance and conductance, the dynamic equations of the cable model in Fig. E.4 can be written as follows:

$$L_1 \frac{di_1}{dt} = -R_1 i_1 + v_{in} - v_{out} \tag{E.5a}$$

$$L_2 \frac{di_2}{dt} = -R_2 i_2 + v_{in} - v_{out} \tag{E.5b}$$

$$L_3 \frac{di_3}{dt} = -R_3 i_3 + v_{in} - v_{out} \tag{E.5c}$$

$$\frac{C}{2} \frac{dv_{in}}{dt} = i_{in} - i_1 - i_2 - i_3 - \frac{G}{2} v_{in} \tag{E.5d}$$

$$\frac{C}{2} \frac{dv_{out}}{dt} = i_1 + i_2 + i_3 - i_{out} - \frac{G}{2} v_{out} \tag{E.5e}$$

The state vector is defined as $\boldsymbol{x} = [i_1\ i_2\ i_3\ v_{in}\ v_{out}]^T$, the input vector as $\boldsymbol{u} = [i_{in}\ i_{out}]^T$. To verify the accuracy of the state-space model, a frequency scan is performed and compared to the wideband model, with its physical parameters provided in Table E.1. The verification results are shown in Fig. E.6, where the model shows sufficient accuracy up to around 400 Hz. For comparison, a single RL branch mode is also included, which shows significant deviation from the wideband model, at a much lower frequency (around 4 Hz).

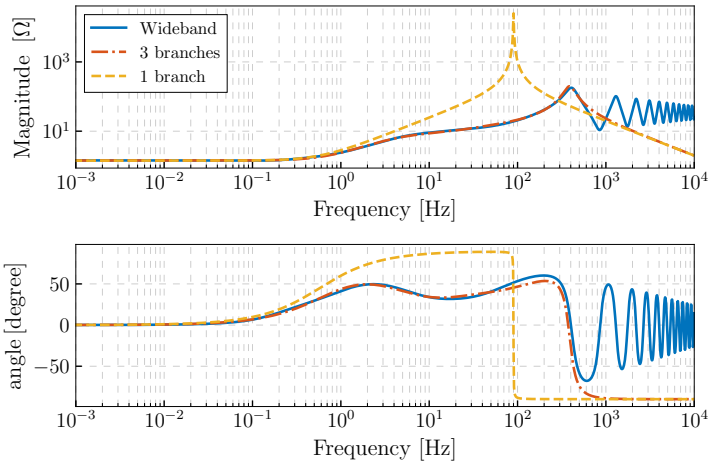

Figure E.6: Verification of the state space cable model

Table E.1: Cable physical data [81]

Parameter	**Conductor 1**	**Conductor 2**	**Conductor 3**
Inside radius R_{in}	0	0.0487	0.0547
Outside radius R_{out}	0.0195	0.0517	0.0587
Resistivity ρ	1.68E-08	2.20E-07	1.80E-07
Relative permeability μ	1	1	10
Insulator permeability μ	1	1	1
Insulator permittivity ϵ_r	2.658	2.3	2.3
Insulator loss factor	0.001	0.001	0.001
Phase number KPH	1	0	0

Table E.2: Fitting results

Parameter	**Value**	**Parameter**	**Value**
r_1	0.2157 Ω/km	l_1	0.26468 mH/km
r_2	0.1862 Ω/km	l_2	1.2 mH/km
r_3	0.0165 Ω/km	l_3	3.7 mH/km

List of Figures

1.1 InterOPERA project consortium [21]. . . . 4
1.2 Future vision of multi-vendor MTDC grids [21]. . . . 4
1.3 Source-load partitioning for impedance-based stability analysis. . . . 10
1.4 Block diagram of the source-load relationship for impedance-based stability analysis. . . . 10
1.5 Thesis structure. . . . 16
1.6 Schematic representation of the contribution related to DC grid equivalent models for standalone compliance and interoperability assessment. . . . 17

2.1 Schematic of the Modular Multilevel Converter with its Arm Average Model (MMC-AAM). 21
2.2 Common MMC submodule topologies. . . . 22
2.3 MMC equivalent circuit utilizing the $\Sigma - \Delta$ variables. . . . 26
2.4 MMC arm capacitor voltages and currents in steady state with their corresponding FFT decomposition. . . . 27
2.5 Average Value Model (AVM) MMC considered when internal energy control is implemented. . . . 31
2.6 Overall MMC control structure. . . . 32
2.7 MMC modulation strategies: (a) Uncompensated Modulation (b) Compensated Modulation. . . . 34
2.8 Different dq reference frames used in the MMC control. . . . 35
2.9 Block diagram of the SRF-PLL. . . . 35
2.10 Block diagram of the Δ currents control. . . . 36
2.11 Block diagram of the Circulating Current Suppression Controller (CCSC) structure under UCM strategy. . . . 37
2.12 Σ currents control structure for the CM strategy. Only i_z^{Σ} control is implemented in the MMC-AVM. . . . 38
2.13 Active/Reactive power control block diagram. . . . 39
2.14 DC voltage control block diagram. . . . 39
2.15 MMC energy control structure for CM strategy. . . . 40
2.16 VSM-GFM synchronization control structure. . . . 41
2.17 AC voltage control structure for GFM strategy with Transient Damping Resistor (TDR). 42
2.18 MMC validation setups: (a) Setup 1 for constant active power control mode (b) Setup 2 for constant DC voltage control mode. . . . 43
2.19 Validation of the MMC LTI model under control setting 1 - DC voltage disturbance. . . . 44
2.20 Validation of the MMC LTI model under control setting 1 - Active power reference step change. . . . 44

2.21 Validation of the MMC LTI model under control setting 1 - DC voltage reference change. 45
2.22 Validation of the MMC LTI model under control setting 1 - DC power disturbance. . . 45

3.1 Hierarchical control structure of MTDC grids. 49
3.2 Illustration of DC voltage operating ranges in an MTDC grid. 51
3.3 DC voltage control modes. 53
3.4 DC voltage droop control concept. 54
3.5 Multi-segment DC voltage droop control. 55
3.6 Additional Segments of multi-segment droop to account for voltage limitation and power headroom exploitation. 56
3.7 Distinction between static and dynamic response of DC voltage droop control. 56
3.8 DC voltage droop implementation options. 57
3.9 Three-terminal HVDC system under study. 58
3.10 Time-domain validation of the linearized 3TDC grid against the non-linear EMT model for the 3TDC system under study. 59
3.11 Eigenvalue trajectories for different values of k_d^A varying from 0.002 pu to 0.2 pu, while $k_d^B = 0.1$ pu. 60
3.12 Eigenvalues trajectories with different values of k_d^A varying from 0.002 pu to 0.005 pu, while $k_d^B = 0.1$ pu. 60
3.13 Participation factor analysis of the unstable eigenvalues. 61
3.14 Eigenvalues trajectories with different values of τ_r^P varying from 30 ms to 200 ms, while $k_d^A = 0.0025$ pu $k_d^B = 0.1$ pu. 61
3.15 Eigenvalues trajectories with different values of k_d^B varying from 0.002 pu to 0.2 pu, while $k_d^A = 0.1$ pu. 62
3.16 Time-domain validation of the unstable case identified in the small-signal analysis, with $k_d^A = 0.0025$ pu and $k_d^B = 0.1$ pu. 63
3.17 Time-domain validation of the stable case with $k_d^A = 0.002$ pu, $k_d^B = 0.1$ pu and $\tau_r^P =$ 100 ms. 63
3.18 Time-domain validation of the stable case with $k_d^A = 0.1$ pu and $k_d^B = 0.002$ pu. 64
3.19 Design space for the two DC voltage droop control options. 65
3.20 Different GFM control strategies found in the literature. 66
3.21 DC voltage droop implementation options with GFM control. 68
3.22 Test setup 2 used to study GFM control and DC voltage droop. 69
3.23 Time-domain response of the MMC with VSM-GFM control and DC voltage droop Scheme A, for different values of inertia constant H. 70
3.24 Time-domain response of the MMC with VSM-GFM control and DC voltage droop Scheme A, for different values of damping coefficient D. 70
3.25 Time-domain response of the MMC with matching-GFM control and DC voltage droop Scheme B, for different values of η. 71
3.26 Time-domain response of the MMC with matching-GFM control and DC voltage droop Scheme B, for different values of lag time constant τ_p. 71
3.27 Time-domain response of the MMC with matching-GFM control and DC voltage droop Scheme B, for different values of lead time constant τ_z. 72

3.28 Time-domain response comparison between matching-GFM control and VSM-GFM control with equivalent inertial and damping response. 72
3.29 Three-terminal HVDC system under study with GFM control and DC voltage droop. . 73
3.30 Time-domain validation of the linearized model against the non-linear EMT model. . . 74
3.31 System poles when varying the droop gain of MMC2 k_d^A from 0.01 pu to 0.2 pu, while $k_d^B = 0.1$ pu. 75
3.32 Participation factor analysis of the unstable eigenvalues. 76
3.33 Variation of : (a) the inertial constant H from 0.5 s to 5 s, (b) the damping coefficient D from 0.1 pu to 1 pu of MMC2, while $k_d^A = 0.03$ pu and $k_d^B = 0.1$ pu. 76
3.34 System poles with varying the droop gain of MMC3 k_d^B from 0.01 pu to 0.2 pu, while $k_d^A = 0.1$ pu. 77
3.35 System response when k_d^A is changed to 0.02 pu at t=5 s and $k_d^B = 0.1$ pu. 77
3.36 System response to a -0.5 pu step change in MMC3 AC power setpoint at t=5 s, with $k_d^B = 0.01$ pu and $k_d^A = 0.1$ pu. 78

4.1 MMC-AVM model for low-frequency DC-side impedance derivation, simplified by neglecting AC-side dynamics. 83
4.2 Outer control representation of the DC-side MMC-AVM. 84
4.3 Test setup for frequency scan of the MMC-DC side impedance using the MMC-AAM model. 85
4.4 Comparison of the DC-side impedance frequency response between the DC-side AVM in constant power mode and a frequency scan of the MMC-AAM. The simplified model accurately captures low-frequency behavior up to around 25 Hz. 86
4.5 DC-side MMC-AVM with DC reactor for stability analysis using impedance-based criterion. 86
4.6 Impedance frequency response of the DC-side MMC AVM in constant power mode versus inductive grid impedance. Increasing L_{dcr} reduces the gain crossover frequency, decreasing the phase margin and potentially causing instability. 87
4.7 Comparison of the DC-side impedance frequency response between the MMC-AVM in constant power mode and with DC voltage droop control ($k_d = 0.1$ p.u.) 87
4.8 Impedance frequency response of the DC-side MMC AVM with DC voltage droop control versus the DCR impedance of 600 mH. 88
4.9 Standalone MMC test setup with DC reactor for validation of the low-frequency MMC impedance analysis and performing further studies. 88
4.10 Process of deriving the DC-side impedance at the DC-PoC from the corresponding state-space representation. 89
4.11 Comparison of the DC-side impedance frequency response between the MMC-AAM frequency scan and the derived MMC-DC side impedance from the state-space model. The results show good agreement in both magnitude and phase across the frequency range of 1 Hz to 1k Hz. 89
4.12 Frequency response of the return ratio for different MMC operating points P_0 with $L_{dcr} = 400$ mH. The phase margin decreases as the power increases in inverter direction (positive P_0). 90

4.13 Frequency response of the return ratio for the standalone MMC operating in constant power mode $\mathcal{L}(s)$ for different values of L_{dcr}. Increasing L_{dcr} reduces the magnitude without affecting the phase, leading to instability above a critical value $L_{dcr}^{cr} = 198$ mH. 90
4.14 Frequency response of the return ratio for different outer control strategies with $L_{dcr} =$ 400 mH and $P_0 = 1$ p.u. Both DC voltage droop control and DC voltage control mode improve the phase margin compared to constant power mode. 91
4.15 Effect of DC voltage droop control on the return ratio for $L_{dcr} = 400$ mH. A higher droop action (lower k_d) increases the phase margin and improves damping in the low-frequency range. 92
4.16 Stability map of the standalone MMC operating in constant power mode, showing the stable and unstable regions for different values of L_{dcr} and operating points P_0. Larger L_{dcr} values reduce the stable operating region, especially in inverter mode (positive P_0). 92
4.17 Principle of active damping: a lead compensator generates a voltage signal v_{lead} in response to DC current variations, which can be considered as a virtual impedance. . . 93
4.18 Integration of the lead compensator into the MMC control structure, acting on the zero-sequence circulating current i_z^{Σ}. 93
4.19 Return ratio with and without lead compensation for $L_{dcr} = 400$ mH and $P_0 = 1$ p.u. Lead compensation improves the phase margin from -5° to 28°, thus stabilizing the system. 94
4.20 DC voltage response of the MMC to a step disturbance comparing uncompensated and lead-compensated systems with $P_0 = 1$ p.u. and $L_{dcr} = 400$ mH. 94
4.21 Four-terminal meshed DC grid under study. 95
4.22 Eigenvalues of the 4T DC grid at operating point 1 with St1&2 in inverter mode, showing instability as DCR values increase. 96
4.23 Participation factor analysis of the unstable eigenvalues of the 4TDC grid at operating point 1, showing the main contributing states. 97
4.24 Eigenvalues of the 4T DC grid at operating point 2 with St1&2 in rectifier mode, the system remains stable for all DCR values. 97
4.25 Eigenvalues of the 4T DC grid at operating point 1 but with St2 switched to DC voltage droop control, showing system stability for all DCR values. 98
4.26 Eigenvalues of the 4T DC grid at operating point 1 with lead compensator applied to St1&2, showing system stability for all DCR values. 98
4.27 Time-domain response of the 4TDC grid considering Case 1; St1 and St2 in inverter mode, with 400 mH DCRs. 99
4.28 Time-domain response of the 4TDC grid considering Case 2; St1 and St2 in rectifier mode, with 400 mH DCRs. 100
4.29 Time-domain response of the 4TDC grid considering Case 3; droop control is applied to St2 at $t = 5$ s, with 400 mH DCRs. 100
4.30 Time-domain response of the 4TDC grid considering Case 4; lead compensator is applied to St1 and St2 at $t = 5$ s, with 400 mH DCRs. 101
4.31 Magnitude frequency response from AC power reference of St1 to DC voltages at each station, for Cases 1 and 2. St1 and St2 in UCM and CM respectively, with no DCRs in the grid. 103

4.32 Magnitude frequency response from AC power reference of St1 to DC voltages at each station, for Cases 3 and 4. St1 and St2 in UCM and CM respectively, with DCRs of 300 mH at each station. 103
4.33 Time-domain DC voltage responses to a power step at St1 for the four cases considered. Without DCRs, DC voltages respond similarly; with DCRs, responses are decoupled, and CM increases voltage deviation at the station closest to the disturbance (St1). . . 104

5.1 Concept of AC and DC grid equivalents for standalone compliance and stability assessment of converter stations. 109
5.2 Three-terminal DC grid under study. 110
5.3 Three-terminal DC-grid model for deriving the grid impedance at DC-PoC1. 111
5.4 Methodology to derive the DC-grid impedance at the DC-PoC from the corresponding state-space representation. 111
5.5 Comparison between the analytically derived grid impedance and the frequency scan result. 111
5.6 Time-domain response of the DC current at DC-PoC1 to a step change in the DC voltage source. 112
5.7 Impact of DCR size on the grid impedance seen at DC-PoC1. 113
5.8 Impact of the DCR size: (a) Changing only L_{dcr}^{St1}, with L_{dcr}^{St2} and L_{dcr}^{St3} maintained at 200 mH and (b) Changing only L_{dcr}^{St2} and L_{dcr}^{St3}, with L_{dcr}^{St1} maintained at 200 mH. 113
5.9 Grid impedance seen at DC-PoC1 for different operating points considering P-mode operation of the remote stations. 114
5.10 Impact of the control mode of Station 2 on the grid impedance at DC-PoC1. 115
5.11 Impact of the droop gain k_d of Station 2 on the grid impedance at DC-PoC1. 116
5.12 Impact of the operating point on the grid impedance at DC-PoC1 when Station 2 operates in Vdc-droop control mode. 116
5.13 Impact of the grid strength of the remote stations on the grid impedance at DC-PoC1. 117
5.14 Impact of the GFM control of the remote stations on the grid impedance at DC-PoC1. 118
5.15 RLC equivalent model connected to the converter station. 119
5.16 Validation of the RLC model against the full grid impedance when both remote stations are in P-mode following (5.1), with different operating points for St 2&3. 119
5.17 Extended RLC equivalent to cover droop control mode of station 2. 120
5.18 Validation of the extended RLC model against the full grid impedance when St 2 operates in DC voltage droop following (5.3), with different operating points for St 3. . . . 121
5.19 Comparison between the fitted grid impedance and the actual grid impedance when both remote stations are in P-mode, with different operating points for St 2&3. 122
5.20 Comparison between the fitted grid impedance and the actual grid impedance for Case 2 (Station 2 operating in DC voltage droop control mode), with different operating points for St 3. 122
5.21 Implementation of the frequency-dependent grid impedance in time-domain simulation. 123
5.22 Step reference response of the DC voltage of Station 1 for the 3T grid model, the RLC model, and the frequency-dependent model. 124
5.23 Step reference response of the DC voltage of Station 1 for the 3T grid model, the extended RLC model, and the frequency-dependent model. 124

5.24 Bode plot of Z_{MMC}, Z_{eq1}, and the return ratio $\mathcal{L} = \frac{Z_{MMC}}{Z^{dc}_{eq1}}$. 125
5.25 Nyquist plot of the return ratio $\mathcal{L} = \frac{Z_{MMC\cdot}}{Z^{dc}_{eq1}}$. 125
5.26 Bode plot of the Z_{MMC}, Z^{dc}_{fit}, and the return ratio $\mathcal{L} = \frac{Z_{MMC}}{Z^{dc}_{fit}}$ (a) Full plot (b) Zoomed plot. 126
5.27 (a) Nyquist plot of the return ratio $\mathcal{L} = \frac{Z_{MMC}}{Z^{dc}_{fit}}$ (b) Zoomed plot. 127
5.28 Comparison of the closed-loop poles obtained with the full grid model, the RLC model, and the frequency-dependent fitted model. 127
5.29 DUT response to a 0.05 step change in the DC voltage setpoint at $t = 2$s. 128
5.30 Flowchart for the application of the proposed equivalent models in a multi-vendor compliance testing procedure. 130

B.1 Park transformation 142
B.2 Clarke transformation. 142

C.1 MMC validation setups: (a) Setup 1 for constant active power control mode (b) Setup 2 for constant DC voltage control mode. 144
C.2 Validation of the MMC-LTI model under control setting 2 - CM and GFL control - Setup 1 - DC voltage disturbance 144
C.3 Validation of the MMC-LTI model under control setting 2 - CM and GFL control - Setup 1 - AC active power reference step change. 144
C.4 Validation of the MMC-LTI model under control setting 2 - CM and GFL control - Setup 2 - DC voltage reference change 3 - DC voltage reference change. 145
C.5 Validation of the MMC-LTI model under control setting 2 - CM and GFL control - Setup 2 - Active power reference step change. 145
C.6 Validation of the MMC-LTI model under UCM and GFM control - Setup 1 - DC voltage disturbance. 146
C.7 Validation of the MMC-LTI model under UCM and GFM control - Setup 1 - AC active power reference step change. 146
C.8 Validation of the MMC-LTI model under CM and GFM control - Setup 1 - DC voltage disturbance. 147
C.9 Validation of the MMC-LTI model under CM and GFM control - Setup 1 - AC active power reference step change. 147

E.1 General representation of the wideband cable model. 157
E.2 Frequency dependence of the per-length cable parameters. 158
E.3 Equivalent π model with parallel branches. 159
E.4 Equivalent π model with three parallel branches. 159
E.5 Vector fitting of the series impedance per km z with three branches. 159
E.6 Verification of the state space cable model 160

List of Tables

2.1 MMC LTI model validation scenarios 43
2.2 Step tests for MMC LTI model validation 43

3.1 Three-terminal DC grid system parameters 58
3.2 GFM functional requirements proposed in [143] 65
3.3 Three-terminal DC grid system parameters with GFM control 73
3.4 Design space considerations for DC voltage droop with GFM control 79

4.1 Operating point 1 of the 4T DC grid. 95
4.2 Operating point 2 of the 4T DC grid. 96
4.3 Mitigation measures to the stability issues introduced by DCRs in the 4T DC grid, with practical considerations for each solution. 102

5.1 Comparison between the two proposed DC equivalent models. 128

A.1 MMC physical parameters 139
A.2 MMC control parameters 140
A.3 AC grid parameters 140

B.1 Base values for the per-unit system 141

C.1 MMC LTI model validation scenarios 143
C.2 Step tests for MMC LTI model validation 143

E.1 Cable physical data [81] 160
E.2 Fitting results 160

Bibliography

[1] European Commission, "The European Green Deal." Official website of the European Union, 2024. Accessed: 2024-05-22.

[2] J. Dakic, M. Cheah-Mane, O. Gomis-Bellmunt, and E. Prieto-Araujo, "Hvac transmission system for offshore wind power plants including mid-cable reactive power compensation: Optimal design and comparison to vsc-hvdc transmission," *IEEE Transactions on Power Delivery*, vol. 36, pp. 2814–2824, Oct. 2021.

[3] U. Axelsson, "The gotland hvdc light project - experiences from trial and commercial operation," in *16th International Conference and Exhibition on Electricity Distribution (CIRED 2001)*, vol. 2001, pp. v1–3–v1–3, IEE, 2001.

[4] O. E. Oni, I. E. Davidson, and K. N. Mbangula, "A review of lcc-hvdc and vsc-hvdc technologies and applications," in *2016 IEEE 16th International Conference on Environment and Electrical Engineering (EEEIC)*, pp. 1–7, IEEE, June 2016.

[5] *HVDC Grids: For Offshore and Supergrid of the Future*. Wiley, Feb. 2016.

[6] ABB, "Abb power grids supports china to build multi-terminal power transmission projects," 2020. Press release, June 15, 2020. Accessed: 2026-03-09.

[7] Hitachi Energy, "Changji-guquan uhvdc link," 2019.

[8] M. Barnes, "HVDC VSC projects," *VSC-HVDC Newsletter*, vol. 9, Mar. 2021.

[9] D2.1, "Resilience needs and objectives," deliverable d2.1, HVDC Wise, 2023.

[10] J. A. Ansari, C. Liu, and S. A. Khan, "MMC Based MTDC Grids: A Detailed Review on Issues and Challenges for Operation, Control and Protection Schemes," *IEEE Access*, vol. 8, pp. 168154–168165, 2020.

[11] North Sea Wind Power Hub, "North sea wind power hub consortium," 2024. Accessed: 2024-05-20.

[12] The National HVDC Centre, "Aquila interoperability package: Multi-terminal, multi-vendor dc hub," 2024. Accessed: 2024-05-20.

[13] M. Wang, W. Leterme, G. Chaffey, J. Beerten, and D. Van Hertem, "Multi-vendor interoperability in hvdc grid protection: State-of-the-art and challenges ahead," *IET Generation, Transmission & Distribution*, vol. 15, pp. 2153–2175, Mar. 2021.

[14] P. Torwelle, K. Shinoda, P. Verrax, A. Bertinato, H. F. de Barros, D. Gomez-Acero, M. Elsodany, E. Witz, and A. Saçıak, "Functional requirements for hvdc grid systems and subsystems," deliverable d2.1, InterOPERA, 2024. [Online].

[15] W. B4.85, "Interoperability in hvdc systems based on partially open software," Tech. Rep. TB961, CIGRE, 2025.

[16] ENTSO-E, "Entso-e standardized control interface for hvdc sil/hil conformity tests," tech. rep., European Network of Transmission System Operators for Electricity, 2020.

[17] IEC, "High voltage direct current (hvdc) grid systems and connectedconverter stations - guideline and parameter lists for functional specifications - part 1: Guideline," tech. rep., TS 63291, 2023.

[18] CENELEC, "Hvdc grid systems and connected converter stations – guideline and parameter lists for functional specifications – part 1: Guidelines," Technical Specification CLC/TS 50654-1:2020, European Committee for Electrotechnical Standardization, 2020.

[19] D9.3, "Final Recommendations For Interoperability of Multivendor HVDC Systems," tech. rep., BEST PATHS, 2018.

[20] PROMOTioN project, "Executive summary," tech. rep., PROMOTioN - Progress on Meshed HVDC Offshore Transmission Networks, 2020.

[21] Interopera Project, "Interopera."

[22] J.-J. E. Slotine and W. Li, *Applied nonlinear control*. Englewood Cliffs, NJ [u.a.]: Prentice Hall, internat. ed. ed., 1991.

[23] P. Kundur, J. Paserba, V. Ajjarapu, G. Andersson, A. Bose, C. Canizares, N. Hatziargyriou, D. Hill, A. Stankovic, C. Taylor, T. Van Cutsem, and V. Vittal, "Definition and classification of power system stability ieee/cigre joint task force on stability terms and definitions," *IEEE Transactions on Power Systems*, vol. 19, pp. 1387–1401, Aug. 2004.

[24] M. Larsson, "Harmonic resonance and control interoperability analysis for hvdc connected wind farms," 2017.

[25] C. Yin, X. Xie, S. Xu, and C. Zou, "Review of oscillations in vsc-hvdc systems caused by control interactions," *The Journal of Engineering*, vol. 2019, pp. 1204–1207, Dec. 2018.

[26] Y. Cheng, L. Fan, J. Rose, S.-H. Huang, J. Schmall, X. Wang, X. Xie, J. Shair, J. R. Ramamurthy, N. Modi, C. Li, C. Wang, S. Shah, B. Pal, Z. Miao, A. Isaacs, J. Mahseredjian, and J. Zhou, "Real-world subsynchronous oscillation events in power grids with high penetrations of inverter-based resources," *IEEE Transactions on Power Systems*, vol. 38, pp. 316–330, Jan. 2023.

[27] N. Hatziargyriou, J. Milanovic, C. Rahmann, V. Ajjarapu, C. Canizares, I. Erlich, D. Hill, I. Hiskens, I. Kamwa, B. Pal, P. Pourbeik, J. Sanchez-Gasca, A. Stankovic, T. Van Cutsem, V. Vittal, and C. Vournas, "Definition and classification of power system stability – revisited & extended," *IEEE Transactions on Power Systems*, vol. 36, pp. 3271–3281, July 2021.

[28] W. C4.49, "Multi-frequency stability of converter-based modern power systems," tech. rep., CIGRE, 2024.

[29] H. Wu, X. Wang, and L. H. Kocewiak, "Impedance-based stability analysis of voltage-controlled mmcs feeding linear ac systems," *IEEE Journal of Emerging and Selected Topics in Power Electronics*, vol. 8, pp. 4060–4074, Dec. 2020.

[30] T. Gebremedhin, Y. Chen, L. Xu, and D. Chen, "Interactions and stability analysis of grid-forming and grid-following converters in close proximity: an impedance-based approach," *IET Conference Proceedings*, vol. 2024, pp. 263–269, Mar. 2025.

[31] H. D. Hui Ding, Y. W. Yankun Wu, Y. Z. Yi Zhang, Y. M. Yulong Ma, and R. Kuffel, "System stability analysis of xiamen bipolar mmc-hvdc project," in *12th IET International Conference on AC and DC Power Transmission (ACDC 2016)*, pp. 41 (6 .)–41 (6 .), Institution of Engineering and Technology, 2016.

[32] K. Ji, H. Pang, J. Yang, and G. Tang, "Dc side harmonic resonance analysis of mmc-hvdc considering wind farm integration," *IEEE Transactions on Power Delivery*, vol. 36, pp. 254–266, Feb. 2021.

[33] K. Ji, G. Tang, J. Yang, Y. Li, and D. Liu, "Harmonic stability analysis of mmc-based dc system using dc impedance model," *IEEE Journal of Emerging and Selected Topics in Power Electronics*, vol. 8, pp. 1152–1163, June 2020.

[34] G. Bergna-Diaz, J. Freytes, X. Guillaud, S. D'Arco, and J. A. Suul, "Generalized Voltage-Based State-Space Modeling of Modular Multilevel Converters With Constant Equilibrium in Steady State," *IEEE Journal of Emerging and Selected Topics in Power Electronics*, vol. 6, pp. 707–725, jun 2018.

[35] T. Roose, A. Lekic, M. M. Alam, and J. Beerten, "Stability analysis of high-frequency interactions between a converter and hvdc grid resonances," *IEEE Transactions on Power Delivery*, vol. 36, pp. 3414–3425, Dec. 2021.

[36] M. Cheah-Mane, J. Arevalo-Soler, D. Moutevelis, E. Mateu-Barriendos, E. Prieto-Araujo, O. Gomis-Bellmunt, J. Renedo, M. Martin-Almenta, E. Nuño-Martinez, S. Martinez-Villanueva, J. Jung, N. Kim, and Y. Kwon, "A new paradigm for small-signal stability analysis in modern power systems: Challenges, models, and methods in power systems rich in power electronics," *IEEE Power and Energy Magazine*, vol. 24, pp. 67–81, Jan. 2026.

[37] Y. Zhu, Y. Gu, Y. Li, and T. Green, "Participation analysis in impedance models: The grey-box approach for power system stability," *IEEE Transactions on Power Systems*, vol. 37, pp. 343–353, Jan. 2022.

[38] F. Cecati and M. Liserre, "Interoperability specifications for multi-vendor converter-dominated grid: A robust stability perspective," *IEEE Transactions on Smart Grid*, vol. 16, pp. 3003–3016, July 2025.

[39] R. Eriksson, "On the centralized nonlinear control of hvdc systems using lyapunov theory," *IEEE Transactions on Power Delivery*, vol. 28, pp. 1156–1163, Apr. 2013.

[40] G. C. d. Oliveira, G. Damm, R. M. Monaro, L. F. Lourenço, M. J. Carrizosa, and F. Lamnabhi-Lagarrigue, "Nonlinear control for modular multilevel converters with enhanced stability region

and arbitrary closed loop dynamics," *International Journal of Electrical Power & Energy Systems*, vol. 126, p. 106590, Mar. 2021.

[41] H. Khalil, *Nonlinear Systems*, vol. [Hauptbd.]. Upper Saddle River, NJ: Prentice Hall, 3. ed. ed., 2002.

[42] K. Ogata, *Modern control engineering*. Prentice-Hall, 2010.

[43] P. Kundur, *Power system stability and control*. McGraw-Hill, 1994.

[44] P. Rault, F. Colas, X. Guillaud, and S. Nguefeu, "Method for small signal stability analysis of VSC-MTDC grids," in *2012 IEEE Power and Energy Society General Meeting*, IEEE, jul 2012.

[45] H. R. A. Mohamed and Y. A.-R. I. Mohamed, "Active damping of vsc-mtdc grid equipped with interline power flow controller," *IEEE Access*, vol. 10, pp. 54372–54385, 2022.

[46] H. R. A. Mohamed and Y. A.-R. I. Mohamed, "Assessment and Mitigation of DC Breaker Impacts on VSC-MTDC Grid Equipped With Power Flow Controller," *IEEE Open Journal of Power Electronics*, vol. 4, pp. 237–251, 2023.

[47] J. Freytes, S. Akkari, P. Rault, M. M. Belhaouane, F. Gruson, F. Colas, and X. Guillaud, "Dynamic analysis of mmc-based mtdc grids: Use of mmc energy to improve voltage behavior," *IEEE Transactions on Power Delivery*, vol. 34, pp. 137–148, Feb. 2019.

[48] B. Ayalew, M. S. E. Moursi, A. A. Durra, and E. F. El-Saadany, "Dc inertia support scheme for mmcs in hvdc transmission system integrating offshore wind farm," *IEEE Transactions on Power Delivery*, pp. 1–13, 2024.

[49] R. Middlebrook, "Input filter considerations in design and application ofswitching regulators," in *IEEE IAS Annual Meeting, Chicago, USA*, 1976.

[50] J. Sun, "Impedance-Based Stability Criterion for Grid-Connected Inverters," *IEEE Transactions on Power Electronics*, vol. 26, pp. 3075–3078, Nov. 2011.

[51] X. Wang, F. Blaabjerg, and W. Wu, "Modeling and analysis of harmonic stability in an ac power-electronics-based power system," *IEEE Transactions on Power Electronics*, vol. 29, pp. 6421–6432, Dec. 2014.

[52] B. Wen, D. Dong, D. Boroyevich, R. Burgos, P. Mattavelli, and Z. Shen, "Impedance-based analysis of grid-synchronization stability for three-phase paralleled converters," *IEEE Transactions on Power Electronics*, vol. 31, pp. 26–38, Jan. 2016.

[53] T. Roose, *Small-Signal Modeling and Stability Analysis of Multi-Terminal DC Systems for Low- and High-Voltage Applications*. PhD thesis, KU Leuven, 2023.

[54] Y. Liao and X. Wang, "Impedance-based stability analysis for interconnected converter systems with open-loop rhp poles," *IEEE Transactions on Power Electronics*, vol. 35, pp. 4388–4397, Apr. 2020.

[55] M. Amin, M. Molinas, J. Lyu, and X. Cai, "Impact of power flow direction on the stability of vsc-hvdc seen from the impedance nyquist plot," *IEEE Transactions on Power Electronics*, vol. 32, pp. 8204–8217, Oct. 2017.

[56] L. Xu, L. Fan, and Z. Miao, "Dc impedance-model-based resonance analysis of a vsc–hvdc system," *IEEE Transactions on Power Delivery*, vol. 30, pp. 1221–1230, June 2015.

[57] Z. Li, Z. Wang, Y. Wang, T. Yin, N. Mei, B. Yue, and W. Lei, "Accurate impedance modeling and control strategy for improving the stability of dc system in multiterminal mmc-based dc grid," *IEEE Transactions on Power Electronics*, vol. 35, pp. 10026–10049, Oct. 2020.

[58] A. J. Agbemuko, J. L. Dominguez-Garcia, E. Prieto-Araujo, and O. Gomis-Bellmunt, "Advanced Impedance-Based Control Design for Decoupling Multi-Vendor Converter HVDC Grids," *IEEE Transactions on Power Delivery*, vol. 35, pp. 2459–2470, Oct. 2020.

[59] Y. Liao, H. Wu, X. Wang, M. Ndreko, R. Dimitrovski, and W. Winter, "Stability and Sensitivity Analysis of Multi-Vendor, Multi-Terminal HVDC Systems," *IEEE Open Journal of Power Electronics*, vol. 4, pp. 52–66, 2023.

[60] C. Zhang, H. Zong, X. Cai, and M. Molinas, "On the relation of nodal admittance- and loop gain-model based frequency-domain modal methods for converters-dominated systems," *IEEE Transactions on Power Systems*, vol. 38, pp. 1779–1782, Mar. 2023.

[61] T. Roose, D. Lee, and J. Beerten, "Hybrid mimo method for impedance-based stability analysis of mtdc systems," *International Journal of Electrical Power & Energy Systems*, vol. 172, p. 111254, Nov. 2025.

[62] M. Amin and M. Molinas, "Small-signal stability assessment of power electronics based power systems: A discussion of impedance- and eigenvalue-based methods," *IEEE Transactions on Industry Applications*, vol. 53, pp. 5014–5030, Sept. 2017.

[63] L. Liu, A. Shetgaonkar, and A. Lekić, "Interoperability of classical and advanced controllers in MMC based MTDC power system," *International Journal of Electrical Power and Energy Systems*, vol. 148, p. 108980, June 2023.

[64] P. Rault, O. Despouys, A. Petit, H. Saad, D. Vozikis, S. Gao, J. Freytes, M. Narayanan, M. Ramet, M. Zeller, and P. Askvid, "Implementation of a dedicated control to limit adverse interaction in multi-vendor HVDC systems," in *15th IET International Conference on AC and DC Power Transmission (ACDC 2019)*, Institution of Engineering and Technology, 2019.

[65] A. Riccobono and E. Santi, "Comprehensive review of stability criteria for dc power distribution systems," *IEEE Transactions on Industry Applications*, vol. 50, pp. 3525–3535, Sept. 2014.

[66] Y. Liao, X. Wang, and F. Blaabjerg, "Passivity-based analysis and design of linear voltage controllers for voltage-source converters," *IEEE Open Journal of the Industrial Electronics Society*, vol. 1, pp. 114–126, 2020.

[67] R. Marquardt, A. Lesnicar, and J. Hildinger, "Modulares stromrichterkonzept für netzkupplungsanwendung beihohen spannungen," in *The ETG-Fachtagung*, 2002.

[68] S. P. Teeuwsen, "Modeling the trans bay cable project as voltage-sourced converter with modular multilevel converter design," in *2011 IEEE Power and Energy Society General Meeting*, pp. 1–8, IEEE, July 2011.

[69] M. A. Perez, S. Ceballos, G. Konstantinou, J. Pou, and R. P. Aguilera, "Modular multilevel converters: Recent achievements and challenges," *IEEE Open Journal of the Industrial Electronics Society*, vol. 2, pp. 224–239, 2021.

[70] R. Marquardt, "Modular multilevel converter: An universal concept for hvdc-networks and extended dc-bus-applications," in *The 2010 International Power Electronics Conference - ECCE ASIA -*, IEEE, June 2010.

[71] K. Sharifabadi, L. Harnefors, R. Teodorescu, S. Norrga, and H. P. Nee, *Design, Control, and Application of Modular Multilevel Converters for HVDC Transmission Systems*. Wiley and Sons, Incorporated, John, 2016.

[72] H. Saad, X. Guillaud, J. Mahseredjian, S. Dennetiere, and S. Nguefeu, "MMC Capacitor Voltage Decoupling and Balancing Controls," *IEEE Transactions on Power Delivery*, vol. 30, pp. 704–712, apr 2015.

[73] J. Peralta, H. Saad, S. Dennetiere, J. Mahseredjian, and S. Nguefeu, "Detailed and averaged models for a 401-level mmc–hvdc system," *IEEE Transactions on Power Delivery*, vol. 27, pp. 1501–1508, July 2012.

[74] H. Saad, J. Peralta, S. Dennetiere, J. Mahseredjian, J. Jatskevich, J. A. Martinez, A. Davoudi, M. Saeedifard, V. Sood, X. Wang, J. Cano, and A. Mehrizi-Sani, "Dynamic averaged and simplified models for mmc-based hvdc transmission systems," *IEEE Transactions on Power Delivery*, vol. 28, pp. 1723–1730, July 2013.

[75] H. Saad, S. Dennetiere, J. Mahseredjian, P. Delarue, X. Guillaud, J. Peralta, and S. Nguefeu, "Modular Multilevel Converter Models for Electromagnetic Transients," *IEEE Transactions on Power Delivery*, vol. 29, pp. 1481–1489, jun 2014.

[76] H. Zhang, M. M. Belhaouane, F. Colas, R. Kadri, F. Gruson, and X. Guillaud, "On comprehensive description and analysis of mmc control design: Simulation and experimental study," *IEEE Transactions on Power Delivery*, vol. 36, pp. 244–253, Feb. 2021.

[77] A. Zama, A. Benchaib, S. Bacha, D. Frey, S. Silvant, and D. Georges, "Linear feedback dead-beat control for modular multilevel converters: Validation under faults grid operation mode," *IEEE Transactions on Industrial Electronics*, vol. 68, pp. 3181–3191, Apr. 2021.

[78] H. Yang, Y. Chen, W. Li, X. He, W. Sun, Y. Chi, and Y. Li, "Average-value model of modular multilevel converters considering capacitor voltage," in *2016 IEEE Applied Power Electronics Conference and Exposition (APEC)*, pp. 1462–1467, IEEE, Mar. 2016.

[79] A. Beddard, C. E. Sheridan, M. Barnes, and T. C. Green, "Improved Accuracy Average Value Models of Modular Multilevel Converters," *IEEE Transactions on Power Delivery*, vol. 31, pp. 2260–2269, oct 2016.

[80] G. Song, T. Wang, X. Huang, and C. Zhang, "An improved averaged value model of mmc-hvdc for power system faults simulation," *International Journal of Electrical Power & Energy Systems*, vol. 110, pp. 223–231, Sept. 2019.

[81] J. Freytes, *Small-signal stability analysis of Modular Multilevel Converters and application to MMC-based Multi-Terminal DC grids*. PhD thesis, CENTRALE LILLE, 2017.

[82] K. Ilves, A. Antonopoulos, S. Norrga, and H.-P. Nee, "Steady-state analysis of interaction between harmonic components of arm and line quantities of modular multilevel converters," *IEEE Transactions on Power Electronics*, vol. 27, pp. 57–68, Jan. 2012.

[83] Q. Tu, Z. Xu, and L. Xu, "Reduced Switching-Frequency Modulation and Circulating Current Suppression for Modular Multilevel Converters," *IEEE Transactions on Power Delivery*, vol. 26, pp. 2009–2017, jul 2011.

[84] D. C. Ludois and G. Venkataramanan, "Simplified terminal behavioral model for a modular multilevel converter," *IEEE Transactions on Power Electronics*, vol. 29, pp. 1622–1631, Apr. 2014.

[85] J. Freytes, S. Akkari, J. Dai, F. Gruson, P. Rault, and X. Guillaud, "Small-signal state-space modeling of an HVDC link with modular multilevel converters," in *2016 IEEE 17th Workshop on Control and Modeling for Power Electronics (COMPEL)*, IEEE, jun 2016.

[86] N.-T. Trinh, M. Zeller, K. Wuerflinger, and I. Erlich, "Generic model of mmc-vsc-hvdc for interaction study with ac power system," *IEEE Transactions on Power Systems*, vol. 31, pp. 27–34, Jan. 2016.

[87] J. Beerten, G. B. Diaz, S. D'Arco, and J. A. Suul, "Comparison of small-signal dynamics in mmc and two-level vsc hvdc transmission schemes," in *2016 IEEE International Energy Conference (ENERGYCON)*, pp. 1–6, IEEE, Apr. 2016.

[88] R. Irnawan, F. da Silva, C. Bak, and T. Bregnhoj, "Evaluation of half-bridge modular multilevel converter model for vsc-hvdc transient stability studies," in *13th IET International Conference on AC and DC Power Transmission (ACDC 2017)*, pp. 17 (6 .)–17 (6 .), Institution of Engineering and Technology, 2017.

[89] A. Antonopoulos, L. Angquist, and H.-P. Nee, "On dynamics and voltage control of the Modular Multilevel Converter," in *13th European Conference on Power Electronics and Applications*, 2009.

[90] A. a. J. Far and D. Jovcic, "Circulating current suppression control dynamics and impact on MMC converter dynamics," in *2015 IEEE Eindhoven PowerTech*, IEEE, June 2015.

[91] V. Najmi, M. N. Nazir, and R. Burgos, "A new modeling approach for modular multilevel converter (mmc) in d-q frame," in *2015 IEEE Applied Power Electronics Conference and Exposition (APEC)*, pp. 2710–2717, IEEE, Mar. 2015.

[92] G. Bergna, J. A. Suul, and S. D' Arco, "State-space modelling of modular multilevel converters for constant variables in steady-state," in *2016 IEEE 17th Workshop on Control and Modeling for Power Electronics (COMPEL)*, pp. 1–9, IEEE, June 2016.

[93] J. Freytes, G. Bergna, J. Are Suul, S. D' Arco, H. Saad, and X. Guillaud, "State-space modelling with steady-state time invariant representation of energy based controllers for modular multilevel converters," in *2017 IEEE Manchester PowerTech*, pp. 1–7, IEEE, June 2017.

[94] G. F. Gontijo, M. K. Bakhshizadeh, L. H. Kocewiak, and R. Teodorescu, "State space modeling of an offshore wind power plant with an mmc-hvdc connection for an eigenvalue-based stability analysis," *IEEE Access*, vol. 10, pp. 82844–82869, 2022.

[95] F. Z. Dejene, M. Abedrabbo, G. Bergna-Diaz, J. Beerten, and D. Van Hertem, "Design of robust mmc controls considering hvdc grid protection: Small signal-based tuning," *IEEE Transactions on Power Delivery*, vol. 36, pp. 3914–3924, Dec. 2021.

[96] T. Li, A. M. Gole, and C. Zhao, "Harmonic instability in mmc-hvdc converters resulting from internal dynamics," *IEEE Transactions on Power Delivery*, vol. 31, pp. 1738–1747, Aug. 2016.

[97] N. R. Chaudhuri, R. Oliveira, and A. Yazdani, "Stability Analysis of Vector-Controlled Modular Multilevel Converters in Linear Time-Periodic Framework," *IEEE Transactions on Power Electronics*, vol. 31, pp. 5255–5269, jul 2016.

[98] J. Zhu, J. Hu, S. Wang, and M. Wan, "Small-signal modeling and analysis of mmc under unbalanced grid conditions based on linear time-periodic (ltp) method," *IEEE Transactions on Power Delivery*, vol. 36, pp. 205–214, Feb. 2021.

[99] Z. Xu, B. Li, L. Han, J. Hu, S. Wang, S. Zhang, and D. Xu, "A complete hss-based impedance model of mmc considering grid impedance coupling," *IEEE Transactions on Power Electronics*, vol. 35, pp. 12929–12948, Dec. 2020.

[100] J. Lyu, X. Zhang, X. Cai, and M. Molinas, "Harmonic state-space based small-signal impedance modeling of a modular multilevel converter with consideration of internal harmonic dynamics," *IEEE Transactions on Power Electronics*, vol. 34, pp. 2134–2148, Mar. 2019.

[101] S. Huang, J. Xu, K. Wang, G. Li, and F. Xing, "Harmonic space-state based analytical modeling of modular multilevel converters for fast simulation," in *2023 IEEE 14th International Symposium on Power Electronics for Distributed Generation Systems (PEDG)*, pp. 1059–1066, IEEE, June 2023.

[102] P. De Rua, O. C. Sakinci, and J. Beerten, "Comparative study of dynamic phasor and harmonic state-space modeling for small-signal stability analysis," *Electric Power Systems Research*, vol. 189, p. 106626, Dec. 2020.

[103] L. Harnefors, A. Antonopoulos, and H.-P. Nee, "Global asymptotic stability of modular multilevel converters with measurement lag and circulating-current control," in *2013 15th European Conference on Power Electronics and Applications (EPE)*, pp. 1–10, IEEE, Sept. 2013.

[104] W. Wang, *Operation, Control and Stability Analysis of Multi-Terminal VSC-HVDC Systems*. PhD thesis, The University of Manchester, 2015.

[105] A. Yazdani and R. Iravani, *Voltage-Sourced Converters in Power Systems Modeling, Control, and Applications*. Wiley & Sons, Incorporated, John, 2010.

[106] H. Saad, *MODÉLISATION ET SIMULATION D'UNE LIAISON HVDCDE TYPE VSC-MMC*. PhD thesis, École Polytechnique de Montréal, Mar. 2015.

[107] K. Shinoda, J. Freytes, A. Benchaib, J. Dai, H. Saad, and X. Guillaud, "Energy difference controllers for mmc without dc current perturbations," in *2nd International Conferenceon HVDC (HVDC2016 - CIGRE)*, 2016.

[108] E. Sanchez-Sanchez, E. Prieto-Araujo, and O. Gomis-Bellmunt, "The Role of the Internal Energy in MMCs Operating in Grid-Forming Mode," *IEEE Journal of Emerging and Selected Topics in Power Electronics*, vol. 8, pp. 949–962, jun 2020.

[109] J. Arévalo-Soler, E. Sánchez-Sánchez, E. Prieto-Araujo, and O. Gomis-Bellmunt, "Impact analysis of energy-based control structures for grid-forming and grid-following MMC on power system dynamics based on eigenproperties indices," *International Journal of Electrical Power and Energy Systems*, vol. 143, p. 108369, Dec. 2022.

[110] ENTSO-E, "Grid forming capability of power park modules," tech. rep., ENTSO-E, 2025.

[111] N. Mohammed, S. Ahmed, and C. Konstantinou, "Comparative frequency- and time-domain analysis of four grid-forming inverters: Droop, vsm, matching, and dvoc," *International Journal of Electrical Power & Energy Systems*, vol. 172, p. 111302, Nov. 2025.

[112] F. Kelada, J. Buire, and N. HadjSaid, "Comparative study of decentralized grid-forming converter controls for inverter-based microgrids," in *2023 IEEE Power & Energy Society General Meeting (PESGM)*, pp. 1–5, IEEE, July 2023.

[113] A. Tayyebi, D. Gross, A. Anta, F. Kupzog, and F. Dorfler, "Frequency stability of synchronous machines and grid-forming power converters," *IEEE Journal of Emerging and Selected Topics in Power Electronics*, vol. 8, pp. 1004–1018, June 2020.

[114] T. Qoria, *Grid-forming control to achieve a 100% power electronics interfaced power transmission systems*. PhD thesis, Ecole Nationale Superieure de Arts et Metiers, 2020.

[115] Y. Gu, W. Li, and X. He, "Analysis and Control of Bipolar LVDC Grid With DC Symmetrical Component Method," *IEEE Transactions on Power Systems*, vol. 31, pp. 685–694, jan 2016.

[116] J. Freytes, T. Qoria, O. Jasim, C. Barker, S. Trivedi, and K. K. Math, "Power pole balancing control methods for hvdc bipole offshore schemes," *IET Conference Proceedings*, vol. 2025, pp. 205–209, Apr. 2025.

[117] W. B4.58, "Control Methodologies for Direct Voltage and Power Flow in a Meshed HVDC Grid," tech. rep., CIGRE, 2017.

[118] J. Beerten and R. Belmans, "Analysis of Power Sharing and Voltage Deviations in Droop-Controlled DC Grids," *IEEE Transactions on Power Systems*, vol. 28, pp. 4588–4597, nov 2013.

[119] W. Wang and M. Barnes, "Power Flow Algorithms for Multi-Terminal VSC-HVDC With Droop Control," *IEEE Transactions on Power Systems*, vol. 29, pp. 1721–1730, jul 2014.

[120] E. Jiménez, M. J. Carrizosa, A. Benchaib, G. Damm, and F. Lamnabhi-Lagarrigue, "A new generalized power flow method for multi connected dc grids," *International Journal of Electrical Power & Energy Systems*, vol. 74, pp. 329–337, Jan. 2016.

[121] J.-C. Fernandez-Perez, F. M. Echavarren Cerezo, and L. Rouco Rodriguez, "Linear power flow algorithm with losses for multi-terminal vsc ac/dc power systems," *IEEE Transactions on Power Systems*, vol. 37, pp. 1739–1749, May 2022.

[122] B. Li, W. Wang, Y. Liu, B. Li, and W. Wen, "Research on power flow calculation method of true bipolar vsc-hvdc grids with different operation modes and control strategies," *International Journal of Electrical Power & Energy Systems*, vol. 126, p. 106558, Mar. 2021.

[123] "Definition of a standard processfor interaction studies with emtsimulation in multi-vendorprojects," tech. rep.

[124] J.-O. Lee, Y.-S. Kim, and J.-H. Jeon, "Generic power flow algorithm for bipolar DC microgrids based on Newton–Raphson method," *International Journal of Electrical Power and Energy Systems*, vol. 142, p. 108357, nov 2022.

[125] C. K. Jat, F. G. Puricelli, J. Beerten, H. Ergun, and D. V. Hertem, "Unified power flow model for bipolar hvdc grids in unbalanced operation," *IEEE Transactions on Power Systems*, pp. 1–13, 2025.

[126] C. Cardozo, H. Clémot, B. de Foucaud, J. Pouget, P. Rault, S. Dennetière, T. Qoria, and S. Hansen, "Design of bipolar mt hvdc grids: Contingency analysis and preliminary dynamic studies," *Electric Power Systems Research*, vol. 251, p. 112201, Feb. 2026.

[127] InterOPERA, "Detailed functional specifications - overall demonstrator definition," tech. rep., D3.3n, 2025.

[128] T. Nakajima and S. Irokawa, "A control system for hvdc transmission by voltage sourced converters," in *199 IEEE Power Engineering Society Summer Meeting. Conference Proceedings (Cat. No.99CH36364)*, vol. 2 of *PESS-99*, pp. 1113–1119, IEEE.

[129] W. Lu and B.-T. Ooi, "Dc overvoltage control during loss of converter in multiterminal voltage-source converter-based hvdc (m-vsc-hvdc)," *IEEE Transactions on Power Delivery*, vol. 18, pp. 915–920, July 2003.

[130] ENTSO-E, "Network Code on Load-Frequency Control and Reserves," tech. rep., ENTSO-E, 2013.

[131] N. R. Chaudhuri and B. Chaudhuri, "Adaptive Droop Control for Effective Power Sharing in Multi-Terminal DC (MTDC) Grids," *IEEE Transactions on Power Systems*, vol. 28, pp. 21–29, feb 2013.

[132] Y. Li, J. Zhao, H. Liu, Q. Kong, Y. Zhao, L. Cheng, and Z. Wang, "Adaptive Droop Control of the VSC-MTDC Distribution Network Considering Power & Voltage Deviation," *Frontiers in Energy Research*, vol. 9, feb 2022.

[133] Y. Wang, F. Qiu, G. Liu, M. Lei, C. Yang, and C. Wang, "Adaptive Reference Power Based Voltage Droop Control for VSC-MTDC Systems," *Journal of Modern Power Systems and Clean Energy*, vol. 11, no. 1, pp. 381–388, 2023.

[134] EU, "Establishing a guideline on electricity transmission system operation 2017/1485," tech. rep., COMMISSION REGULATION, 2017.

[135] C. D. Barker and R. S. Whitehouse, "Further developments in autonomous converter control in a multi-terminal hvdc system," in *10th IET International Conference on AC and DC Power Transmission (ACDC 2012)*, pp. 1–6, 2012.

[136] T. K. Vrana, L. Zeni, and O. B. Fosso, "Dynamic active power control with improved undead-band droop for hvdc grids," in *10th IET International Conference on AC and DC Power Transmission (ACDC 2012)*, pp. 1–6, 2012.

[137] K. Shinoda, A. Benchaib, J. Dai, and X. Guillaud, "Over- and Under-Voltage Containment Reserves for Droop-Based Primary Voltage Control of MTDC Grids," *IEEE Transactions on Power Delivery*, vol. 37, pp. 125–135, feb 2022.

[138] K. Shinoda, M. Elsodany, J.-C. Gonzalez, J. Dai, A. Benchaib, and S. Bacha, "Comparison between DC Voltage Droop Schemes and Grid-Following & Grid-Forming Control in AC Systems in View of Interoperability of MTDC grids," in *2023 25th European Conference on Power Electronics and Applications (EPE'23 ECCE Europe)*, IEEE, sep 2023.

[139] W. Wang, M. Barnes, and O. Marjanovic, "Stability limitation and analytical evaluation of voltage droop controllers for VSC MTDC," *CSEE Journal of Power and Energy Systems*, vol. 4, pp. 238–249, jun 2018.

[140] F. Thams, S. Chatzivasileiadis, and R. Eriksson, "DC voltage droop control structures and its impact on the interaction modes in interconnected AC-HVDC systems," in *2017 IEEE Innovative Smart Grid Technologies - Asia (ISGT-Asia)*, IEEE, dec 2017.

[141] M. Elsodany, K. Shinoda, J. Dai, A. Bertinato, and S. Bacha, "Assessment of two dc voltage droop options for small-signal stability in mmc-based multi-terminal dc grids," in *13th International Conference on Power Electronics, Machines and Drives (PEMD 2024)*, pp. 497–504, Institution of Engineering and Technology, 2024.

[142] J. Beerten, S. D'Arco, and J. Suul, "Cable Model Order Reduction for HVDC Systems Interoperability Analysis," in *11th IET International Conference on AC and DC Power Transmission*, Institution of Engineering and Technology, 2015.

[143] D2.2, "Grid-forming functional requirements for hvdc converter stations and dcconnected power park modules in multi-terminal multi-vendor hvdc systems," tech. rep., InterOPERA, 2024.

[144] E. Rokrok, T. Qoria, A. Bruyere, B. Francois, and X. Guillaud, "Classification and dynamic assessment of droop-based grid-forming control schemes: Application in HVDC systems," *Electric Power Systems Research*, vol. 189, p. 106765, dec 2020.

[145] J. Rocabert, A. Luna, F. Blaabjerg, and P. Rodríguez, "Control of power converters in ac microgrids," *IEEE Transactions on Power Electronics*, vol. 27, pp. 4734–4749, Nov. 2012.

[146] L. Zhang, L. Harnefors, and H.-P. Nee, "Power-Synchronization Control of Grid-Connected Voltage-Source Converters," *IEEE Transactions on Power Systems*, vol. 25, pp. 809–820, may 2010.

[147] L. Harnefors, M. Hinkkanen, U. Riaz, F. M. M. Rahman, and L. Zhang, "Robust analytic design of power-synchronization control," *IEEE Transactions on Industrial Electronics*, vol. 66, pp. 5810–5819, Aug. 2019.

[148] B. B. Johnson, S. V. Dhople, A. O. Hamadeh, and P. T. Krein, "Synchronization of parallel single-phase inverters with virtual oscillator control," *IEEE Transactions on Power Electronics*, vol. 29, pp. 6124–6138, Nov. 2014.

[149] M. Colombino, D. Groz, J.-S. Brouillon, and F. Dorfler, "Global phase and magnitude synchronization of coupled oscillators with application to the control of grid-forming power inverters," *IEEE Transactions on Automatic Control*, vol. 64, pp. 4496–4511, Nov. 2019.

[150] D. Gros, M. Colombino, J.-S. Brouillon, and F. Dorfler, "The effect of transmission-line dynamics on grid-forming dispatchable virtual oscillator control," *IEEE Transactions on Control of Network Systems*, vol. 6, pp. 1148–1160, Sept. 2019.

[151] Q.-C. Zhong and G. Weiss, "Synchronverters: Inverters that mimic synchronous generators," *IEEE Transactions on Industrial Electronics*, vol. 58, pp. 1259–1267, Apr. 2011.

[152] S. D'Arco, J. A. Suul, and O. B. Fosso, "A Virtual Synchronous Machine implementation for distributed control of power converters in SmartGrids," *Electric Power Systems Research*, vol. 122, pp. 180–197, may 2015.

[153] K. M. Cheema, "A comprehensive review of virtual synchronous generator," *International Journal of Electrical Power & Energy Systems*, vol. 120, p. 106006, Sept. 2020.

[154] R. Ofir, U. Markovic, P. Aristidou, and G. Hug, "Droop vs. virtual inertia: Comparison from the perspective of converter operation mode," in *2018 IEEE International Energy Conference (ENERGYCON)*, pp. 1–6, IEEE, June 2018.

[155] E. Rokrok, T. Qoria, A. Bruyere, B. Francois, and X. Guillaud, "Effect of Using PLL-Based Grid-Forming Control on Active Power Dynamics Under Various SCR," in *IECON 2019 - 45th Annual Conference of the IEEE Industrial Electronics Society*, IEEE, oct 2019.

[156] C. Arghir and F. Dorfler, "The Electronic Realization of Synchronous Machines: Model Matching, Angle Tracking, and Energy Shaping Techniques," *IEEE Transactions on Power Electronics*, vol. 35, pp. 4398–4410, Apr. 2020.

[157] C. Arghir, T. Jouini, and F. Dörfler, "Grid-forming control for power converters based on matching of synchronous machines," *Automatica*, vol. 95, pp. 273–282, Sept. 2018.

[158] L. Huang, H. Xin, Z. Wang, K. Wu, H. Wang, J. Hu, and C. Lu, "A Virtual Synchronous Control for Voltage-Source Converters Utilizing Dynamics of DC-Link Capacitor to Realize Self-Synchronization," *IEEE Journal of Emerging and Selected Topics in Power Electronics*, vol. 5, pp. 1565–1577, Dec. 2017.

[159] Y. Pang, A. Egea-Alvarez, J. C. Gonzalez-Torres, K. Shinoda, F. Perez, and A. Benchaib, "Dc voltage stability analysis and enhancement for grid-forming-based mtdc systems," *IEEE Transactions on Power Electronics*, pp. 1–4, 2024.

[160] G. Shafique, J. Boukhenfouf, F. Gruson, F. Colas, and X. Guillaud, "Dc voltage control with grid-forming capability for enhancing stability of hvdc system," *Journal of Modern Power Systems and Clean Energy*, vol. 13, no. 1, pp. 66–78, 2024.

[161] Y. Wang, Z. Yuan, J. Fu, Y. Li, and Y. Zhao, "A feasible coordination protection strategy for mmc-mtdc systems under dc faults," *International Journal of Electrical Power & Energy Systems*, vol. 90, pp. 103–111, 2017.

[162] P. Torwelle, A. Bertinato, B. Raison, T. D. Le, and M. Petit, "Fault current calculation in mtdc grids considering mmc blocking," *Electric Power Systems Research*, vol. 207, p. 107662, June 2022.

[163] F. Mohammadi, K. Rouzbehi, M. Hajian, K. Niayesh, G. B. Gharehpetian, H. Saad, M. Hasan Ali, and V. K. Sood, "Hvdc circuit breakers: A comprehensive review," *IEEE Transactions on Power Electronics*, vol. 36, pp. 13726–13739, Dec. 2021.

[164] C. Foote, S. Rangasamy, A. Khan, B. Marshall, A. Bertinato, H. Bekkouri, S. Neira Castillo, P. Judge, S. Finney, and S. S. H. Yazdi, "Options for mitigating converter blocking during clearance of dc faults," *IET Conference Proceedings*, vol. 2025, pp. 332–338, Apr. 2025.

[165] W. Wang, M. Barnes, O. Marjanovic, and O. Cwikowski, "Impact of DC Breaker Systems on Multiterminal VSC-HVDC Stability," *IEEE Transactions on Power Delivery*, vol. 31, pp. 769–779, apr 2016.

[166] X. Lu, W. Xiang, W. Lin, and J. Wen, "Small-signal modeling of mmc based dc grid and analysis of the impact of dc reactors on the small-signal stability," *International Journal of Electrical Power and Energy Systems*, vol. 101, pp. 25–37, Oct. 2018.

[167] K. Shinoda, A. Benchaib, and J. Dai, "Small-Signal Stability of HVDC System Comprising DC Reactors," in *2020 22nd European Conference on Power Electronics and Applications (EPE 20 ECCE Europe)*, IEEE, Sept. 2020.

[168] J. Freytes, P. Rault, F. Gruson, F. Colas, and X. Guillaud, "Dynamic impact of mmc controllers on dc voltage droop controlled mtdc grids," in *2016 18th European Conference on Power Electronics and Applications (EPE 16 ECCE Europe)*, pp. 1–10, IEEE, Sept. 2016.

[169] J. Freytes, F. Gruson, F. Colas, P. Rault, H. Saad, and X. Guillaud, "Simplified Model of Droop-Controlled MTDC Grid-Influence of MMC Energy Management on DC System Dynamics," in *2018 Power Systems Computation Conference (PSCC)*, IEEE, jun 2018.

[170] K. Shinoda, A. Benchaib, J. Dai, and X. Guillaud, "Virtual Capacitor Control: Mitigation of DC Voltage Fluctuations in MMC-Based HVdc Systems," *IEEE Transactions on Power Delivery*, vol. 33, pp. 455–465, feb 2018.

[171] E. Sanchez-Sanchez, E. Prieto-Araujo, A. Junyent-Ferre, and O. Gomis-Bellmunt, "Analysis of MMC Energy-Based Control Structures for VSC-HVDC Links," *IEEE Journal of Emerging and Selected Topics in Power Electronics*, vol. 6, pp. 1065–1076, sep 2018.

[172] S. Samimi, F. Gruson, P. Delarue, F. Colas, M. M. Belhaouane, and X. Guillaud, "Mmc stored energy participation to the dc bus voltage control in an hvdc link," *IEEE Transactions on Power Delivery*, vol. 31, pp. 1710–1718, Aug. 2016.

[173] M. Cespedes, L. Xing, and J. Sun, "Constant-power load system stabilization by passive damping," *IEEE Transactions on Power Electronics*, vol. 26, pp. 1832–1836, July 2011.

[174] J. Beerten, S. D'Arco, and J. A. Suul, "Identification and Small-Signal Analysis of Interaction Modes in VSC MTDC Systems," *IEEE Transactions on Power Delivery*, vol. 31, pp. 888–897, Apr. 2016.

[175] Q. Fu, W. Du, H. Wang, B. Ren, and X. Xiao, "Small-Signal Stability Analysis of a VSC-MTDC System for Investigating DC Voltage Oscillation," *IEEE Transactions on Power Systems*, vol. 36, pp. 5081–5091, nov 2021.

[176] A. J. Agbemuko, J. L. Domínguez-García, E. Prieto-Araujo, and O. Gomis-Bellmunt, "Dynamic modelling and interaction analysis of multi-terminal vsc-hvdc grids through an impedance-based approach," *International Journal of Electrical Power and Energy Systems*, vol. 113, pp. 874–887, Dec. 2019.

[177] Y. Zhou, D. D. Nguyen, P. C. Kjær, and S. Saylors, "Connecting wind power plant with weak grid - challenges and solutions," in *2013 IEEE Power & Energy Society General Meeting*, pp. 1–7, IEEE, 2013.

[178] Y. Zhang, S.-H. F. Huang, J. Schmall, J. Conto, J. Billo, and E. Rehman, "Evaluating system strength for large-scale wind plant integration," in *2014 IEEE PES General Meeting | Conference & Exposition*, IEEE, July 2014.

[179] D. Wu, G. Li, M. Javadi, A. M. Malyscheff, M. Hong, and J. N. Jiang, "Assessing impact of renewable energy integration on system strength using site-dependent short circuit ratio," *IEEE Transactions on Sustainable Energy*, vol. 9, pp. 1072–1080, July 2018.

[180] W. Dong, H. Xin, D. Wu, and L. Huang, "Small signal stability analysis of multi-infeed power electronic systems based on grid strength assessment," *IEEE Transactions on Power Systems*, vol. 34, pp. 1393–1403, Mar. 2019.

[181] C. Henderson, A. Egea-Alvarez, P. Papadopoulos, R. Li, L. Xu, R. Da Silva, A. Kinsella, I. Gutierrez, and R. Pabat-Stroe, "Exploring an impedance-based scr for accurate representation of grid-forming converters," in *2022 IEEE Power & Energy Society General Meeting (PESGM)*, pp. 1–5, IEEE, July 2022.

[182] S. O. Sanni, M. F. Akorede, and G. A. Olarinoye, "Strength assessment of electric power systems containing inverter-based distributed generation," *Electric Power Systems Research*, vol. 207, p. 107825, June 2022.

[183] S. O. Sanni, O. O. Mohammed, S. Chakraborty, A. I. Abdullateef, A. O. Otuoze, O. Ikotun, and E. B. Agyekum, "On the choice of system strength metrics for the allocation and sizing of synchronous condensers in power grids," *IEEE Access*, vol. 13, pp. 83781–83793, 2025.

[184] R. Fernandes, S. Achilles, and J. MacDowell, "Report to nerc erstf for composite short circuit ratio (cscr) estimation guideline," *GE Energy Consulting*, 2015.

[185] A. Bayo-Salas, J. Beerten, and D. Van Hertem, "Analytical methodology to develop frequency-dependent equivalents in networks with multiple converters," in *2017 IEEE Manchester PowerTech*, IEEE, June 2017.

[186] A. Ibrahim, "Frequency dependent network equivalents for electromagnetic transients studies: a bibliographical survey," *International Journal of Electrical Power & Energy Systems*, vol. 25, pp. 193–199, Mar. 2003.

[187] W. C4.56, "Electromagnetic transient simulation models for large-scale system impact studies in power systems having a high penetration of inverter-connected generation," Tech. Rep. TB881, CIGRE, 2022.

[188] C. Buchhagen, C. Rauscher, A. Menze, and J. Jung, "Borwin1 - first experiences with harmonic interactions in converter dominated grids," in *International ETG Congress 2015*, 2015.

[189] Y. Lamrani, T. Prevost, C. Cardozo, C. Zanabria, F. Colas, and X. Guillaud, "Frequency-averaged grid impedance metric for identifying weakest buses in power electronics-dominated systems," in *2025 IEEE Kiel PowerTech*, pp. 1–7, IEEE, June 2025.

[190] A. Ramirez, "Vector fitting-based calculation of frequency-dependent network equivalents by frequency partitioning and model-order reduction," *IEEE Transactions on Power Delivery*, vol. 24, pp. 410–415, Jan. 2009.

[191] E. Commission, "Commission regulation (eu) 2016/1447 of 26 august 2016 establishing a network code on requirements for grid connection of high voltage direct current systems and direct current-connected power park modules," *Official Journal of the European Union*, 2016.

[192] E. Prieto-Araujo, A. Egea-Alvarez, S. Fekriasl, and O. Gomis-Bellmunt, "DC Voltage Droop Control Design for Multiterminal HVDC Systems Considering AC and DC Grid Dynamics," *IEEE Transactions on Power Delivery*, vol. 31, pp. 575–585, apr 2016.

[193] J. Beerten, *Modeling and Control of DC Grids*. PhD thesis, KU Leuven, 2013.

[194] G. Bergna, J. A. Suul, and S. D'Arco, "Impact on small-signal dynamics of using circulating currents instead of ac-currents to control the dc voltage in mmc hvdc terminals," in *2016 IEEE Energy Conversion Congress and Exposition (ECCE)*, pp. 1–8, IEEE, Sept. 2016.

[195] J. Freytes, G. Bergna, J. A. Suul, S. D'Arco, F. Gruson, F. Colas, H. Saad, and X. Guillaud, "Improving small-signal stability of an mmc with ccsc by control of the internally stored energy," *IEEE Transactions on Power Delivery*, vol. 33, pp. 429–439, Feb. 2018.

[196] G. Bergna-Diaz, J. A. Suul, and S. D'Arco, "Energy-Based State-Space Representation of Modular Multilevel Converters with a Constant Equilibrium Point in Steady-State Operation," *IEEE Transactions on Power Electronics*, vol. 33, pp. 4832–4851, jun 2018.

[197] F. Ahmadloo and S. P. Azad, "Identifying suitable DC system models for an independent design of VSC controllers in MTDC grids," *International Journal of Electrical Power & Energy Systems*, vol. 153, p. 109380, nov 2023.

[198] B. Wen, D. Boroyevich, R. Burgos, P. Mattavelli, and Z. Shen, "Analysis of d-q small-signal impedance of grid-tied inverters," *IEEE Transactions on Power Electronics*, vol. 31, pp. 675–687, Jan. 2016.

[199] B. Gustavsen and A. Semlyen, "Rational approximation of frequency domain responses by vector fitting," *IEEE Transactions on Power Delivery*, vol. 14, pp. 1052–1061, July 1999.

[200] F. G. Puricelli and J. Beerten, "Evaluation of interactions between bipolar hvdc connections with grid-forming converters," *IET Conference Proceedings*, vol. 2025, pp. 85–90, Apr. 2025.

[201] Y. Pang, A. Egea-Alvarez, X. Wang, J. Carlos Gonzalez-Torres, F. Perez, and A. Benchaib, "DC Stability Analysis of Bipolar Grid-Forming MMC Stations in Multi-Terminal HVDC Grids." working paper or preprint, Feb. 2026.

[202] P. Düllmann and W. Leterme, "Functional specification and testing of converter dc-frt in multi-vendor multi-terminal hvdc systems," Apr. 2025.

[203] G. Chaffey, I. Jahn, M. Hoffmann, R. A. Valenzuela, E. P. Araujo, and S. Norrga, "Functional modelling for hvdc grids – state-of-the-art and future outlook," in *Proceedings of the CIGRE Session 2024*, (Paris, France), CIGRE, 2024. Study Committee B4: DC systems and power electronics.

[204] C. J. O'Rourke, M. M. Qasim, M. R. Overlin, and J. L. Kirtley, "A Geometric Interpretation of Reference Frames and Transformations: dq0, Clarke, and Park," *IEEE Transactions on Energy Conversion*, vol. 34, pp. 2070–2083, dec 2019.